Study of multi-scale interaction and dissipation based on gyro-kinetic model in fusion plasmas

This PhD thesis has been carried out by

Paul P. Hilscher

at the

Graduate School of Energy Science,
Department of Fundamental Energy Science

under the supervision of

Prof. Yasuaki Kishimoto

Abstract

A successful magnetically confinement of plasma requires the understanding and control of turbulence and transport over a vast range of scales, e.g. from large scale MHD fluctuations to micro-scale drift wave turbulence such as the ion (electron) temperature gradient (ITG/ETG) modes, as well as the interaction between those scales, the energy transfer mechanism, and dissipation of energy through stable modes. This thesis is thus devoted to the numerical study of the cross-scale interaction between the ITG instability and a static magnetic island based on a gyrokinetic model.

As a powerful tool to study the multiscale turbulence and interaction, a massive parallel gyrokinetic code, named gkc++ , has been developed first using C++/Cilk+ to handle the huge computational requirements of evolving the five dimensional phase space as an initial value problem (IVP).

Regarding the code's application, the role of stable modes in a mode coupled gyrokinetic system is investigated. The Landau damping in collisionless discretized gyrokinetic Vlasov simulations is known to originate from the phase-mixing of marginally stable Case–van Kampen (CvK) eigenmodes, which leads to a recurrence phenomenon. Using eigenvalue analysis, we show that a collisionality β_c has a strong damping effect on the CvK eigenmodes. Further, we find that there exists a critical collisionality at which the CvK eigenmodes are damped down to the analytically estimated Landau damping rate, then a Landau eigenmode consistent with Landau's theory emerges and the recurrence phenomenon disappears. We discover that the critical collisionality depends on the resolution in velocity space, i.e. a higher (lower) resolution requires a lower (higher) collisionality. In addition, we address whether the stabilization effect of Landau damped stable modes is properly evaluated in a coupled Vlasov-Poisson ITG system, e.g. where the coupling arises from an external vortex flow. It is shown using a reduced model that the stabilization effect of the mode coupling between unstable and stable modes works properly and is not influenced whether Landau damping arises through phase mixing of the CvK eigenmodes or a true Landau eigenmode.

Third, the linear properties of the short-wavelength ITG modes were studied using an integral code. The short wavelength ITG mode was confirmed to exist over a wide range of parameters. In multiscale turbulence simulations using the gkc++ code including a static magnetic island, it is found that a small magnetic island stabilizes the ITG mode by inducing poloidal coupling between unstable and stable modes which enables the dissipation of energy. However, larger islands have a strong destabilization effect through the formation of new rational surfaces. Most importantly, this destabilization effect is mainly caused by the short-wavelength ITG mode due to a resonance effect (double-ITG formation), which is found to originate from its smaller mode structure width and thus is more sensitive to rational surface formation due to the finite-size island.

Acknowledgments

During the last four years of my PhD study, I realized, that this is one thing I could not do alone. I relied on so many people who supported me in my research and my private life and shaped me to become a better scientist and a better (or worse ?) man.

First, I would like to express my gratitude to my supervisors Prof. Yasuaki Kishimoto, Prof. Jiquan Li and Prof. Kenji Imadera for giving me the opportunity of pursuing a PhD in their lab. The discussions with them, were crucial in finding the right viewpoint on my research and "asking" the right questions. I have always admired their ability to formulate scientific ideas in simple to understand terms, I hope that during the years, I learned some of that and their efforts were not in vain. Also I thank my referees Prof. Nakamura and Prof. Maekawa for valuable comments.

To master Japan's everyday life, Ms. Nakamura was of irreplaceable help. She always willingly helped me with filling out lots of paper work and explaining me the Japanese way-of-life. Also, I would like to thank everyone behind the Global COE program of the Kyoto university. The discussions with the professors and students about the environmental issues in relation to CO_2 emission, broadened my viewpoint and greatly enriched my experience of studying at the Kyoto university. In this case, special thanks to Ms. Hirano, who patiently processes all our questions and requests.

A very special thanks goes to my family and my mother, Alice, without her support I would have not been able to finish this PhD study. Also, my fiancee Kana who supported and helped me in every aspect of my life. I thank Waturo, Yuki and Mie, for their great company during numerous occasions at eating Okonomiyake in Waiten or Gyoza at Hanasaki, which always cheered me up during frustrating times.

Further, I would like to thank all the people who shared with me the tears and joy of studying in Japan. Especially the "Ohbaku-gang" (Noony, Maryla, Valerie, John, Martin, ...) made my first years in Japan a joy. Thanks all ! The fun and the experiences I had are unforgettable.

My deepest gratitude goes to Taco bar Masta, who became a mentor and friend during the time in Japan. He patiently endured my complaints and frustration and motivated me to keep on going in times I wanted to throw away everything and go back to Germany; without him, this thesis would have never been written. I thank Reiko and Kanapi.

If studying left enough time, I was very glad to play with the Kyoto university's water polo team and the Kobe water polo team (special thanks to Mr. Kunimasa and Sono). Also, Ali's effort to encourage me to stay healthy and fit by playing table tennis with him will always be highly appreciated.

During the PhD study, I finally learned many things — but in every single second I relied on the things I was taught before, thus my gratitude to Prof. Christlieb, Prof. Dullemonde, Prof. Camenzind, Prof. Hujeirat and the Kepler Seminar, whose efforts were hopefully not in vain. Also I am deeply grateful to all the countless anonymous people who shared their knowledge and their altruistic help on mailing list, blogs, forums and stackoverflow. I thank Nectarine Demoscene Radio for the great tunes during lonely coding nights. Finally, I would like to express my gratitude to all the contributors to open source software, who devoted their spare time and developed the numerous tools I used during my research, especially to mentioned matplotlib, scipy and ipython.

Special thanks goes to Kevin Obrejan, Philippe Mathieu, Federoff Vasiliy, Ali Ahamd and William Pringle for proof-reading this thesis and providing valuable feedback.

Finally, I am grateful to the Japanese society for allowing me to pursue my study in this country and their financial support through the Monbukagakusho scholarship.

September 2013

Dedicated to those who appreciate the sharing of knowledge.

Scientific contributions during this PhD study

Published peer-reviewed papers

- P.P. Hilscher, K. Imadera, J. Q. Li and Y. Kishimoto, "Role of stable modes in the ITG driven instability in a mode coupled system", accepted for publication in Plasma and Fusion Research
- P.P. Hilscher, K. Imadera, J. Q. Li and Y. Kishimoto, "The effect of weak collisionality on damped modes and its contribution to mode coupling in gyrokinetic simulation", Physics of Plasma, (8), 082127 (2013)
- Paul P. Hilscher, Kenji Imadera, Jiquan Li and Yasuaki Kishimoto; "Gyrokinetic Simulations of Short-Wavelength ITG Instability in the Presence of a Static Magnetic Island", Plasma and Fusion Research, 8, 2403040 (2013)
- Jiquan Li, Kenji Imadera, Paul Hilscher, Yasuaki Kishimoto and Zhengxiong Wang; "Multi-Scale Turbulence Simulation in Magnetic Fusion Plasma", Nuclear Science and Technology, 2 (2011)
- Ken-ichi Amano, Daisuke Miyazaki, Liew Fong Fong, Paul Hilscher, Taro Sonobe; "Temperature control technology by heat capacity change upon lock and key binding", Physics Letters A, 2, 375 (2010)

Published non-referred papers

- Paul P. Hilscher, Kenji Imadera, Jiquan Li, and Yasuaki Kishimoto; *Towards Gyrokinetic Simulations of Multi-Scale Micro-Turbulence in Tokamaks*, Proceeding of the Second International Symposium of Globa COE Program, "Energy Science in the Age of Global Warming (..)", pp295-301, 2012
- Paul P. Hilscher, Kenji Imadera, Jiquan Li, and Yasuaki Kishimoto; *Gyro-Kinetic Simulation of ion Temperature Gradient Driven Drift Wave Instability in the Presence of a Magnetic Island*, Special Edition of Jointed Symposium of Kyoto University Global COE and Ajou University, "Energy Science in the Age of Global Warming (..)", pp239-244, 2011

Contents

. **Abstract** iii

. **Acknowledgments** v

. **Scientific contributions** vii

I. Background 1

1. Introduction 3
1.1. Natural occurring fusion processes . . . 3
1.2. The sun in a bottle . . . 5
1.3. Turbulence . . . 7
1.4. Outline of this thesis . . . 8

2. The gyrokinetic Vlasov–Maxwell equations 11
2.1. The gyro-averaging procedure . . . 12
2.2. The single-particle Lagrangian . . . 14
2.3. The guiding-center one-form . . . 15
2.3.1. Transforming the equilibrium quantities . . . 16
2.3.2. Transforming the perturbed quantities . . . 17
2.4. Transformation into the gyro-center coordinates . . . 18
2.5. The gyrokinetic Vlasov equation . . . 21
2.5.1. The δf equation in local slab geometry . . . 22
2.6. The field equations . . . 23
2.6.1. Poisson's equation . . . 24
2.6.2. Ampère's equation for $A_{1\parallel}$ . . . 26
2.7. The gyro-averaging operator in Fourier space . . . 27
2.8. The Lenard–Bernstein collisional operator . . . 28
2.9. Observables . . . 29
2.10. Brief introduction to Tokamak geometry . . . 31

2.10.1. Simplified three dimensional geometries . . . 32
2.10.2. Two-dimensional sheared slab geometry . . . 33
2.10.3. Two-dimensional constant-θ geometry . . . 33

II. Research work **35**

3. Numerical implementation of the gkc++ solver **37**
3.1. Solver internals . . . 37
3.1.1. Numerical grid . . . 37
3.1.2. Calculation of derivatives using finite differences . . . 41
3.1.3. Time step integration . . . 43
3.1.4. The Courant-Levy-Friedrich (CFL) condition . . . 46
3.1.5. Solving the field equations . . . 47
3.1.6. The Vlasov equation . . . 48
3.1.7. Eigenvalue solver . . . 51
3.2. Benchmarking . . . 51
3.2.1. Profiling . . . 52
3.3. Parallelization . . . 52
3.3.1. Overview over state-of-the-art computer architecture . . . 53
3.3.2. Inter CPU parallelization (vectorization) . . . 54
3.3.3. Inter-node parallelization (OpenMP) . . . 56
3.3.4. Intra-node parallelization (MPI) . . . 56
3.3.5. Hybrid-parallelization . . . 60
3.4. Summary . . . 63

4. Eigenvalue analysis of damping in the Vlasov–Poisson system **65**
4.1. Overview of Landau damping . . . 65
4.1.1. Vlasov's approach . . . 67
4.1.2. Landau's approach . . . 67
4.1.3. The plasma dispersion function . . . 70
4.1.4. Case and van Kampen's approach . . . 70
4.2. Derivation of the simplified gyrokinetic equation system . . . 73
4.3. Damping in discretized Vlasov simulations . . . 75
4.4. The discretized gyrokinetic operator . . . 78
4.5. Eigenvalue analysis of the gyrokinetic operator . . . 79
4.6. Mechanism of collisionless Landau damping . . . 80
4.7. Matrix in Fourier–Hermite basis . . . 82
4.7.1. Landau damping in Fourier–Hermite basis . . . 84
4.8. Role of the Lenard-Bernstein collision on the recurrence . . . 86
4.8.1. Effect of diffusive term . . . 90

4.9. Landau damping in Fourier–Hermite basis with collisionality 91
4.10. The role of the CvK eigenmodes in poloidal mode coupling 93
4.11. Summary 100

5. Investigation of ITG and ETG turbulences **101**
5.1. The ion temperature gradient mode 101
5.1.1. Adiabatic electron approximation 102
5.1.2. Linear study 103
5.1.3. The short-wavelength ITG instability 104
5.1.4. Parameter scan over η_i 108
5.1.5. Parameter scan over $\hat{s}$ 108
5.1.6. Quasi-linear heat flux estimates 109
5.2. The electron temperature gradient mode 112
5.2.1. Adiabatic ion response 112
5.2.2. Debye length effects λ_{De} 113
5.3. Nonlinear study of the ETG instability 113
5.3.1. Convergence test on the heat flux 115
5.4. Nonlinear study of the ITG 117
5.4.1. Comparing heat fluxes from ETG with ITG 117
5.4.2. Short-wavelength contributions to heat flux 119
5.5. The ITG with kinetic Electrons (linear case) 121
5.5.1. Parameter scan over m_{ie} 121
5.5.2. Parameter scan over η_e 123
5.6. The ITG with kinetic Electrons (nonlinear case) 123
5.6.1. Parameter scan over m_{ie} 124
5.6.2. Parameter scan over η_e 126
5.6.3. Large scale run 126
5.7. Summary 127

6. The ITG mode in presence of a static magnetic island **129**
6.1. Basic properties of magnetic islands 129
6.1.1. Theoretical investigations 130
6.2. Numerical study of magnetic island formation 130
6.2.1. Introduction to the numerical code 131
6.2.2. Simulation results 131
6.3. Magnetic island influence on the ITG 133
6.3.1. Inclusion of static magnetic perturbation 134
6.3.2. Expanding the ψ Poisson bracket 134
6.3.3. Calculating the magnetic island width 136
6.3.4. Rational surface separation 137
6.4. Linear study of ITG with magnetic island modification 139

6.4.1. Linear dynamics with adiabatic electrons . . . 139
6.4.2. Magnetic island destabilization mechanism . . . 142
6.4.3. Minimal model for destabilization through shw-ITG mode . . . 143
6.4.4. Formation of global mode and zonal flow oscillations . . . 145
6.4.5. Investigation the zonal flow oscillations . . . 146
6.4.6. Parameter scan over η_i . . . 146
6.4.7. Parameter scan over $\hat{s}$ . . . 148
6.4.8. Importance of the flux-surface averaging term . . . 148
6.5. Analysis of ITG on magnetic island including kinetic electrons . . . 149
6.5.1. Parameter scan over the ion-electron mass ratio (m_{ie}) . . . 149
6.5.2. Parameter scan over η_i . . . 151
6.5.3. Parameter scan over η_e . . . 152
6.6. Nonlinear analysis of ITG on magnetic island . . . 153
6.7. Summary . . . 156

7. Outroduction **157**
7.1. Conclusion . . . 157
7.2. Extensions of this PhD study . . . 160
7.2.1. Chapter 3: Improving the gkc++ solver . . . 160
7.2.2. Chapter 4: Landau damping in the discretized system . . . 160
7.2.3. Chapter 5: Short-wavelength destabilization of the ITG . . . 160
7.2.4. Chapter 6: Interactions of ITG, ETG and magnetic island . . . 161
7.3. Final remark . . . 161

Appendix **162**

A. Benchmarking the numerical code **163**
A.1. The plasma dispersion function . . . 163
A.2. Notes on the Bessel functions used in gyrokinetics . . . 165
A.3. Dispersion relation in shearless slab geometry . . . 166
A.3.1. Comparison to the numerical solution . . . 168
A.4. Dispersion relation in non-local geometry . . . 168
A.4.1. Numerical benchmark for sheared slab geometry . . . 169

Bibliography **171**

Part I.

Background

1 | Introduction

Probably the biggest challenge in the 21st century is to reduce and cope with the impact of global warming which is caused by the emission of CO_2, and to establish a carbon free energy supply.

A majority of the energy currently consumed is provided through the burning of fossil fuels such as coal, oil and gas. However, it has been found that the emission of carbon dioxide is affecting earth's climate and leads to a rise in the average global temperatures. Current studies predict that without drastic measures, the average temperatures will rise by more than three degrees by the year 2100, which will endanger the habitats of mankind and many other species, who cannot adapt quick enough to the changing climate conditions. Reducing the emission of greenhouses gases has so far demonstrated to be of very limited success. With the exponential growth of the economies of the less industrialized countries to adopt the living standards of the "western world" and their energy demand to rise by the same level — most of it provided by fossil fuels — CO_2 emission is likely to increase. Hence, the search for alternative and cheap energy supply becomes even more urgent

Renewable energies such as wind, solar and wave energy have shown to be successful to partially replace fossil fueled based energy production. However, to close the gap and completely substitute fossil fuels, nuclear energy production has to be considered as a serious alternative. However, fission based nuclear energy production showed a strong decline in the aftermath of the Fukushima disaster. A promising solution on the horizon is *nuclear fusion*. Nuclear fusion is a very promising technology which is considered to be safe, with a practically unlimited fuel supply and - in contrast to nuclear fission - safe in operation.

1.1 | Natural occurring fusion processes

Life on earth depends on our sun. The sun's light heats the earth to temperatures where water remains mostly liquid and provides an energy source which is used by plants for photosynthesis. Each second the sun releases a tremendous amount of energy in the form of light (4×10^{26}J) which equals 500 000 years of the total energy consumption of the human population (1×10^{21}J). But how does the sun produces its energy ? The answer

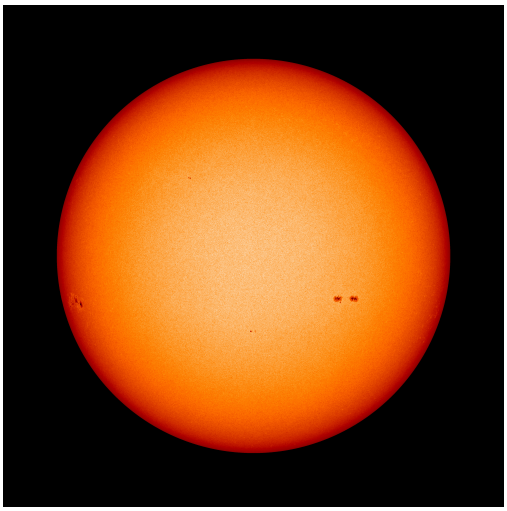

Figure 1.1: *Picture of our sun in the visible spectra taken at February 28, 2013 [image credit : NASA]. The sun is a hot glowing ball of gravitational bound plasma with a surface temperature of 6000K. The energy is produced in the sun's core, where the temperature reaches up to 15.2 Million Kelvin, allowing the ions to overcome the electrostatic repulsion and the fusion of hydrogen into helium. It is estimated that the sun's fusion process has lasted for over 4.6 billion years and will continue to do so for another 5 billion years.*

to this question wasn't found until von Weizsäcker (1937) and von Weizsäcker (1938). Our sun shown in Fig. 1.1 mainly consist of ionized hydrogen particles (97%) with a fraction of ionized helium particles. At the sun's core, the temperature and density is large enough so that the hydrogen ions are fast enough to overcome the repulsive electrostatic force between each other and come close enough to form a diproton. In most cases, the diproton quickly decays again into separate protons, however, within a very small likelihood the *weak nuclear force* triggers the β^+ decay of one proton into a neutron and forms a deuteron given by the following reaction process

$$ {}^1_1\mathrm{H} + {}^1_1\mathrm{H} \rightarrow {}^2_1\mathrm{D} + e^+ + \nu_e + 0.42\ \mathrm{Mev} \quad , \tag{1.1a} $$

$$ e^- + e^+ \rightarrow 2\gamma + 1.02\ \mathrm{MeV} \quad , \tag{1.1b} $$

where ${}^1_1\mathrm{H}$ is the ionized hydrogen and ${}^2_1\mathrm{D}$ denotes a deuteron, an isotope of the hydrogen consisting of a proton and neutron, ν_e is an electron neutrino and e^+ is the positron which is formed during the β^+ decay of the diproton. Once a deuteron is produced, the following reaction process which is know as the proton-proton-chain I is much faster as it is governed by the *strong nuclear force*, namely

$$ {}^2_1\mathrm{D} + {}^1_1\mathrm{H} \rightarrow {}^3_2\mathrm{He} + \gamma + 5.49\ \mathrm{MeV} \quad , \tag{1.2a} $$

$$ {}^3_2\mathrm{He} + {}^3_2\mathrm{He} \rightarrow {}^4_2\mathrm{He} + 2{}^1_1\mathrm{H} + 12.86\ \mathrm{MeV} \quad , \tag{1.2b} $$

where He is helium nuclide. Overall light elements are fused into heavier elements with a large release of energy through radiation and kinetic energy of the nuclides. This fusion reaction process releases an energy, which for 1g of hydrogen equals the burning energy of 74 tons of coal.

The sun is not the only star which gets its energy from the fusion process, indeed all the stars in the universe are powered by fusion processes, although the fusion process

may be different depending on the size of the sun and age, e.g. once the hydrogen is nearly depleted, the sun's core does not produce enough energy to counterweight the gravitational pull, the core contracts and heats up. If temperature rises to around 42 Million Kelvin, helium burning starts, where helium fuses into fluorine. However, once again the helium is depleted, the core contracts again and fluorine burning is started. One might think that this process continues infinitely, however, this is not the case. The yield from fusion of hydrogen is far larger than the fusion of helium, due to the increased electrostatic repulsion of the double-charged helium. The limit, where energy is gained through fusion is reached for iron $^{56}_{26}$Fe, for heavier elements, fusion requires energy while fission becomes beneficial.

1.2 | The sun in a bottle

The first known man made fusion was achieved *Nov 1, 1952 at the Eniwetok Atoll*, namely the ignition of the first hydrogen bomb. In order to achieve fusion the hydrogen bomb uses a staged approach, where an initial nuclear fission bomb is ignited. The radiation pressure from the fission bomb compresses and heats up a lithium / deuterium mixture and provides the neutrons that are absorbed by the lithium and trigger a fission reaction of the lithium into tritium. The tritium then fusions with the deuteron to helium releasing a large amount of energy.

However, achieving a controlled nuclear fusion for non-military usage proved to be much more difficult. The sun achieves the condition suitable for the sustained fusion process through its immense size, which compresses the gas through the gravitational force, thus leading to a high temperature and density at the center. On earth, we have to rely on an other mechanism to confine the plasma. However, we cannot simply confine the plasma in a closed box, as we face the problem that no material is known, which is capable of withstanding the immense pressure and temperature required for the fusion process over a long time. Instead, in the study of magnetically confined plasmas, the property, that a hot gas loses its electrons and becomes ionized is exploited. Ionized particles follow magnetic field lines, which are constructed in such a way that the particles are trapped and any contact with the machine's wall is avoided.

Various configurations have been developed, where the most popular ones being the Tokamak, the Stellarator, and the Heliotron. In the Tokamak outer coils generate a toroidal magnetic field in a donut shape configuration. Additionally, a transformer is placed in the center of the Tokamak to induce a current in the plasma, which creates an inner magnetic field which compresses the plasma through a pinch effect. However, compressing the plasma by the magnetic field is similar to squeezing a balloon — it tries to escape in various direction — leading to an instability. Lawson (1957) showed that a successful operation of the Tokamak for energy generation depends approximately only on plasma triple product given by the confinement time τ_c, the plasma density n_e and

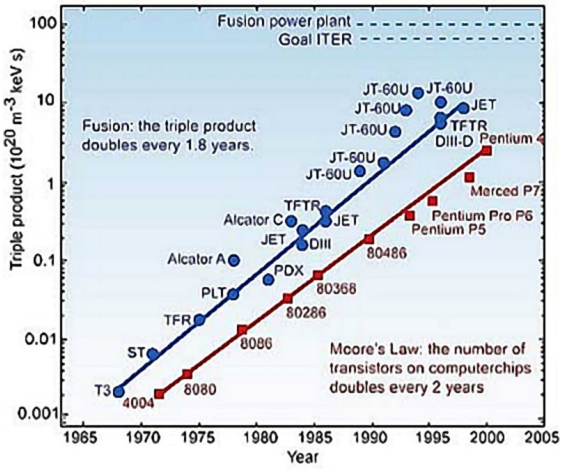

Figure 1.2: *Improvement of the plasma triple product in over three decades shows an exponential growth similar to the famous Moore's law known in computer science [image credit : EFDA]. Lawson showed that a self-sustaining fusion reaction (so-called burning plasma) requires the plasma triple product to exceed* $n_e T \tau_e > 10^{21} keVs/m^3$. *A further improvement of the plasma triple product will come from a new generation of fusion machines such as the now being built ITER Tokamak in Cadarache, France.*

the temperature T_e. Although the first experiments were promising, the plasma triple product was many orders of magnitude smaller than is required to achieve fusion.

During the period of more than 50 years scientists improved their understanding of magnetic plasma confinement and steadily increased the triple product. However, every increase of the temperature and/or density most often came along with new instabilities, which had to be understood and controlled which made progress a tedious task. In Fig. 1.2 the progress of the triple product is shown for over more than half a century. Improvements in plasma confinement theory, better numerical modeling, and better/larger experiments increased our understanding of a confined plasma and allowed the increase of the plasma triple product. It is anticipated that for the next generation machines, such as ITER, finally we will be able to have a positive net energy balance, where the energy output from the fusion inside the plasma is larger than the energy injected to heat the plasma. The next machine on the road map, the *ITER* sketched in Fig. 1.3, is a next experimental Tokamak device, build by an international collaboration between nine participating countries. The goal of ITER is to show the viability of nuclear fusion for electricity production. If the experiments will be successful, it will open the way for DEMO, a hypothetical Tokamak, whose goal is to show the viability of the Tokamak for industrial scale electricity production. However, still many hurdles have to be taken before we benefit from electricity produced through fusion inside the Tokamak. One remaining major hurdle are *turbulences* on various scales and their interaction with each other, which strongly increases heat and particle transport from the hot plasma core to the cooler plasma edge and thus drastically reduces fusion efficiency and the achievable fusion triple product.

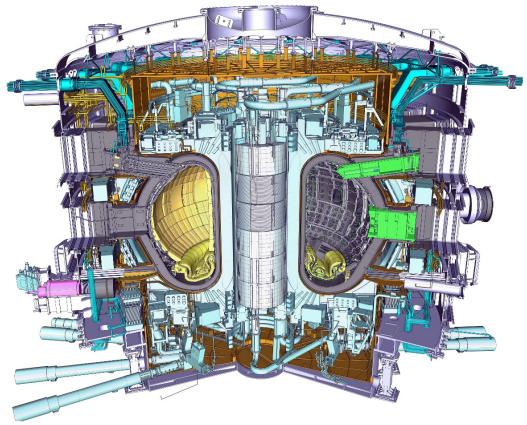

Figure 1.3: *Sketch of the ITER Tokamak vessel [image credit : ITER Organization (2011)]. The hot plasma is magnetically confined in the torus shaped chamber. The toroidal magnetic field is produced through superconducting coils. In the center of the torus is the solenoid — the primary coil — where an increasing current is driven to induce a current in the secondary coil: the plasma. Further, various heating and diagnostics systems are shown.*

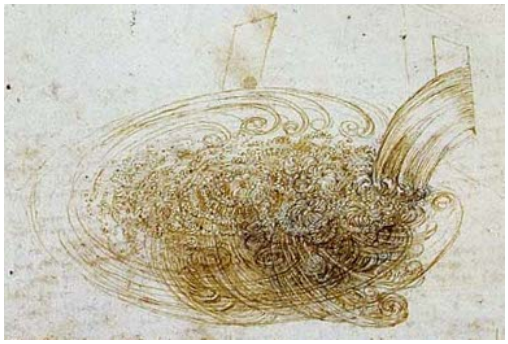

Figure 1.4: *Leonardo da Vinci impressions on turbulence. We find a broad scale of eddy sizes. Small eddies are moved by larger eddies, which feed along the larger eddies. Smaller eddies are moved by large eddies and small eddies, however have no influence on the larger eddies. Even smaller eddies are finally influenced by shear (and in some cases bulk) viscosity.*

1.3 | Turbulence

Turbulence is described as "*the most important unsolved problem of classical physic*" by the famous theoretician Richard Feynman. Turbulence can be observed in many aspects of everyday life, such as river (wind) flow or boiling water. Leonardo da Vinci, the famous polymath in the Renaissance period, was one of the first who characterized turbulence, when he observed how water from a pipe drops into a pond. He sketched his observation (see in Fig. 1.4) and described his impression of turbulence as:

> The small eddies are almost numberless, and large things are rotated only by large eddies and not by small ones, and small things are turned by both small eddies and large.

What Leonardo da Vinci described is now known as a hierarchy of eddies and the dissipation of energy through an energy cascade. Here, the energy injects at the large scales and forms large eddies, such large eddies feed small eddies, these small eddies feed even smaller eddies, and so on, until the energy is finally dissipated away by viscosity. Turbulence has the further properties: imagine a ball thrown into the pond. The ball will

follow the motion of large eddies. However, on a smaller scale, the ball's motion will look randomly, chaotic and non-determinant. This property makes a general theory of turbulence difficult to obtain, and limits it to a statistical description.

Turbulence also arises inside the plasma in the Tokamak, which shares many similarities to fluids. The origin of plasma turbulence is many fold, e.g., in the Tokamak, plasma is not static but is differentially rotating in the toroidal and poloidal directions. If the gradient of the angular velocities is large enough, the Kelvin-Helmholtz instability, which is a classic hydrodynamics instability, is excited and leads to turbulence.

The temperature and density gradients from the plasma core to the plasma edge leads to another instability, the so-called temperature gradient instability, which arises on very small scales of the order of *mm* for the ions and sub-*mm* order for the electrons and is thus termed micro-scale instability. The micro-scale turbulences is accompanied by a *turbulent transport* of heat and particles from the hot and dense center region of the plasma to its cooler and less dense outer edge. The heat and particle flow attributed to turbulent transport are of many orders of magnitude larger than a simple diffusion process would suggest – with a bad impact on plasma confinement performance. Thus, the understanding of turbulent transport and its reduction or suppression is crucial for a successful Tokamak operation.

Studying the plasma turbulence originating from the temperature gradient instabilities inside the Tokamak is a very challenging task because unlike fluid turbulence, the plasma in the core region of the Tokamak is mainly collisionless and assuming a Gaussian velocity distribution is not justified. To investigate the plasma turbulence accurately, it is insufficient to evolve moments of the phase space distribution, such as density, momentum, and energy; but the phase space distribution itself has to be evolved in order to accurately account for kinetic effects of the plasma such as finite Larmor radius and Landau damping. However, to investigate these microscale turbulences, we need an advanced theory; and the name of this theory is *gyrokinetics*.

1.4 | Outline of this thesis

This thesis studies the microscale turbulences that arises from the ion and electron temperature gradient in magnetically confined fusion plasmas using a massive parallel gyrokinetic simulation code. The outline of the thesis is the following :

- In chapter 2 we outline the derivation of the gyrokinetic Vlasov equation and the gyrokinetic Poisson's and Ampere's equation.

- In chapter 3 we describe the discretization of the gyrokinetic equation system and discuss the various modules of the numerical solver gkc++ developed during this PhD study. As the computations require a massive parallelization effort, we

present the parallelization methods and their benchmarks obtained on state-of-the-art supercomputers.

- In chapter 4 we discuss Landau damping in the linearized, discretized gyrokinetic Vlasov-Poisson equation system. We find that the discretized collisionless system can not reproduce certain damping characteristics properly, as the collisionless Landau damping originates from the phase-mixing of semi-stable Case-van Kampen eigenmodes which restricts damping within a finite recurrence time. The addition of a small collisionality through the Lenard-Bernstein operator damps the recurrence and for a large enough collisionality, recurrence disappears and Landau damping arises through an eigenmode of the equation system itself. Finally, we investigate whether the stabilization mechanism through linear mode-coupling of stable and unstable modes is affected by the Landau damping mechanism: phase-mixing in the collisionless case or a Landau eigenmode in the (weak) collisional case.

- In chapter 5 we study the linear properties of the ion and electron temperature gradient instability by solving numerically the gyrokinetic dispersion relation in the two-dimensional sheared slab geometry in form of a nonlinear eigenvalue problem. Multiple branches of the solution are investigated including the so-called short-wavelength instability. The difference between the case with adiabatic and kinetic electrons is emphasized and parameter scans are performed to understand the influence of the electron temperature gradient and electron mass on the ion temperature gradient instability. Finally, we investigate nonlinear properties by solving the gyrokinetic equations as an initial value problem using the gkc++ code.

- In chapter 6 we investigate the multi-scale interaction between the ion temperature gradient and a static magnetic island. The magnetic island triggers the geometrical coupling between the modes of the ion temperature gradient leading to its stabilization. However, we find that once a critical island width is exceeded, the short-wavelength region of the ion temperature gradient is strongly destabilized. The destabilization mechanism is elucidated using a minimal model and we deducted that the destabilization mechanism shares similarities to the reversed-sheared slab excitation. For the nonlinear ion temperature gradient evolution, we observe a drastically increase of heat flux due to the magnetic island perturbation.

- In chapter 7 we conclude our research efforts and give several suggestions for the extension of this research.

- In the appendix we derive the analytical solution of the dispersion relation and benchmark it with gkc++ to confirm its correctness.

The author wishes a pleasant read.

2 | The gyrokinetic Vlasov–Maxwell equations

A magnetic confined fusion plasma inhibits various instabilities over a wide range of spatial and temporal scales. An overview of the most important instabilities and their spatial-temporal location in the Tokamak is shown in Fig. 2.1. The largest spatial scale is

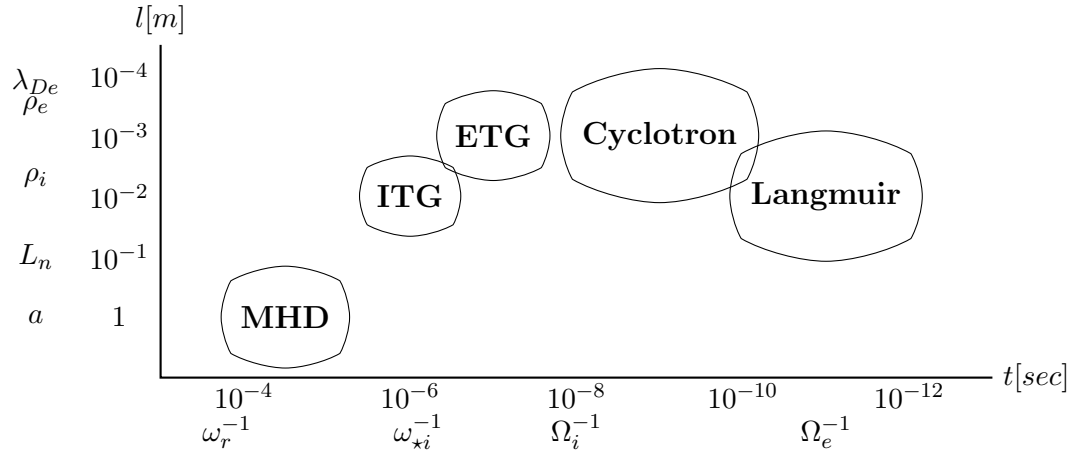

Figure 2.1.: *The instabilities in a Tokamak plasma spans multiple order of magnitudes in the spatial and temporal scales. Understanding these instabilities, and their interaction between them is crucial for a successful operation of a Tokamak [adapted from Idomura et al. (2006)].*

the machine size scale length $l \sim a$, on which the slowly evolving magneto-hydrodynamics (MHD) instabilities takes place with a time scale of the order of the resistive time scale $\omega \sim \omega_r$. These large scale MHD instabilities are changing the general topology of the equilibrium field through the reconnection of the magnetic field lines, which leads, e.g., to kink modes or the formation of magnetic islands. The next major spatial scale, termed micro-scale, is the scale of the ion temperature gradient instability (ITG), which is of a relatively low frequency (diamagnetic frequency) $\omega \sim \omega_{\star i}$ and with a spatial scale which is of the order of the gyro-radius of the ions $l \sim \rho_i$. This ITG instability is assumed to be the dominant contribution to the anomalous heat fluxes observed in Tokamaks. At the same spatial scale $l \sim \rho_i$, but with a frequency of the order of the gyro-frequency

of the ions Ω_i, is the instability which arises from the gyro-motion of the ions along the equilibrium field lines. This scale is of special interest for heating the plasma through the *ion cyclotron resonance heating* (ICRH). Similar to the ITG, the electrons inhibit an instability which is called the electron temperature gradient (ETG) instability, however, its spatial scale is an order of the ion-electron mass ratio ($\sqrt{m_{ie}} \sim 40$ for a hydrogen plasma) smaller $l = \rho_i/\sqrt{m_{ie}}$ compared to the ions, and its (real) frequency is larger by $\omega_e = -\omega_i\sqrt{m_{ie}}$. As the ITG, the ETG is thought to contribute significantly to the anomalous fluxes.

A successful operation of a Tokamak requires the control of all the instabilities and turbulences involved from the various spatial-temporal scales. However, tracking the evolution of instability in the whole spatial-temporal scale in a numerical simulation is not feasible for a machine size simulations as the required computational cost is of many orders of magnitude larger than is feasible today. Thus models have to be developed in order to decouple various scales from each other, but by still keeping the most important physics. Here, we are mainly interested in studying the evolution of micro-instabilities such as the ETG and the ITG. However, the electrons and ions are performing gyro-motion along the guiding field, which is on the fast-time scale, while the ITG/ETG instabilities themselves are rather slowly evolving low-frequency instabilities. Thus, we seek a perturbation theory, which removes the fast time scale from the gyro-motion but which still keeps the important physical effects from the finite gyro-radius attributed to the gyro-motion. This is done by the gyro-averaging procedure.

2.1 | The gyro-averaging procedure

In order to derive the gyrokinetic equations, we use a so-called *gyro-averaging procedure*, which decouples the fast gyro-motion of the electrons and ions and describes the time evolution of their gyro-centers instead as shown in Fig. 2.2, where we exploit the so-called *gyrokinetic ordering*, which is normally satisfied in a Tokamak core plasma. The gyro-averaging procedure consists of several steps, which are shown in Fig. 2.3. The main assumptions are, e.g., Brizard and Hahm (2007), that a magnetized plasma obeys the following orderings,

$$\frac{\omega}{\Omega_i} \sim \frac{\phi_1}{\phi_0} \sim \frac{|\mathbf{A}_1|}{|\mathbf{A}_0|} \sim \frac{\nabla B_0}{B_0} \sim \mathcal{O}(\epsilon) \quad , \quad \frac{\rho}{l} \sim \mathcal{O}(1) \quad , \tag{2.1}$$

for a smallness parameter $\epsilon \ll 1$. The first term, states that the frequency of interest, e.g., the drift frequency, is small compared to the frequency of the gyro-motion Ω_i. The second and third term state that the perturbation of the electrostatic potential ϕ_1 and magnetic field line fluctuations $\mathbf{A}_1$ are small compared to the equilibrium quantities, such as the guiding field $\mathbf{A}_0$. The fourth term states that the gradient of the guiding field is small compared to the equilibrium magnetic field. However, we allow fluctuations

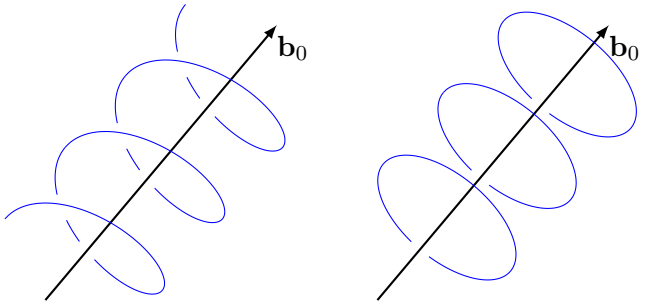

(a) *Gyro-motion over field line* **(b)** *Evolution of gyro-rings*

Figure 2.2.: *Gyrokinetics removes the gyro-angle dependence and instead threads the evolution of gyro-rings [adapted from Görler (2009)]. The gyro-ring size will depend on μ, while the speed of motion along $\mathbf{b}_0$ on $v_\parallel$ coordinate.*

perpendicular to the guide field with a length scale l to be $\mathcal{O}(1)$ over the gyro-radius ρ. This is considered as the usually gyrokinetic ordering. We note however that many of these orderings have been relax over the time, for example, to investigate plasmas including a strong $\mathbf{E}\times\mathbf{B}$ shearing flow by Miyato et al. (2009), the inclusion of centrifugal and Coriolis forces arising from plasma rotation by Peeters et al. (2009), or relaxing ω/Ω_i, in order to included the effects of the cyclotron motions of the ions/electrons to investigate ICRH in so-called *high-frequency gyrokinetics* investigated by Kolesnikov et al. (2007).

Once a plasma satisfy the gyrokinetic ordering, the gyro-averaging procedure can be applied to remove the gyro-angle dependency and thus the fast time scale from the Vlasov–Poisson equation system. The modern formulation of the gyro-averaging procedure was pioneered by Cary and Littlejohn (1983) and Hahm (1988) and is based on the *Lie transform method*. The general strategy follows a two-step approach. In the first step, we start from the single-particle Lagrangian in an electromagnetic field and perform a coordinate transformation of the particle Lagrangian into guiding-center coordinates, where we absorb the gyro-angle in $\mathcal{O}(1)$ by a proper choice of the gauge function S. In the second step, we apply the Lie transform method to transform into gyro-center coordinates, where the $\mathcal{O}(\epsilon)$ terms of the single-particle Lagrangian are now included *but* approximated by their averaged quantities over one gyro-motion, see Fig. 2.2. Finally we use the Euler–Lagrange equations to derive the gyrokinetic Vlasov equation.
Please note that for the derivation of the gyrokinetic equation system, for Sec(2.2) - Sec(2.5), we will closely follow the procedure as given by Dannert (2006) with only minor notational differences.

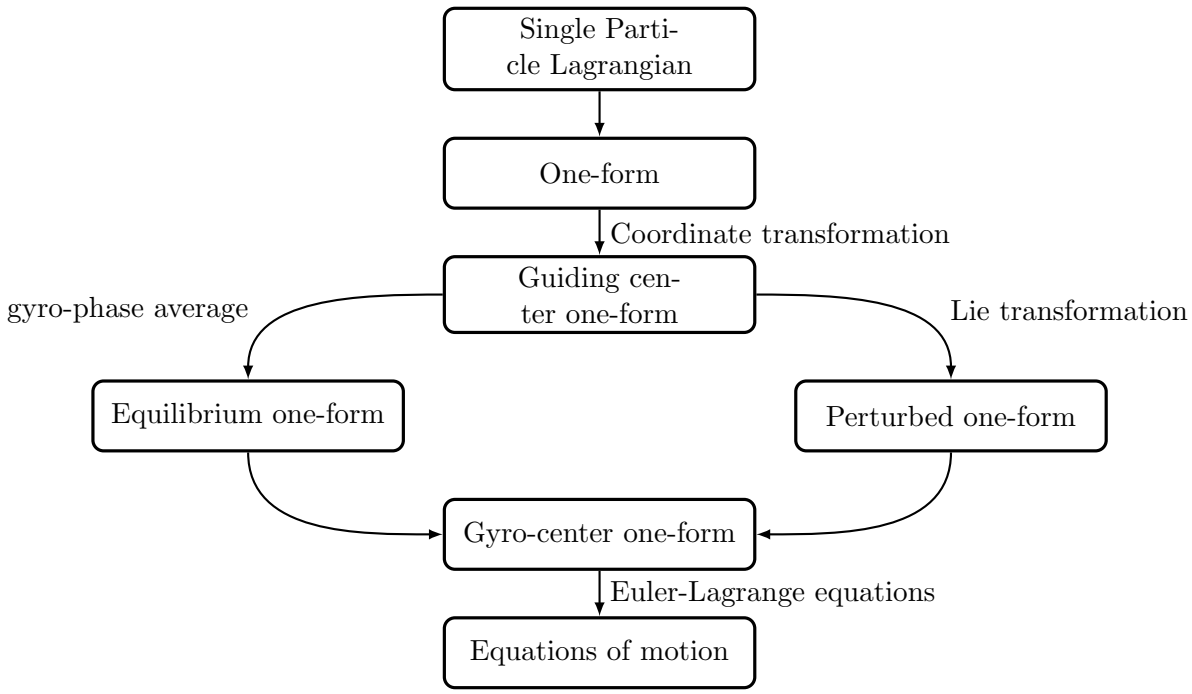

Figure 2.3.: *Outline of the gyro-averaging procedure to derive the gyrokinetic Vlasov equations [adapted from Görler (2009)].*

2.2 | The single-particle Lagrangian

A non-relativistic particle in a magnetic field can be described through its Lagrangian in the particles coordinates $\mathbf{x}$ given by

$$\mathcal{L} = \underbrace{\left[m\mathbf{v} + \frac{q}{c}\mathbf{A}(\mathbf{x})\right] \cdot \dot{\mathbf{x}}}_{\text{sympletic part}} - \underbrace{\left[\frac{1}{2}mv^2 + q\phi(\mathbf{x})\right]}_{\text{Hamilotonian part}} \quad , \tag{2.2}$$

where q is the particles charge and m its mass, and ϕ is the *electrostatic potential* and $\mathbf{A}$ the *magnetic vector potential*. Once the Lagrangian is known, the equations of motion can be found by taking the variations of $\mathcal{L}$,

$$S = \delta \int \mathcal{L}\,\mathrm{d}t + \mathrm{d}S = 0 \quad . \tag{2.3}$$

Note that the Lagrangian exhibits a *gauge freedom* $\mathrm{d}S$ due to the fact that adding a term $\mathrm{d}S$ to the Lagrangian leads the action integral Eq.(2.3) invariant, as it is only

dependent on the endpoints and not a specific path taken. This fact will be later used in the derivation. In the next step, we absorb the factor $\mathrm{d}t$ by creating a one-form γ, which is defined by $\gamma = \gamma_\zeta dz^\zeta$, where we we use Einstein's sum convention (meaning we sum over equal indices of covariant and contravariant components). The one-form of the Lagrangian in (2.2) is given by

$$\gamma = \left[m\mathbf{v} + \frac{q}{c}\mathbf{A}(\mathbf{x})\right] \cdot \mathrm{d}\mathbf{x} - \left[\frac{1}{2}mv^2 + q\phi(\mathbf{x})\right] \mathrm{d}t \quad . \tag{2.4}$$

Once the one-form is formed, the equations of motion can be obtained from the *Euler–Lagrange equations*, see Cary and Littlejohn (1983), given by

$$\left(\frac{\partial \gamma_\xi}{\partial \zeta} - \frac{\partial \gamma_\zeta}{\partial \xi}\right) \frac{\mathrm{d}z^\xi}{\mathrm{d}t} = 0 \quad . \tag{2.5}$$

The importance of the Lagrangian formulation is its independence on the coordinate system, e.g., the equation of motions do not change by a coordinate transformation from one choice of a generalized coordinates system to an other choice of generalized coordinate system. This is manifested by the fact that the action integral in Eq.(2.3) is itself just a scalar. Due to this invariance, we can write

$$\gamma_\mu dz^\mu = \Gamma_\mu dZ^\mu \quad . \tag{2.6}$$

Our goal is to find a coordinate system, where our original one-form γ, which includes all spatial and temporal scales, transforms into a simpler Γ, which does not include the fast time scale from the gyro-motion.

2.3 | The guiding-center one-form

In the magnetic fusion core plasma, the particles are performing gyro-motion along the strong magnetic guide field $\mathbf{B} = \boldsymbol{\nabla} \times \mathbf{A}$. Assuming only small perturbation in the perpendicular direction, we transform into a more appropriate coordinate system in order to simplify the Lagrangian $\mathcal{L}$ defined in Eq.(2.4). This coordinate system we wish to transform into is the so-called *guiding-center coordinate system* shown in Fig. 2.4. The transformation rules from $\mathbf{z} = (t, \mathbf{x}, \mathbf{v}) \rightarrow \mathbf{Z} = \left(t, \mathbf{X}, v_\parallel, \mu, \theta\right)$ are given by

$$\mathbf{X} = \mathbf{x} - \rho\,\mathbf{a} \quad , \qquad v_\parallel = \mathbf{b}(\mathbf{x}) \cdot \mathbf{v} \quad , \tag{2.7a}$$

$$\mu = \frac{mv_\perp^2}{2B(\mathbf{x})} \quad , \qquad \mathbf{a}(\theta) = (\mathbf{e}_1 \cos\theta - \mathbf{e}_2 \sin\theta) \quad , \tag{2.7b}$$

where $\mathbf{X}$ is the guiding center coordinate, $v_\parallel$ is the velocity along the equilibrium magnetic field line unit vector given by $\mathbf{b}$, such that $\mathbf{B} = |\mathbf{B}| \cdot \mathbf{b}(\mathbf{x})$. The gyro-radius

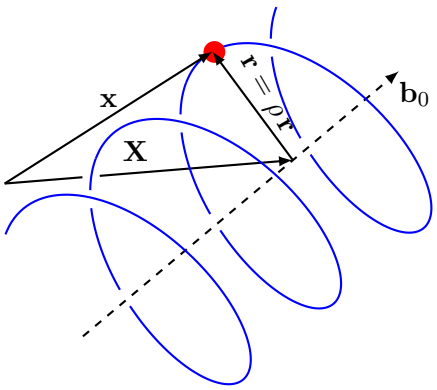

Figure 2.4: *Sketch of the guiding-center coordinate* $\mathbf{X}$*, which maps the particle coordinates* $(\mathbf{x}, \mathbf{v})$ *to the guiding-center* $\big(\mathbf{X}, v_\parallel, \mu, \theta\big)$*. Note that* $\mathbf{a} \cdot \mathbf{b}_0 = 0$*.*

ρ is defined by $\rho = v_\perp/\Omega(\mathbf{X})$, where Ω is the gyro-frequency given by $\Omega = qB/m$. $\mu = mv_\perp^2/2B_0$ is the first adiabatic invariant and θ is the gyro-angle. The guiding-center coordinate system is spanned by $(\mathbf{e}_1, \mathbf{e}_2, \mathbf{b})$, where $\mathbf{e}_1$, $\mathbf{e}_2$ are orthogonal unit vectors and $\mathbf{b}$ is the unit vector in the direction of the guiding field. The inverse transformation from $\mathbf{Z} = \big(t, \mathbf{X}, v_\parallel, \mu, \theta\big) \to \mathbf{z} = (t, \mathbf{x}, \mathbf{v})$ is given by

$$\mathbf{x} = \mathbf{X} + \rho(\mathbf{X})\,\mathbf{a}(\theta) \quad , \quad \mathbf{v} = v_\parallel \mathbf{b} + v_\perp \mathbf{c}(\theta) \quad , \tag{2.8a}$$

$$\mathbf{c}(\theta) = -\mathbf{e}_1 \sin\theta - \mathbf{e}_2 \cos\theta \quad , \tag{2.8b}$$

where we used the gyro-kinetic ordering (2.1) assuming only a slow variation of the background magnetic field.

2.3.1 | Transforming the equilibrium quantities

The transformation of the particle coordinate one-form γ given in Eq.(2.4) to the guiding-center one-form Γ is achieved by applying the transformation for scalar quantities in Eq.(2.6).

$$\Gamma_\zeta = \gamma_\xi \frac{dz^\xi}{dZ\zeta} \quad , \tag{2.9}$$

for $\zeta = (t, \mathbf{x}, \mathbf{v})$. For the first variable t, we note that the do not transform the time

$$\Gamma_t = \gamma_t = -\frac{1}{2} v_\parallel^2 - \mu B(\mathbf{X}) - e\phi(\mathbf{X}) \tag{2.10}$$

Dannert (2006) gives following result for the transformed one-from in Z,

$$\Gamma_{\mathbf{X}} = \gamma_{\mathbf{X}} \frac{\mathrm{d}z^{\mathbf{x}}}{\mathrm{d}Z^{\mathbf{X}}} = m\mathbf{v} + \frac{q}{c}\mathbf{A}(\mathbf{X}) - \mathbf{A}(\mathbf{X}) \cdot \mathbf{a}(\theta) \frac{\mu}{\mathbf{B}(\mathbf{X})\, v_{\perp}(\mathbf{X})} \nabla_{\mathbf{X}} B(\mathbf{X}) \quad , \tag{2.11a}$$

$$\Gamma_{v_{\parallel}} = \gamma_{\mathbf{X}} \frac{\mathrm{d}z^{\mathbf{x}}}{\mathrm{d}Z^{\mathbf{X}}} = 0 \quad , \tag{2.11b}$$

$$\Gamma_{\boldsymbol{\mu}} = \gamma_{\mathbf{X}} \frac{\mathrm{d}z^{\mathbf{x}}}{\mathrm{d}Z^{\mu}} = \frac{\mathbf{A}(\mathbf{X}) \cdot \mathbf{a}(\theta)}{v_{\perp}(\mathbf{X})} \quad , \tag{2.11c}$$

$$\Gamma_{\boldsymbol{\theta}} = \gamma_{\mathbf{X}} \frac{\mathrm{d}z^{\mathbf{x}}}{\mathrm{d}Z^{\theta}} = \frac{m v_{\perp}^2}{\Omega(\mathbf{X})} + \mathbf{A}(\mathbf{X}) \cdot \mathbf{c}(\theta) \frac{q}{c} \frac{v_{\perp}}{\Omega(\mathbf{X})} \quad , \tag{2.11d}$$

where the transform over $\mathrm{d}z^{\zeta = v_{\parallel}}$ vanishes, as the particle coordinates one-form γ is independent of $\mathrm{d}\mathbf{v}$. We now introduce the *gyro-angle averaging* over θ, which states the average value over one gyro-motion, defined by

$$\tilde{A} = \frac{1}{2\pi} \int_0^{2\pi} A\left(\mathbf{X}, v_{\parallel}, \mu, \theta\right) \, \mathrm{d}\theta \quad , \tag{2.12}$$

where A is an arbitrary variable in guiding-center coordinates. Using the gyro-angle averaging on the one-form in (2.11) gives,

$$\tilde{\Gamma}_{\mathbf{X}} = m v_{\parallel} \mathbf{b} + \frac{q}{c}\mathbf{A}(\mathbf{X}) \quad , \quad \Gamma_{v_{\parallel}} = 0 \quad , \tag{2.13a}$$

$$\tilde{\Gamma}_{\boldsymbol{\mu}} = 0 \quad , \quad \tilde{\Gamma}_{\boldsymbol{\theta}} = \frac{m v_{\perp}^2}{\Omega} \quad , \tag{2.13b}$$

where the oscillating terms $\mathbf{a}(\theta)$ and $\mathbf{c}(\theta)$ drop out to due averaging. Using the gyro-averaging Thus our zeroth-order one-form in guiding center coordinates $\left(\mathbf{X}, v_{\parallel}, \mu, \theta\right)$ has the form

$$\tilde{\Gamma}_0 = \left(m v_{\parallel} \mathbf{b} + \frac{q}{c}\mathbf{A}\right) \cdot \mathrm{d}\mathbf{X} + \frac{\mu B}{\Omega} \mathrm{d}\theta - \left[\frac{1}{2} m v_{\parallel}^2 + \mu B + e\phi\right] \mathrm{d}t \quad , \tag{2.14}$$

which is now independent on the gyro-angle θ.

2.3.2 | Transforming the perturbed quantities

When deriving $\tilde{\Gamma}_0$, we assumed that the change in the fields $(\phi, \mathbf{A})$ within one gyro-radius is small and can thus be neglected. Now we also take perturbations into account, by expanding $\phi = \phi_0 + \phi_1$ and $\mathbf{A} = \mathbf{A}_0 + \mathbf{A}_1$ such that $\phi_1 \sim \epsilon$ and $\mathbf{A}_1 \sim \epsilon$ and assuming a vanishing background electric potential $\phi_0 = 0$. Thus our one-form in particle coordinates is written as $\gamma = \gamma_0 + \gamma_1 + \mathcal{O}(\epsilon^2)$ with

$$\gamma_0 = \left(m\mathbf{v} + \frac{q}{c}\mathbf{A}_0\left(x\right)\right) \cdot \mathrm{d}\mathbf{x} - \frac{m}{2} v^2 \, \mathrm{d}t \quad , \tag{2.15}$$

$$\gamma_1 = \frac{q}{c} A_1(\mathbf{x}) \cdot \mathrm{d}\mathbf{x} - \frac{q}{c}\phi_1 \, \mathrm{d}t \quad . \tag{2.16}$$

The transformation of $\gamma_0 \to \Gamma_0$ has been accomplished in the previous section and is thus unchanged. Transforming the first order one-form γ_1 into guiding-center coordinates gives

$$\Gamma_1 = \frac{q}{c}\mathbf{A}_1 \cdot \mathrm{d}\mathbf{X} + \frac{\mathbf{A}_1 \cdot \mathbf{a}}{v_\perp}\,\mathrm{d}\mu + \frac{mv_\perp}{B_0}\mathbf{A}_1 \cdot \mathbf{c}\,\mathrm{d}\theta - e\phi_1\,\mathrm{d}t \quad . \tag{2.17}$$

The first-order one-form Γ_1 now includes oscillatory terms through the $\mathbf{c}\,\mathrm{d}\theta$ component. Simply using the average over the gyro-motion (2.12) is not allowed, as for the gyrokinetic ordering (2.1) we assumed the gradients of the perturbed quantities to be of $\mathcal{O}(\epsilon)$. Thus, in order to remove the oscillatory term, we will thus make use of the Lie transform method.

2.4 | Transformation into the gyro-center coordinates

We seek for a transformation which removes the gyro-angle (θ) dependence in Γ_1 in Eq.(2.17). This best done using the Lie perturbation method[1] which gives a well defined procedure on how to transform our guiding-center one-form Γ_1 into a gyro-center one-form $\bar{\Gamma}_1$ which is independent of the gyro-angle θ. As the zeroth-order one-form Γ_0

[1] An individual Lie transform is defined as the near-identity transform T_n and its inverse T_n^{-1} which can be written in the form

$$T_n = \exp\left(\sum\nolimits_n \frac{\epsilon^n}{n!}L_n\right) \qquad \text{or} \qquad T^{-1} = \exp\left(-\sum \frac{\epsilon^n}{n!}L_n\right) \quad , \tag{2.18}$$

where L_n is the *Lie derivative* and $\epsilon \ll 1$ is a small parameter of the problem. We can combine many individual Lie transforms into a Lie transform which can be written as

$$\bar{X}^\mu = TX^\mu \quad , \tag{2.19}$$

with $T = \ldots T_3 T_2 T_1$ and X^μ the guiding-center coordinate system and $\bar{X}^\mu$ the Lie transformed *gyro-center* coordinate system. The guiding-center one-form $\Gamma = \Gamma_\mu dX^\mu$ for example transforms under the Lie transform according to the rule

$$\bar{\Gamma} = T^{-1}\Gamma + dS \quad . \tag{2.20}$$

to the gyro-center one-form $\bar{\Gamma}$ and dS is once again the gauge function. The operator L_n acts on one-forms as

$$(L_n\gamma)^\mu = g_n^\sigma\left(\frac{\partial\gamma_\mu}{\partial z^\sigma} - \frac{\gamma_\sigma}{\partial z^\mu}\right) \quad . \tag{2.21}$$

where g_n^μ is the generator of the Lie transform T_n, which satisfies $\partial X^\mu/\partial\epsilon^n = g_n^\mu(\mathbf{X})$ and $\Gamma = \Gamma_\mu dX^\mu$, where Γ is the one-form in gyro-center coordinates $\Gamma = \Gamma_\theta dX^\theta$, and X_θ is the new coordinates. The choice is the generating function g is completely arbitrary, so with g_n^μ and S_n we have $2N+1$ components to bring Γ_n to the desired form. But we have to be aware of that whatever we choose for g_n^μ and S_n, it will later affect the polarization equation for ϕ and $A_\parallel$. By expanding $\Gamma = \exp(-\epsilon L_g)\gamma + dS$ using $\gamma = \gamma_0 + \epsilon\gamma_1 + \epsilon^2\gamma_2 + \ldots$ and the expansion of the exponential coefficient

in the guiding-center coordinates in Eq.(2.14) does not include any dependence on θ, the zeroth-order one-form in the gyro-center coordinates is equal, i.e. $\bar{\Gamma}_0 = \Gamma_0$. The transformation rule for the Lie transform to transform Γ_1 into $\bar{\Gamma}_1$ is given by

$$\bar{\Gamma}_{1\zeta} = \Gamma_{1\zeta} - g_1^{\xi}\left(\frac{\partial \Gamma_{0\zeta}}{\partial Z^{\xi}} - \frac{\partial \Gamma_{0\xi}}{\partial Z^{\zeta}}\right) + \frac{\partial S_1}{\partial Z^{\zeta}} \quad , \tag{2.23}$$

where Γ_1 is our perturbed one-form, Γ_0 our zeroth-order one-form and g_1^{ξ} our Lie generators and $\zeta = \left(\mathbf{X}, v_{\parallel}, \mu, \theta\right)$. We now have to find our generators g^{ξ} so that the dependence of the gyro-angle is removed. We do not transform time, thus our generator for the time is given by $g_1^t = 0$. Previous calculation leading to Eq.(2.13a) showed that the terms $\Gamma_{0v_{\parallel}} = 0$ and $\Gamma_{0\mu} = 0$. For $\bar{\Gamma}_{1\theta}$, $\bar{\Gamma}_{1\mu}$ and $\bar{\Gamma}_{1v_{\parallel}}$ Dannert (2006) showed that by applying Eq.(2.23), we get

$$\bar{\Gamma}_{1\theta} = \frac{m v_{\perp}\left(\mathbf{X},\mu\right)}{B_0}\mathbf{A}_1\left(\mathbf{X}+\mathbf{r}\right)\cdot\mathbf{c}(\theta) - g_1^{\mu}\frac{mc}{q} + \frac{\partial S_1}{\partial \theta} \quad , \tag{2.24a}$$

$$\bar{\Gamma}_{1\mu} = \frac{A_1\left(\mathbf{X}+\mathbf{r}\right)\cdot\mathbf{a}(\theta)}{v_{\perp}\left(\mathbf{X},\mu\right)} + g_1^{\theta}\frac{mc}{q} + \frac{\partial S_1}{\partial \mu} \quad , \tag{2.24b}$$

$$\bar{\Gamma}_{1v_{\parallel}} = g_1^{\mathbf{X}}\cdot m\mathbf{b} + \frac{\partial S_1}{\partial v_{\parallel}} \quad . \tag{2.24c}$$

If we choose our generators g_1^{μ}, g_1^{θ} and $g_1^{\mathbf{X}}$ equal to

$$g_1^{\mu} = \frac{q}{mc}\left(\frac{m v_{\perp}}{B_0}\mathbf{A}_1(\mathbf{X}+\mathbf{r})\cdot\mathbf{c} + \frac{\partial S_1}{\partial \theta}\right) \quad , \quad g_1^{\mathbf{X}}\cdot\mathbf{b}_0 = -\frac{1}{m}\frac{\partial S_1}{\partial v_{\parallel}} \quad , \tag{2.25a}$$

$$g_1^{\theta} = -\frac{q}{mc}\left(\frac{\mathbf{A}(\mathbf{X}+\mathbf{r})\cdot\mathbf{a}}{v_{\perp}} + \frac{\partial S_1}{\partial \mu}\right) \quad , \tag{2.25b}$$

we get $\bar{\Gamma}_{1\theta} = \bar{\Gamma}_{1\mu} = \bar{\Gamma}_{1v_{\parallel}} = 0$ for the corresponding gyro-center components. Finally, we need to calculate the one-form components $\Gamma_{1,\mathbf{X}}$ and $\Gamma_{1,t}$. The gyro-center one-form $\Gamma_{1,\mathbf{X}}$ can be calculated to

$$\bar{\Gamma}_{1\mathbf{X}} = \frac{q}{c}\mathbf{A}_1\left(\mathbf{X}+\mathbf{r}\right) + \frac{q}{c}g_1^{\mathbf{X}}\times\mathbf{B}_0^{\star} - g_1^{v_{\parallel}}m\mathbf{b}_0 + \nabla S_1 \quad , \tag{2.26}$$

$-\epsilon L_g = L_0 + \epsilon L_1 + \epsilon^2 L_2^2 + \ldots$, we can break up Γ into its orders which gives.

$$\bar{\Gamma}_0 = dS_0 + \Gamma_0 \quad , \tag{2.22a}$$

$$\bar{\Gamma}_1 = dS_1 + \Gamma_1 - L_1\Gamma_0, \quad , \tag{2.22b}$$

$$\bar{\Gamma}_2 = dS_2 + \Gamma_2 - L_1\Gamma_1 + (\tfrac{1}{2}L_1^2 - L_2)\Gamma_0 \quad , \tag{2.22c}$$

$$\bar{\Gamma}_3 = \cdots \quad , \tag{2.22d}$$

where we already fixed dS_0 to reduce the gyro-angle dependence by one-order. So the first order the GC coordinates and GY coordinates are equivalent.

where we defined the *extended vector potential* $\mathbf{A}_0^\star$ and *extended magnetic field* $\mathbf{B}_0^\star$ as

$$\mathbf{A}_0^\star = \mathbf{A}_0 + \frac{mc}{q} v_\parallel \mathbf{b} \quad , \qquad \mathbf{B}_0^\star = \nabla \times \mathbf{A}_0^\star \quad , \tag{2.27}$$

to simplify. If we choose

$$g_1^{v_\parallel} = \frac{1}{m B_{0\parallel}^\star} \left(\frac{q}{c} \mathbf{B}_0^\star \cdot \widetilde{\mathbf{A}_1 (\mathbf{X} + \mathbf{r})} + \mathbf{B}_0^\star \nabla S_1 \right) \quad , \tag{2.28a}$$

$$g_1^{\mathbf{X}} = -\frac{1}{B_{0\parallel}^\star} \left(\mathbf{b}_0 \times \widetilde{\mathbf{A} (\mathbf{X} + \mathbf{r})} + \frac{1}{m} \frac{\partial S}{\partial v_\parallel} \mathbf{B}_0^\star + \frac{c}{q} \mathbf{b}_0 \times \nabla S_1 \right) \quad , \tag{2.28b}$$

where $\widetilde{A_1 (\mathbf{X} + \mathbf{r})}$ is defined as (respectively for ϕ)

$$\widetilde{A_1 (\mathbf{X} + \mathbf{r})} = \mathbf{A}_1 (\mathbf{X} + \mathbf{r}) - \langle \mathbf{A} (\mathbf{x} + \mathbf{r}) \rangle \quad , \tag{2.29}$$

Eq. (2.26) simplifies to $\bar{\Gamma}_{1\mathbf{X}} = \langle A_1 (\mathbf{X} + \mathbf{r}) \rangle$, where $\langle \, \rangle$ denotes that $\mathbf{A}$ is gyro-averaged using the operator defined in Eq.(2.12) and includes only the oscillatory part. The only remaining term is the one-form of the time component $\bar{\Gamma}_t$, which is given by

$$\bar{\Gamma}_{1t} = \Gamma_{1t} - g_1^{\mathbf{X}} \frac{\partial \Gamma_{0t}}{\partial \mathbf{X}} - g_1^{v_\parallel} \frac{\partial \Gamma_{0t}}{\partial v_\parallel} - g_1^{\mu} \frac{\partial \Gamma_{0t}}{\partial \mu} - g_1^{\theta} \frac{\partial \Gamma_{0t}}{\partial \theta} - \frac{\partial S_1}{\partial t} \quad . \tag{2.30}$$

Dannert (2006) argued that the derivatives ∇S, $\nabla_\parallel$, $\partial_{v_\parallel} S$, $\partial_t S$ can be dropped as they are of the order of $\mathcal{O}(\epsilon)$, except for $\nabla_\theta S$, which is of the order of $\mathcal{O}(1)$. If we choose the gauge function to

$$\begin{aligned} \frac{\partial S_1}{\partial \theta} = \frac{1}{\Omega} \Bigg(& q\widetilde{\phi(\mathbf{X} + \mathbf{r})} + \frac{1}{B_{0\parallel}} \left(\mathbf{b}_0 \times \widetilde{\mathbf{A}_1 (\mathbf{X} + \mathbf{r})} \right) \cdot \nabla (\mu B_0) \\ & - \frac{q v_\parallel}{c} \frac{\mathbf{B}_{0\parallel}^\star}{B_{0\parallel}^\star} \widetilde{\mathbf{A}_1 (\mathbf{X} + \mathbf{r})} - \frac{q}{c} \widetilde{\mathbf{A}_1 (\mathbf{X} + \mathbf{r})} \cdot \mathbf{u}_\perp \Bigg) \quad , \end{aligned} \tag{2.31}$$

all oscillating terms in Eq.(2.30) are canceled through the gauge function and we arrive at

$$\bar{\Gamma}_{1t} = -e \langle \phi (\mathbf{X} + \mathbf{r}) \rangle + \frac{q}{c} \langle \mathbf{A} (\mathbf{X} + \mathbf{r}) \cdot u_\perp \rangle \quad . \tag{2.32}$$

Combining the $\tilde{\Gamma}_0$ and $\tilde{\Gamma}_1$ terms together, gives the *gyrokinetic one-form*,

$$\begin{aligned} \tilde{\Gamma}_{0,1} = \tilde{\Gamma}_0 + \tilde{\Gamma}_1 = & \left(m v_\parallel \mathbf{b}_0 + \frac{q}{c} \mathbf{A}_0 (\mathbf{X}) + \frac{q}{c} \langle \mathbf{A}_1 \rangle \right) \cdot \mathrm{d}\mathbf{X} + \frac{\mu m c}{q} \mathrm{d}\theta \\ & - \left(\frac{1}{2} m v_\parallel^2 + \mu B_0 (\mathbf{X}) + q \langle \phi_1 \rangle - \frac{q}{c} \langle \mathbf{A}_1 \cdot \mathbf{u}_\perp \rangle \right) \mathrm{d}t \quad . \end{aligned} \tag{2.33}$$

Note that the equilibrium quantities are taken at the gyro-center $\mathbf{X}$, while the perturbed quantities are taken at the position $\mathbf{X} + \mathbf{r}$.

2.5 | The gyrokinetic Vlasov equation

Liouville's theorem states that the phase-space over the trajectory is conserved, so that

$$\frac{\mathrm{d}f}{\mathrm{d}t} = 0 \quad , \tag{2.34}$$

which for our gyro-center coordinates system $(\mathbf{X}, v_\parallel, \mu)$ results in

$$\frac{\partial f}{\partial t} + \dot{\mathbf{X}} \cdot \nabla f + \dot{v}_\parallel \frac{\partial f}{\partial v_\parallel} + \dot{\mu}\frac{\partial f}{\partial \mu} = 0 \quad . \tag{2.35}$$

The derivatives of each coordinate can be obtained by solving the Euler–Lagrange equations (2.5) to get the equations of motion, namely

$$\left(\frac{\partial \gamma_\xi}{\partial \zeta} - \frac{\partial \gamma_\zeta}{\partial \xi}\right)\frac{\mathrm{d}z^\xi}{\mathrm{d}t} = 0 \quad . \tag{2.36}$$

The calculations were done in detail by Szepsi (2012), thus we only present his results here :

$$\dot{\mathbf{X}}: \ \dot{\mathbf{X}} = v_\parallel \mathbf{b}_0 + \frac{B_0}{B^\star_{0\parallel}}\left(\mathbf{v}_\chi + \mathbf{v}_D\right) \quad , \tag{2.37a}$$

$$\theta: \ \dot{v}_\parallel = \frac{\dot{\mathbf{X}}}{m v_\parallel}\left[q\left\langle \mathbf{E}\right\rangle - \mu\nabla\left(B_0 + \left\langle B_{1\parallel}\right\rangle\right)\right] \quad , \tag{2.37b}$$

$$\mu: \ \dot{\mu} = 0 \quad , \tag{2.37c}$$

$$v_\parallel: \ \dot{\theta} = \Omega - \frac{q}{mc}\partial_\mu\left(\frac{q}{c}\left\langle \mathbf{A}_{1\parallel}\right\rangle v_\parallel - q\left\langle \phi_1\right\rangle - \mu\left\langle B_{1\parallel}\right\rangle\right) \quad , \tag{2.37d}$$

where we introduced the common definition of the electric field $\mathbf{E} = -\nabla\left\langle\phi\right\rangle - \mathbf{b}_0 c^{-1}\partial_t\left\langle A_{1\parallel}\right\rangle$, and the generalized velocity $\mathbf{v}_D = \mathbf{v}_C + \mathbf{v}_{\nabla B_0}$, with the following definitions:

$$\mathbf{v}_c = \frac{v_\parallel^2}{\Omega}\left(\nabla \times \mathbf{b}_0\right)_\perp \qquad \text{Curvature drift} \quad , \tag{2.38a}$$

$$\mathbf{v}_{\nabla B_0} = \frac{\mu}{m\Omega}\mathbf{b}_0 \times \nabla B_0 \qquad \text{(equilibrium) grad-B drift} \quad , \tag{2.38b}$$

and $\mathbf{v}_\chi = \mathbf{v}_{\mathbf{B}_{1\perp}} + \mathbf{v}_\chi + \mathbf{v}_{\nabla \mathbf{B}_{1\parallel}}$, with

$$\mathbf{v}_{\mathbf{B}_{1\perp}} = \frac{\left\langle \mathbf{B}_{1\perp}\right\rangle}{B_0} v_\parallel \qquad \text{streaming along } \mathbf{B}_{1\perp} \quad , \tag{2.39a}$$

$$\mathbf{v}_\chi = -\frac{c}{B_0^2}\nabla\chi \times \mathbf{B}_0 \qquad \text{generalized } \mathbf{E}\times\mathbf{B} \text{ drift} \quad , \tag{2.39b}$$

$$\mathbf{v}_{\nabla B_{1\parallel}} = \frac{\mu}{m\Omega}\nabla \mathbf{b}_0 \times \left\langle B_{1\parallel}\right\rangle \qquad \text{(perturbed) grad-B drift} \quad , \tag{2.39c}$$

where we introduced the *generalized fields* given by

$$\chi = \langle \phi \rangle - \frac{v_\parallel}{c} \langle A_{1\parallel} \rangle + \frac{\mu}{q} \langle B_{1\parallel} \rangle \quad . \tag{2.40}$$

We note that from $\dot{\mu} = 0$, we see indeed that μ is indeed an adiabatic invariant in gyrokinetics. The gyrokinetic Vlasov equation (2.35) with the terms can be applied to geometries consistent with the gyrokinetic ordering. As throughout this thesis we will restrict ourselves to the slab geometry, all terms arising from the curvature or magnetic field gradients vanishes, i.e. $\mathbf{v}_c = \mathbf{v}_{\nabla B_0} = 0$. Also, as we do not take perturbations of the parallel magnetic field component into account, we set $B_{1\parallel} = 0$ and $B_0/B_{0\parallel} \sim 1$. The simplified gyrokinetic Vlasov equation for slab geometry then takes the form

$$\frac{\partial f}{\partial t} = - \left(v_\parallel \mathbf{b}_0 + \mathbf{v}_\chi \right) \nabla f - \left(v_\parallel \mathbf{b}_0 + \mathbf{v}_\chi \right) \cdot q \langle \mathbf{E} \rangle \frac{\partial f}{\partial v_\parallel} \quad . \tag{2.41}$$

2.5.1 | The δf equation in local slab geometry

To simplify our equation system, we note that the transport time scales are long compared to the turbulence fluctuations, so that we can separate the distribution function f into a static Maxwellian part f_0 and a perturbed, time-dependent part f_1, i.e. $f_1/f_0 \sim \mathcal{O}(\epsilon)$, so that $f = f_0 + f_1$. This procedure is known as the δf *split*. The Maxwellian is given by

$$f_0(\mathbf{X}, v_\parallel, \mu) = \frac{n(\mathbf{X}}{\sqrt{2\pi m T(\mathbf{X})}^3} \exp\left(- \frac{m {v_\parallel}^2 - 2\mu B_0}{2T(\mathbf{X})} \right), \tag{2.42}$$

which is assumed to only have radial (X) dependence. For our *local setup* investigated here, we assume a radial narrow flux-tube, where the density n and temperature T can be assumed constant, however, we will keep the corresponding gradients. To overcome the problem calculating the time derivative $\partial_t A_{1\parallel}$ on the right-hand side of the Vlasov equation, a so-called *canonical momentum approach* is used, where a modified distribution function g_1 and an additional auxiliary variable G_1 are defined,

$$g_1 = f_1 - \frac{q}{T} v_\parallel \langle A_{1\parallel} \rangle \qquad , \qquad G_1 = g_1 + q\chi f_0 \quad . \tag{2.43}$$

The time derivative is now absorbed in the left-hand side of the Vlasov equation, which results in

$$\frac{\partial g_1}{\partial t} = \mathbf{v}_\chi \cdot \nabla f_0 + \mathbf{v}_\chi \cdot \nabla G_1 + v_\parallel \mathbf{b}_0 \cdot \nabla G_1 + \underbrace{\frac{\mathbf{b}_0}{m} \cdot q \langle E \rangle \frac{\partial f_1}{\partial v_\parallel}}_{\mathcal{O}(\epsilon)} \quad . \tag{2.44}$$

Where from now on the parallel nonlinearity is neglected as in the usual gyro-ordering it is of $\mathcal{O}(\epsilon)$, however, it needs to be included in order to monitor the energy conservation of the gyrokinetic equation system as discussed by Brizard (1989). Using the δf approximation on Eq.(2.41) gives for the Maxwellian term

$$\nabla f_0 = \left[\frac{\nabla n}{n} + \left(\frac{m v_\parallel^2 + 2\mu B_0}{2T} - \frac{3}{2}\right)\frac{\nabla T}{T}\right] f_0 \quad , \tag{2.45a}$$

$$\frac{\partial f_0}{\partial v_\parallel} = -\frac{m v_\parallel}{T} f_0 \quad , \tag{2.45b}$$

$$\frac{\partial f_0}{\partial \mu} = -\frac{B_0}{T} f_0 \quad . \tag{2.45c}$$

Defining $\omega_n = \nabla n/n$ and $\omega_T = \nabla T/T$. The δf Vlasov equation is given by

$$\begin{aligned}\frac{\partial f_1}{\partial t} = &\underbrace{-\frac{c}{B_0}\left[\omega_n + \omega_T\left(\frac{m v^2 + 2\mu B}{2T} - \frac{3}{2}\right)\right]\frac{\partial \chi}{\partial y} f_0}_{\mathbf{v}_\chi \cdot \nabla f_0} \quad \underbrace{+ \quad v_\parallel \frac{\partial G_1}{\partial z}}_{v_\parallel b_0 \cdot \nabla G_1} \\ &\underbrace{+ \quad \frac{c}{B_0}\left(\frac{\partial \chi}{\partial x}\frac{\partial G_1}{\partial y} - \frac{\partial \chi}{\partial y}\frac{\partial G_1}{\partial x}\right)}_{\mathbf{v}_\chi \cdot \nabla G_1} \quad ,\end{aligned} \tag{2.46}$$

where the last terms is the so-called $\mathbf{E} \times \mathbf{B}$ nonlinearity. For the normalization of the equation to make it suitable for numerical simulations the reader is referred to Dannert (2006).

2.6 | The field equations

To close the Vlasov equation (2.44), we have to determine the perturbed fields ϕ_1 and $A_{1\parallel}$ from the field equations. Poisson's equation (Ampere's equation) connects the zeroth-order moment (first-order moment) of the distribution function f_1 to the corresponding field ϕ_1 ($A_{1\parallel}$). However, as Poisson's equation and Ampere's equation are formulated in the particle coordinates $\mathbf{x}$, but our distribution function f_1 is defined in the gyro-center coordinates $\tilde{\mathbf{X}}$, we need to employ first the Lie transform method to *pull-back* the distribution function from the gyro-center coordinates $\tilde{\mathbf{X}}$ to the guiding center coordinates $\mathbf{X}$. A spatial ring-average operator δ is then used to link the particle coordinates $\mathbf{x}$ of the field equations to the guiding-center coordinates $\mathbf{X}$. The procedure is shown in Fig. 2.5.

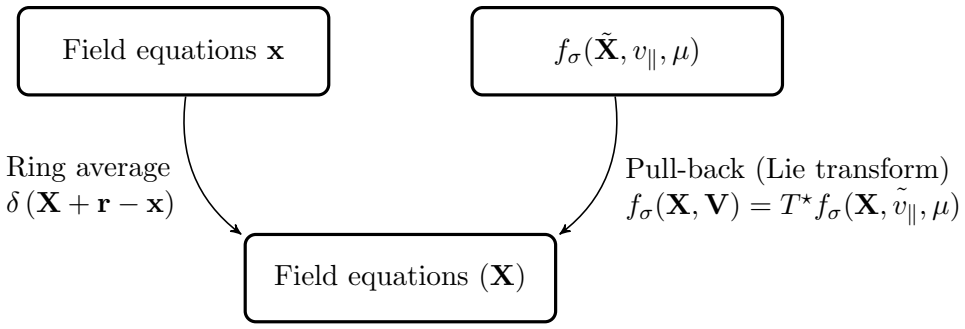

Figure 2.5.: *The field equations have to be first formulated in guiding center coordinates. Using the inverse Lie transform, the gyro-center phase-space function is transformed from gyro- to guiding-center coordinates.*

Figure 2.6: *Schematic description of the $\delta(\mathbf{X}+\mathbf{r}-\mathbf{x})$ function : density of the guiding center expressed through densities on the particle coordinates [adapted from Scott (2006)].*

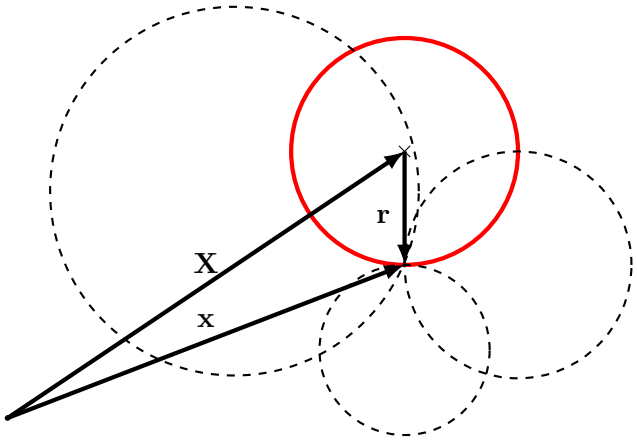

2.6.1 | Poisson's equation

The electric potential is calculated using the non-relativistic *Poisson's equation* (in cgs-units),

$$\nabla^2\phi(\mathbf{x}) = -4\pi\sum_\sigma q_\sigma n_\sigma(\mathbf{x}) \quad , \tag{2.47}$$

where q_σ is the charge of the species σ and n_σ is the number density. All variables in above equation are evaluated at the particle coordinates $\mathbf{x}$. Following Fig. 2.5, we first transform above equation to the guiding center coordinates we employ the spatial ring average $\delta(\mathbf{X}+\mathbf{r}-\mathbf{x})$ operator, has the meaning shown in Fig. 2.6. The density is the zeroth/zeroth-order moment of the distribution function, with $\mathrm{d}Z = \mathrm{d}\mathbf{X}\,\mathrm{d}v_\parallel\,\mathrm{d}\mu\,\mathrm{d}\theta$, we

get

$$n_\sigma(\mathbf{x}) = \int f_\sigma(\mathbf{x},\mathbf{v})\,\mathrm{d}\mathbf{v} \tag{2.48a}$$

$$= \frac{B_0}{m_\sigma}\int \delta(\mathbf{X}+\mathbf{r}-\mathbf{x}) f_\sigma(\mathbf{X}, v_\parallel, \mu, \theta)\mathrm{d}\mathbf{Z} \quad . \tag{2.48b}$$

Note that the integral is over the whole phase-space, however, the ring-average operator acts only on $\mathbf{X}$. The additional term B_0/m_σ arises from the Jacobian of the transform. Here, we used $f(\mathbf{X}, v_\parallel, \mu, \theta)$, but as we used for the Vlasov equation the phase space distribution is defined at the gyro-center coordinates $f(\tilde{\mathbf{X}}, v_\parallel, \mu, \theta)$, we have to transform from $\hat{\mathbf{X}} \to \mathbf{X}$. This is done using the Lie transform:

$$f_\sigma(\mathbf{X}, v_\parallel, \mu) = f_\sigma(\tilde{\mathbf{X}}, v_\parallel, \mu) + g_1^\zeta \frac{\partial}{\partial\zeta} f_\sigma(\tilde{\mathbf{X}}, v_\parallel, \mu) \quad . \tag{2.49}$$

The sum over the Lie generators is of the order of ϵ, thus we apply again the δf split and keep terms only up to order ϵ. The transformation part now only involves the Maxwellian part f_0 given in Eq.(2.45) and its derivatives in Eq.(2.42). Using our previously calculated Lie generators in Eq.(2.25a-c) and Eq.(2.28) and neglecting any radial variation of the Maxwellian part, we get

$$g_1^{\mathbf{X}}\frac{\partial f_{0\sigma}}{\partial \mathbf{X}} = \mathcal{O}(\epsilon^2) \quad , \quad g_1^{\mu}\frac{\partial f_{0\sigma}}{\partial \mu} = -\frac{1}{T}\left(q\widetilde{\phi} - q v_\parallel \left\langle A_{1\parallel}\right\rangle\right) f_{0\sigma} \quad , \tag{2.50a}$$

$$g_1^{v_\parallel}\frac{\partial f_{0\sigma}}{\partial v_\parallel} = -q\frac{v_\parallel}{T}\left\langle A_{1\parallel}\right\rangle f_{0\sigma} \quad , \quad g_1^{\theta}\frac{\partial f_{0\sigma}}{\partial \theta} = 0 \quad , \tag{2.50b}$$

where last term dropped as $\partial f_0/\partial_\theta = 0$. Thus Eq.(2.49) results in

$$f(\mathbf{X}) = f(\tilde{\mathbf{X}}) - \frac{q}{T}\left(\phi_1 - \langle\phi_1\rangle\right) f_0 \quad , \tag{2.51}$$

where $\left\langle A_{1\parallel}\right\rangle$ cancels out and we replaced the oscillating part with its original definition $\widetilde{\phi} = \phi(\mathbf{X}+\mathbf{r}) - \langle\phi(\mathbf{x}+\mathbf{r})\rangle$. Using now Eq.(2.47) with Eq.(2.49) and Eq.(2.48a) gives

$$n(\mathbf{x}) = \frac{B_0}{m}\int \delta(\mathbf{X}+\mathbf{r}-\mathbf{x})\left\{f(\mathbf{X}) + \frac{q}{T}\left[\phi\left(\mathbf{X}+\mathbf{r}\right) - \langle\phi\left(\mathbf{X}\right)\rangle\right] f_0\right\}\mathrm{d}Z \quad . \tag{2.52}$$

Finally the integral term has to be evaluated. The first term only depends on spatial coordinate variables and can be directly integrated, which gives the averaged density over the gyro-ring as

$$\langle n\rangle = \frac{B_0}{m}\int \delta(\mathbf{X}+\mathbf{r}-\mathbf{x})\; f_1\left(\mathbf{X}\right)\; \mathrm{d}\mathbf{X}\,\mathrm{d}v_\parallel\,\mathrm{d}\mu\,\mathrm{d}\theta \quad . \tag{2.53}$$

The second term, $\phi(\mathbf{x})$, can also be directly integrated to get

$$\frac{B_0}{m}\frac{q}{T}\int \delta(\mathbf{X}+\mathbf{r}-\mathbf{x})\ \phi_1(\mathbf{X}+\mathbf{r})\, f_0\ \mathrm{d}\mathbf{X}\,\mathrm{d}v_\parallel\,\mathrm{d}\mu\,\mathrm{d}\theta = \frac{qn_0}{T}\phi(\mathbf{x}) \quad , \tag{2.54}$$

where n_0 is the equilibrium density. The last part is gyro-averaged potential $\langle\phi(\mathbf{X})\rangle$, which is is a function of $\mathbf{X}$ and μ and the integration gives does get gyro-averaged again over a Maxwellian background,

$$\langle\langle\phi\rangle\rangle = \frac{B_0}{m}\int \delta(\mathbf{X}+\mathbf{r}-\mathbf{x})\ \langle\phi_1(\mathbf{X})\rangle\,\frac{q}{T}f_0\ \mathrm{d}\mathbf{X}\,\mathrm{d}v_\parallel\,\mathrm{d}\mu\,\mathrm{d}\theta \tag{2.55a}$$

$$= \frac{B_0}{m}\int \delta(\mathbf{X}+\mathbf{r}-\mathbf{x})\ \langle\phi_1(\mathbf{X})\rangle\,\frac{q}{T}f_0\ \mathrm{d}\mathbf{X}\,\mathrm{d}\mu\,\mathrm{d}\theta \quad , \tag{2.55b}$$

where in the last step we integrated over the parallel velocity $v_\parallel$. Plugging above derivation into Poisson's equation (2.47) and denoting the corresponding f_1 to each species by σ results in the gyrokinetic Poisson's equation

$$\lambda_D^2\nabla^2\phi = -\sum_\sigma\Big[\langle n_\sigma\rangle + \phi - \langle\langle\phi\rangle\rangle_\sigma\Big] \tag{2.56}$$

where we defined the Debye length by $\lambda_D^2 = T/\left(4\pi n_0 q^2\right)$. In the case when ion dynamics are investigated, we can usually assume $\lambda_D \lll 1$, and the left-hand side becomes negligible, in that case, above equation is also known under the name *quasi-neutrality condition*.

2.6.2 | Ampère's equation for $A_{1\parallel}$

For the *Ampère's equation*, we follow a similar procedure as for Poisson's equation. Ampere's equation is given by (in cgs-units)

$$\nabla^2\mathbf{A} - \frac{1}{c^2}\frac{\partial^2\mathbf{A}}{\partial t} = -\frac{4\pi}{c}\mathbf{j} \quad , \tag{2.57}$$

where $\mathbf{A}$ is the magnetic vector potential. For Ampere's equations the perpendicular currents $\mathbf{j}_\perp$ are usually much smaller than the parallel currents $j_\parallel$, thus they are usually neglected (however, it may become important for spherical Tokamaks). The time derivative can be neglected due to gyrokinetic ordering (low frequency).

$$\nabla_\perp^2 A_{1\parallel} = \frac{4\pi}{c}\sum_\sigma j_{\parallel\sigma} \tag{2.58a}$$

$$= \frac{4\pi}{c}\sum_\sigma q_\sigma\int v_\parallel f_\sigma(\mathbf{x},\mathbf{v})\ \mathrm{d}\mathbf{v} \quad . \tag{2.58b}$$

Again, we use the ring-average operator, and the Lie back transform, to get $j_{1\parallel,\sigma}$ from $f(\tilde{\mathbf{X}}, v_\parallel, \mu)$,

$$j_{1\parallel,\sigma} = \frac{B_0}{m_\sigma} q_\sigma \int \delta\left(\mathbf{X} + \mathbf{r} - \mathbf{x}\right) v_\parallel \left[f_\sigma\left(\mathbf{X}, \mathbf{V}\right) + g_1^\zeta \frac{\partial}{\partial \zeta} f_\sigma\left(\mathbf{X}, \mathbf{V}\right) \right] \mathrm{d}Z \tag{2.59a}$$

$$= \frac{B_0}{m_\sigma} q_\sigma \int \delta\left(\mathbf{X} + \mathbf{r} - \mathbf{x}\right) v_\parallel f_\sigma\left(\mathbf{X}, \mathbf{V}\right) \mathrm{d}Z \quad , \tag{2.59b}$$

where we performed the δf split and found that the terms of the form $v_\parallel f_{0\sigma}$ are anti-symmetric in $v_\parallel$ and thus drop out. Also we assumed no background current from the Maxwellian. Performing the remaining term in integral (2.59a) gives the gyro-averaged parallel current

$$\left\langle j_{1\parallel,\sigma} \right\rangle = \frac{B_0}{m_\sigma} q_\sigma \int \delta(\mathbf{X} + \mathbf{r} - \mathbf{x}) v_\parallel f(\mathbf{X}, \mathbf{V}) \, \mathrm{d}Z \tag{2.60}$$

such that the Ampere's equation (2.58a) is given by

$$\nabla_\perp^2 A_{1\parallel} = -\frac{4\pi B_0}{c} \sum_\sigma \frac{q_\sigma}{m_\sigma} \left\langle j_{1\parallel,\sigma} \right\rangle \quad . \tag{2.61}$$

2.7 | The gyro-averaging operator in Fourier space

The gyro-averaging e.g. for the variable $\phi(\mathbf{x})$ can be directly calculated using in Eq.(2.12). However, after a numerical discretization of the grid, we face the problem that while $\phi(\mathbf{x})$ is part of our computational grid, $\phi(\mathbf{x}+\mathbf{r})$ may lie outside. Lee (1987) and Lin and Lee (1995) suggested therefore that in the case of $k_\perp^2 \lesssim 2$, we can use use a 4-point averaging routine, with a computational cost of $\mathcal{O}(N)$, to calculate the gyro-averaging, where the double-average term is calculated using weighted averages.

For the case we are also interested in short-wavelength phenomenon $k_\perp > 2$, Nishimura et al. (2006) and T. Görler et al. (2011) showed that it is advantageous to setup a gyro-averaging matrix using a finite element basis with Hermite interpolation functions. The matrix entries can be calculated beforehand without having to know the value of $\phi(\mathbf{x})$. The gyro-averaging is then obtained by a simple matrix-vector product, with a computational cost of $\mathcal{O}(N^2)$.

For the case of local simulations with a homogeneous background and a periodic radial and poloidal domain, we can calculate the gyro-average analytically using following identity:

$$\langle \phi(\mathbf{x}) \rangle = \frac{1}{2\pi} \int_{\theta=0}^{2\pi} \mathrm{d}\theta \; \phi(\mathbf{x}) = \frac{1}{2\pi} \int_{\theta=0}^{2\pi} \mathrm{d}\theta \; \phi(\mathbf{X} + \mathbf{r}) \quad . \tag{2.62a}$$

Transforming into Fourier space gives

$$\langle \phi(\mathbf{k}) \rangle = \frac{1}{2\pi} \int_{\theta=0}^{2\pi} \mathrm{d}\theta \int_{\mathbf{k}} \mathrm{d}\mathbf{k}\, \phi(\mathbf{k}) \cdot e^{i\mathbf{k}(\mathbf{X}+\mathbf{r})} \tag{2.63a}$$

$$= \frac{1}{2\pi} \int_{\theta=0}^{2\pi} \mathrm{d}\theta \int_{\mathbf{k}} \mathrm{d}\mathbf{k}\, \phi(\mathbf{k}) \cdot e^{i\mathbf{k}\mathbf{X}} e^{i\mathbf{k}\cdot\mathbf{r}} \quad , \tag{2.63b}$$

using the usual rule of the scalar product $\mathbf{r} \cdot \mathbf{k} = |\mathbf{r}||\mathbf{k}| \cos\theta = \rho k_\perp \cos\theta$, with the definition of $k_\perp = \sqrt{k_x^2 + k_y^2}$ results in

$$\langle \phi(\mathbf{k}) \rangle = \frac{1}{2\pi} \int_{\mathbf{k}} \mathrm{d}\mathbf{k}\, \phi(\mathbf{k}) \cdot e^{i\mathbf{k}\mathbf{X}} \int_{\theta=0}^{2\pi} \mathrm{d}\theta\, e^{i\rho k_\perp \cos\theta} \tag{2.64a}$$

$$= \int_{\mathbf{k}} \mathrm{d}\mathbf{k}\, \phi(\mathbf{k}) \cdot e^{i\mathbf{k}\mathbf{X}} J_0(\lambda) \quad , \tag{2.64b}$$

with $\lambda = \rho k_\perp$. After performing the Fourier back transformation, we get the gyro-averaged variable in real space. Here, J_0 is the *Bessel function of the first kind*[2] shown in Fig. 2.7a. The gyro-averaging effect on a randomly chosen variable $\phi(\mathbf{x})$ is shown in Fig. 2.8. The double-average over the Maxwellian background can be also expressed analytically in Fourier space, where the derivation can be found in Szepsi (2012),

$$\langle\langle \phi(\mathbf{x}) \rangle\rangle = \int_{\mathbf{k}} \mathrm{d}\mathbf{k}\, \phi(\mathbf{k})\, I_0(b) e^{-b} \cdot e^{i\mathbf{k}\mathbf{X}} \sim \int_{\mathbf{k}} \mathrm{d}\mathbf{k}\, \phi(\mathbf{k})\, \frac{b}{1+b} e^{i\mathbf{k}\mathbf{X}} \quad , \tag{2.67}$$

where $b = \rho_{ts}^2 [k_x^2 + k_y^2$ and I_0 is the *modified Bessel function*. The latter term shows the Padé approximant which is often used to reduce computational cost as discussed by Scott (2006). The dependence is shown in Fig. 2.7b.

2.8 | The Lenard–Bernstein collisional operator

Fusion plasmas are essentially collisionless on the timescales relevant within the δf formulation. However, for numerical reasons a Lenard–Bernstein (LB) operator, as given

[2] One of the possible definition of a Bessel function of the first kind can be found in Abramowitz and Stegun (1964):

$$J_n(z) = \frac{i^{-n}}{\pi} \int_0^\pi \mathrm{d}\theta\, e^{iz\cos\theta} \cos(n\theta) \quad , \tag{2.65}$$

with $n = 0$ and substituting above equation with $\theta' = \theta - \pi$

$$\frac{1}{\pi} \int_\pi^{2\pi} \mathrm{d}\theta\, e^{iz\cos\theta} = \frac{1}{\pi} \int_0^\pi \mathrm{d}\theta'\, e^{iz\cos(\theta'-\pi)} = \frac{1}{\pi} \int_0^\pi \mathrm{d}\theta'\, e^{-iz\cos\theta'} = J_0(-z) \quad , \tag{2.66}$$

Finally, noting the symmetry property of the Bessel function $J_0(-z) = J_0(z)$ we get the desired result.

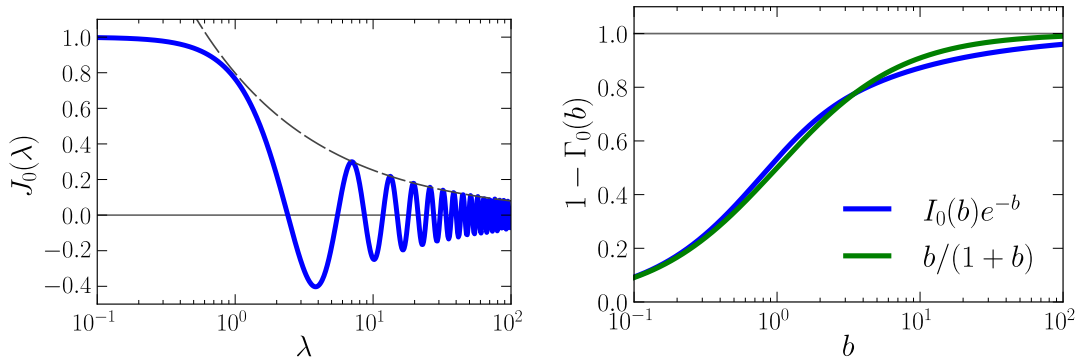

(a) *Bessel* J_0 **(b)** $1-\Gamma_0$

Figure 2.7.: *The left figure shows the dependence of the* J_0*, where the dashed line shows its asymptotic expansion with* $\overline{J_0(z)} \sim z^{-1/2}$*. The right figure shows* $1-\Gamma_0$ *used for double-averaging.*

by Lenard and Bernstein (1958),

$$\mathcal{C}_{\mathrm{LB}} = \beta_C \frac{\partial}{\partial v_\parallel}\left[v_\parallel f_1 + v_0^2 \frac{\partial f_1}{\partial v_\parallel}\right] \quad , \tag{2.68}$$

is introduced, where v_0 is the mean square velocity of the species. The collisionality β_c is usually chosen small, to not influence the simulation results. The LB operator does conserve the particle number density, however it does not conserve momentum and energy. For long-time simulations however, we can introduce correction terms as suggested by Shinsuke Satake and Sugama (2008); Satake et al. (2008) in order to guarantee conservation of energy and momentum. Note, that this collisional operator does not take any gyro-motion into account. A gyro-phased averaged Lenard-Bernstein operator can be found in Clemmow and Dougherty (1969). Also the LB operator is restricted to collisions in the parallel velocity space, however, a more advanced Lorentz operator which takes collision in $v_\parallel$ and μ into account should be included in order to study neoclassical effects.

2.9 | Observables

Experiments do not have a direct access to the distribution function $f_{1\sigma}$, but can measure the radial particle Γ_σ and heat χ_σ fluxes of a species σ. In numerical simulations, these quantities, given in particle coordinates $\mathbf{x}$, are obtained from the moments of the

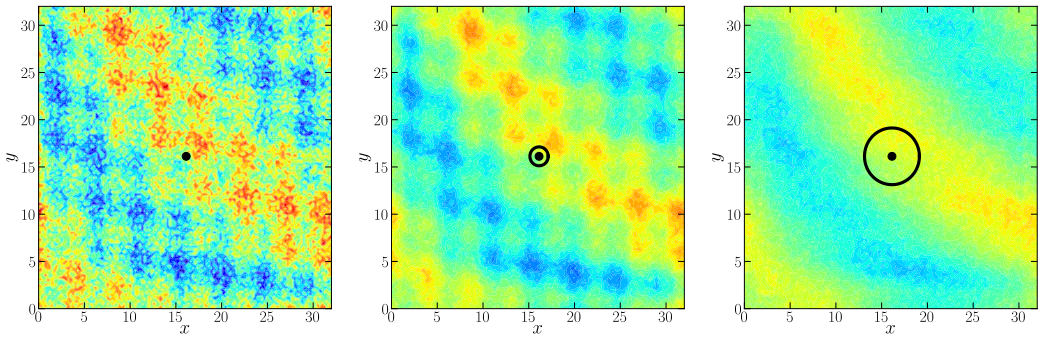

(a) *Original Potential* **(b)** *Ring average for* $\rho = 1$ **(c)** *Ring average for* $\rho = 3$

Figure 2.8.: *Effect of gyro-averaging for a random potential for various gyro-radii. A smoothing effect is observed for the ring average.*

distribution function

$$\Gamma_\sigma(\mathbf{x}) = \int v(\mathbf{x}) f_{1\sigma}(\mathbf{x}, \mathbf{v}) \qquad \mathrm{d}^3 dv \quad , \tag{2.69a}$$

$$\chi_\sigma(\mathbf{x}) = \int \frac{1}{2} m_\sigma v^2 v_x f_{1\sigma}(\mathbf{x}, \mathbf{v}) \quad \mathrm{d}^3 v \quad . \tag{2.69b}$$

However, our distribution function is given in gyro-center coordinates $\tilde{\mathbf{X}}$. Thus — similar in deriving the field equations — we have to transform from gyro-center coordinates to particle coordinates. A general rule for calculating the corresponding moments from the gyro-center distribution function was given by Görler (2009) and Lapillonne (2009). The moments relevant for the calculation of the electrostatic heat and particle fluxes are then given by

$$M_{00} = \pi \left(\frac{2B}{m}\right) \int \frac{B^\star}{B_0} \langle f_1 \rangle \, \mathrm{d}v_\parallel \, \mathrm{d}\mu - \frac{n_0 B_0}{T_0^2} q_\sigma \left[\phi_1 - \langle\langle \phi \rangle\rangle\right] \quad , \tag{2.70}$$

$$M_{20} = \pi \left(\frac{2B}{m}\right) \int \frac{B^\star}{B_0} \langle f_1 \rangle \, v_\parallel^2 \mathrm{d}v_\parallel \, \mathrm{d}\mu - \frac{n_0 B_0}{T_0^2} v_{Ta}^2 q_\sigma \left[\phi_1 - \langle\langle \phi \rangle\rangle\right] \quad , \tag{2.71}$$

$$M_{02} = \pi \left(\frac{2B}{m}\right)^2 \int \frac{B^\star}{B_0} \langle f_1 \rangle \, \mu \mathrm{d}v_\parallel \, \mathrm{d}\mu - \frac{n_0 B_0}{T_0^2} \left(\frac{2B_0}{m}\right) q_\sigma \left[\phi_1 - \int \langle \phi \rangle \, \mu e^{\frac{\mu B_0}{T_0}} \mathrm{d}\mu\right] \quad . \tag{2.72}$$

The corresponding electrostatic heat fluxes in shearless slab geometry are given by

$$\Gamma_\sigma = \frac{\partial \phi_1}{\partial y} M_{00} \qquad , \qquad \chi_\sigma = -\frac{\partial \phi_1}{\partial x} \left(M_{20} + M_{02}\right) \quad . \tag{2.73}$$

Note that the moments on right-hand side of the field equations would be equivalently given by the M_{00} for the Poisson's equation, and M_{10} moments for Ampere's equation.

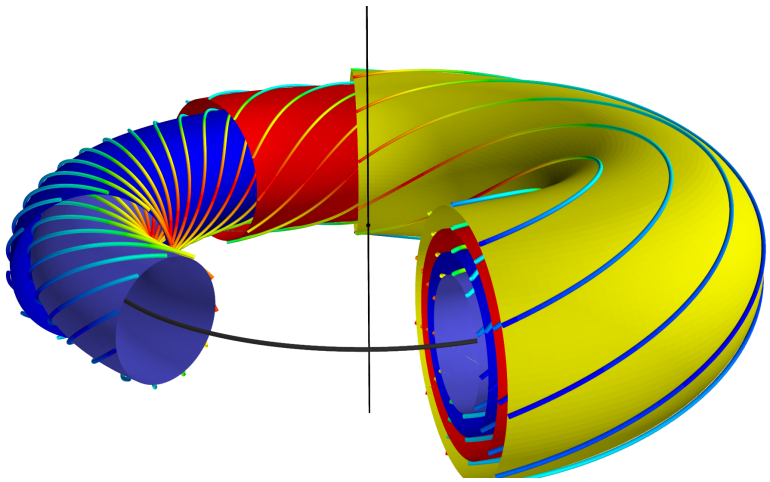

Figure 2.9: *Flux surfaces and field lines of a circular shaped Tokamak. Note that the safety factor is usually different for each flux surfaces.*

2.10 | Brief introduction to Tokamak geometry

The first machines scientist used to try to achieve fusion plasma, where the so-called *magnetic mirrors*. There, a strong guide field is produced by multiple coils, with a stronger magnetic field at the ends. By conservation of the first adiabatic this should in principle confine the plasma. However, it was quickly realized that a so-called *loss-cone instability* limited the confinement performance. In order to circumvent the loss-cone instability, the magnetic field tube is bended so that its ends met. The charged particles would follow the field lines until their lines attach to themselves. During this movement, however, the ∇B drift will push them outwards, which led to a loss of confinement. Thus a transformer is used to induce a current inside the plasma (inductive current drive), which produces an additional poloidal magnetic field. Both fields combine, so that the resulting magnetic field is tilted as shown in Fig. 2.9. When we now follow the magnetic field line, then on average, the particle will spent half their time on the outboard side of the plasma, where the ∇B drift would push them out of the plasma. But the particles will spent the other half of their revelation time on the inward side, where the ∇B drift would push them outward — or in this case into the plasma. With this setup the ∇B drift could be successful compensated, and a confinement established. This setup is known as a Tokamak. The tilt of the magnetic field lines is quantized through the *safety factor* given by

$$q(r) = \frac{1}{2\pi} \oint \frac{1}{R} \frac{B_\phi(r)}{B_p(r)} \mathrm{d}s \quad , \tag{2.74}$$

where B_ϕ is the poloidal component of the magnetic filed and B_r its radial component, For some specific values of $q(r_{rs}) = N/M$, where N is the number of poloidal turns and

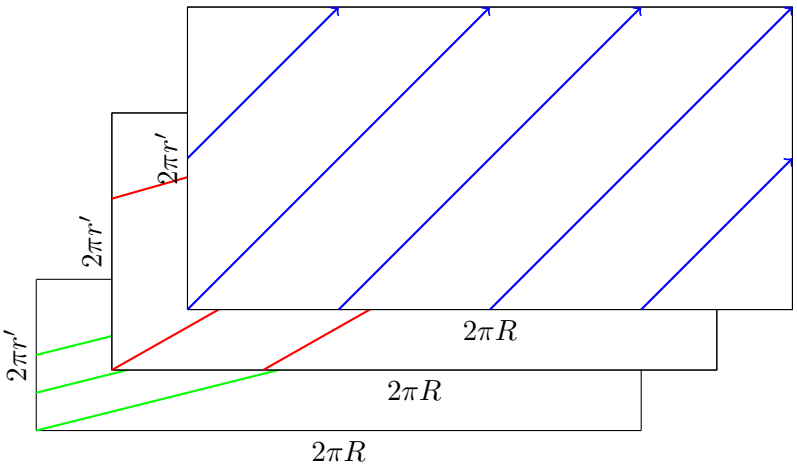

Figure 2.10: *Unwounded flux surfaces from the Tokamak shown in Fig. 2.9. The length is given by $L_z = 2\pi R$ and the width by $L_y = 2\pi r$. The angle of the field line is given by the safety factor $q = m/n$.*

M the number of poloidal turns, the magnetic field lines will connect to themselves. This may drive instability, such as magnetic reconnection, as a small magnetic perturbation of field lines, will reach back after M turns and may result in self-amplification. Another important factor is the *shearing rate* defined by $\hat{s} = (r/q)(\mathrm{d}q/\mathrm{d}r)$, where we need to assure that $\hat{s} > 1$ in order to avoid ideal MHD instabilities such as *kink modes*.

Simulating a whole torus with a resolution up to the ion or even electron gyro-radius will be far too expensive. Thus, a common approach is to restrict the simulation domain to one specific field line tube and align the coordinate system to the magnetic field lines. Multiple approximate geometries using this approach exist, for example, the $s-\alpha$ geometry, or even more advanced geometries obtained directly from MHD calculations, which do take elongation and triangularity into account such as discussed by Burckel et al. (2010). Here, we will use more simpler geometries, such as the two-dimensional sheared and shearless slab geometries.

2.10.1 | Simplified three dimensional geometries

In Fig. 2.10 an unwounded flux surface is shown. The length of the flux surface is given by $L_z = 2\pi R$, where the width is given by $L_y = 2\pi r$. Note that for a large-aspect ratio Tokamak $\epsilon = \frac{r}{R} \ll 1$ toroidal effects can be neglected. If we neglect the curvature and shearing of the magnetic field line are neglected, we get the *shearless slab* geometry, where the magnetic field is simply given by $B_0 = \hat{z}$. The parallel wavenumber is then simply given by

$$k_\parallel = \mathbf{B}\cdot\mathbf{k} = \begin{pmatrix} 0 \\ 0 \\ 1 \end{pmatrix} \cdot \begin{pmatrix} k_x \\ k_y \\ k_z \end{pmatrix} = k_z \quad . \tag{2.75}$$

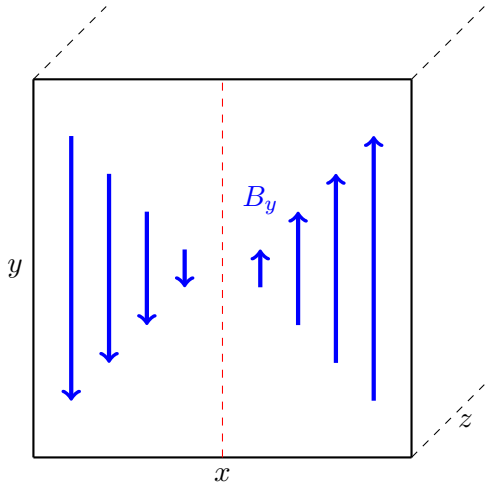

Figure 2.11: *Sketch of a two-dimensional sheared slab geometry (adapted from Fitzpatrick). The plasma is homogeneous in the toroidal z-direction. Also the radial boundaries are assumed to be perfectly conducting walls. The red line denotes the rational surface. Blue lines denote the strength of B_y. We have also periodicity in y-direction.*

2.10.2 | Two-dimensional sheared slab geometry

When we are close to a rational surface, we can write the magnetic field as $B_0 = [\hat{z} + \hat{s}\hat{y}]$, so that the parallel wavenumber, which points along the magnetic field line is given by

$$k_{\parallel} = \mathbf{B} \cdot \mathbf{k} = \begin{pmatrix} 0 \\ \hat{s}x \\ 1 \end{pmatrix} \cdot \begin{pmatrix} k_x \\ k_y \\ k_z \end{pmatrix} = \hat{s}xk_y + k_z \quad . \tag{2.76}$$

From the turbulence structure, we know that $k_z \ll 1$, and thus we can additionally drop the z-dependence. Thus we end up with a geometry, with a structure as sketch in Fig. 2.11. Note, that we have an x-dependence of the shearing rate, where the location of the rational surface is at x_0. In the sheared slab geometry, the drift-waves become preferable unstable along the ration surface.

2.10.3 | Two-dimensional constant-θ geometry

In the constant θ-geometry, we assume a homogeneous plasma in the z-direction, where the magnetic field has a constant angle θ to the z-direction ($B_0 = [\hat{z} + \theta\hat{y}]$) so that the parallel wavenumber is given by

$$k_{\parallel} = \begin{pmatrix} 0 \\ \theta \\ 1 \end{pmatrix} \cdot \begin{pmatrix} k_x \\ k_y \\ k_z \end{pmatrix} = \theta k_y \quad , \tag{2.77}$$

where the k_z term drops out due to homogeneity assumption. This geometry was used, e.g., by Nakata et al. (2011) to study the properties of the ETG turbulence.

Part II.

Research work

3 | Numerical implementation of the gkc++ solver

The nonlinear gyrokinetic equation system can not be solved analytically except for the most simplified cases. A numerical solution procedure has to be employed, where the gyrokinetic equations discussed in Sec. 2.5.1 and Sec. 2.6 are discretized and the time evolution of the distribution function is numerically integrated. In the following sections we will describe the internals of the *G*yro*K*inetic *C*ode gkc++ which was developed by the author during this PhD which will then be employed in Ch. 5 and Ch. 6 to study the multi-scale interactions in magnetically confined plasmas.

3.1 | Solver internals

The gyrokinetic equation system is solved as an initial value problem (IVP), where we choose a small perturbation $f_{1\sigma}(t = 0)$ which is then integrated in time. For a numerical simulation code, it is crucial to benchmark the obtained numerical result to analytical results in order to confirm the correct implementation of the terms and to investigate the effect of the numerical discretization. For example, the phenomenon arising from the discretization of the parallel velocity space will be discussed in chapter 4 and in the appendix A, the gkc++ code is benchmarked to a simplified analytical solution to confirm its correctness and normalizations.

3.1.1 | Numerical grid

The distribution function $f_{1\sigma}(x, y, z, v_\parallel, \mu; t)$ is a continuous function of the three spatial variables (x, y, z), two velocity variables $(v_\parallel, \mu)$, and the continuous time (t), with either one or more species σ. While the spatial dimensions have a finite extend given by the lengths $x \in [-L_x/2, L_x/2]$, $y \in [0, L_y]$, $z \in [0, L_z]$, the extend of the velocity variables $v_\parallel \in (-\infty, \infty)$ and $\mu \in [0, \infty)$ is infinite. In all cases, we need to take the boundary conditions into account, which either may be periodic, i.e. $f_1(0, \dots) = f_1(L_x, \dots)$, zero, or other any other boundary.

gkc++ is a Vlasov type solver, which solves the gyrokinetic equation system on a fixed grid. For a numerical solution, the distribution function has to be discretized to include

only a finite number of points in each dimension, namely

$$f_{1\sigma}(x_n, y_n, z_n, v_{\parallel}, \mu_m; t_l) \quad , \tag{3.1}$$

such that the values of the $f_{1\sigma}$ are only known at the points x_n (and respectively for the other dimensions). With an increase of the number of discretization points, that is by increasing the resolution, the simulation should become more exact, however, the computational requirements also increases with the number of grid points N. Because of that, N is chosen a small as possible but still large enough to resolve the physics. By doubling the resolution, i.e., $N' = 2N$, the physical quantities, such as the observables given in Sec. 2.9, should be comparable, which is then known as a *converged solution*. In principle, we are free to choose our discretization method of each domain, however, this will have a large affect on the way derivatives are calculated, as well as the numerical accuracy. With an optimized choice, it is possible to find a converged solution at a minimal computational cost. In the following, we will describe the choice made for the gkc++ code to discretized the distribution function. Unless otherwise stated, these domains are chosen to be periodic.

Radial and toroidal discretization

For the discretization of the spatial dimensions in x and z, we choose an equidistant grid. In this case, the continuous radial variable x is then the discretized into a discrete and finite number of points x_n, according to the rule

$$x_n = -\frac{L_x}{2} + \frac{L_x}{N_x} \cdot n \qquad , \quad \text{where} \quad n = 0, 1, \ldots, N_x - 1 \quad , \tag{3.2}$$

and L_x is the length of the radial dimension with a total of N_x discretization points. The z dimension is dealt with the same way. We note again that N_x should be chosen large enough such that the physical process is captured well and similar results are obtained with increased resolutions. Note that for $N_x \to \infty$, we should capture all physical effects, however, there are few exceptions to that, for example, even for $N_x \to \infty$, we still have a countable set, and as such a continuum cannot be represented. The choice of N_x will also influence our *numerical error*, which arises when calculating derivatives.

Discretization of poloidal direction

In all cases investigated here, the poloidal direction is periodic with no variations of the background magnetic field line along the y direction. Thus we choose to directly evolve Fourier methods in order to simplify the calculation of the derivatives along the y direction. The transform from a real space variable to the Fourier space, is given by

the discrete Fourier transformation (DFT),

$$A(x,m) = \sum_{y_i=0}^{N_y-1} A(x,y_i) e^{ik_y(m)y} \quad , \quad \text{with} \quad k_y(m) = \frac{2\pi}{L_y} \cdot m \quad , \tag{3.3}$$

where k_y is the corresponding poloidal *wavenumber* and m denotes the poloidal *mode number*. Note that we used a summation instead of an integral, which implies an equidistant discretization. Here, m is a non-negative integer, which accounts for the fact that our variables are real quantities ($\mathrm{Im}\{f_{1\sigma}(x,y,\dots\} = 0$) thus it is sufficient to evolve only positive modes, as the negative modes can be obtained by taking the complex conjugate of the positive modes $A(x,k_y) = A(x,-k_y)^\star$. This effectively reduces the computational cost by half. We sum up to $m = N_y/2 + 1$ which corresponds to the so-called *Nyquist* frequency and represents the highest frequency which can be represented on this regular spaced grid in Fourier space. However, as $A(x,m)$ is complex, the information content is equivalent. The advantage of the Fourier method is the simplicity in calculating the derivatives, which becomes a simple multiplication in Fourier space given by

$$\partial_y A(x,y) \to ik_y A(x,k_y) \quad . \tag{3.4}$$

Directly using the Fourier transformation rule Eq.(3.3) would result in a computational complexity of the order of $\mathcal{O}(N^2)$, as the transform includes two summations. However, Cooley and Tukey (1965) showed that for a array of the size $N = 2^n$, the computational complexity of the Discrete Fourier transform can be reduced to $\mathcal{O}(N \log N)$, by applying a procedure called now the *Fast Fourier Transformation* (FFT). Subsequently, the condition on the size of N was relax, so that most state-of-the-art FFT implementations such as the implementation used for gkc++ , Frigo and Johnson (2005), are $\mathcal{O}(N \log N)$ for arbitrary sizes of N. The implementation by Frigo and Johnson (2005) additionally supports SIMD optimization, multi-threading capabilities, and distributed parallelization through MPI, making it the best choice for high-performance applications.

Parallel velocity integration $v_\parallel$

For the dimensions x, y, and z, we use an equidistant discretization for the parallel velocity. However, in contrast to the spatial dimensions, which are of finite size, the velocity dimensions are not. Still, we can apply a lower/upper cut-off at $\pm L_v$ for the parallel velocity space dimension by noting that our background Maxwellian decays exponentially ($\propto \exp\left[v_\parallel^2/v_{te}^2\right]$). If the cut-off length L_v, is chosen large enough, so that $f_0(\pm L_v) \lll 1$, and such that the wings will have negligible contributions. With the finite cut-off length $\pm L_v$, we use Eq.(3.2) to equidistantly discretize the parallel velocity space.

In order to solve the field equations described in Sec. 2.6, e.g. Poisson's equation, we have to integrate over the velocity space of the distribution function $f_{1\sigma}(\mathbf{X}, v_\parallel, \mu)$. Here, for the equidistant parallel velocity dimension, the *rectangle rule* is used. It is given by

$$\int_{v=-L_v}^{L_v} f(v_\parallel)\,\mathrm{d}v_\parallel \approx \sum_{n=0}^{N_v-1} \Delta v\, f(v_n) \qquad \text{, with} \quad \Delta\, v = \frac{2L_v}{N_v} \quad . \tag{3.5}$$

Although the rectangle rule is only a first order method,

$$\int_{v=-L_v}^{L_v} f(v_\parallel)\,\mathrm{d}v_\parallel \approx \Delta v \sum_{n=0}^{N_v-1} \frac{f(v_{n+1}) + f(v_n)}{2} = \Delta v \sum_{n=1}^{N_v-2} f(v_n) + \frac{f(-L_v) + f(L_v)}{2} \quad , \tag{3.6}$$

the values at the cut-off $f(-L_v) \lll 1$ and $f(L_v) \lll 1$ are negligible, such that it effectively becomes the second order *trapezoidal rule*. We could use a higher order integration scheme for the parallel velocity direction, however, that would require a non-equidistant discretization, which is not recommended as this would increase the complexity of calculating the derivatives in the collisional operator.

Perpendicular velocity integration μ

In contrast to the parallel velocity dimension, the dimension for μ ranges from $\mu \in [0, \infty)$, with $\lim_{\mu\to\infty} f_0(\mu) = 0$, but $f_0(\mu = 0) \neq 0$. Thus using an equidistant discretization with the rectangle rule Eq.(3.5) would require a very large number of mesh points N_μ to give acceptable results. However, as μ is an adiabatic and neoclassical effects are neglected (collisions in μ), we can take advantage of the fact that no derivatives in the μ direction appear in the equations and thus a higher order integration scheme, such as the *Gaussian quadrature*, can be chosen. The general rule for Gaussian quadrature (shifted and rescaled) is given by

$$\int_0^{L_\mu} f(\mu) = \frac{L_\mu}{2} \sum_n w_n f\left(\frac{L_\mu}{2}\mu_n + \frac{L_\mu}{2}\right) \quad , \tag{3.7}$$

where w_n are the weights, μ_n are the nodes and L_μ is the perpendicular velocity cut-off, chosen such that $f_0(L_\mu) \lll 1$. The weights and nodes are free to choose, however, we can choose them to increase the integration order (which in the optimal case is equivalent to the number of discretization points in case of a smooth function). Slight modification of Eq.(3.7) exits with different choices of w_n and μ_n such as the Gauss-Legendre, Gauss-Radau and Gauss-Lobatto integration schemes with weights and nodes shown in Fig. 3.1a. A benchmark simulation shows the superiority of the Gaussian integration scheme, which gives already convergent results with $N_\mu = 8$ and $L_\mu = 9$

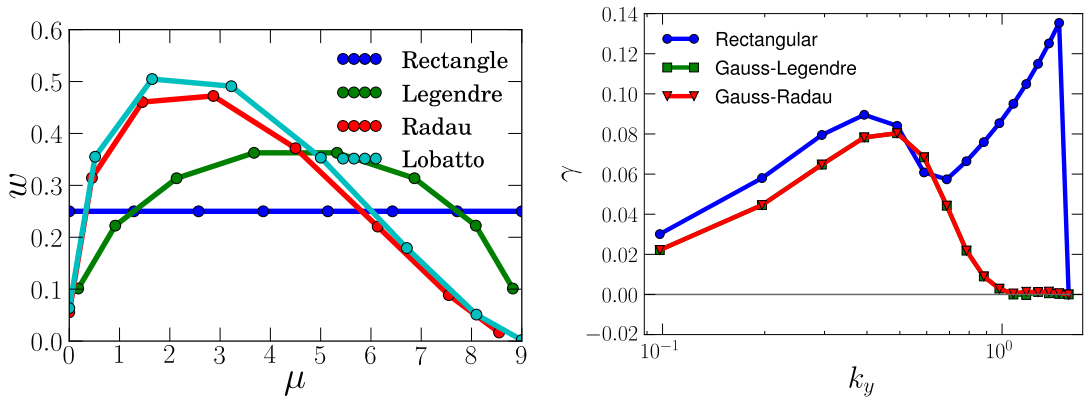

(a) *Nodes / Weights* **(b)** *Growth rates*

Figure 3.1.: *The nodes and weights for several integration rules is shown in the left figure for the rectangle, Gauss-Legendre and Gauss-Radau. The right figure shows the linear growth rates obtained for the test case (A), see Tab.(3.2), using $N_\mu = 8$. The Gaussian integration schemes quickly convergence in contrast to the first order rectangle method.*

compared to the rectangle rule, which requires $N_\mu \geq 64$ to give convergent results of the linear growth rates as shown in Fig. 3.1b. Differences between Gauss-Legendre, Gauss-Radau and Gauss-Lobatto are negligible for the case investigated here.

3.1.2 | Calculation of derivatives using finite differences

Apart from the poloidal direction (calculating the derivative in Fourier space is a multiplication which does not exhibit any errors), for the other directions, the derivatives have to be calculated using a finite number of points. One of the simplest discretization stencil for a first derivative for an equi-distant discretized grid is e.g. the *second-order central-differences* (CD-2) stencil given by

$$\frac{\partial A}{\partial z} = A_{z;z} = \frac{A_{n-1} - A_{n+1}}{2\,\Delta z} \equiv (2\Delta z)^{-1}\,[-1\;0\;1] \quad , \tag{3.8}$$

where the last term shows the corresponding *stencil notation*. A summary of the various finite differences stencils used in gkc++ for the discretization of the derivative operator is shown in Tab. 3.1. In general, we can distinguish different stencils by certain properties such as the cut-off error, phase, and gain errors. The gain error of a stencil denotes the damping of a pure sinusoidal wave depending on the its wavenumber as shown in Fig. 3.2a. Another crucial error is the so-called mapping as shown by Pueschel et al. (2010). For example, assuming a Fourier mode $A \propto \hat{A} \exp(-ik_\zeta \zeta)$ of the second-order

Name	Derivative	Order	Stencil
Upwind Difference	1 (∂_x)	1 (ϵ)	$(\zeta)^{-1}\left[\begin{array}{ccc} -1 & 1 & 0 \end{array}\right]$
Upwind Difference	1 (∂_x)	3	$(\zeta)^{-1}\left[\begin{array}{ccc} -1 & 1 & 0 \end{array}\right]$
Central Difference	1 (∂_x)	4	$(12\zeta)^{-1}\left[\begin{array}{ccccc} -2 & 8 & 0 & -8 & 2 \end{array}\right]$
Central Difference	2 (∂_x^2)	4	$\left(12\zeta^2\right)^{-1}\left[\begin{array}{ccccc} -1 & 16 & -30 & 16 & -1 \end{array}\right]$
Hyper-diffusion Term	4 (∂_x^4)	2	$\left(12\zeta^2\right)\left[\begin{array}{ccccc} -1 & 16 & -30 & 16 & -1 \end{array}\right]$

Table 3.1.: *Finite difference stencils used in gkc++ for an equidistant discretized grid. The usage of higher order (more accurate) stencils is desirable, however, a wider stencil increases the computational cost and the number of ghost cells to be used at the boundaries.*

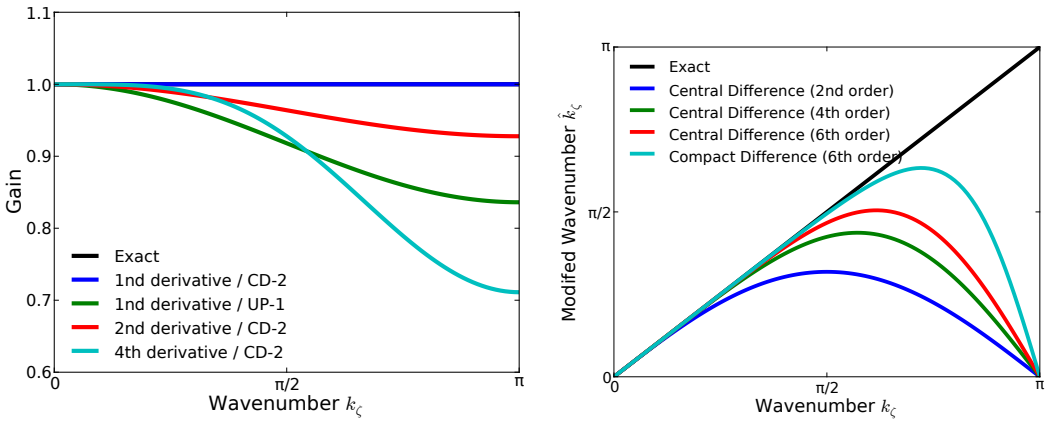

(a) *Gain G vs k*

(b) *Modified Wavenumber*

Figure 3.2.: *Left figure shows the numerical gain, while the right figure shows the mapping of high-k components to low-k components for the CD-2, CD-4, CD-6 and 6th order compact stencil. Higher order methods reduces the impact of gain and mapping, however, with an increase of computational cost.*

central-difference stencil in the ζ dimension ($\partial_\zeta = (2\Delta z)^{-1}[1, 0, -1]$), leads to

$$\frac{\partial A}{\partial \zeta} = ik_z A = \frac{A(\zeta + \Delta\zeta) - A(\zeta - \Delta\zeta)}{2\Delta\zeta} = \frac{\sin(k_\zeta \Delta\zeta)}{k_\zeta \Delta\zeta} ik_\zeta A \equiv h(\zeta) ik_\zeta A \quad , \tag{3.9}$$

where $h(ik_\zeta)$ is an undesirable mapping function and thus leads to undesirable growth in the high-k region (which would especially introduce a large error for the poloidal direction). The mapping for various stencils are shown in Fig. 3.2b. Pueschel et al. (2010) showed that the mapping effect can be reduced by including a small hyper-diffusive term, however, in general, higher-order discretization stencils are favorable as they have have better error properties, however, higher order stencils are usually wider and thus we have to provide more ghost cells for the boundaries and the computational

cost increases as well. For future improvements, it may be fruitful to use more advanced schemes, such as the implicit discretization (compact stencils) given by Lele (1992), the IDO-CF scheme suggested by Imadera et al. (2009) or the multi-moment scheme suggested by Kawano et al. (2011), in order to minimize the discretization errors.

3.1.3 | Time step integration

The left-hand side of the gyrokinetic Vlasov's equation (2.44) includes the time derivative of the perturbed distribution function. Like for the spatial discretization, we need to discretize the time derivative in order to evolve $f_{1\sigma}(t)$ in time as an *initial value problem* (IVP). A simple method for the time discretization is the *Euler forward* method, which is given by

$$\frac{f_{1\sigma}^{t+\Delta t} - f_{1\sigma}^{t}}{\Delta t} = \mathcal{L}_\sigma\left(f_{1\sigma}^{t}\right) + \mathcal{N}_\sigma\left(f_{1\sigma}^{t}\right) + \mathcal{C}_\sigma\left(f_{1\sigma}^{t}\right) \quad , \tag{3.10}$$

where $f_{1\sigma}^{t}$ is the value at the current time t, $f_{1\sigma}^{t+\Delta t}$ is the value at a later time given by $t + \Delta t$ and $\Delta t > 0$ is the time step size. With this discretization, we can choose a random *initial perturbation* $f_{1\sigma}(t = 0)$ at the initial time $t = 0$ and evolve $f_{1\sigma}$ in time using Eq.(3.10) with a predefined Δt until a maximum time $t_{\max}$ is reached. However, the Euler forward time discretization scheme will in most cases ($\mathrm{Im}(\omega) > 0$) produce growing non-physical oscillations in $f_{1\sigma}$ for $\Delta t > 0$, which leads to a numerical overflow (*floating point exceptions*). In order to prevent this situation, similarly to the discussion of spatial derivatives in Sec. 3.1.2, we have to make use of more elaborated time integration schemes to guarantee numerically stable simulations. As with spatial discretization, time discretization schemes have different *truncation error* and different *stability* regions. The various time integration schemes can be roughly divided into two classes: explicit and implicit time discretization schemes.

Explicit time discretization

Explicit time integration schemes are given by

$$U^{t+1} = U^{t} + \mathcal{I}(t, U^{t}, U^{t-1}, \dots)\Delta t, \quad , \tag{3.11}$$

where U is the variable to integrate, t the time step, $\mathcal{I}$ is the time integration scheme which itself may use k time integration sub-steps. The right-hand side only depends on the current and previous time steps, thus makes it an *explicit* scheme. The methods implemented into gkc++ are the third-order and fourth-order Runge-Kutta methods described in the next section.

The Runge-Kutta scheme

For most simulations we advance the time using the fourth-order accurate *Runge-Kutta method* (RK4), which can be found in most text books about numerics. The RK-4 method is a multi-step scheme with four integration sub-steps given by

$$f_{1\sigma}^{t_{n+1}} = f_{1\sigma}^{t_n+\Delta t} = f_{1\sigma}^{t_n} + \tfrac{1}{6}\Delta t\,(k_1 + 2k_2 + 2k_3 + k_4) \quad , \tag{3.12a}$$

with the coefficients given by (subsequently the 1σ term is dropped for readability)

$$k_1 = f(t_n) \quad , \quad k_3 = f(t_n + \tfrac{1}{2}\Delta t, f_n + \tfrac{1}{2}\Delta t k_2) \quad , \tag{3.13a}$$

$$k_2 = f(t_n + \tfrac{1}{2}\Delta t, f_n + \tfrac{1}{2}\Delta t k_1) \quad , \quad k_4 = f(t_n + \Delta t, f_n + \Delta t k_3) \quad . \tag{3.13b}$$

Each of the four sub-steps requires the evaluation of Vlasov-Poisson system (and the storage of corresponding variables). Alternatively, we can also use the third-order Runge-Kutta method (RK-3), given by

$$f_{t_{n+1}} = f_{t_n+\Delta t} = f_{t_n} + \frac{1}{6}\Delta t\,(h_1 + 4h_2 + h_3) \tag{3.14}$$

with the coefficients given by

$$h_1 = f(t_n) \quad , \quad h_3 = f(t_n + \Delta t, f_n - \Delta t k_1 + 2k_2\Delta t) \quad ,$$

$$h_2 = f(t_n + \tfrac{1}{2}\Delta t, f_n + \tfrac{1}{2}\Delta t k_1) \quad . \tag{3.15a}$$

For the RK-3 method, only three evolutions and storage variables are required for the time integration.

Stability consideration of explicit time integration methods

The explicit time integration schemes presented (Euler forward method, the RK-4 and RK-3 methods) are restricted to certain stability considerations such as the maximum stable time step size Δt. A necessary condition for numerical stability is that all eigenvalues ω of the (linear) gyrokinetic system lie within the stable region of the time integration scheme. Following Karniadakis (2007), the stability of the RK-4 method can be investigated by examining the equation $\frac{dU}{dt} = \lambda U$. For each sub-step, e.g., $X_1 = \lambda U^n$, $X_2 = \lambda(U^n + \frac{1}{2}\lambda U^n \delta t), \ldots$ and thus for the total time step we get,

$$U^{n+1} = U^n + \tfrac{1}{6}\delta t\,[X_1 + X_2 + 2X_3 + X_4] \tag{3.16a}$$

$$= U^n \underbrace{\left[1 + \lambda\delta t + \tfrac{\lambda^2\Delta t^2}{2} + \tfrac{\lambda^3\Delta t^3}{6} + \tfrac{\lambda^4\Delta t^4}{24}\right]}_{G} \quad . \tag{3.16b}$$

The inner bracket is the growth factor G, which is required to be $G \leq 1$ to avoid the growth of numerical oscillations. Using $\mu = \lambda\Delta t$, we get $1 + \mu + \frac{\mu^2}{2} + \frac{\mu^3}{6} + \frac{\mu^4}{24} = e^{i\theta}$, with

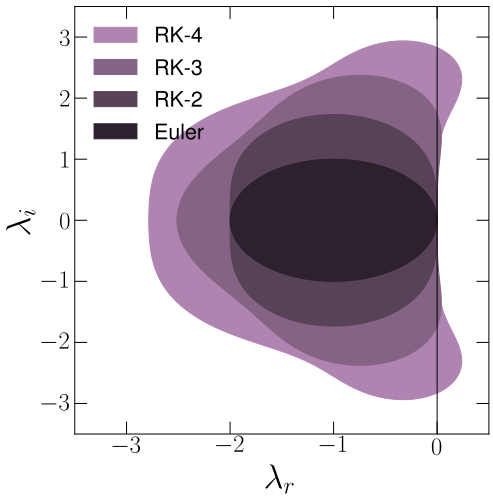

Figure 3.3: *Stability region of the Euler forward, RK-2, RK-3 and RK-4 time integration method. The solid line with* $\mathrm{Re}(\lambda) = 0$ *divides the systems into systems which are stable* ($\lambda_r < 0$) *and systems which exhibit instability growth* ($\lambda_r > 0$). *Higher order integration schemes have a larger stability region. In contrast to the Euler forward and RK-2 method, the stability region of the RK-3 and RK-4 method also extends into the positive real plane which makes them suitable for studying system which exhibits growth such as the ion temperature gradient instability.*

$\theta \in [0, 2\pi]$. The stability region $|\mu(\theta)| \leq 1$ can then be numerically determined and is shown in Fig. 3.3. The eigenvalues of the (linear) discretized gyrokinetic equation system can be computed by gkc++ when run as an eigenvalue solver, as described in Sec. 3.1.7. However, knowing only the largest absolute eigenvalue $\max(|\omega|)$ is usually sufficient for an approximation of the maximum stable time step size, which can be found using, e.g. the *power iteration*. In case of the gyrokinetic equation which investigate an *instability growth*, some eigenvalues with $\mathrm{Re}(\omega) > 0$, such that the *Euler forward* and the second order Runge-Kutta method (RK2) are *unconditionally unstable* and employing them will generate numerical oscillations leading to an error. The stability region of the RK-3 and RK-4 extends into the positive real plane and thus should be stable for reasonable chosen time steps.

Although the time integration error is larger compared to RK-4. Note that the stability region of the RK-3 method is smaller compared to the RK-4 method as shown in Fig. 3.3. Thus the maximum linear stable time-step for the RK-3 method is about 30% smaller than that for the RK-4 method, which makes up for its numerical cost. As shown later, this changes for nonlinear simulations where the maximum stable time-step is additionally restricted by the CFL condition.

Implicit time discretization

For an implicit discretization, not only the values of the current and previous values need to be known, but also value of the next time step U^{n+1} appears on the right-hand side of

$$\frac{U^{n+1} - U^{n-k}}{\Delta t} = F(t, U^{n+1}, U^n, U^{n-1}, \dots), \quad , \tag{3.17}$$

The advantage of implicit methods is that they are often unconditionally stable, however, we need to solve equations such as $U^{n+1} = F(U^n)$, which requires the inversion of the gyrokinetic operator. Using the matrix-free implicit integration procedure as provided by Balay et al. (2012), Eq.(3.17) can also be computed through an iteration procedure without explicitly setting up the matrix F. Unfortunately, although we can choose larger time-steps for implicit integration procedures, it is far from outweighing does not by far outweighing the time required for one individual time step.

3.1.4 | The Courant-Levy-Friedrich (CFL) condition

The Courant-Levy-Friedrich (CFL) conditions is a fundamental tool governing the stability of numerical solutions of differential equations using explicit time integration schemes. Namely the CFL condition restricts the maximum time step to ensure stability; for the one-dimensional advection equation, we denote

$$\mathrm{CFL} = \frac{L_v \Delta t}{\Delta v} \quad , \tag{3.18}$$

where L_v is the maximum velocity, Δv is the grid step, and Δt is the time step. In order to assure stability of the time integration scheme it is found empirically that $\mathrm{CFL} < 1/2$ has to be fulfilled (better estimation for the CFL which do also take the spatial discretization scheme into account exists, however, the difference is only minor). For the case of a linear gyrokinetic simulation, the maximum time step is restricted by the parallel motion along the field line given by

$$\Delta t_{\mathrm{lin}} = \frac{\Delta v}{L_v} \cdot \mathrm{CFL} \quad , \tag{3.19}$$

where L_v is the cut-off velocity and L_z is the length of the toroidal domain with N_z the number of discretization points. However, once nonlinear effects become important, the $E \times B$ drift velocity generally further restricts the time step:

$$\Delta t_{\mathrm{nl}} = \max\left(\frac{\Delta y}{\partial\chi/\partial x}, \frac{\Delta x}{\partial\chi/\partial y}\right) \cdot \mathrm{CFL} \quad . \tag{3.20}$$

The simulation time step has to be chosen such that always $\Delta t \leq \min\left(\Delta t_{nl}, \Delta t_{lin}\right)$.

Benchmark of time integration method

Here, we compare the time-integration of the third order Runge-Kutta (RK-3) with the fourth order Runge-Kutta (RK-4) method to get an idea of the calculation cost. The computational cost for a simulations with a setup $L_x = 64, L_y = 64$ and $N_x = 256, N_y = 128$ with $\theta = 1$, $\eta_i = 5$ is shown in Fig. 3.4a. In Fig. 3.4a the time step size Δt over the simulation time is shown. The RK-4 time step method does support a large time

step due to its larger stability region as shown in Fig. 3.3, however it does not outweighs the increased computational cost as shown in Fig. 3.4b, where the RK-3 method is more efficient. In the nonlinear region, the time step is restricted by the stricter CFL

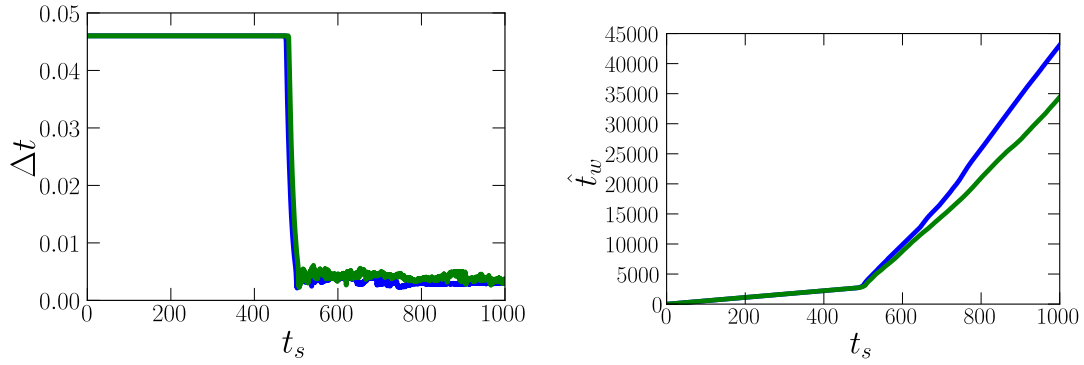

(a) *Time step size Δt vs t* **(b)** *Wall clock time t_W vs t*

Figure 3.4.: *Comparison between explicit RK-3 and RK-4. We find that RK-4 is the superior compared to RK-4 in the linear region. In the nonlinear where time step sizes are comparable, RK-3 performance 30% faster. The heat flux is comparable with fluctuations within a small margin, however diverges for longer time period, due to larger integration error of the RK-3 scheme. Variables are the time step size Δt, the simulation time t_s, and the wall clock time t_w.*

condition, thus the RK-3 method is faster, however, its higher time integration error is visible and this overall makes the RK-4 method more preferable. We note that we find a large jitter for linear simulations from the simulations time vs. wall clock time over time, which needs some further investigations.

3.1.5 | Solving the field equations

The gyrokinetic equation system is an integro-differential system consisting of the Vlasov equation and the fields equations. The solution of the field equations including the gyro-averaging is basically a three step procedure outlined in Fig. 3.5. For the numerical solution, the distribution function needs to be Fourier transformed in x domain using the FFT algorithm $f_{1\sigma}(x, k_y, \dots) \rightarrow f_{1\sigma}(k_x, k_y, \dots)$ so that the gyro-averaging can be performed using the Bessel function and the field equations solved. A back transformation of the gyro-averaged field quantities is finally required, i.e., $\langle \phi(k_x, k_y) \rangle_{\sigma\mu} \rightarrow \langle \phi(x, k_y) \rangle_{\sigma\mu}$.

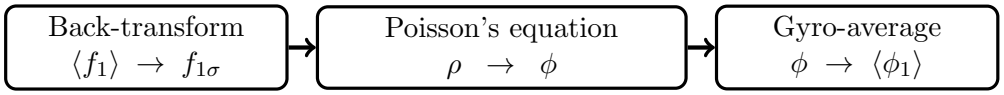

Figure 3.5.: *Solving the field equations is in general a three step procedure, here shown for ϕ.*

In order to calculate the gyro-averaged fields, we use the Bessel function of the first kind J_0. The Bessel function is a so-called *special function*, which is not provided by the *standard libraries* of the majority of programming languages such as *Fortran* or *C++*. The CPU of itself provides only efficient operators for multiplications, addition and subtraction, while divisions, square roots, exponential and trigonometric functions are usually implemented through iteration methods. More complicated functions, such as these special functions have to be implemented as an external library call. Computation of these *special functions* employs asymptotic expansions, recurrence relations and interpolation methods for calculations. An algorithm for the computation of Bessel functions J_0 and I_0 can be found in Zhang and Jin (1996). For gkc++ , we employ the freely available *SPECFUN* library as provided by Cody (1993). As the calculation of J_0 and I_0 is computationally expensive, it may be beneficial to pre-calculate their (constant) values at the initialization phase of the simulations instead of calculating them in every time step.

3.1.6 | The Vlasov equation

After calculating the gyro-averaged fields $\langle\phi\rangle_{\sigma\mu}$, $\langle A_{1\parallel}\rangle$, all terms on the right-hand side of the Vlasov equation Eq.(2.44) are known and can be solved:

$$\frac{\partial f_{1\sigma}\left(x, k_y, z, v_\parallel, \mu\right)}{\partial t} = \mathcal{L}_{\text{lin}} + \mathcal{N}_{\mathbf{E}\times\mathbf{B}} + \mathcal{C}_{\text{LB}} + \mathcal{K}_{\text{hyp}} + \mathcal{K}_{\text{Kr}} \quad . \tag{3.21}$$

The linear terms $\mathcal{L}_{\text{lin}}$ and $\mathcal{C}_{\text{LB}}$ are discretized using fourth-order central differences for the x, z and $v_\parallel$ directions. The latter two terms, $\mathcal{K}_{\text{hyp}}$ and $\mathcal{K}$ are only included for numerical reasons. The hyper-diffusion operator $\mathcal{K}_{\text{hyp}}$ is included to reduce (numerical) stencil errors, when calculating the derivative of the toroidal direction z to damp erroneous small scale fluctuations, as discussed by Pueschel et al. (2010). The Krook operator $\mathcal{K}(x)$ is used to damp eventual non-physical fluctuations in the vicinity of the radial boundaries and is given by $\mathcal{K}_{\text{Kr}} = -\kappa(x) f_{1\sigma}$, where $\kappa(x)$ is only non-zero close to the boundaries. The $\mathcal{N}_{\mathbf{E}\times\mathbf{B}}$ term is the nonlinear term, which requires special care to fulfill the mode-coupling relations, as will be discussed below.

Pseudo-spectral approach

Note that as discussed in Sec.(3.1.1), we evolve Fourier modes in the poloidal direction. Thus, when we consider the multiplication of two variables $A(x, k_y)$, $B(x, k_y)$, the multiplication rule is given by:

$$\sum_{k''=k+k'} \hat{C}(x, k_y'') e^{-ik_y'' y} = \left(\sum_k \hat{A}(x, k_y) e^{-ik_y y}\right)\left(\sum_{k'} \hat{B}(x, k_y) e^{-ik_y' y}\right) \quad . \tag{3.22}$$

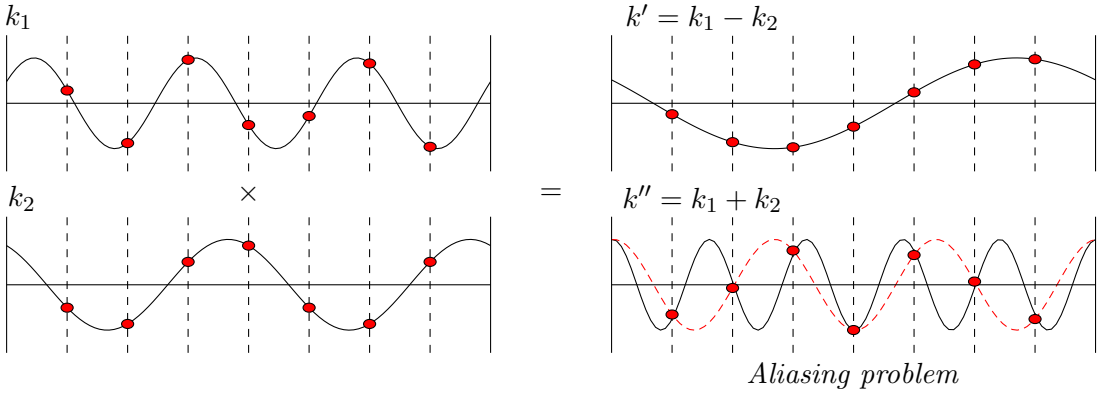

Figure 3.6.: *A quadratic nonlinearity coupled both modes an produces new modes given by* $k = k_1 \pm k_2$*. The largest frequency the grid can resolve is the below the Nyquist frequency given here by* $k_y max = N_y/2$*. If a nonlinearity produces wave above the Nyquist frequency the grid cannot resolves it anymore and it get mapped back, here,* $k'_y = 3 - 2 = 1$ *and* $k''_y = 3 + 2 = 5 \equiv 3$*. This aliasing problem causes numerical oscillations leading to non-physical results and thus has to be avoided.*

In order to calculate the above product, the right-hand size is expanded and a mode-matching condition $k'' = k' + k$ is used. Note that, although we only evolve positive modes ($k'' \geq 0$) as the variables $A(x, y)$ are real on the right-hand side (as $A(x, y)$ and $B(x, y)$ are real variables), negative modes, which are given by the complex conjugates of the positive modes, have to be also included in the mode coupling relations. As can be seen, calculating the sum requires an operation count of the order $\mathcal{O}(N^2)$. In contrast to that, the calculation the multiplication of $A(x, y)$ and $B(x, y)$ in real space only requires $\mathcal{O}(N)$. It is thus advantageous to transform the variables back to real space $A(x, k_y), B(x, k_y) \rightarrow A(x, y), B(x, y)$ using the Fast Fourier transformation, perform the multiplication in real space and back-transform. The computational cost will be then reduced to $\mathcal{O}(N \log(N))$.

However, in the above case we will find that modes appear with wavenumbers $k''_{max} = k_{max} + k'_{max}$, which cannot be resolved on the grid anymore. For a better understanding, we consider a discrete mesh of length L with N points. The highest wave number which can be produced is the *Nyquist* frequency of $k_{\max} = \pi(N/L)$. If two variables A and B consist of only one wave with k_A and k_B, the Poisson bracket produces a new wave-wave $k = k_A \pm k_B$ due to coupling. The mode $k_A + k_B \leq k_{\max}$ can be represented on the finite grid, but not $k_A + k_B > k_{\max}$. This case leads to a so-called *aliasing effect*. When directly calculating the mode-coupling relation in Eq.(3.22), we ignore modes with $k > k_{\max}$. However, in the case of the calculation in real space aliasing appears as shown in Fig. 3.6.

The usual *anti-aliasing* scheme is to zero-pad the size of $A(x, k_y)$ by a factor 3/2,

perform the multiplication in real space and after the back-transform we neglect the padded values. However, anti-aliasing can only be applied to the y direction while the x direction would still suffer from aliasing effects, producing non-physical numerical oscillations.

The Morinishi scheme

Due to the aliasing problem calculating the non-linear Poisson bracket $[\chi, g]$ is not trivial. Arakawa (1966) succeeded to design a numerical scheme which conserves the momentum and the kinetic energy (namely the $L1$ and the $L2$ norm). As shown by Morinishi et al. (1998) this successfully avoids the numerical problems arising from aliasing. Although mainly used in hydrodynamics, Idomura et al. (2007) successfully applied the *Morinishi scheme* in plasma turbulence simulations, and it is now used by e.g. Imadera (2011). The Morinishi scheme is based on following idea: the Poisson bracket equation has following identity,

$$[A,B] = \frac{\partial A}{\partial x}\frac{\partial B}{\partial y} - \frac{\partial A}{\partial y}\frac{\partial B}{\partial x} = \frac{\partial}{\partial y}\left(\frac{\partial A}{\partial x}B\right) - \frac{\partial}{\partial x}\left(\frac{\partial A}{\partial y}B\right) \quad , \tag{3.23a}$$

$$= \alpha\left(\frac{\partial A}{\partial x}\frac{\partial B}{\partial y} - \frac{\partial A}{\partial y}\frac{\partial B}{\partial x}\right) + (1-\alpha)\left(\frac{\partial}{\partial y}\left(\frac{\partial A}{\partial x}B\right) - \frac{\partial}{\partial x}\left(\frac{\partial A}{\partial y}B\right)\right) \quad . \tag{3.23b}$$

where α can be an arbitrary real value. Although analytically identical, Morinishi found that for $\alpha = \frac{1}{2}$, the numerical scheme conserves momentum and energy when central difference is used to discretized A and B. In the discretized equation system using CD-4 discretization for a variable A in the equidistant discretized dimension x and y, $A_{x;x,y}$ is given by

$$\left[\frac{\partial A}{\partial x}\right]_{x,y} = A_{x;x,y} = \frac{8\left(A_{x+1,y} - A_{x-1,y}\right) - \left(A_{x+2,y} - A_{x-2,y}\right)}{12\Delta x} \quad , \tag{3.24}$$

with the usual definition of an equidistant grid discretization, e.g. $\Delta x = L_x/N_x$. The Poisson bracket for $[A,B]$ is calculated by

$$\begin{aligned}\Xi_{yx} = 8\,&\left(\left(A_{y;x,y} + A_{y;x+1,y}\right)B_{y,x+1} - \left(A_{y;x,y} + A_{y;x-1,y}\right)B_{y,x-1}\right)\\ &- \left(\left(A_{y;x,y} + A_{y;x+2,y}\right)B_{y,x+2} - \left(A_{y;x,y} + A_{y;x-2,y}\right)B_{y,x-2}\right)\end{aligned} \tag{3.25}$$

$$\begin{aligned}\Xi_{xy} = 8\,&\left(\left(A_{y;x,y} + A_{y+1;x,y}\right)B_{y+1,x} - \left(A_{y;x,y} + A_{y-1;x,y}\right)B_{y-1,x}\right)\\ &- \left(\left(A_{y;x,y} + A_{y+2;x,y}\right)B_{y+2,x} - \left(A_{y;x,y} + A_{y-2;x,y}\right)B_{y-2,x}\right)\end{aligned} \tag{3.26}$$

This results

$$[A,B] = \frac{\Xi_{xy}}{24\Delta x} + \frac{\Xi_{yz}}{24\Delta y} \quad . \tag{3.27}$$

The nonlinearity is calculated in real coordinates, thus a Fourier transformation has to be applied. Thus allows again calculating the nonlinearity within $\mathcal{O}(N\log(N))$ time. A similar procedure can be applied to calculate the parallel nonlinearity $\mathcal{N}_{v_\parallel}$. We note that in contrast to simple derivation and multiplication, nonlinear simulations using the Morinishi scheme require the usage of an additional boundary cell (so-called *extended boundaries*).

3.1.7 | Eigenvalue solver

When the linear part of the right-hand side of the gyrokinetic equation system is written as a linear operator $\mathcal{L}_{\mathrm{gk}}$ and we assume a harmonic time dependence $f_{1\sigma} \propto \exp(-i\omega t)$ for the left-hand side, the equation system takes the form of an eigenvalue equation given by

$$-i\omega f_{1\sigma} = \mathcal{L}_{\mathrm{gk}} \cdot f_{1\sigma} \quad , \tag{3.28}$$

where ω is the corresponding eigenvalue. The time integration as an *initial value problem* allows us to find only the most unstable eigenmodes of the gyrokinetic operator. By solving the eigenvalue problem itself, we can find not only the most unstable eigenmode, but further sub-dominant eigenmodes as shown by Roman et al. (2010) and Merz et al. (2012). However, directly setting up the gyrokinetic matrix is not practical due to its size, thus Roman et al. (2010) proposed to extract the eigenvalues by applying a matrix-free iteration method employing the Krylov-Schur method as provided by Hernandez et al. (2003, 2005).

However, in case we are only interested in performing initial value simulations, e.g. for the nonlinear case, instead of solving the whole eigenstate, we can easiliy find the maximum absolute eigenvalue $|\omega|_{\max}$, from which we can estimate the maximum linear time step Δt by as shown by Fig. 3.3. $\omega_{\max}$ can be found using the *power iteration method*, however, we found that using the Krylov-Schur is more robust and shows a better convergence compared to the simpler power iteration method.

3.2 | Benchmarking

Although C++is a very powerful and feature rich language, it lacks proper methods to handle large multi-dimensional statical and/or dynamical allocated arrays in contrast to Fortran-90 and later Fortran standards. For efficient simulations, we employ the following strategy: we use external, well optimized libraries such as FFTW by Frigo and Johnson (2005), HDF-5 by The HDF Group (2000-2013), PETSc [Balay et al. (2012)], and elemental by [Poulson et al. (2013)]. Second, we use the *Cilk plus* extensions for C++which features so-called *array notation*. This extension allows multi-dimensional array handling in C++en par with Fortran-90 and allows improved vectorization support and thus a better exploitation of the CPU resources.

Here, we will study the numerical solution of three base cases, termed *Case (A)*, *Case (B)* and *Case (C)* in more detail. Thus here we present the general parallelization idea, for the following three scenarios shown in Tab.(3.2)

Case	A	B	C
Type	Electro-static (two-dimensional)	Electromagnetic ITG-ke (two-dimensional)	Electrostatic (Sheared Slab)
N_x	256	256	256
N_y	65	65	65
N_z	1	1	32
$N_{v_\parallel}$	48	48	48
N_μ	16	16	16
N_σ	1+(adiab)	2	1 + adiab
	$\beta_c = 1 \times 10^{-4}$	$\beta_c = 1 \times 10^{-4}$	$\beta_c = 1 \times 10^{-4}$

Table 3.2.: *Three base scenarios to be used in benchmarking gkc++ . Case(A) is important mainly for Ch.(5), while Case(B) is important for Ch.(6), where we include a static electromagnetic perturbation and include kinetic electrons. The Case(C) is relevant for benchmarking the code. The simulation domain is chosen in such a way to represent a well converged case.*

3.2.1 | Profiling

In order to understand where the majority of the computational time is spent, we perform a *functional profiling* for our three cases. *Profiling* can be enabled through compiler options. Thanks to this tool, after the numerical solution is completed, a log is generated showing the computational time spent in individual procedures. Knowing the *hot path* of the simulation code allows concentrating the effort on a better optimization of the computational most intensive routines. In Fig. 3.7, we show a sunburst diagram, where the inner layers call the outer layers. We see that for all cases the calculation of the Vlasov equation is the most demanding part (which is not surprising as it involves calculations in a five-dimensional array) . Inside the Vlasov function itself, the majority of the time is spent in the Fourier transformation (forward and backward) when calculating the Morinishi scheme. The other half is spent calculating the finite difference stencil of the Morinishi scheme. Calculating the fields is less than 20% of the computational time, of which again about half time time is used for solving the field quantities, while the other half is spent in the gyro-averaging procedure.

3.3 | Parallelization

The evolution of the gyrokinetic phase-space function is a demanding task due to its five-dimensionality and the usual high resolution requirement in order to resolve the

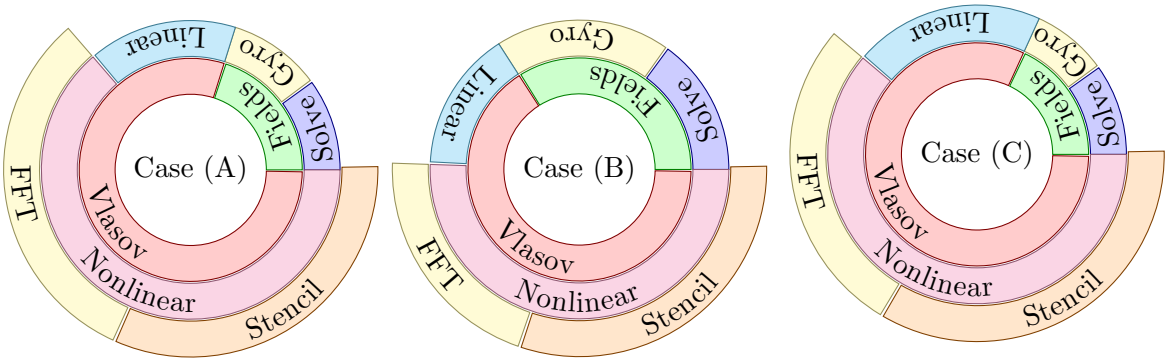

Figure 3.7.: *Results of profiling of the gkc++ code for the cases (A-C) are shown in a sunburst diagram. The angle of the circle segment corresponds to the fraction of the total computational time spent. Inner layers corresponds to low hierarchy, upper layer to higher hierarchy. All cases show that the majority of the time is spent within the Vlasov solver, where roughly two thirds of the total computational time is spent on calculating nonlinearity.*

physical phenomenon. This makes the use of parallelization crucial, where the problem to solve is divided into smaller chunks, each of them being solved on a different CPU. However, these CPUs have to be synchronized and boundary data has to be shared, which introduces an overhead limiting the scalability, as described by Amdahl (1967) and is now known as *Amdahl's law*.

3.3.1 | Overview over state-of-the-art computer architecture

In order to achieve a good scalability, a knowledge of the computer system is essential in order to exploit all the parallelism provided by the system. In Fig. 3.8, we show a schematic graph of a state of the art computer architecture referred to as cc-NUMA system(*cache-coherent non uniform memory access*). The computation itself is done within the CPU core. Each core has its own cache (Level 1 and Level 2 caches), where the computational data is temporarily mirrored from the main memory. The core can access data from the Level 1 cache usually within a very few instructions cycles. The ideal situations is where all the computational data fits inside the L1-cache, such that the CPU can quickly access the data and perform computation. However, usually the size of the L1-cache is relatively small, the data does not fit into the L1-cache, a heuristic is used to pre-fetch the data into the L1-cache before it is used. In case the heuristic was not able to provide the required data, a *cache-miss* occurs. The data has to be fetched either from the Level 2 cache (where the CPU is on a wait state for a couple of dozen cycles). In the worst situations, data has to be fetched from the main memory which takes around two orders of magnitude longer, during which the CPU has to wait.

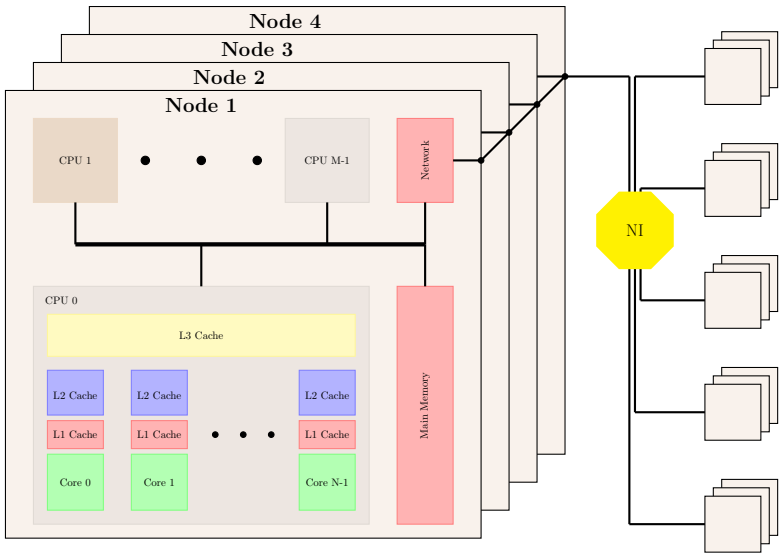

Figure 3.8.: *Outline of a state-of-the-art cc-NUMA system. Computational units are organized in a strong hierarchical fashion. Sharing date through lowest hierarchy, such as CPU cores, is much faster and with much lower latency, than sharing between higher hierarchies, such as computational nodes or racks. Simulation codes have to be optimized to take the hierarchical structure into account.*

Finally, for inter-node communication, data is exchanged between different nodes using the relatively slow network interconnect.

3.3.2 | Inter CPU parallelization (vectorization)

Modern CPU cores are able to process multiple data within one instruction, which is referred to as SIMD (*Single Instruction, Multiple Data*). These CPU can have usually four or more double precision SIMD lanes which allows to process data in parallel as shown in Fig. 3.9. Exploiting SIMD parallelism is crucial in order to achieve a high performance. In ideal cases, the compiler is able to exploit the SIMD lanes. Practically, hints about data alignment and data inter-dependence have to be provided to the compiler using *pragmas* to allow vectorization.

In Fig. 3.10, we show the achieved floating point performance versus the peak performance. The information was obtained by making use of so-called hardware counters, which measures the number of floating point operations performed, as provided e.g. by Browne et al. (2000). We find that for the Case (A) we have achieved over 40% of the peak performance of the CPU core. This value can be considered as good. By counting vectorized floating point operations vs. non-vectorized operations, we could confirm that most operations are indeed vectorized.

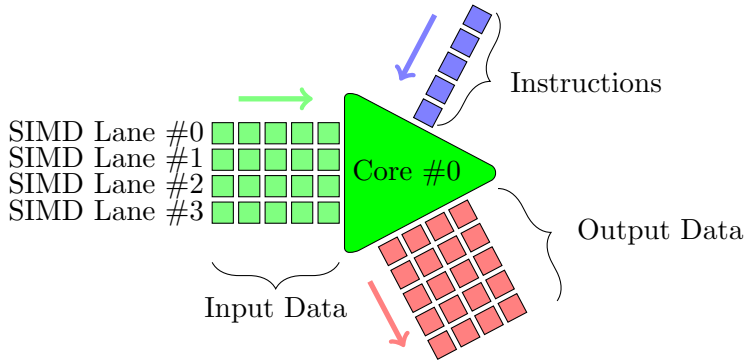

Figure 3.9: *Parallelization using SIMD. A CPU core can exploit SIMD parallelism when a single instruction is applied to multiple data streams at once and thus increasing the overall performance of the computation.*

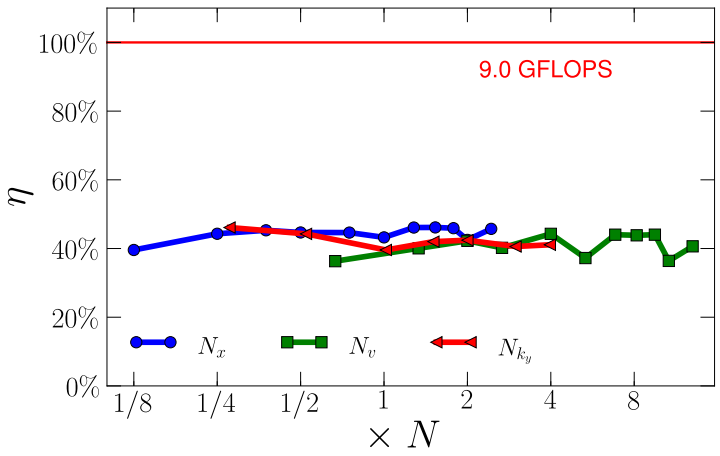

Figure 3.10: *Single threaded performance. The measured peak performance (showed as red line) was found to be GFLOPS*=9.0 *using an optimized benchmark tool (double precision). The average performance for multiple time steps is shown for difference values of decomposition. The performance is stable over a wide range of grid sizes. Good performance was obtained with* 40% *of the peak performance.*

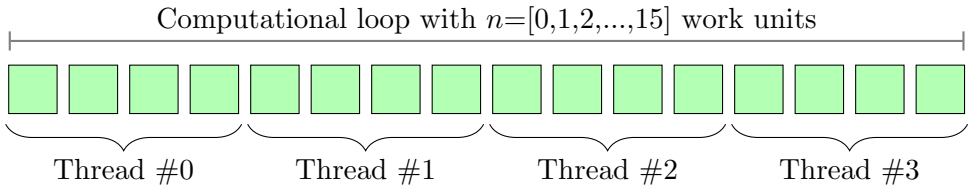

Figure 3.11.: *Visualization of loop parallelization with OpenMP. The workload, here shown as blocks, is divided evenly (assuming static scheduling) between four threads, each of them usually runs on a separate CPU core. In the best case scenario, only a quarter of the time is required to proceed the loop. However, usually, the CPU cores share common resources which can limit ideal scalability.*

3.3.3 | Inter-node parallelization (OpenMP)

The processing units inside the node share a common memory, which is referred to as shared memory systems. This shared memory can be used for synchronization of CPU units inside the node. Board (2008) is a compiler extension which simplifies the creation of individual programming threads which are synchronized at specific points. OpenMP provides constructs in order to share work within one program between various treads by compiler *pragmas*. The most common usage is loop parallelization, where work of the loop is divided between different threads such as shown in Fig. 3.11. OpenMP is implemented using threads, where every time the code enters an OpenMP section, threads are created, the section is processed in parallel, and after the loop finishes, threads are destroyed. This thread creation and destruction requires time and thus limits the parallelization rate if loops are too small. Also, threads usually share a common resource, such as main memory bus, where scalability may be limited to due limited bandwidth. In order to assure an efficient parallelization rate, we create the threads before the main loop is entered and synchronize them at few specific points. For the cases (A) we show the corresponding parallelization rate for a strong scaling using OpenMP in Fig. 3.12. We find that we achieve a good scaling of about 80% for up to 4 threads. For 8 threads the parallelization efficiency drops to 50%, where using more threads does not further improve the performance of the program anymore which may lie of not parallelized sections such as the Fourier solver, communication overhead, as well as memory bound of the computation.

3.3.4 | Intra-node parallelization (MPI)

Forum (1993) (Messaging Passing Interface) is an interface which provides a mechanism to exchange messages between different instances of the same program, where each instance can be distinguished by a unique rank id. This enables us to decompose each dimension of our multi-dimensional domain into smaller chunks as shown in Fig. 3.13.

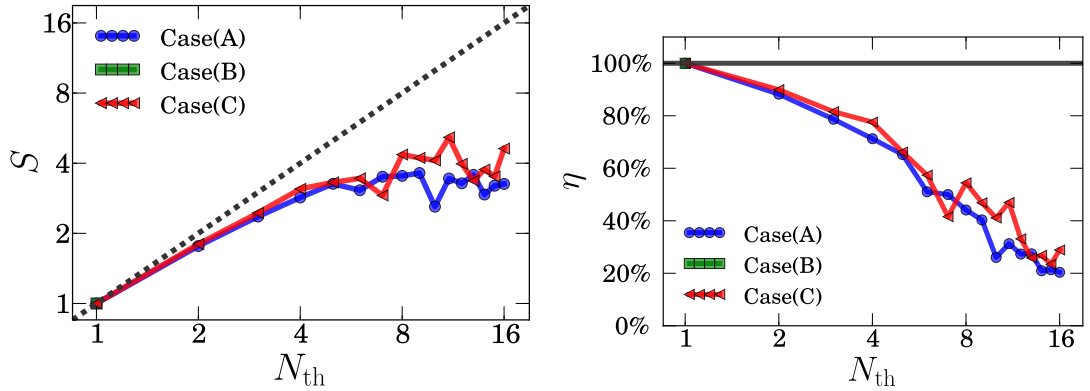

(a) *Speedup vs Thread number* **(b)** *Efficiency vs Thread number*

Figure 3.12.: *OpenMP scaling vs thread numbers for cases (A) and (C). Both cases show very similar scaling characteristics : A good scaling up to four threads ($\eta \sim 80\%$), increasing the thread count further, shows a strong saturation, where a maximum speedup of 4 is achieved, suggesting a bandwidth limitation for $N_{th} > 4$.*

In contrast to the serial version, we now have to additionally update the boundary points between the chunks themselves. Note that the finer we divide our domain into smaller chunks, the more the boundary becomes dominant. During the boundary communication, the CPU cannot continue the numerical communication (unless advanced methods such as overlaying communication-computation are employed). This introduces an overhead, which reduces the achievable parallelization efficiency. Note that we do not decompose over the poloidal direction as we evolve Fourier modes directly which would introduce a large communication overhead when performing the calculations of the nonlinear the Vlasov equation. Here, we show the scaling of the parallelization in dependence of the numbers of MPI instances. We have to distinguish between *strong scaling* (constant problem size) and *weak scaling* (increasing problem size) - here, we only discuss the strong scaling. The number of ghost cells depends on the stencil width. In our case, we have two ghost cells in the z direction, but have three ghost cells (*extended ghost cells*) for x-direction to avoid a second boundary exchange when calculating the nonlinearity.

Domain decomposition in x-direction

The strong scaling for the decomposition in the x dimension for our previously defined three problem cases A-C is shown in Fig. 3.14. We find a good scaling for all cases with around 70% efficiency for up to 16 MPI instances. This good scalability is rather surprising as the calculation of the field equations as well as gyro-averaging are performed in Fourier space, which requires $(x, k_y) \rightarrow (k_x, k_y) \rightarrow (x, k_y)$. During these Fourier transformations, the data has to be transposed, which is done using the communication

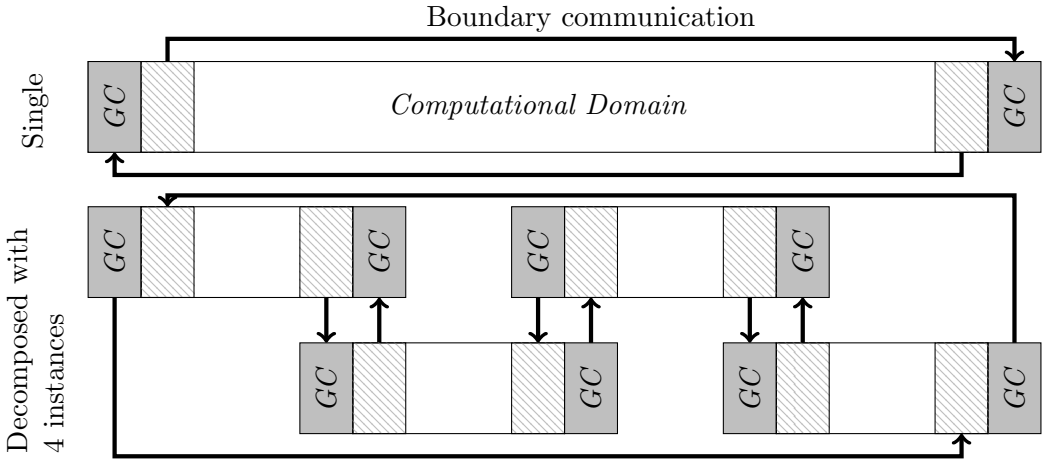

Figure 3.13.: *Sketch of the MPI decomposition using four instances for the dimension z. The decomposition splits the computational domain into smaller chunks in the expense that communication overhead increases through boundary exchange, e.g. ghost cells (GC), with increasing decompositions.*

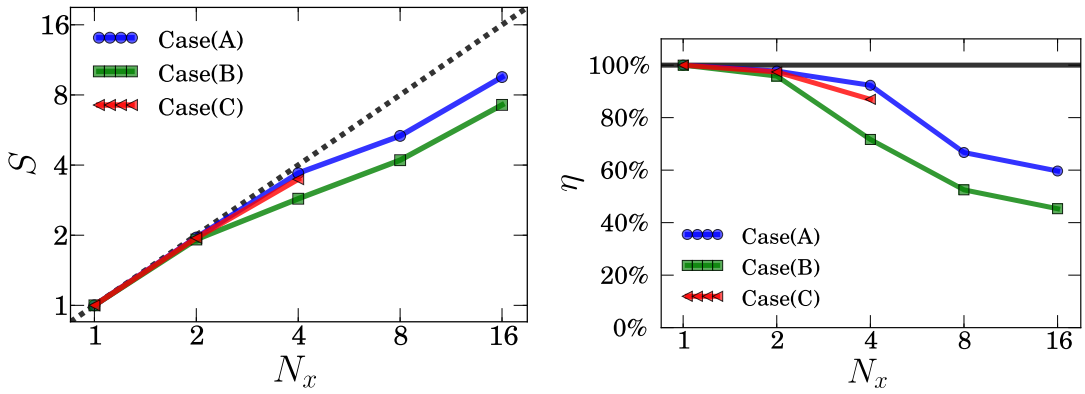

Figure 3.14.: *Parallelization with grid decomposition over the x-dimension. Left figure shows speedup over decomposition number. The right figure shows the corresponding parallelization efficiency. A satisfactory scalability of $\eta \sim 60\%$ is found for $N_x = 16$ for a Case(A). Case (C) exceeded the memory limit and thus we could not shows the scalability beyond 4 MPI instances.*

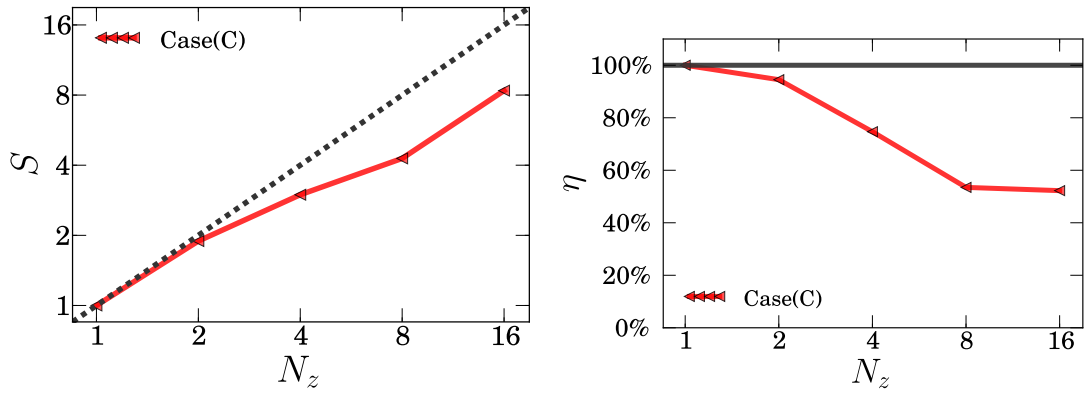

Figure 3.15.: *Parallelization with grid decomposition over z-dimension. Left figure shows speedup over decomposition, the figure on the right shows the corresponding efficiency. Only Case (C) included the z-dimension. Scaling is favorable as the gyro-averaging and field equations are not influences by this decomposition. Only boundary exchange for the Vlasov part is necessary Efficiency is* $\eta \sim 60\%$ *for 8 instances, from where we found saturation.*

intensive (slow) `MPI_Alltoall` transformation. Indeed scalability decreases when electromagnetic effects are taken into account, as an additional field has to be transposed which additionally increases the communication overhead.

Domain decomposition in z-direction

The scaling in z-direction is shown in Fig. 3.15. Here, only *Case C* is shown, as *A* and *B* are two-dimensional in the field quantities and thus cannot be decomposed in z-direction. Decomposition in z dimension is efficient as gyro-averaging as well as the field equations themselves are independent on the z direction in our field-aligned coordinates, as we neglected $\lambda_D k_\parallel \lll 1$ in the Poisson's equation, thus essentially only the boundaries for the finite difference stencil in the parallel direction have to be communicated for the boundary conditions.

Domain decomposition in $v_\parallel$-direction

In Fig. 3.16 the decomposition along the $v_\parallel$-dimension is shown. Parallelization is less efficient for a large CPU number. This comes comes not as a surprise as the field equations depend only on the moments of the phase-space function and thus the field equations cannot be efficiently parallelized for the field equations as well as gyro-averaging procedure. Thus a large path cannot be parallelized which results in a bad scalability. However, as shown above the major part of the computational time is spend within the Vlasov part, thus a satisfying parallelization is obtained for up to 4 CPUS.

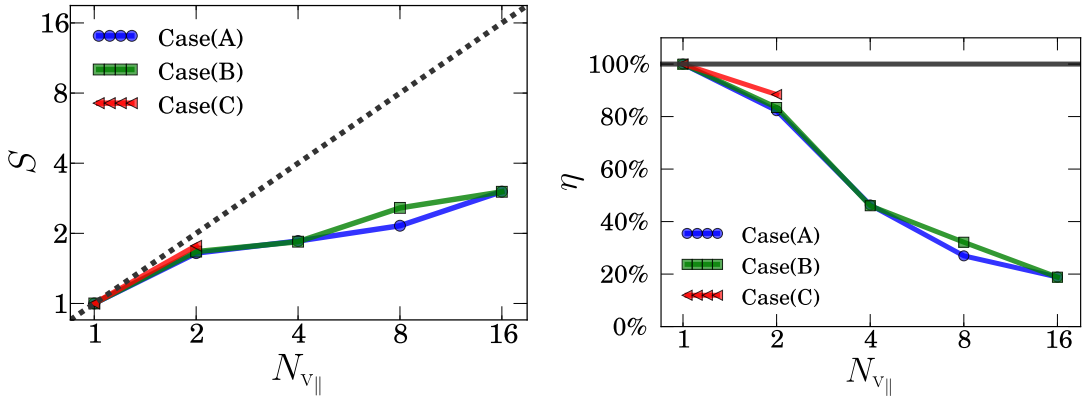

Figure 3.16.: *Parallelization with grid decomposition over $v_\parallel$-dimension. Left figure shows speedup over decomposition, the figure on the right shows the corresponding efficiency. Decomposition efficiency is bad, as the $v_\parallel$ decomposition is only effective for the Vlasov part, while gyro-averaging and field equation solution are essentially serialized. A good parallelization efficiency is achieved up to $N_{v_\parallel} = 2$, from where it drops of quickly. Case (C) exceeds memory limit as in the $x-$ decomposition.*

Domain decomposition in μ-direction

In Fig. 3.17 the decomposition over the adiabatic constant μ is shown. We have generally a favorable scaling, as no boundaries have to be exchanged (neo-classical are neglected). However, similar to the $v_\parallel$ decomposition, the field equations depend on the velocity moments, and thus parallelization of the field equation solver is limited for N_μ decomposition. However, this can be overcome by directly solving the field equations and gyro-transformation of the fields within the same solution step.

Domain decomposition in σ-direction

Finally, in Fig. 3.18 the decomposition over the species (σ) is shown. The scaling is very similar to Fig. 3.17. And indeed behaviour is similar as usually collisions between different species are neglected and thus no boundary exchange is required.

3.3.5 | Hybrid-parallelization

Finally to optimize scalability for a given problem, we do not only decompose in one dimension, but we decompose in various dimensions in order to find the best scalability. In Fig. 3.19, the hybrid-parallelization is shown (loop decomposition and domain decomposition) is shown. Here, we note that the strong scaling is dominated by communication overhead. With our hybrid simulations scenario it is possible to hide the communication overhead by using the master thread for communications and the slave

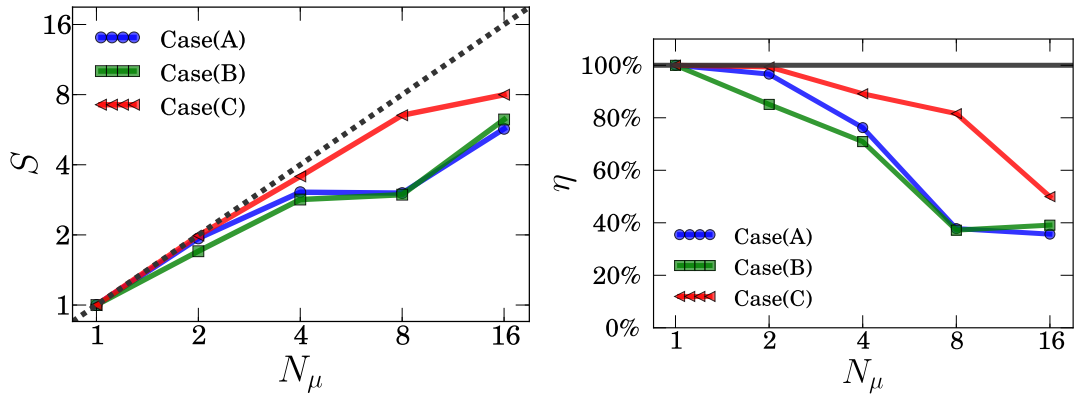

Figure 3.17.: *Parallelization with grid decomposition over μ-axis. Left figure shows speedup over decomposition, the figure on the right shows the corresponding efficiency. For the μ decomposition, The Vlasov part, as well as the gyro-averaging part are parallelized, only the field solution are serialized. Scalability is satisfactory up to a decomposition of $N_\mu = 4$ for Cases (A) and (B), while scaling is more favorable for Case (C), with good scalability up to $N_\mu = 8$.*

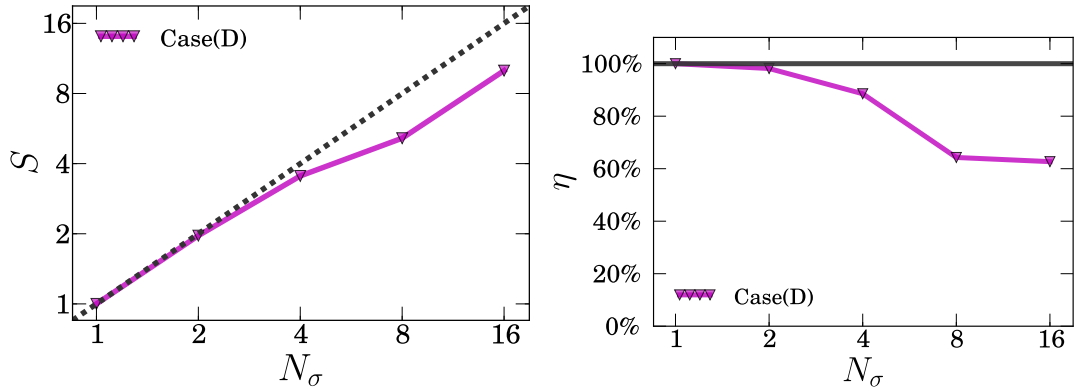

Figure 3.18.: *Parallelization with grid decomposition over σ-axis for Case(D) for N_σ. Left figure shows speedup over decomposition, the figure on the right shows the corresponding efficiency. For the μ decomposition. Scalability is very similar to the decomposition of N_μ, only the field equation part is serialized.*

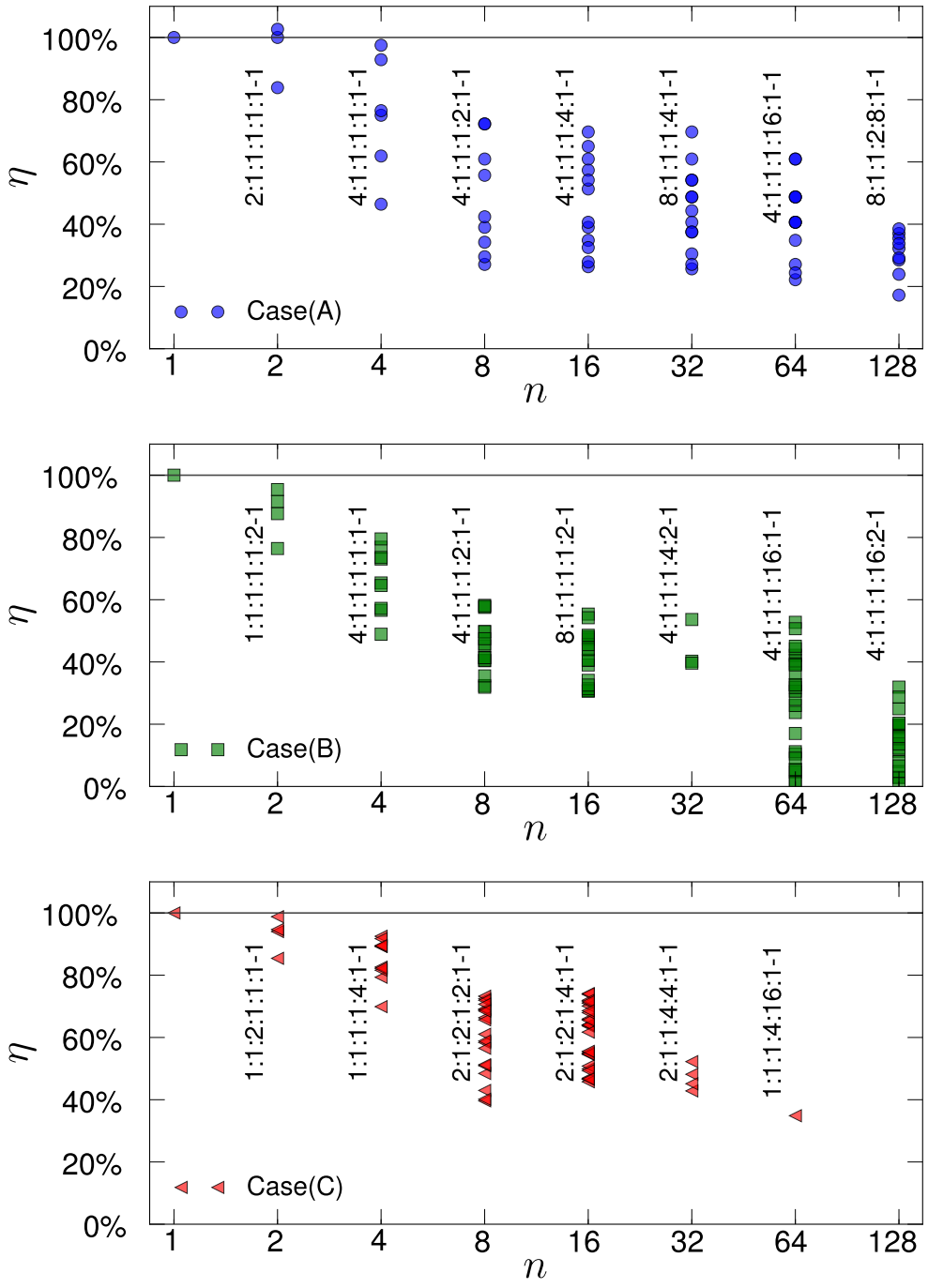

Figure 3.19.: *Strong scaling efficiency for hybrid parallelization for cases (A)-(C). Each Cases(A) to (C) are shown from top to bottom. The best decomposition for a specific number of cores is shown as a tuple of the form* $N_x : 1 : N_z : N_{v_\parallel} : N_\mu - N_{th}$. *We found that the scalability is very sensitive to the chosen decomposition. For medium range CPU numbers,* $n \sim 64$, x *and* μ *decomposition gives best scalability.*

thread can perform different calculations. Additionally, we note that strong scaling rule (same problem size) is usually replaced by weak scaling (increasingly larger problem size), which usually shows a much better scaling.

3.4 | Summary

The outline of the numerical solution procedure of the gyrokinetic equation system was given. This included among others: the discretization stencil, calculation of the linear and nonlinear terms and the time integration scheme. The importance of the CFL condition as a stability parameter was stressed out, as well as the dynamical adjustment of the time step to simulate with the maximum stable time step. The gyrokinetic code gkc++ , which was developed during this PhD, was introduced. For an investigation of multi-scale turbulences in gyrokinetics, the code was parallelized to be used on shared memory and distributed computer systems. Three use-cases are discussed, benchmarked and optimized to ensure the codes scalability over a wide range of parameters.

4 | Eigenvalue analysis of damping in the Vlasov–Poisson system

In this chapter, we will systematically investigate the characteristics of stable modes originating from kinetic damping in an unsheared slab geometry by comparing two approaches, i.e., a gyrokinetic Vlasov simulation as an initial value problem (IVP) and the corresponding numerical eigenvalue analysis in a discretized velocity space that is the same as in the IVP. Especially, we investigate if the stabilization effect through stable modes is properly evaluated beyond the recurrence time, which is unavoidable in kinetic simulations using the Vlasov approach as pioneered by Cheng and Knorr (1976), in a linearly mode-coupled system. In a gyrokinetic plasma, unstable modes such as the ion temperature gradient modes (ITG) coexists with stable Landau damped modes. In turbulent simulations, the steady-state spectrum after saturation is determined by the balance between the energy source and the sink which corresponds to unstable and stable modes. Also, stable modes can become nonlinearly excited and act as a means of dissipation as discussed by Hatch et al. (2012) and Terry et al. (2006). However, if these stable modes are correctly reproduced is still not yet answered yet. By the end of this chapter, will will confirm that the stabilization mechanism of linear mode coupling works indeed beyond recurrence time.

4.1 | Overview of Landau damping

Assuming a non-magnetized, collisionless plasma with ions and electrons, which is homogeneous in the x- and y direction, the time evolution of the distribution function $f_{i,e}$ of the ions (i) and electrons (e) can be described by the Vlasov–Poisson equation system,

$$\underbrace{\frac{\partial f_\sigma}{\partial t} + v_\parallel \frac{\partial f_\sigma}{\partial z} + \frac{q}{m}\frac{\partial \phi}{\partial z}\frac{\partial f_\sigma}{\partial v} = 0}_{\textit{Vlasov's equation}} \quad , \quad \underbrace{\nabla^2 \phi = 4\pi\rho = 4\pi \sum_{\sigma=i,e} q_\sigma \int f_\sigma \, \mathrm{d}v_\parallel}_{\textit{Poisson's equation}} \quad , \tag{4.1}$$

where ϕ is the electrostatic potential and the derivatives in x and y dropped out due to homogeneity. For further analysis, we assume a static, fixed ion and electron back-

ground f_0 with a small, time-dependent perturbed part f_1 and neglect the nonlinear contributions from $\partial_v f_1$. In the view point of the electrons, the ion mass is large, thus we further assume immobile ions ($m_i \to \infty$) such that the Vlasov equation does not have to be solved for the ions. Skipping the index for x and y, the perturbed distribution function is given by $f_e(z, v)$. Finally, we assume the parallel direction to be periodic, which allows us to use a Fourier expansion in the spatial dimension $f_1 \propto \exp(ik_\parallel z)$ and $\phi \propto \exp(ik_\parallel z)$, so that the reduced Vlasov–Poisson equation system is then given by

$$\frac{\partial f_1}{\partial t} = -vik_\parallel f_1 - \tfrac{q_e}{m_e} ik_\parallel \phi \partial_v f_0 \quad , \qquad {k_\parallel}^2 \phi = -4\pi q_e \int_{v_\parallel=-\infty}^{\infty} f_1 \, \mathrm{d}v_\parallel \quad . \tag{4.2}$$

We can choose now an initial f_1 and integrate above equation in time as an *initial value problem* (IVP). We explicitly note that the IVP does not posses any singularity and can be solved using numerical integration such as described by Cheng and Knorr (1976). However, prior to the time where computers became available, scientist relied on analytic solutions of which we would like to given an overview by revisiting the derivations for the Landau damping. For a more general overview on Landau damping the reader is referred to Ryutov (1999). In the following, we will skip the parallel sign in $\left(v_\parallel, k_\parallel\right) \to (v, k)$ to improve readability. Assuming a Fourier expansion in time $f_1 \propto \exp(-i\omega t)$, the Vlasov's equation (4.2) can be written as

$$-i\omega f_1 = -vikf_1 - \frac{q_e}{m_e} ik\phi\partial_v f_0 \quad \to \quad f_1 = -\frac{\frac{q_e}{m_e}\phi\partial_v f_0}{v - \omega/k} \quad , \tag{4.3}$$

which is then plugged into the Poisson's equation to give

$$1 + \frac{\omega_{pe}}{k^2} \int_{v=-\infty}^{\infty} \frac{\partial_v f_0}{v - \omega/k} \, \mathrm{d}v = 0 \quad , \tag{4.4}$$

where in the last step the Poisson's equation was used in the left-hand side to get the *dispersion relation* and defined the *electron plasma frequency* as $\omega_{pe} = 4\pi q_e^2/m_e$. Above equation has a singularity for the *resonant position* at $\omega/k_\parallel = \zeta$, where the integrand becomes infinite. To calculate this term, we may first assume $v \ll \zeta$, and expand the integral in powers of k, such that

$$\frac{1}{v - \zeta} = -\frac{1}{\zeta}\left(\frac{1}{1 - v/\zeta}\right) = -\frac{1}{\zeta}\left[1 + v/\zeta + \left(\frac{v}{\zeta}\right)^2 + \left(\frac{v}{\zeta}\right)^3 + \left(\frac{v}{\zeta}\right)^4 + \ldots\right] \quad . \tag{4.5}$$

Using above expansion in Eq.(4.4) up to second order and assuming f_0 to be a Maxwellian given by $f_0 = (1/\sqrt{\pi v_{te}^2}) \exp\left[-v^2/v_e^2\right]$, where v_e is the thermal velocity of the electrons defined by $v_{te} = \sqrt{2T/m}$, the even contributions drop out due to symmetry which results

in

$$\int_{v=-\infty}^{\infty} \frac{\partial_v f_0}{v-\zeta}\,\mathrm{d}v = \int_{v=-\infty}^{\infty} \partial_v f_0 \left(-\frac{1}{\zeta}\left[1+\left(\frac{v}{\zeta}\right)+\left(\frac{v}{\zeta}\right)^2+\left(\frac{v}{\zeta}\right)^3\right]\right)\mathrm{d}v \tag{4.6a}$$

$$= \frac{1}{\zeta}\int_{v=-\infty}^{\infty} f_0\left(\frac{1}{\zeta}+\frac{2v}{\zeta^2}+\frac{3v^2}{\zeta^3}\right)\mathrm{d}v \tag{4.6b}$$

$$= \frac{1}{\zeta^2}+\frac{3v_{te}^2}{\zeta^4} \tag{4.6c}$$

where in the second step we integrated by parts. With this approximation the dispersion relation in (4.4) is given by $\omega^2-\omega_{pe}^2-3\omega_{pe}^2k^2v_{te}^2/\omega^2=0$, which is known as the *Langmuir dispersion relation*, which frequency is pure real.

4.1.1 | Vlasov's approach

The equation system (4.2) was investigated by Vlasov (1938), who studied the effect of an electrostatic wave inside the plasma. Vlasov suggested, to use the *Cauchy principal value* defined by

$$\text{P.V.}\int_{v=-\infty}^{\infty}\frac{\partial_v f_0}{v-\zeta}\,\mathrm{d}v = \lim_{\epsilon\to 0^+}\left[\int_{-\infty}^{\zeta-\epsilon}\frac{\partial_v f_0}{v-\zeta}\,\mathrm{d}v+\int_{\zeta+\epsilon}^{\infty}\frac{\partial_v f_0}{v-\zeta}\,\mathrm{d}v\right] \quad , \tag{4.7a}$$

to calculate the singular integral. However, also in this case, we find that the dispersion relation predicts a frequency ω which is pure real.

4.1.2 | Landau's approach

Landau (1946) argued that using the principal value to calculate the singular integral is not justified. Instead, the *Laplace transform* should be used to regard Eq.(4.2) as an initial value problem with an initial perturbation of $f_1(t=0)$ at the initial time $t=0$, where the initial perturbation is assumed to be entire (e.g. can be expressed as a *convergent power series*). The Laplace transformed equation with $t\geq 0$ is given by

$$\mathcal{L}\left\{f_1(v,t)\right\} = \int_{t=0}^{\infty} f_1(v,t)e^{-st}\,\mathrm{d}t = \tilde{f}_1(v,s) \quad , \tag{4.8}$$

where s is the so-called *complex frequency variable*. The inverse Laplace transformation is given by

$$\mathcal{L}^{-1}\left\{\tilde{f}_1(v,s)\right\} = \frac{1}{2\pi}\int_{s=-\infty+i\sigma}^{\infty+i\sigma}\tilde{f}_1(s,t)e^{st}\,\mathrm{d}s = f_1(v,t) \quad , \tag{4.9}$$

where the integration is along the real plane and the real variable σ needs to be chosen such that $i\sigma$ is larger than the imaginary part of all singularities of $f_1(s,t)$ in the complex plane. Note that for $\sigma=0$ the Laplace inverse is identical to the inverse Fourier

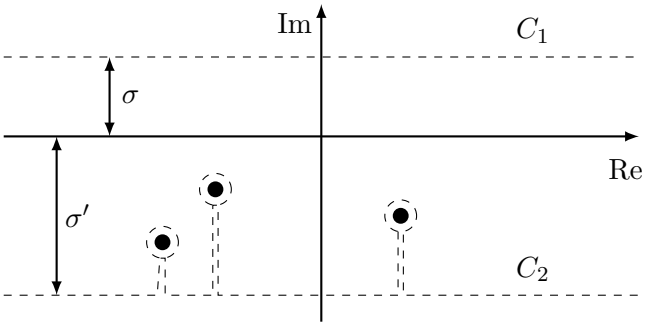

Figure 4.1: *Complex plane and contours applied. Contour of the inverse Laplace transform $\mathcal{L}^{-1}$ is shifted to σ' to ensure quick decay, however, C_2 needs to be changed to include poles from the new contour. Singularities are dots. [Adapted from Stix]*

transform. Loosely following Froese (2005), the Laplace transform of the derivative is given by

$$\mathcal{L}\left\{\frac{\partial f_1}{\partial t}\right\} = s f_1(v,s) - f_1(v,0) \quad , \tag{4.10}$$

with $f_1(v,0)$ is the initial part, such that the Laplace transform of Vlasov's equation (4.2) is given by

$$(s + ikv)\, f_1(v,s) + \tfrac{q_e}{m_e} ik\phi \partial_v f_0 = f_1(v,0) \quad . \tag{4.11}$$

After rearranging for $f_1(v,s)$ and inserting into Poisson's equation, we arrive at

$$k^2\phi = -\omega_{pe}\phi ik \int_{-\infty}^{\infty} \frac{\partial_v f_0}{s+ikv}\,\mathrm{d}v - 4\pi q_e \int_{-\infty}^{\infty} \frac{f_1(v,0)}{s+ikv}\,\mathrm{d}v \quad . \tag{4.12}$$

Simple rearrangements and using the definition of the electric field given by $E = -ik\phi$ yields

$$E(k,s) = \underbrace{\frac{\frac{4\pi q_e}{k} i \int_{v=-\infty}^{\infty} \frac{f_1(v,0)}{s+ikv}\,\mathrm{d}v}{1 - i\frac{\omega_{pe}}{k}\int_{v=-\infty}^{\infty} \frac{\partial_v f_0}{s+ikv}\,\mathrm{d}v}}_{D(k,s)} = \frac{A}{D(k,s)} \quad , \tag{4.13}$$

where $D(k,s)$ is the dispersion relation and the initial perturbation denoted by A arises only as a scalar. To get the time evolution, we need to perform the inverse Laplace transform. Although, we can choose σ large enough to ensure that all singularities are below $\mathrm{Im}(s_n) < \sigma$. Landau's approach was to shift the integration contour C_1 *below* them, and integrate over a modified contour C_2 as shown in Fig. 4.1. The integral along both contours will be equivalent as long as all singularities between C_1 and C_2 are taken into account. The advantage is that we can push C_2 arbitrarily small such that its horizontal contributions can be made negligible small in the long-time limit for large t as only the uppermost pole will be significant.

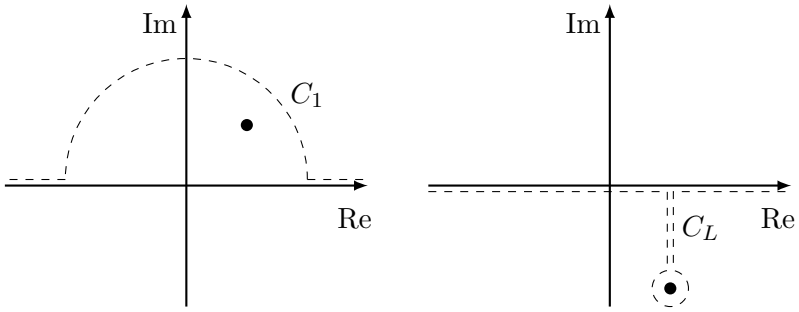

Figure 4.2: *Landau contour deformation C_L and analytic continuation. [Adapted from Stix]*

Here, again the singular integral appears, but instead of using the principal value integral, we integrate the integral over a complex contour to avoid the singularity. The integral involving the dispersion relation has singularities at $v = \zeta$. The integral is given by the

$$D\left(k,s\right) = k^2 + \omega_{pe} ik \oint_{C_1} \frac{\partial_v f_0}{s + ikv}\,\mathrm{d}v \tag{4.14a}$$

$$= k^2 + \omega_{pe} ik \left[2\pi i \sum \mathrm{Res}\left\{\frac{v f_0}{s + ikv}\right\}\right] \quad . \tag{4.14b}$$

For the inverse Laplace transformation all singularities needs to be taken into account. However, for the long time limit, i.e., $t \to \infty$, only the least damped will remain

$$\lim_{t\to\infty} = e^{s_1 t} \frac{iA}{D(k,s)} \quad . \tag{4.15}$$

To get the time evolution of ϕ, we thus need to know the position of the poles of $D(k,s)$, using Cauchy's residues theorem. However, we shifted our integration contour for the inverse Laplace transform, such that we need to deform our integration contour to a new Landau contour and use analytic continuation, as shown in Fig. 4.2.

$$D(k,s) = 1 - \frac{1}{k} \oint_C \frac{1}{s + ikv} \frac{-v}{\sqrt{2\pi}} \exp\left(-\frac{-v^2}{2v_t^2}\right) \tag{4.16}$$

having infinitely zeros ($\frac{s}{kv_t}$), we need to find using $s = -i\omega$.

We found that $E(k,t)$ will be determined from the uppermost pole of $E(k,s)$ and the poles from $E(k,s)$ are determined from the zeros in the denominator in Eq.(4.13). The Landau dispersion $D(k,s) = 0$ can then be obtain through integration along the contour C_L shown in Fig. 4.2, which gives

$$D(k,s) = 1 + \frac{\omega_p^2}{k} \oint_{C_L} \frac{\partial_v f_0}{v - \zeta}\,\mathrm{d}v \tag{4.17a}$$

$$= 1 - \frac{\omega_p^2}{k^2} \left[\mathrm{P.V.} \int_{-\infty}^{\infty} \frac{\partial_v f_0}{v - \zeta}\,\mathrm{d}v + i\pi \left.\frac{\partial f_0}{\partial v}\right|_{v=\zeta}\right] \quad . \tag{4.17b}$$

The imaginary term is given, assuming f_0 being a Maxwellian, by

$$i\pi \left.\frac{\partial f_0}{\partial v}\right|_{v=\zeta} = -i\frac{2\pi\omega}{k\sqrt{\pi v_{te}^2}} \exp\left[-\frac{\omega^2}{k^2 v_{te}^2}\right] \quad . \tag{4.18}$$

We can neglect the thermal correction in the multiplicative factor such that $\omega^2 \sim \omega_p^2$, however need to keep it in the exponential factor. The principal value is calculated by assuming *weak damping* and a large phase velocity, such that $v \ll \zeta$ as in Eq.(4.6a), to

$$D(k,s) = 1 + \frac{\omega_p^2}{k^2} - i\frac{2\pi\omega_p^3}{k^3\sqrt{\pi}v_{te}^3} \exp\left[-\frac{\omega^2}{k^2 v_{te}^2}\right] \quad . \tag{4.19}$$

In contrast to Vlasov's derivation, the dispersion relation obtained by Landau has a negative imaginary part and an electrostatic wave inside a collisionless plasma is damped.

4.1.3 | The plasma dispersion function

For the derivation using the Landau's approach, we had to make two assumption, namely assuming weak damping, to justify the contour integration, and the *fluid approximation* to expand the denominator of. Both assumptions can be dropped in case we make directly use of the *plasma dispersion function* Z, see Ap.(A.1), with $\zeta = \omega/v_{te}k$, the dispersion relation is given by

$$Z(\zeta) = \frac{1}{\sqrt{\pi}} \int_{u=\infty}^{\infty} \frac{e^{-u^2}}{u-\zeta}\,\mathrm{d}u \qquad \rightarrow \qquad 1 + k^2 + \zeta\,\mathrm{Z}(\zeta) = D(\omega,k) = 0 \quad . \tag{4.20}$$

The residual of of the dispersion relation over the complex plane is shown $|D(\omega,k)| = \mathrm{Res}$ in Fig. 4.3 for $k = 1$ and $v_{te} = 1$. Only where the residual vanishes, a solution of the dispersion relation is found. We find multiple solutions ω_n, where $D(\omega_n, k) = 0$, however, in most case only the least damped value is of interest as it dominates the solution in the long time (as the other modes are damped away mode quickly).

4.1.4 | Case and van Kampen's approach

Our derivation of the Landau damping problem is yet incomplete. Namely, although we know the time evolution of the electrostatic potential ϕ, we do not know the time evolution of the distribution function f_1 itself — as ϕ itself corresponds only to the zeroth moment of f_1. On the other hand, when the time evolution of f_1 is known, the evolution of ϕ can be easily determined from Poisson's equation. This point was stressed out by van Kampen (1955), who studied the eigenmodes of the Vlasov–Poisson equation system shown in (4.2).

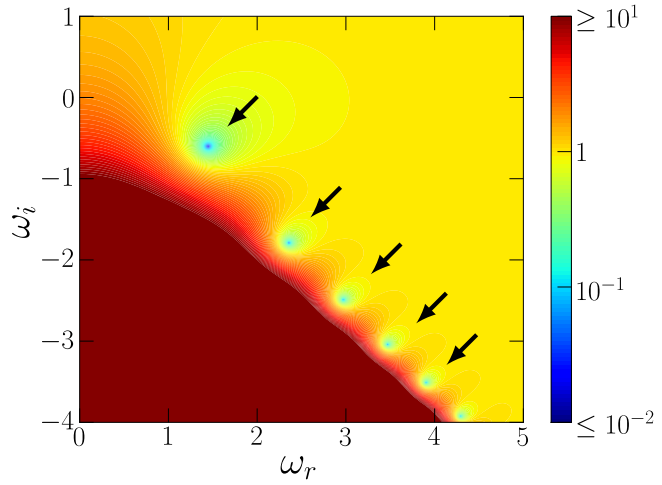

Figure 4.3: *Residual of $|D(\omega, k_\parallel)| = Res$ on the complex plane. $|D(\omega, k_\parallel)|$ has multiple zeros as indicated by the arrows, where the residual vanishes. For the linear Landau damping problem, only the solution with lowest decay rate will be dominant after the initial (or transient) phase. Note that the dispersion is symmetric along the real axis, as $Z(\omega) = Z(-\omega)$.*

Using following definitions: $f_1(x, v, t) = \hat{f}_1(v)e^{-i\omega t+ikx}$, $\eta(v) = \frac{\omega_e^2}{k^2}\frac{\partial f_0}{\partial v}$, and $\zeta = \omega/k$, and substituting the electrostatic potential in Vlasov's equation using Poisson's equations gives the following eigenvalue equation:

$$(v - \zeta)\,\hat{f}_{1,\zeta}(v) = \eta(v)\int_{-\infty}^{\infty} \hat{f}_{1,\zeta}(v')\,\mathrm{d}v' \quad . \tag{4.21}$$

As discussed by Nicholson (1983), the eigenfunctions of above eigenvalue equation are given by

$$\hat{f}_{1,\zeta}(v) = \text{P.V.}\left[\frac{\eta(v)}{v-\zeta}\right] + \delta\,(v-\zeta)\left[1 - \text{P.V.}\int_{v=\infty}^{\infty}\frac{\eta(v')}{v'-\zeta}\,\mathrm{d}v'\right] \quad , \tag{4.22}$$

where the δ is Dirac's δ function and the principal value (P.V.) is defined by

$$\text{P.V.}\left(\frac{1}{v-\zeta}\right) = \begin{cases} \frac{1}{v-\zeta} & v \neq a \\ \lim_{x\to a^{\pm}} \frac{1}{v-\zeta} & v = a \end{cases} \quad . \tag{4.23}$$

That the singular eigenfunction $\hat{f}_{1,\zeta}$ solves indeed Eq.(4.21) for any real ζ can be easily confirmed by plugging it back. Interestingly, the eigenvalue spectra is a continuum of marginally stable (ω has only real part) velocity space eigenmodes. These eigenmodes are termed *Case–van Kampen eigenmodes*. As ω' is pure real, no damping of the electrostatic potential is found if only one eigenmode is considered. So how a damping can be achieved? The whole concept of the singular eigenmodes is physically a bit counter-intuitive as a finite number of particles cannot reside within an infinitesimal small area (as assumed by the δ function). Also, a single eigenmode cannot be "physical", as stated by Nicholson (1983), as strictly speaking the δ functions violates the

small perturbation assumption used for linearization. Nevertheless, even with a singular eigenfunction, smooth functions can be reproduced once a *band* of CvK eigenmodes is taken into account such that f_1 is given by

$$f_1 e^{ikz} = e^{ikz} \int_{\omega=-\infty}^{\infty} c(\omega) \hat{f}_{1,\omega}\, e^{-i\omega t}\, \mathrm{d}\omega \quad , \tag{4.24}$$

where c is a perturbation coefficient. The distribution function f_1 is obtained from the integral over the continuum of eigenfunctions, namely Nicholson (1983) gives

$$\begin{aligned} f_1(x,v,t) = e^{ikx}\eta(v)\ \text{P.V.} \int \frac{c(\omega)e^{-i\omega t}}{v-\zeta}\,\mathrm{d}\omega \qquad & +e^{ikz} k\, e^{-ikvt} c(\omega = kv) \\ - k\, e^{ikz-ikvt}\, c(\omega = kv)\ \text{P.V.} \int_{-\infty}^{\infty} \frac{\eta(v')}{v'-v}\,\mathrm{d}v' \quad , & \end{aligned} \tag{4.25}$$

plugging f_1 into Poisson's equation yields

$$\phi(x,t) = \frac{4\pi e}{k^2} e^{ikz} \int_{v=-\infty}^{\infty} e^{-ikvt} c(\omega = kv)\,\mathrm{d}v \quad , \tag{4.26}$$

such that the time evolution of the potential is define by *band* of CvK eigenmodes which are *phase-mixing*.

The equivalence of Landau's approach and the approach of van Kampen was shown by Case (1959). Also, Case (1959) showed that the spectrum has additionally, not only a continuous part, but also a discrete part in case of a non-Maxwellian plasma. The discrete part is important once f_0 is non-Maxwellian, such as for the *bump-on tail instability*, see Denavit (1985) and Shoucri (1979) for a general overview, where Simon and Rosenbluth (1976) showed that an unstable eigenmode ($\mathrm{Im}(\omega') > 0$) and is complex conjugate arises from the discrete part of the spectrum. This point has been additionally verified by Bratanov (2011) in case of a magnetized plasma in present of temperature and density gradients. The eigenmodes of the Vlasov-Poisson systems are then given by

$$g(v,t) = \sum_i a_i e^{-kvt} f_i(v) + \int A(v) e^{ikvt} f_v(u)\,\mathrm{d}v \quad , \tag{4.27}$$

so that the time evolution of the electric potential is

$$\phi(t) = \frac{4}{k^2} \left\{ \sum_i a_i e^{ikvt} + \int A(v) e^{ikvt}\,\mathrm{d}v \right\} \quad , \tag{4.28}$$

where $A(v)$ is the continuous part and a_i is a possible discrete part.

4.2 | Derivation of the simplified gyrokinetic equation system

We now extend our study of Landau damping to the gyrokinetic system. Our simulation domain is a periodic two-dimensional slab configuration in a domain (x, y), where (x, y) is the radial and poloidal coordinate as described in Sec.(2.10.3). The constant magnetic field B_0 has a constant angle θ to the homogeneous z-direction, i.e., $\mathbf{B} = B_0\,(\hat{z} + \theta\hat{y})$, where $\theta \ll 1$. As before, we perform the δf split, where the ion distribution function f is split into an equilibrium part f_0 and the perturbed time dependent part f_1, i.e. $f = f_0 + f_1$ and electrons are adiabatically treated. Physical quantities are normalized as

$$\left(\frac{k_x}{\rho_{ti}}, \frac{k_y}{\rho_{ti}}, \frac{v_\parallel}{v_{ti}}, \frac{\mu B_0}{m_i v_{ti}^2}, \frac{t v_{ti}}{L_n}, \frac{\theta L_n}{\rho_{ti}}\right) \quad \rightarrow \quad \left(k_x, k_y, v_\parallel, \mu, t, \theta\right) \quad , \tag{4.29a}$$

$$\left(\frac{f_0 v_{ti}}{n_{0i}}, \frac{f_1 L_n v_{ti}}{\rho_{ti} n_{0i}}, \frac{\phi e L_n}{v_{ti}}\right) \quad \rightarrow \quad (f_0, f_1, \phi) \quad , \tag{4.29b}$$

where n_{0i} is the ion equilibrium density, $v_{ti} = \sqrt{T_i/m_i}$ the ion thermal velocity, $\rho_{ti} = v_{ti}/\Omega_i$ the ion thermal gyro-radius, T_i the ion temperature and $\Omega_i = eB_0/m_i c$ the gyro-frequency and (k_x, k_y) the wavenumber in (x, y) direction, respectively. The equilibrium part is given by $f_0 = 1/\sqrt{2\pi}\exp\left(-v_\parallel^2/2\right)\exp\left(-\mu\right)$ and the perturbed time dependent part f_1, so that $f = f_0 + f_1$. We expand all spatial dimensions in Fourier harmonics as for the guiding-center perturbed distribution function with frequency ω

$$f_1(\bar{x}, v_\parallel, \mu, t) \propto \sum_{k_\perp} f_{1,k_\perp} \times \exp\left(ik_x\bar{x} + k_y\bar{y} - \omega t\right) \quad , \tag{4.30}$$

and the potential $\phi(\bar{x})$ in guiding-center coordinates and the gyro-averaged potential $\langle\phi(\bar{x} + \bar{\rho})\rangle$ in gyro-center coordinates

$$\phi(\bar{x}, t) = \sum_{k_\perp} \phi_{k_\perp} \exp\left(ik_x\bar{x} + k_y\bar{y} - \omega t\right) \quad , \tag{4.31}$$

$$\langle\phi(\bar{x} + \bar{\rho}, t)\rangle = \sum_{k_\perp} J_0(k_\perp\bar{\rho})\phi_{k_\perp} \exp\left(ik_x\bar{x} + k_y\bar{y} - \omega t\right) \quad , \tag{4.32}$$

where $\bar{x}$ and $\bar{\rho}$ are the guiding-center coordinates and the Larmor radius, so that $\bar{x} + \bar{\rho}$ represents the particle coordinate. The z-dependence drops out due to the homogeneity, so that the parallel wavenumber reduces to $k_\parallel = \theta k_y$. The normalized linearized gyrokinetic equation system is given by

$$\begin{aligned}\frac{\partial f_{1,k_\perp}}{\partial t} = &-ik_y\left[1 + \frac{\eta_i}{2}\left(v_\parallel^2 + 2\mu - 3\right)\right] J_0(\lambda)\phi_{k_\perp} f_0 \\ &- i\theta k_y v_\parallel \left(f_{1,k_\perp} + J_0(\lambda)\phi_{k_\perp} f_0\right) + \mathcal{C}_{LB} \quad ,\end{aligned} \tag{4.33}$$

where $\eta_i \equiv L_T/L_n$ is a parameter defined by the temperature gradient scale length $L_T \equiv |\partial \ln T_i/\partial x|$ and the density gradient scale length $L_n \equiv |\partial \ln n_i/\partial x|$, and J_0 is the zeroth order Bessel function of the first kind and $\lambda = \sqrt{2\mu k_\perp^2}$. $\mathcal{C}_{LB}$ is the Lenard-Bernstein Lenard and Bernstein (1958) type collision operator defined as

$$\mathcal{C}_{LB} = \beta_c \frac{\partial}{\partial v_\parallel}\left(\frac{\partial f_{1,k_\perp}}{\partial v_\parallel} + v_\parallel f_{1,k_\perp}\right) \quad , \tag{4.34}$$

where β_c is the normalized collisional frequency. The Vlasov equation is coupled to the Poisson equation given by

$$\left[\left(1-\Gamma_0(k_\perp^2)\right)+1\right]\phi_{k_\perp} = \int_{-\infty}^{\infty} \mathrm{d}v_\parallel \int_0^{\infty} \mathrm{d}\mu\; J_0(\lambda) f_{1,k_\perp} \quad , \tag{4.35}$$

where $k_\perp^2 = k_x^2 + k_y^2$. Here, $\Gamma_0(k_\perp^2) = I_0(k_\perp^2)e^{-k_\perp^2}$, where I_0 is the modified Bessel function of the first kind.

For further simplification, we assume the distribution in the perpendicular velocity direction μ to be Maxwellian, so that the total distribution can be expressed as $f_{k_\perp} = \left[f_0(v_\parallel) + f_{1,k_\perp}(v_\parallel)\right] e^{-\mu}$. Then the integration over μ can be performed analytically in Eq.(4.33) and Eq.(4.35) using the identities,

$$\int_{\mu=0}^{\infty} J_0(\lambda)\, e^{-\mu}\, \mathrm{d}\mu = e^{-k_\perp^2/2} \quad , \tag{4.36a}$$

$$\int_{\mu=0}^{\infty} \mu\, J_0(\lambda)\, e^{-\mu}\, \mathrm{d}\mu = \left(1 - \frac{k_\perp^2}{2}\right) e^{-k_\perp^2/2} \quad . \tag{4.36b}$$

This leads to a modified gyro-averaging operator in the form of $\bar{\phi}_{k_\perp} = \exp\left(-k_\perp^2/2\right)\phi_{k_\perp}$. This reduced equation system has the advantage of removing the perpendicular dimension from the system, while finite Larmor radius (FLR) effects are still kept up to the first order as was used, e.g., by Watanabe and Sugama (2002). Finally, the reduced gyrokinetic equation system we will study is given by

$$\begin{aligned}\frac{\partial f_{1,k_\perp}}{\partial t} = &-ik_y\left[1 + \tfrac{1}{2}\eta_i\left(v_\parallel^2 - k_\perp^2 - 1\right)\right]\bar{\phi}_{k_\perp} f_0 \\ &- i\theta k_y v_\parallel\left(f_{1,k_\perp} + \bar{\phi}_{k_\perp} f_0\right) + \mathcal{C}_{LB} \quad ,\end{aligned} \tag{4.37}$$

and Poisson's equation for the electric potential takes the form

$$\left[\left(1-\Gamma_0(k_\perp^2)\right)+1\right]\phi_{k_\perp} = \int_{-\infty}^{\infty} \mathrm{d}v_\parallel\, f_{1,k_\perp} e^{-k_\perp^2/2} \quad . \tag{4.38}$$

In the following, $v_\parallel$, $\phi_{k_\perp}$ and $f_{1,k_\perp}$ are written as v, ϕ, f_1 for simplicity.

Using a Laplace transform with respect to time and integrating over velocity space in the collisionless limit, we obtain the dispersion relation given by

$$2 - \Gamma_0\left(k_\perp^2\right) + e^{-k_\perp^2}\left\{1 + \frac{\eta_i}{\sqrt{2}\theta}\zeta + \frac{1}{\sqrt{2}\theta}\left[1 - \frac{\eta_i}{2}\left(1 + k_\perp^2\right) + \eta_i\zeta^2 + \sqrt{2}\theta\zeta\right] Z(\zeta)\right\} = 0 \quad , \quad (4.39)$$

where $\zeta = \omega/\sqrt{2}\theta k_y$. The velocity integral is calculated using the Fried-Conte plasma dispersion function defined as $Z(\zeta) = i\sqrt{\pi}e^{-\zeta^2}\left(1 + \mathrm{erf}\left(i\zeta\right)\right)$. For more details, the reader is referred to the appendix (A.3). Fixing η_i, θ and k_x, we use Müllers root finding algorithm to get the complex frequency ω for each poloidal mode k_y. In general, the dispersion relation exhibits infinite number of modes.

4.3 | Damping in discretized Vlasov simulations

Here, we solve the gyrokinetic equation system, i.e. Eq.(4.37) and Eq.(4.38), as an initial value problem (IVP). A fourth order Runge-Kutta time integration scheme is used and f_1 is equidistantly discretized in velocity space with endpoints at $v_{\max} = \pm 7$ using typically $N_v = 128$ points. The collisional operator $\mathcal{C}_{LB}$ is included using a fourth order central difference stencil for the discretization of the first and second velocity space derivatives. For the two discretization points at the left and right boundaries of $f_1(v)$ we use two ghost cells set to zero. The fixed time step is set to $\Delta t = 0.05$ such that the CFL condition ($|v_{\max}\theta k_y \cdot \Delta t < 1/2$) is fulfilled for $k_y < 3$. The other physical parameters are $\eta_i = 6$, $\theta = 0.3$ and $k_x = 0$, where it is noticed that $k_x = 0$ provides the largest growth rate of all possible k_x. In the IVP, the initial perturbation in velocity space can be freely chosen, such that we first investigate how the linear mode behaves by the choice of the initial condition. We consider two cases for the initial condition : the first one is the random noise multiplied with the Maxwellian given by $f_1 \propto Rf_0$, where R represents uniform random numbers in the domain $[-1, 1]$, and the second initial perturbation is proportional to the Maxwellian $f_1 \propto f_0$.

The results in the collisionless case are given in Fig. 4.4a and 4.4c which illustrate the time evolution of six poloidal modes, for the different initial velocity distributions mentioned above. The growth rate spectrum for each initial condition and different poloidal modes is shown in Fig. 4.5, together with the theoretical calculations (solid line) as a reference. In the case of the random noise, i.e. Fig. 4.4a, the unstable modes, i.e. $k_y \leq 1.6$, show an exponential grow with growth rates consistent with the theoretical dispersion relation in Fig. 4.5. However, the poloidal modes with $k_y > 1.6$, which should have negative growth rates according to the analytical solution, show no growth nor damping, exhibiting a marginal behavior with small amplitude fluctuations. This feature is also shown in Fig. 4.5 using rectangular markers, which results from the analysis in the time interval $t = [25, 50]$. On the other hand, choosing the Maxwellian as the initial

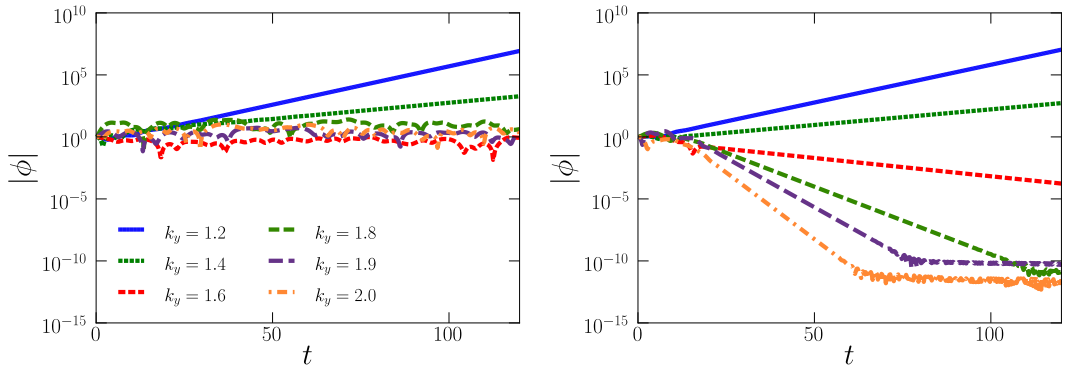

(a) *Random Noise,* $\beta_c = 0$ **(b)** *Random Noise,* $\beta_c = 2 \times 10^{-3}$

(c) *Maxwellian,* $\beta_c = 0$ **(d)** *Maxwellian,* $\beta_c = 2 \times 10^{-3}$

Figure 4.4.: *Time evolution of poloidal Fourier modes of the electrostatic potential* $|\phi|$ *of the IVP solution for different initial perturbation and collisionalities, i.e. (a)* $f_1 \propto Rf_0$, $\beta_c = 0$*; (b)* $f_1 \propto f_0$, $\beta_c = 0$*; (c)* $f_1 \propto Rf_0$, $\beta_c = 2 \times 10^{-3}$ *and (d)*$f_1 \propto f_0$, $\beta_c = 2 \times 10^{-3}$.

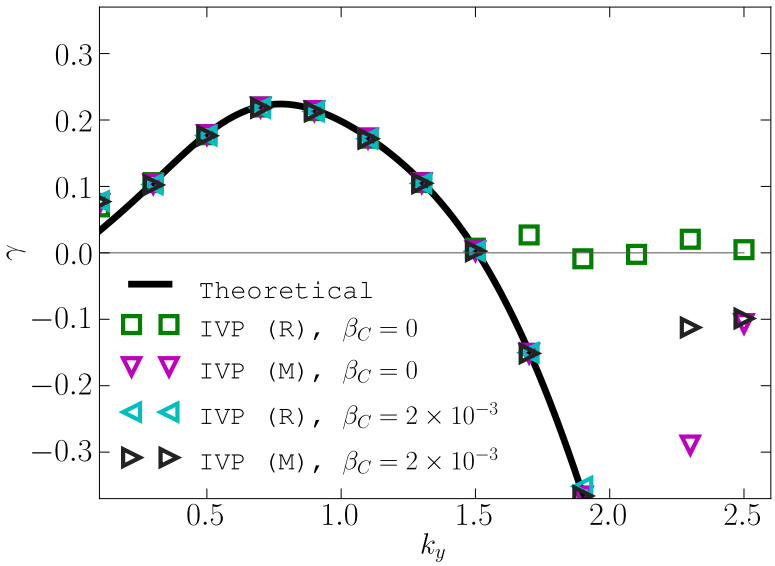

Figure 4.5: *Linear growth rates of the most unstable mode obtained from the analytic solution (line), from the IVP with Maxwellian (M) and the IVP with Random (R) initial perturbation and different collisional frequencies β_c.*

perturbation, the modes with $k_y > 1.6$ show damping at the beginning consistent with the analytical results as seen in Fig. 4.5. However, in later time, the mode reaches back to its initial value and the behavior is repeated, exhibiting a so-called *recurrence*, as seen in Fig. 4.4c. Note that the recurrence is known to be common for damped modes in the discretized numerical simulation of the Vlasov–Poisson system as discussed by Canosa et al. (1974), Knorr (1973) and Knorr and Shoucri (1974).

Now, we include a small collisionality given by $\beta_c = 2 \times 10^{-3}$ in Eq.(4.33). In the case of the random noise for the initial distribution which corresponds to Fig. 4.4b, unstable modes with $k_y \leq 1.6$ are almost same as in the collisionless case, suggesting that collisionality is weak enough so that it does not affect the linear growth rates. However, the higher modes with $k_y > 1.6$, which show marginal behavior in the absence of collisionality, i.e., Fig. 4.4a, turn to be damped with the rate consistent with the theoretical values as shown in Fig. 4.5. When these modes are damped to a certain level, they turn to be almost constant values in time, which we considered to result from numerical round-off errors. In the case of a Maxwellian initial perturbation, see Fig. 4.4d, the damping characteristics for $k_y > 1.6$ are almost the same as those in Fig. 4.4c, however the recurrence phenomena is found to disappear, showing same characteristics as Fig. 4.4b. It is noted that the inclusion of a small collisionality, i.e. $\beta_c = 2 \times 10^{-3}$ in this case, play a role in diminishing the recurrence. In the subsequent sections, we investigate the underlying physical mechanism leading to those prominent characteristics observed in Fig. 4.4, i.e. the role of the initial condition and also of collision for damped modes in gyrokinetic simulations.

4.4 | The discretized gyrokinetic operator

In order to understand the marginal characteristic of the damped modes in the collisionless case, as shown in Fig. 4.4a, we reformulate the gyrokinetic integro-differential equation system as an eigenvalue problem. As in the derivation of the analytic solution, a harmonic time dependence $f_1 \propto \exp(-i\omega t)$ is assumed. Then Eq.(4.37) and Eq.(4.38) can be written as

$$-i\omega f_1 = \mathcal{L}_{k_y}\, f_1 \quad , \tag{4.40}$$

where $\mathcal{L}_{k_y}$ is the linear gyrokinetic operator for the poloidal mode with wavenumber k_y given by Eq.(4.44). To obtain a numerical solution, the velocity space continuum is discretized using N_v number of points, where a cutoff velocity is chosen at $L_{\text{cut-off}} = \pm L_v$ and the velocity perturbation outside the range is assumed to be zero for f_0 and f_1. This is a valid approximation, as long as L_v is chosen enough large so that $\int_{L_v}^{\infty} f_0(v)\mathrm{d}v \lll 1$. Using equidistant points to discretize the velocity space, we get

$$\mathbf{v} = \ldots, 0, 0, \left(-L_v, -L_v + \frac{2L_v}{N_v}, -L_v + \frac{4L_v}{N_v}, \ldots, +L_v\right), 0, 0, \ldots \quad . \tag{4.41}$$

Note that the discretization of the velocity space into N_v points requires that the Maxwellian f_0 and the perturbed distribution function f_1 are also discretized with N_v points. The Vlasov equation in Eq.(4.37) is written as

$$\frac{\partial f_{1,k_\perp;n}}{\partial t} = -ik_y \left[1 + \tfrac{1}{2}\eta_i \left(v_n^2 - k_\perp^2 - 1\right)\right] \bar{\phi}_{k_\perp} f_{0;n} - i\theta k_y v_n \left(f_{1,k_\perp;n} + \bar{\phi}_{k_\perp} f_{0;n}\right) \quad , \tag{4.42}$$

where the gyro-averaged electric field $\bar{\phi}$ is calculated using Eq.(4.38)

$$\bar{\phi}_{\mathbf{k}_\perp} = \frac{\exp\left(-k_\perp^2\right)}{2 - \Gamma_0\left(k_\perp^2\right)} \sum_{m=0}^{N_v-1} f_{1,\mathbf{k}_\perp;m} \Delta v \quad . \tag{4.43}$$

Here, $\bar{\phi}$ is now calculated as a weighted sum over f_1 (in this case the rectangle rule) with $\Delta v = 2L_v/N_v$. The linear discretized gyrokinetic operator, e.g. the right-hand side of Eq.(4.42), for the Vlasov–Poisson integro-differential system Eq.(4.37) and Eq.(4.38) can then be obtained as a $N_v \times N_v$ matrix by using Eq.(4.43) in Eq.(4.42) to get

$$\mathcal{L}_{\mathbf{k}_\perp;nm} = -ik_y \left(\theta v_n \delta_{nm} + \left[1 + \tfrac{1}{2}\eta_i \left(v_n^2 - k_\perp^2 - 1\right) + \theta v_n\right] f_{0;n} \cdot \frac{e^{-k_\perp^2} \Delta v}{1 - \Gamma_0\left(k_\perp^2\right)}\right) \quad . \tag{4.44}$$

The Lenard-Bernstein collisional operator (4.34) is discretized using fourth-order finite difference stencils as given in Tab.(3.1).

With the now derived gyrokinetic operator, Eq.(4.42) can be formulated using a matrix-vector notation as,

$$\frac{\partial}{\partial t}\mathbf{f}_{1,\mathbf{k}_\perp} = \mathcal{L}_{\mathbf{k}_\perp}\mathbf{f}_{1,\mathbf{k}_\perp} \quad . \tag{4.45}$$

In order to solve the problem as an initial value problem, we can discretize the time derivative using e.g. the Euler forward method and evolve an initial perturbation $f_{1,t=0}$ in time, by performing vector-matrix multiplication according to (note that Δt has to be enough small to guarantee numerical stability),

$$f^{t+\Delta n}_{1,\mathbf{k}_\perp} = f^{t}_{1,\mathbf{k}_\perp} + \mathcal{L}_{\mathbf{k}_\perp} \cdot f^{t}_{1,\mathbf{k}_\perp} \ \Delta t \quad . \tag{4.46}$$

However, only the most unstable (the one with the highest growth rate) will be dominating the solution after an initial time. This can bee seen as subsequent multiplication of the $\mathcal{L}_{\mathbf{k}_\perp}$ with $f_{1,\mathbf{k}_\perp}$ will only let the most unstable eigenvector dominant.

Information about all modes can be extracted by calculating all eigenvalues of the linear operator, which have the form

$$-i\omega f_{1,k_\perp} = \mathcal{L}_{\mathbf{k}_\perp} f_{1,\mathbf{k}_\perp} \quad . \tag{4.47}$$

Numerically, the eigenvalue can be calculated once the matrix $\mathcal{L}_{\mathbf{k}_\perp}$ is given, by using an eigenvalue solver as provided LAPACK, i.e. Anderson et al. (1990). Additionally we confirm that by using a matrix-free eigenvalue solver, e.g. SLEPc, where the linear operator $\mathcal{L}_{\mathbf{k}_\perp}$ does not have to be calculated but only the matrix-vector product $\mathcal{L}_{\mathbf{k}_\perp} \cdot f_{1,k_\perp}$ in order to extract the eigenvalues and eigenvectors. Note that as in the solution of the IVP, the operator $\mathcal{L}_{k_y}(N_v \times N_v)$ is discretized. The linear operator $\mathcal{L}_{k_y}$ with the size $N_v \times N_v$ has N_v complex eigenvalues w_n and corresponding eigenfunction $\hat{f}_n$, where $n = \{0, 1, \ldots, N_v - 1\}$. This is in contrast to the analytic dispersion relation, which gives an infinite number of solutions (the Landau roots) ω for a given k_y mode and the solution as an IVP, which in the long time limit gives only one solution (the most unstable mode).

4.5 | Eigenvalue analysis of the gyrokinetic operator

The eigenvalue spectra with equivalent parameters as in Fig. 4.4 is shown in Fig. 4.6a for $k_y = 0.4$, and in Fig. 4.6b for $k_y = 2.2$, in the collisionless case ($\beta_c = 0$). For the unstable mode with $k_y = 0.4$, an eigenvalue corresponding to the Landau mode, which is verified by comparing it's complex frequency to Landau's solution obtained analytically from the dispersion relation, as shown by square markers, exist as expected. Additionally, a damped mode with the exact opposite growth rate but identical frequency appears. This mode is identified as the corresponding time reversed solution and numerically

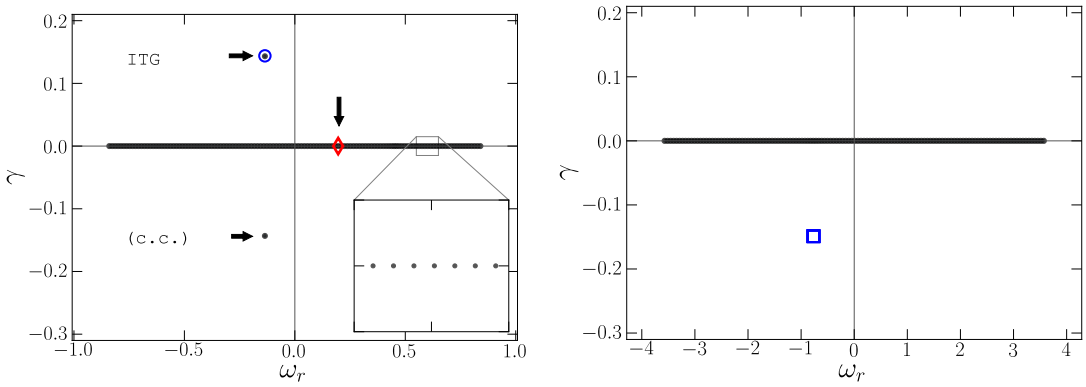

(a) *Eigenvalue spectra for* $k_y = 0.4$ **(b)** *Eigenvalue spectra for* $k_y = 2.0$

Figure 4.6.: *Eigenvalue spectra of gyrokinetic equation system for the case of (a)* $k_y = 0.4$ *and (b)* $k_y = 2.2$*. Landau's solution is shown using square marker. In case (a) the unstable ITG mode arises as complex conjugate pairs and the corresponding eigenfunction is shown in Fig. 4.7a. One of the CvK eigenfunctions (marked by a circle) is shown in Fig. 4.7b. In the case of (b), no damped ITG mode can be found and the spectra consist of only CvK eigenmodes.*

results from solving a pure real matrix, where all eigenvalues arise in conjugate pairs. Interestingly, besides the two eigenmodes related to the ITG mode, e.g. Fig. 4.7a, it can be seen in Fig. 4.6a that there exist many eigenmodes along the real axis with zero growth rate. The number of such mode is found to be $N_v - 2$ (N_v the number of mesh points in velocity space). The typical structure of an eigenfunctions is shown in Fig. 4.7b, which exhibits singular structure. These modes are considered to the discretized Case–van Kampen (CvK) eigenmodes as discussed in Sec. 4.1.4, with additional contributions due to the temperature gradient and gyro-averaging procedure.

On the other hand, for the stable setup with $k_y = 2.0$, only marginal stable eigenvalues are found, while no eigenvalue exists which corresponds to the analytical solution of Eq.(4.39), as shown by the squared marker in Fig. 4.6b. Interestingly, this is contradictory to the analytic solution of Eq.(4.39), but agrees well with the solution from the IVP, which shows a marginal behavior with zero growth rate for the stable modes with $k_y \geq 1.6$ as shown in Fig. 4.4a.

4.6 | Mechanism of collisionless Landau damping

The time evolution of the IVP generally depends on the initial condition as shown in Fig. 4.4a and 4.4c. For instance, if we chose a CvK eigenfunction as an initial condition in velocity space, which is numerically extracted using the eigenvalue solver, the perturbation is found to result in no growth and no damping for both stable and unstable

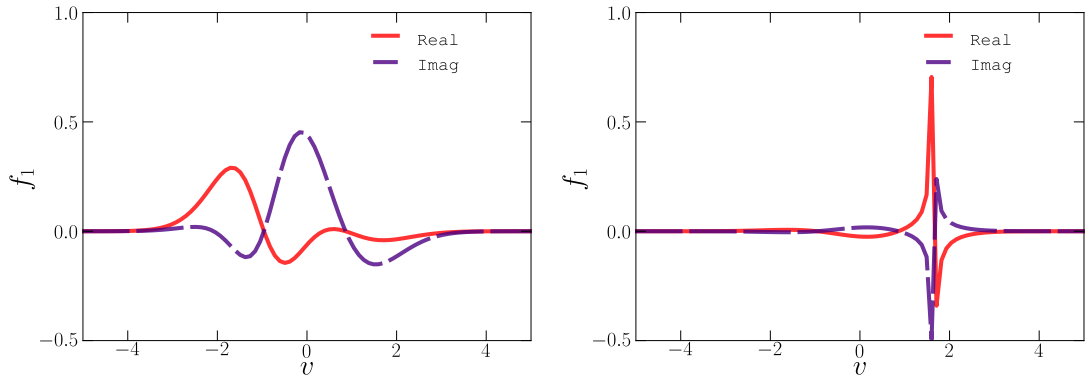

(a) *ITG eigenmode* **(b)** *CvK eigenmode*

Figure 4.7.: *Eigenfunction of the ITG mode (a) and random CvK eigenfunction (b) for* $k_y = 0.4$. *Each corresponding eigenvalue is shown by square and circle marker in Fig.3(a).*

poloidal modes. On the other hand, when a Maxwellian distribution is chosen as initial perturbation, a damped wave is found to be reproduced as shown in Fig. 4.4c, although all eigenmodes obtained from the eigenvalue solver are still marginally stable as found in Fig. 4.6b. To clarify the reason why a Maxwellian distribution leads to a damping, we decompose the Maxwellian initial perturbation in terms of the eigenmodes of $\mathcal{L}_{k_y}$ referred to as $\hat{f}_n$,

$$f_1(v, t = 0) \equiv f_0(v) = \sum_n c_n \hat{f}_n \quad . \tag{4.48}$$

Note that the eigenvectors $\hat{f}_n$ are not orthogonal to each other, so that a linear equation system has to be solved to get the corresponding coefficient c_n. Once these coefficients are determined, the eigenfunctions can be evolved similar to the IVP, but without the need of any time integration scheme using

$$f_1(v, t) = \sum_n c_n e^{-i\omega_n t} \hat{f}_n \quad , \tag{4.49}$$

where ω_n is the eigenvalue with its corresponding eigenfunction $\hat{f}_n$. At $t = 0$, the initial Maxwellian perturbation is obtained for f_1 per construction. In Fig. 4.8, we show the time evolution of the field amplitude for $k_y = 1.8$. For a random noise perturbation (dashed line), damping is not observed, which is consistent with Fig. 4.4a. On the other hand, for the Maxwellian perturbation (solid line), a damping is reproduced, while the electrostatic potential suffers from the recurrence, as is observed in the IVP in Fig. 4.4c. The time scale of the recurrence can be estimated by $T_{\mathrm{rec}} = 2\pi/\Delta\omega_i (= 2\pi/\theta k_y \Delta v)$. The damping rate we obtained during period of the recurrence time, is the same as that

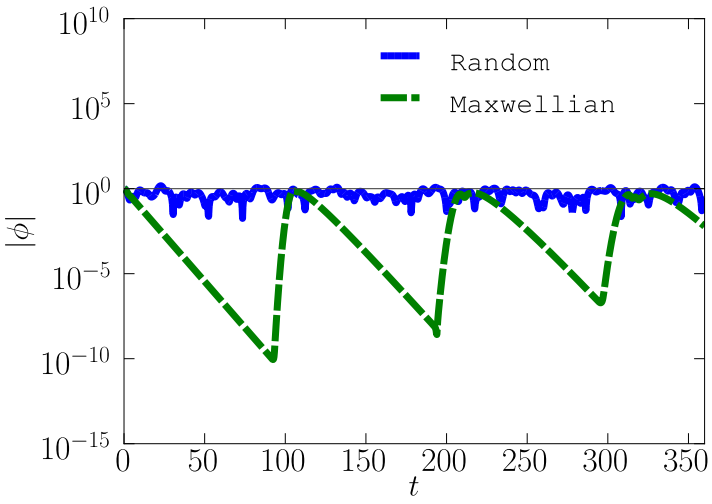

Figure 4.8: *Time evolution of the electrostatic potential $|\phi|$ with $k_y = 2$ for a random perturbation (solid line) and Maxwellian perturbation (dashed line) obtained by evolving the eigenvectors of $\mathcal{L}_{k_y}$.*

predicted by Landau's theory, i.e. the value marked by the rectangular in Fig. 4.6b. However, the eigenvalues are not exactly equidistant, thus after the recurrence time the original state as $t = 0$ is not obtained. Thus, we can confirm that the damping observed in Fig. 4.4c is not the result from a Landau eigenmode with an eigenvalue ω_L in the form $\phi \propto e^{i\omega_L t}$, but from the phase mixing of the CvK eigenfunctions in the discretized Vlasov–Poisson system.

4.7 | Matrix in Fourier–Hermite basis

The collisionless gyrokinetic Vlasov equation (4.37) in constant-θ geometry is slightly rearranged to

$$\frac{i}{\theta k_y}\left[\frac{\partial f_{1,k_\perp}}{\partial t}\right] = \alpha\bar{\phi}_{k_\perp} f_0 + \beta v_\parallel^2 \bar{\phi}_{k_\perp} f_0 + v_\parallel \left(f_{1,k_\perp} + \bar{\phi}_{k_\perp} f_0\right) \quad , \tag{4.50}$$

with the definitions $\alpha = \theta^{-1}\left[1 + \frac{1}{2}\eta_i\left(-k_\perp^2 - 1\right)\right]$ and $\beta = \theta^{-1}\frac{1}{2}\eta_i$, where we first assume $\mathcal{C}_{\mathrm{LB}} = 0$. For further analysis we transform into the Fourier–Hermite basis by expanding

$$f_1 \propto g(u) = \sum_{n=0}^{\infty} a_n h_n(u) \exp\left(-u^2\right) \quad , \tag{4.51}$$

where h_n are the (modified) Hermite polynomials as given by de Souza-Machado et al. (1999). Our definition of the Hermitian polynomials h_n differs slightly from the general "physicist" Hermite polynomials $\hat{H}$ by an additional scaling term

$$h_n = \hat{H}_n \frac{1}{\sqrt{\sqrt{\pi} 2^n n!}} \quad . \tag{4.52}$$

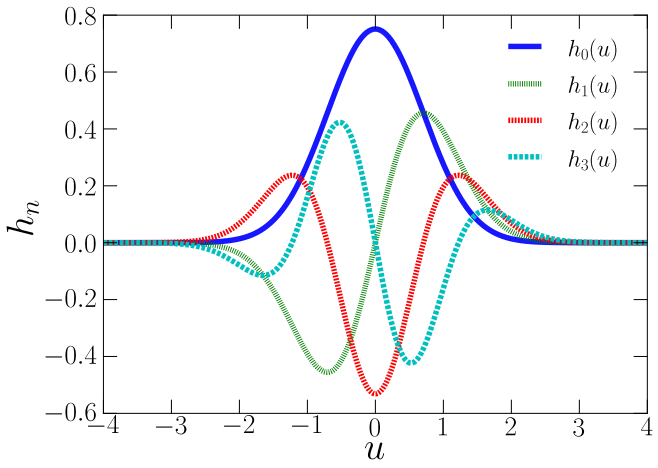

Figure 4.9: *Shown are the first four (modified) Hermite functions with exponential weight, i.e.* $g_n(u) = h_n(u)e^{-u^2}$.

The advantage of this modification is that the (modified) Hermite functions keep the orthogonality directly under the exponential weight $w(u) = \exp(-u^2)$,

$$\int_{u=-\infty}^{\infty} h_n(u)\, h_m(u)\, e^{-u^2}\, \mathrm{d}u = \delta_{nm} \quad , \tag{4.53}$$

in contrast to the classical definition which has non-favorable large scaling terms on the right-hand side. The first four terms are given by

$$h_0 = \frac{1}{\sqrt{\sqrt{\pi}}} \quad , \qquad h_1 = \frac{1}{\sqrt{\sqrt{\pi}}}\frac{1}{\sqrt{2}}u \quad , \tag{4.54a}$$

$$h_2 = \frac{1}{\sqrt{\sqrt{\pi}}}\frac{1}{\sqrt{8}}\left[4u^2 - 2\right] \quad , \qquad h_3 = \frac{1}{\sqrt{\sqrt{\pi}}}\frac{1}{\sqrt{48}}\left[8u^3 - 12x\right] \quad , \tag{4.54b}$$

and shown in Fig. 4.9. Further terms can be obtained by using the (modified) recursion relation,

$$h_{n+1} = u\sqrt{\frac{2}{n+1}}h_n - \sqrt{\frac{n}{n+1}}h_{n-1} \quad . \tag{4.55}$$

Inserting the Hermite expansion (4.51) into the right-hand side of Eq.(4.37), where we first assume $\mathcal{C}_{\mathrm{LB}} = 0$ gives and substitute $v_\parallel = \sqrt{2}u$, and noting that in this case $f_0 = \frac{1}{\sqrt{\pi}}h_0 e^{-u^2}$, gives for the Poisson equation with an adiabatic electron response

$$\phi = \sqrt{2}\frac{e^{-k_\perp^2}}{2 - \Gamma\left(k_\perp^2\right)}\int_{u=-\infty}^{\infty} g\,\mathrm{d}u = \underbrace{\sqrt{2}\frac{e^{-k_\perp^2}}{2 - \Gamma\left(k_\perp^2\right)}a_0}_{\bar{\phi}}\frac{1}{\sqrt{\sqrt{\pi}}} = \hat{\phi}\, h_0 \quad , \tag{4.56}$$

where we used the orthogonality relation. The Vlasov equation is then given by

$$\frac{i}{\theta k_y}\frac{\partial g}{\partial t} = \underbrace{\alpha\bar{\phi}h_0 e^{-u^2}}_{T_1} + \underbrace{2u^2\beta\bar{\phi}h_0 e^{-u^2}}_{T_2} + + \underbrace{\sqrt{2}u\bar{\phi}h_0 e^{-u^2}}_{T_3} + \underbrace{\sqrt{2}ug}_{T_4} \quad . \tag{4.57}$$

For a further simplification, we multiply by h_m and integrate over u. The first term T_1 gives

$$T_1 = \hat{\phi}\alpha \int_{u=-\infty}^{\infty} h_m h_0 e^{-u^2}\,\mathrm{d}u = \hat{\phi}\alpha\,\delta_{m,0} \quad , \tag{4.58}$$

where the other terms vanishes due to the orthogonality condition. The second term and third term are calculated by applying the recursion relation. Using the recursion relation on T_4, shows that in contrast to the other terms no closure can be achieved. Taking all terms together, and assuming a harmonic expansion for $g \propto \exp(-i\omega t)$, we get again the form of an eigenvalue equations,

$$\omega \begin{pmatrix} a_0 \\ a_1 \\ a_2 \\ a_3 \\ a_4 \\ a_5 \\ \vdots \end{pmatrix} = \frac{\theta k_y}{\sqrt{2}} \begin{pmatrix} \alpha\hat{\phi}+\beta\hat{\phi} & 1 & & & & \\ 1+\hat{\phi} & 0 & \sqrt{2} & & & \\ \beta\hat{\phi} & \sqrt{2} & 0 & \sqrt{3} & & \\ & & \sqrt{3} & 0 & \ddots & \\ & & & \sqrt{4} & \ddots & \\ & & & & \ddots & \end{pmatrix} \begin{pmatrix} a_0 \\ a_1 \\ a_2 \\ a_3 \\ a_4 \\ a_5 \\ \vdots \end{pmatrix} \quad , \tag{4.59}$$

where $\mathbf{a}$ is a vector whose n-th component is the Hermite functions of n-th order. Note that for a numerical simulations, we have to cut at a specific a_{N-1}, such that only a finite number of (modified) Hermite functions are included.

For the case with finite collisionalities, the velocity space derivatives in the Lenard-Bernstein operator are calculated from the recursion relation given by $\frac{\partial h_n}{\partial u} = \sqrt{2n}h_{n-1}$. Which after a lengthly calculation the Lenard-Bernstein operator in Hermite basis simply given by

$$\widetilde{\mathcal{C}}_{LB} = -\beta_c \begin{pmatrix} 0 & i & 2i & 3i & 4i & \dots \end{pmatrix}^T \quad . \tag{4.60}$$

4.7.1 | Landau damping in Fourier–Hermite basis

The gyrokinetic operator $\mathcal{H}_{k_y}$ in Fourier–Hermite basis has the advantage that the matrix shown in Eq.(4.59) has a tridiagonal structure (compared to the dense matrix $\mathcal{L}_{k_y}$ in Fourier basis), so that the dynamics can be described by the energy transfer among neighboring Hermite modes. In Fig. 4.10, the time evolution of the amplitude a_n for the

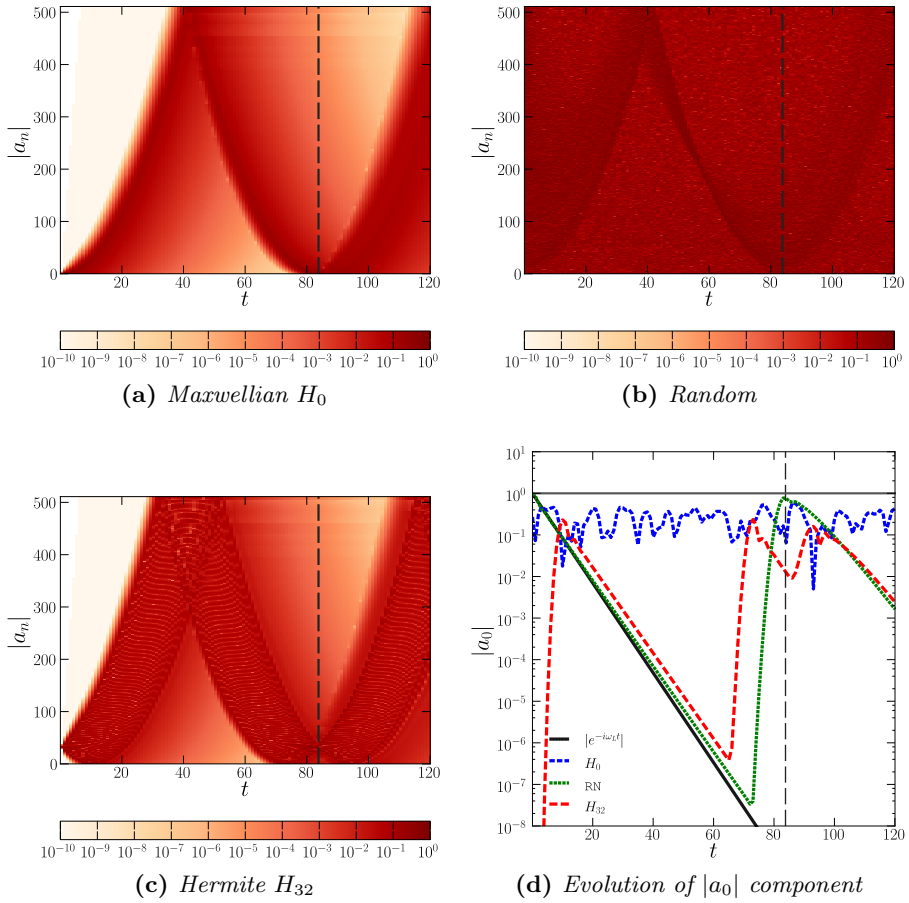

(a) *Maxwellian* H_0 **(b)** *Random*

(c) *Hermite* H_{32} **(d)** *Evolution of* $|a_0|$ *component*

Figure 4.10.: *Time evolution of the amplitude* a_n *for the Hermite basis component for (a) Maxwellian, (b) random noise and (c) 32th order Hermitian* (H_{32}) *initial perturbation. (d) shows the time evolution of* a_0 *for different initial perturbation corresponding to (a), (b) and (c). The time evolution estimated from Landau's theory is also shown as a reference. Time evolution of* a_0 *is shown together with the theoretical Landau damping rate.*

Hermite basis component is shown for an initial perturbation given by 4.10a Maxwellian, 4.10b random noise and 4.10c 32th order Hermite function for $k_y = 1.8$ and $\beta_c = 0$. In case of the Maxwellian initial perturbation, i.e. Fig. 4.10a, where only the a_0 component is finite at $t = 0$, the transport of the perturbation from low order Hermite modes, starting at $a_0 = 1$, to modes of higher order is observed. The time evolution of the corresponding electrostatic potential is shown in Fig. 4.10d

Thus the damping through the phase-mixing of the eigenmodes in velocity space is found to correspond to the increase of the mode number in velocity space described in the Fourier–Hermite basis and to the energy transfer into higher order moments of the phase space function. For the case of a random noise perturbation, i.e. Fig. 4.10b, all Hermite modes are simultaneously excited, so that the transport from low order modes to those of high order is mixed with that from higher order to lower order Hermite modes. As a result, the directionality of the energy transport as shown in Fig. 4.10b, which is the origin of collisionless damping is diminished. As shown in Fig. 4.10c, when the initial perturbation is only given by the a_{32} Hermitian component, the energy is found to evolve in both directions : to higher and lower mode number, which results from the tridiagonal structure of the matrix. It can be seen that the energy is cascaded from the a_{32} component to that of the a_0 component and evolves again towards the higher order a_n components as observed in Fig. 4.10a. In order to see the dynamics clearly, we investigated the time evolution of only the a_0 component, which corresponds to the electrostatic potential, for the three cases of initial perturbations as shown in Fig. 4.10d. The value estimated by Landau's theory is also shown. The damping due to phase mixing and recurrence phenomenon can be seen clearly.

4.8 | Role of the Lenard-Bernstein collision on the recurrence

To study the effect of collision on the recurrence, we investigate the long time behavior of the electrostatic potential in the case of $k_y = 1.8$ for different collisionalities β_c as shown in Fig. 4.11. In the collisionless case ($\beta_c = 0$), the recurrence phenomenon can be seen as in Fig. 4.4c, where the instantaneous damping rate before each recurrence is given by γ_{rec}. Note that γ_{rec} has roughly the same value as that of the Landau damping calculated from the dispersion relation, i.e. $\gamma_{\mathrm{rec}} \sim \gamma_{\mathrm{LD}}$. In the case of $\beta_c = 5 \times 10^{-4}$, a similar recurrence phenomenon is observed as shown in Fig. 4.11. However, the potential is found not to reach back completely to the initial value after the recurrence as in the case of $\beta_c = 0$, but to be damped by a certain level. This feature is repeated, so that the envelope, which connects the points where the potential reaches back to the maximum value in each recurrence event, shows a damping as illustrated by a thin line. We define the damping rate to be $\gamma_\star$. Note that the damping rate of the envelope is smaller than that which takes place during the recurrence, i.e. $\gamma_\star > \gamma_{\mathrm{rec}}$. The damping rate $\gamma_\star$ is found

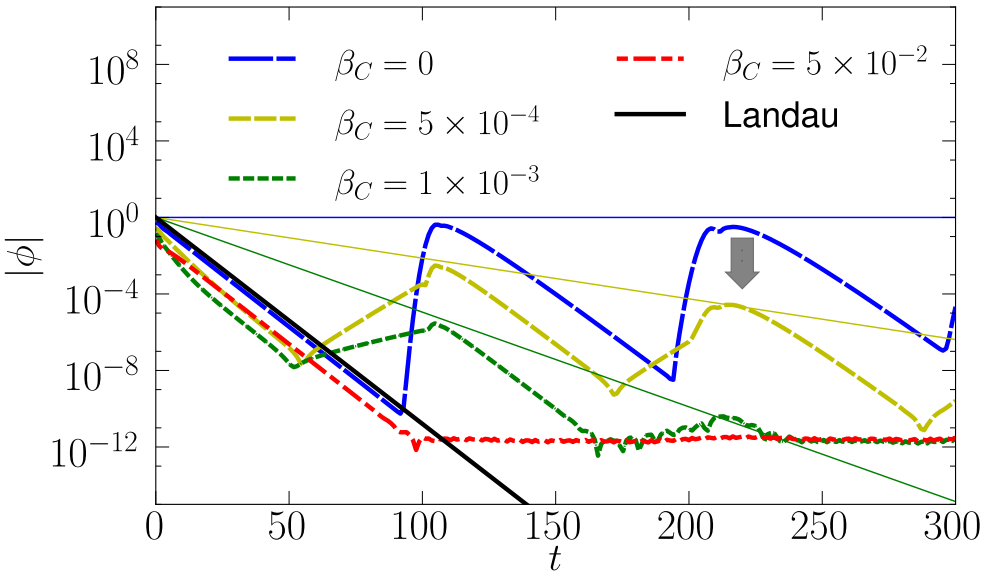

Figure 4.11.: *Evolution of electric potential for $\beta_c = 0, 2\times10^{-4}, 5\times10^{-3}$. For a small β_c, Landau damping occurs by phase mixing, however, the recurrence phenomenon is damped. For higher β_c, a real eigenmode appears. The damping due to other eigenmodes is shown as a reference (dotted blue = $\beta_c = 1 \times 10^{-3}$, dotted red : 5×10^{-2}).*

to increase as β_c increases until it becomes the same value as γ_{LD}, i.e. $\gamma_\star \sim \gamma_{LD}$, which takes place at $\beta_c = \beta_c^\star$. Here, in this case, $\beta_c^\star$ is given by $\beta_c^\star \sim 2.1 \times 10^{-3}$. Interestingly, even if β_c exceeds $\beta_c^\star$, the feature of the damping is not changed as seen in the case of $\beta_c = 5 \times 10^{-2}$. Namely, the damping rate is less influenced by the collisionality and fixed to almost same value as $\gamma_{\rm LD}$.

In order to understand this behavior of the IVP for the collisional case, here use again our eigenvalues analysis as in Sec.4.5, but now including the collisionality $\beta_c > 0$. The eigenvalue spectra for $k_y = 1.8$ for various collisionalities are shown in Fig. 4.12. The arrow corresponds to the growth rate of the majority of the CvK eigenmodes. In the collisionless case ($\beta_c = 0$), all eigenvalues are aligned on the imaginary axis corresponding to zero growth rates as shown in Fig. 4.6b. A low collisionality has a strong influence on the damping rate of CvK eigenmodes, which are now mostly damped as shown by the shift of the arrow in Fig. 4.12a with $\beta_c = 5 \times 10^{-4}$. The damping rate indicated by the arrow is similar to $\gamma_\star$ up to $\beta_c < \beta_c^\star$, which was discussed in Fig. 4.11. Interestingly, once the arrow exceeds the damping rate predicted by Landau's theory due to increased collisionality, one of the CvK eigenmodes changes its structure into that of a Landau damped mode, as can be seen that the eigenvalue of the CvK mode coincides with that of the Landau damped ITG mode as shown by square marker in Fig. 4.12b. Note that these features are consistent with those discussed in Fig. 4.11, where the damping rate is fixed

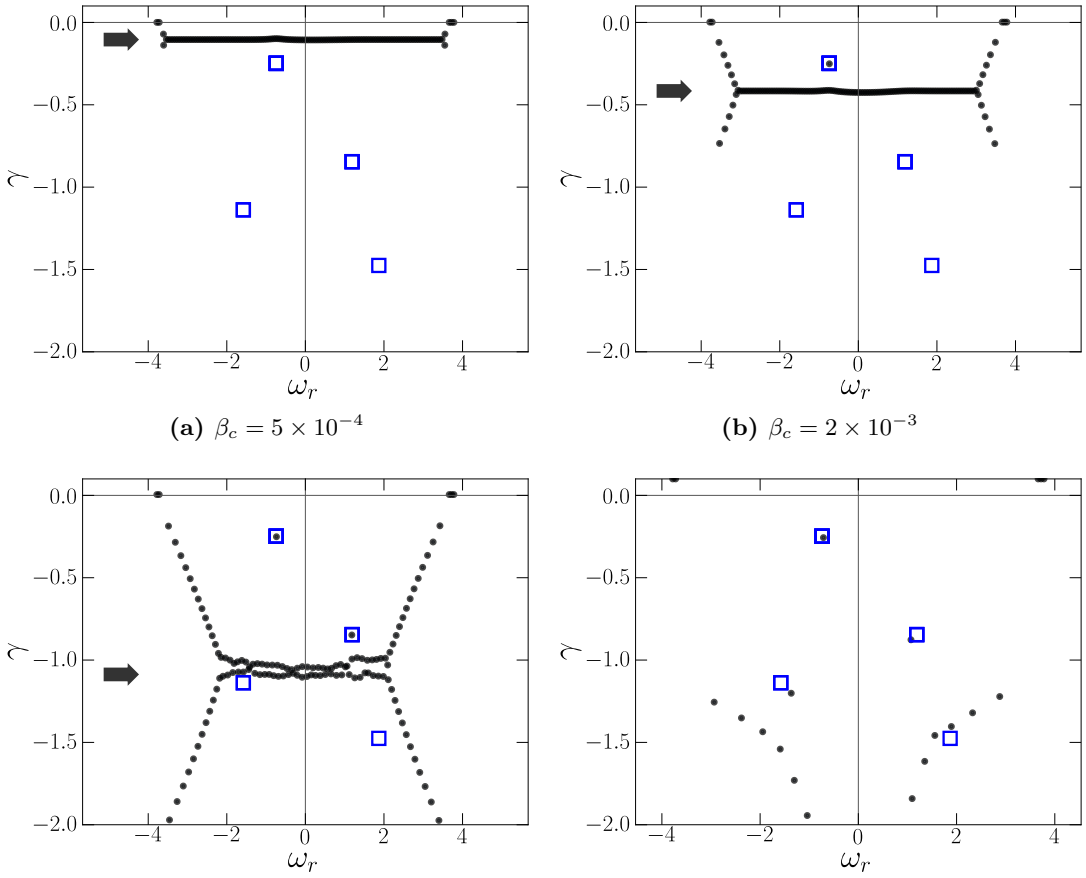

(a) $\beta_c = 5 \times 10^{-4}$ **(b)** $\beta_c = 2 \times 10^{-3}$

(c) $\beta_c = 5 \times 10^{-3}$ **(d)** $\beta_c = 1 \times 10^{-1}$

Figure 4.12.: *Eigenvalue spectra for $k_y = 1.8$ and various collisionalities. The arrow represents the majority of the collapsed CvK eigenmodes. Once β_c is chosen large enough, a true eigenmode of the ITG damped wave appears. An even larger collisionality is required to resolve the stronger damped Landau roots.*

to that of the Landau damped mode once $\beta_c > \beta_c^\star$. Finally, when the collisionality is chosen to be too large, exceeding $\beta_c^\star$, the Landau damping itself is affected by the collision and a collisional damping of the ITG wave becomes apparent as seen in Fig. 4.12d. Note that in this case the damping rate is reduced compared to that of the Landau damping. This is considered to originate from the ceased resonant interaction between particle and ITG wave due to the scattering by the collision, which weakens the damping effect.

In Fig. 4.13, we investigate the damping rate γ with respect to β_c for different resolutions in velocity space N_v for a damped mode with $k_y = 1.8$ based on the same eigenvalue analysis as in Fig. 4.12. The theoretical damping rate is calculated using the dispersion relation Eq.(4.39) neglecting the collisional effect. The dashed lines represent the damping rate of the majority of the CvK eigenmodes along the real frequency ω_r as indicated in Fig. 4.12 using an arrow. Here, we defined this damping rate by γ_{CvK}. In the case of a low velocity space resolution, i.e. $N_v = 32$ (green color), for low collisionality with $\beta_c \leq 10^{-3}$, the damping rate of the CvK mode is almost $\gamma \sim 0$ and depends weakly on β_c. However, as β_c increases, γ_{CvK} increases significantly exceeding the theoretical Landau damping rate. On the other hand, around the collisionality $\beta_c^\star$ that exceeds the Landau damping rate γ_{LD}, the Landau eigenmode emerges as discussed in Fig. 4.11 and Fig. 4.12, which is marked by dot(•) in Fig. 4.13. The Landau damped eigenvalue that corresponds to the Landau damping is less affected by the collisionality as also discussed in Fig. 4.11, so that the eigenvalue is almost constant for the further increase of β_c. For very large collisionalities, i.e. $\beta_c \geq 10^{-1}$, the Landau damping rate itself is changed due to the termination of the resonant interaction as γ deviates from γ_{LD}. As the velocity space resolution increases, the collisionality which is required to damp the CvK eigenmodes exceeding γ_{LD} is reduced, so that a smaller collisionality is enough to resolve the Landau damped eigenmode. Note that in the limit of a high velocity space resolution, e.g. $N_v \to \infty$, the critical β_c tends to zero, i.e. $\beta_c \to 0$. Although CvK eigenmodes above the arrow exist, their real frequencies are large and thus their perturbation in the IVP is negligible. Thus we conclude that for a high resolution in velocity space, a broad range of collisionalities is available in order to resolve the ITG damped mode as a true eigenmode.

The results observed in Fig. 4.13 provides a guideline in performing gyrokinetic simulations, so that the damping of the ITG mode can be properly reproduced. Namely, for a given velocity space resolution N_v, we can find a critical collisionality $\beta_c^\star$ above which the majority of the CvK eigenmodes are damped stronger than the theoretical Landau damping rate, and the damped ITG mode can be reproduced (note that this discussion here refers only to the least damped Landau mode). It is also interesting to note that the effect of smaller collision $\beta_c < \beta_c^\star$ is numerically of less importance because the observed damping is not the true damping of a ITG eigenmode, but from that of the CvK eigenmodes. However, the effect of collision larger with $\beta > \beta_c^\star$ is physical, since it represents the damping effect from the true Landau damped eigenmode. It is also noted that $\beta_c^\star$ depends on k_y, so that when k_y becomes larger, the corresponding $\beta_c^\star$ increases.

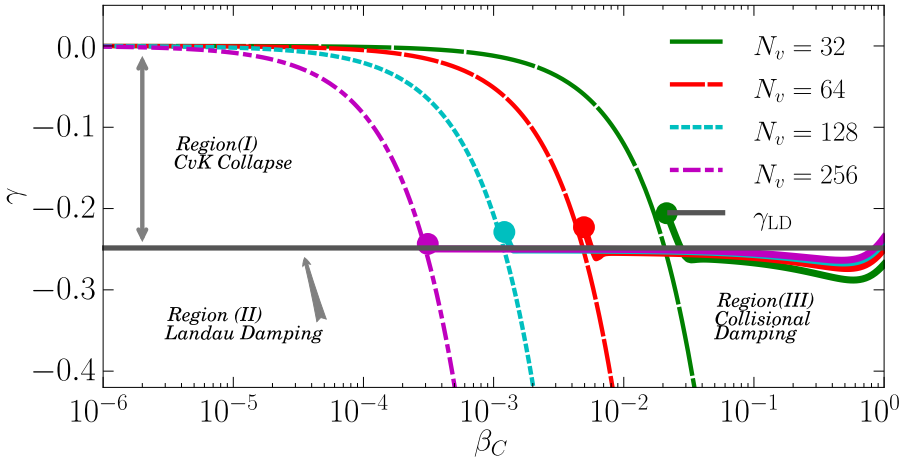

Figure 4.13.: *Growth rates of ITG mode ($k_y = 1.8$) for different collisionality and resolutions compared to Landaus analytical solution. If collisionality is large enough a Landau damped eigenmode appears, as indicated by the dot, which is less sensitive on collisionality than the CvK eigenmodes.*

Therefore, in order to keep $\beta_c^\star$ a higher velocity space resolution N_v is necessary.

The dynamics sensitively depend on the collisionality β_c for a given N_v, so that the accuracy of the numerical method for treating the Lenard-Bernstein operator Eq.(4.34) is important. In order to address this problem, we compare the present numerical method, i.e., the discretization using the fourth order central-difference method with that of using a Fourier expansion method in velocity space to calculate the derivatives. Fig. 4.14 illustrates the results for the case of $N_v = 128$ and $\beta_c = 6 \times 10^{-3}$, where the collisionality is larger than $\beta_c^\star$, i.e. $\beta_c > \beta_c^\star$, so that some of the CvK eigenmodes changed already to Landau damped ITG eigenmodes. It can be seen that the Landau damped eigenmode and the majority of the CvK mode show a good agreement between the two methods, suggesting that the results in Fig. 4.13 can be justified. We see differences only for CvK eigenmodes which damping rate is larger than those of the majority of the CvK eigenmodes. However, these highly damped modes are expected to have little influence on the damping dynamics, since modes with small damping rate dominate the phenomena.

4.8.1 | Effect of diffusive term

The Lenard-Bernstein collisional operator induces a diffusion in velocity spaces which leads to a collapse of the Case–van Kampen modes and if chosen large enough, the appearance of a Landau eigenmode. Bratanov et al. (2013) found that the collapse of the CvK eigenmodes is not only triggered by a diffusivity, but by any even order hyper-

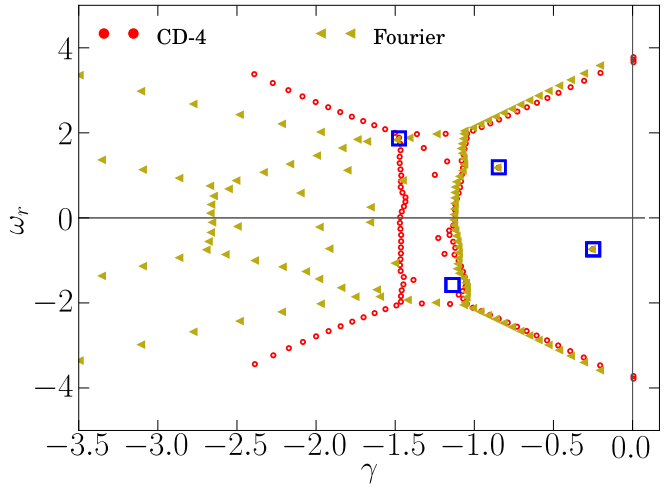

Figure 4.14: *Eigenvalue spectra with $N_v = 128$ and $\beta_c = 6 \times 10^{-3}$. We compare the discretization of the LB-operator using fourth order central differences (CD-4) with a Fourier method, where the derivatives are directly calculated in Fourier space.*

diffusive term. This is confirmed in Fig. 4.15. The effect of the Krook operator, shown in Fig. 4.15a, is that it shifts the growth rate of all eigenvalues, and they become stable. Further we investigate the case with $n = 2$ (regular diffusion) and $n = 4$, $n = 6$ the hyper-diffusion cases. The eigenvalue spectra is shown in Fig. 4.15b-d. The growth of the gyrokinetic mode remains the nearly the same, thus meaning that in contrast to the Krook operator, the effect on the *physical* modes is small. Interestingly, for higher order diffusivity less collisionality β_c is required to damp the CvK eigenmodes.

4.9 | Landau damping in Fourier–Hermite basis with collisionality

We add a finite collisionality β_c for the gyrokinetic operator $\mathcal{H}_{k_y}$ in Fourier–Hermite basis (4.59 including the Lenard-Bernstein collisional term given in (4.60). Parameters are chosen as in Sec. 4.7.1, and the $\beta_c = 5 \times 10^{-4}$ in the weak collisional case. The corresponding eigenvalue spectra is shown in Fig. 4.16a. The initial perturbation is chosen to a Maxwellian, and the system is integrated in time. The time evolution for a few selected time steps is shown in Fig. 4.16. At $t = 0$, only the h_0 is perturbed, for $t > 0$, the energy is transfered to higher order Hermite polynomials. The collisionless (solid) and weak collisional case (dashed lines) are similar for $t = 10$. However, close to the recurrence time, we find that the (weak) collisionality is able to dissipate the energy and thus successfully avoids the reflection. For the collisionless case, as already discussed in Fig. 4.7.1, at the recurrence time, a reflection at the cut-off Hermite function sets in, where energy dissipation is lost due to the lost of directionality.

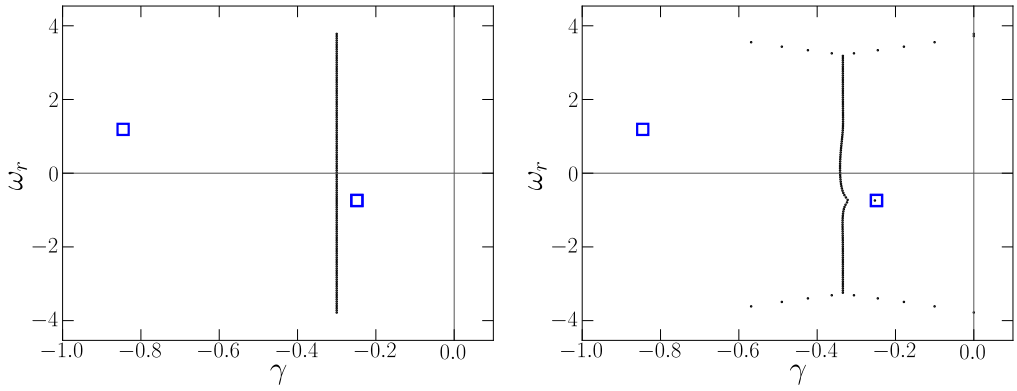

(a) *Krook operator* ($\beta_c = 3 \times 10^{-1}$)

(b) *Diffusion operator* ($\beta_c = 2 \times 10^{-3}$)

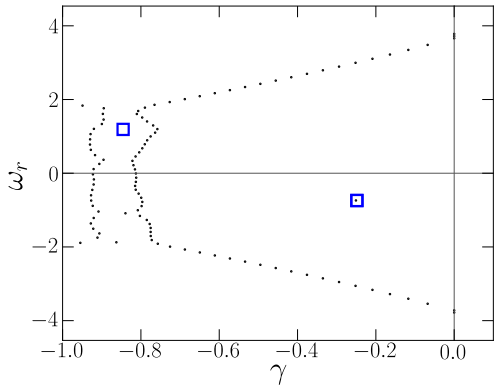

(c) *Hyper-Diffusion* $\partial^4_{v_\parallel}$ ($\beta_c = 2 \times 10^{-5}$)

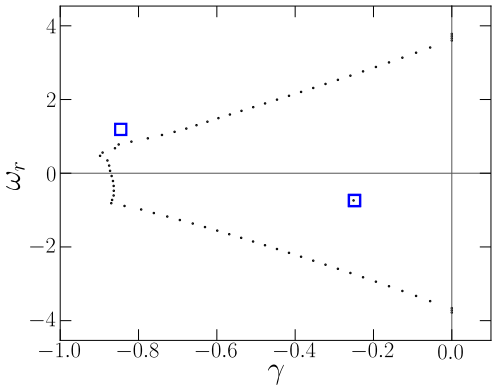

(d) *Hyper-Diffusion* $\partial^6_{v_\parallel}$ ($\beta_c = 2 \times 10^{-7}$)

Figure 4.15.: *Eigenvalues spectra using various orders of diffusion. A higher order diffusivity requires less collisionality to collapse the CvK eigenmodes. The square markers indicate the Landau roots.* ($k_y = 1.8$, $\theta = 0.3$).

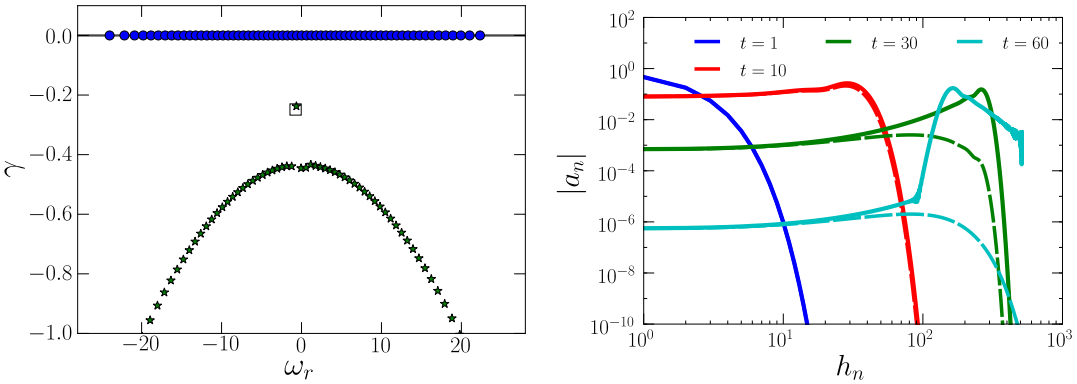

(a) *Eigenvalue spectra* **(b)** *Time evolution in Hermite basis*

Figure 4.16.: *Landau damping in Fourier–Hermite basis. Solid lines is the collisionless case, dashes lines for the weak-collisional case. The time evolution between collisionless and weak-collisional is (quasi)-identical until the recurrence time, where the perturbation gets aliased and reflected. The weak-collisional is capable of dissipating the small-scale oscillations and thus recurrence is avoided.*

4.10 | The role of the CvK eigenmodes in poloidal mode coupling

We have identified two processes in reproducing damping, one is the phase mixing in the collisionless or weak collisionality regime where $\beta_c < \beta_c^\star$ and the other is the Landau damped eigenmode in the regime where $\beta_c > \beta_c^\star$. Note in the former case that the damping rate averaged over a long time scale exceeding the recurrence time is different from that of the Landau damping as discussed in Fig. 4.11, although the damping rate during each recurrence is the same as that of the Landau damping. Here, a question arises whether the role of the kinetic damping due to linearly stable/damped modes properly works for the unstable modes in the presence of coupling which connects two modes.

In order to address this problem, we consider a poloidally coupled system consisting of three modes, i.e. a linearly unstable mode with k_y', a stable mode with k_y'' ($k_y' < k_y''$) and an externally imposed tertiary mode with $k_{\rm ex}$, where a spatial coupling relation among three modes, i.e. $k_y' + k_{\rm ex} = k_y''$, is satisfied. This is considered to be a minimum model of the ITG dynamics in the presence of a magnetic island or a vortex flow as discussed by Wang et al. (2009). Following the idea of the vortex flow, we introduce a potential as a tertiary mode given by

$$\phi_{\rm ex} = \epsilon g(x) \sin\left(k_{\rm ex} y\right) = \frac{-i\epsilon}{2} g(x) \left(e^{ik_{\rm ex}y} - e^{-ik_{\rm ex}y}\right) \quad , \tag{4.61}$$

where $g(x)$ is the radial profile and ϵ represents the amplitude. The potential is included into the gyrokinetic equation Eq.(4.37) through the Poisson bracket[1], which takes the form

$$\begin{aligned}\frac{\partial f_{1,\mathbf{k}_\perp}}{\partial t} = &-ik_y\left(1+\tfrac{1}{2}\eta_i\left[v_\parallel^2 - k_\perp^2 - 1\right]\right)\bar{\phi}_{\mathbf{k}_\perp} f_0 - i\theta k_y v_\parallel \left(f_{1,\mathbf{k}_\perp} + \bar{\phi}_{\mathbf{k}_\perp} f_0\right) \\ &- \left[\phi_{\rm ex}, f_{1,\mathbf{k}_\perp}\right]_{\mathbf{k}_\perp} + \mathcal{C}_{\rm LB} \quad .\end{aligned} \tag{4.62}$$

In the absence of coupling in Eq.(4.62), i.e. $\epsilon = 0$, the most unstable radial wave number is found to be $k_x = 0$. Here, we consider the mode with $k_x = 0$ for $f_{1,\mathbf{k}_\perp}$ even in the presence of the coupling assuming that the coupling in Eq.(4.62) is weak. The radial profile is assumed to be $g(x) \propto x$, so that $\partial_x \phi_{\rm ex}$ has no radial dependence. Then, we obtain the following equations for the ITG mode with wave numbers k_y' and k_y'' as

$$\frac{\partial f_{1,k_y'}}{\partial t} = -ik_y'\left(1+\tfrac{1}{2}\eta_i\left[v_\parallel^2 - k_y'^2 - 1\right]\right)\bar{\phi}_{k_y'} f_0 - i\theta k_y' v_\parallel \left(f_{1,k_y'} + \bar{\phi}_{k_y'} f_0\right) + \mathcal{C}_{\rm LB} \tag{4.63a}$$

$$- \frac{\epsilon}{2}(k_y' + k_{\rm ex}) f_{1,k_y'+k_{\rm ex}} \quad ,$$

$$\frac{\partial f_{1,k_y''}}{\partial t} = -ik_y''\left(1+\tfrac{1}{2}\eta_i\left[v_\parallel^2 - k_y''^2 - 1\right]\right)\bar{\phi}_{k_y''} f_0 - i\theta k_y'' v_\parallel \left(f_{1,k_y''} + \bar{\phi}_{k_y''} f_0\right) + \mathcal{C}_{\rm LB} \tag{4.63b}$$

$$+ \frac{\epsilon}{2}(k_y'' - k_{\rm ex}) f_{1,,k_y''-k_{\rm ex}} \quad .$$

The last terms in Eq.(4.63a) and Eq.(4.63b) originates from the linear poloidal coupling with the neighboring modes. Note that only one coupling pair is retained in Eq.(4.63a) and Eq.(4.63b) neglecting those from $k_y' - k_{\rm ex}$ and $k_y'' + k_{\rm ex}$ in order to see the dynamics in the simplest case.

Assuming the time dependence of $\exp(-i\omega t)$, Eq.(4.63) is cast as

$$-i\omega \begin{pmatrix} f_{1,k_y'} \\ f_{1,k_y''} \end{pmatrix} = \underbrace{\begin{bmatrix} \mathcal{L}_{k_y'} & \mathbf{C}_{k_y''} \\ \mathbf{C}_{k_y'} & \mathcal{L}_{k_y''} \end{bmatrix}}_{\mathcal{L}_{k_y',k_y''}} \begin{pmatrix} f_{1,k_y'} \\ f_{1,k_y''} \end{pmatrix} \quad , \tag{4.64}$$

where $\mathcal{L}_{k_y'}$ and $\mathcal{L}_{k_y''}$ are the linear gyrokinetic operator given in Eq.(4.44) of the uncoupled modes. $\mathbf{C}_{k_y'}$ and $\mathbf{C}_{k_y''}$ are the off-diagonal cross-coupling terms which originate from the external vortex flow given by $\mathbf{C}_{k_y'} = \frac{1}{2}\epsilon k_y' \mathcal{I}$ and $\mathbf{C}_{k_y''} = -\frac{1}{2}\epsilon k_y'' \mathcal{I}$, where $\mathcal{I}$ represents the $N \times N$ identity matrix, so that $\mathcal{C}_{k_y'}$ and $\mathcal{C}_{k_y''}$ are the diagonal matrices. In the absence of coupling, i.e. $\epsilon = 0$, we get $2N$ (not degenerated) eigenvalues, where each N eigenvectors corresponding to those for $\mathcal{L}_{k_y'}$ ($\mathcal{L}_{k_y''}$) have no contributions from $\mathcal{L}_{k_y''}$ ($\mathcal{L}_{k_y'}$), respectively.

[1] Poisson brackets with the definition $[A, B] = \partial_x A \partial_y B - \partial_y A \, \partial_x B$.

However, once coupling becomes finite, i.e. $\epsilon > 0$, a global mode is formed, where each eigenvector of $\mathcal{L}_{k'_y,k''_y}$ has now contributions from both $\mathcal{L}_{k'_y}$ and $\mathcal{L}_{k''_y}$. Here, we choose $k'_y = 1.3$ and $k''_y = 1.8$ and $k_{\mathrm{ex}} = 0.5$, respectively. This gives following mode coupling relation as shown in Fig. 4.17.

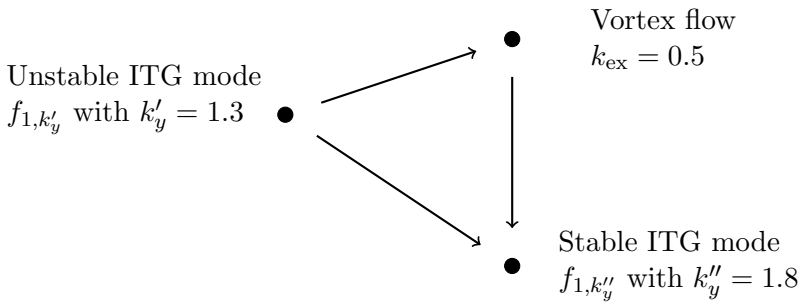

Figure 4.17.: *Sketch of the mode coupling triad between the unstable mode with k'_y, the stable mode with k''_y and the tertiary mode k_{ex}.*

Figure 4.18 shows the eigenvalues of the coupled system $\mathcal{L}_{k'_y,k''_y}$ with $\epsilon = 0.15$ for (a) the collisionless case ($\beta_c = 0$) and (b) collisional case ($\beta_c = 2 \times 10^{-3}$). The two square markers in Fig. 4.18(a) and (b) represent the growth rates for the uncoupled unstable and stable modes calculated from the dispersion relation Eq.(4.39), respectively. In Fig.(4.18)(a), one unstable global mode and its complex conjugate solution can be seen as well as the marginally stable CvK eigenmodes which appear on the real axis. On the other hand, no stable eigenmode is found similar to the discussion in Sec.(4.8). Here, it should be noted that the reduction of the growth rate takes place even when the stable damped eigenmode does not exits. On the other hand, in the collisional case, once the collisionality exceeds the critical value $\beta_c^\star$ as in Fig.(4.18(b), in addition to the unstable mode which growth rate is also reduced as in Fig.(4.18(a), a damped global eigenmode appears as seen in Fig. 4.18(b) which damping rate is reduced from that of the uncoupled case (square marker 2). The reduction of the unstable mode is considered to result from the energy transfer from unstable mode to stable mode through the tertiary mode. From the comparison between Fig. 4.18(a) and (b), it can be seen that even if the damped mode does not exist as an eigenstate in the collisionless or weak collisional case with $\beta_c < \beta_c^\star$, a damping and/or energy dissipation for the unstable mode through the mode coupling with the tertiary mode is persisted.

In order to see the characteristics of the unstable and stable modes, we investigate the growth rate of the unstable and stable modes with respect to β_c in Fig.(4.19). In the case without coupling, i.e. $\epsilon = 0$, as β_c increases, the growth rate of the unstable mode keeps an almost constant value up to $\beta_c \sim 10^{-2}$, whereas the CvK eigenmodes are damped down to $\beta_c^\star$. Then, a new stable eigenmode appears at $\beta_c \sim \beta_c^\star$, which is also less affected for the increase of β_c up to $\beta_c \sim 10^{-1}$ as seen in Fig. 4.19. Note that

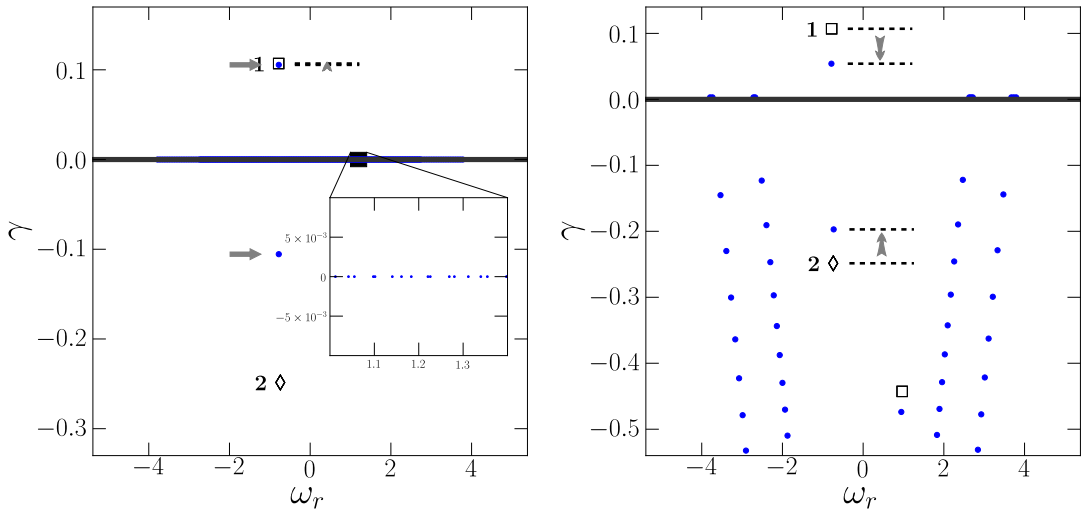

(a) $\beta_c = 0$ **(b)** $\beta_c = 2 \times 10^{-3}$

Figure 4.18.: *Eigenvalue spectra of the coupled poloidal modes with* $k_y' = 1.3$ *and* $k_y'' = 1.8$ *for the collisionless and weak collisional case with* $\epsilon = 0.15$*. The Landau solutions for the uncoupled modes are shown using square markers.*

Figure 4.19: *Growth rate of the coupled mode for different collisionality with* $\epsilon = 0, 0.10, 0.15$*. The lines denoted with* $\gamma_{k_y'}$ *and* $\gamma_{k_y''}$ *correspond to Landau's solution of the uncoupled modes for* k_y' *and* k_y'' *respectively. We see that the growth rate of the stable global mode is sensitive on collisionality, in order to collapse the CvK eigenmodes. The unstable global mode however is not sensitive to collision.*

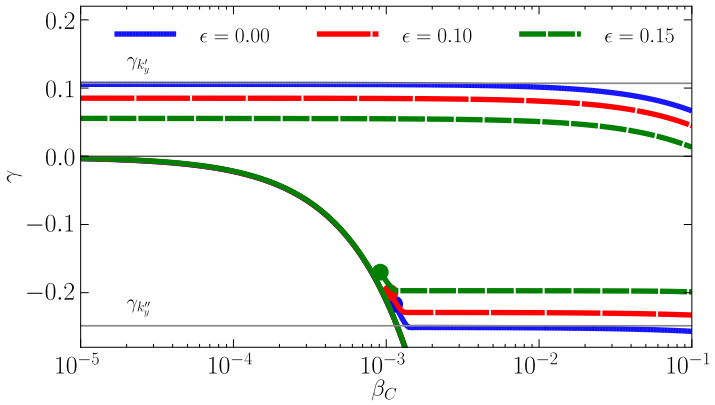

the feature is essentially same as that in Fig. 4.13, where only a single damped mode is discussed. In the case with coupling, i.e. $\epsilon = 0.1$, the growth rate is reduced as discussed in Fig. 4.18(a) which is the case of $\beta_c = 0$, and is also less affected for the increase of β_c up to $\beta_c \sim 10^{-2}$. The CvK eigenmodes also show a similar tendency. However it is found that the damping rate after the damped eigenmode appears decreases from that of the Landau theory as discussed in Fig.(4.18b). The damping rate for $\beta_c > \beta_c^\star$ is also found to be less affected as the case of $\epsilon = 0$. As the coupling effect becomes large, i.e. $\epsilon = 0.15$, the growth rate for unstable mode becomes smaller, whereas the damping rate for the stable modes for $\beta_c > \beta_c^\star$ is also smaller. Thus it is found that the stabilization of the unstable eigenmode takes place without depending on whether the stable eigenmode exits, which results from the collisionality.

Here, we investigate the eigenfunctions in velocity space in the case without coupling ($\epsilon = 0$) in Fig. 4.20 and with coupling in Fig. 4.21. Note that we use same parameters as above, except the velocity resolution is increased to $N_v = 512$. Each case includes unstable and stable modes for $\beta_c = 0$ and $\beta_c = 2 \times 10^{-3}$, and the unstable and stable modes consist of the eigenfunctions $(f_{1,k_y'}, f_{1,k_y''})$, respectively. In the case without coupling ($\epsilon = 0$) and also without collision ($\beta_c = 0$), i.e. Fig. 4.20(a')/(a"), (c')/(c"). For the unstable, $f_{1,k_y'}$ shows a global extent in velocity space, both for the real and imaginary part, which is a typical ITG structure while the contributions from $f_{1,k_y''}$ is zero, since there is no coupling. On the other hand, the stable modes shows a localized, spiky structure in $f_{1,k_y''}$ exhibiting a typical CvK mode, while the contributions from $f_{1,k_y'}$ is zero. In the collisional case with $\beta_c = 2 \times 10^{-3}$ which is larger than the critical value $\beta_c^\star$, the unstable mode (b') shows almost same structure, while the stable mode (d") changes the structure to that of the eigenmode with extend in velocity space.

In the case with coupling ($\epsilon = 0.15$), but without collision ($\beta_c = 0$), i.e. Fig. 4.21 (e) and (g), for the unstable mode, $f_{1,k_y'}$ is almost same as Fig. 4.20(a') while the contribution from the stable mode become effective so that the $f_{1,k_y''}$ exhibits a global structure as seen in Fig.(4.21e"). On the other hand, for the stable mode (g'/g"), a spiky structure also appear for $f_{1,k_y'}$ due to the coupling. In the collisional case with $\beta_c = 5 \times 10^{-3}$, i.e. Fig. 4.21, the unstable mode is almost same as Fig. 4.21(f') and (f") where those for the stable modes (h'/h") are change to a Landau eigenmode with finite extent as Fig. 4.21 both for $f_{1,k_y'}$ and $f_{1,k_y''}$. These features in eigenfunction structure in velocity space is consistent with the results in Fig. 11 and Fig.12.

Finally, in Fig. 4.22 the time evolution of the electrostatic potential in the initial value problem with a random initial perturbation is shown. In case of (a) and (b), the uncoupled system ($\epsilon = 0$) is shown for the individual modes with $k_y' = 1.3$ (solid) and $k_y'' = 1.8$ (dashed). For the collisionless case in (a), the stable mode cannot be resolved unless collisionality is large enough as in (b). However, with poloidal coupling, i.e. $\epsilon = 0.15$, the stabilization effect of k_y' is found to be same for the collisionless case shown in (c) and the collisional case ($\beta_c = 5 \times 10^{-3}$) shown in (d).

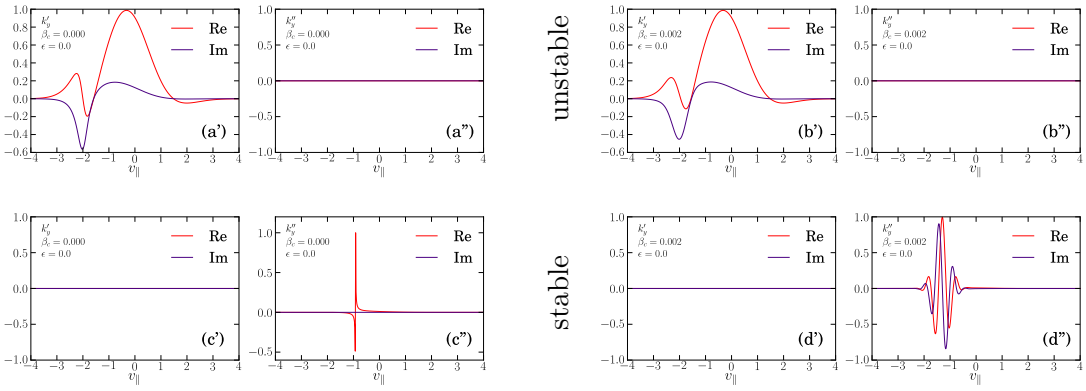

Figure 4.20.: *Eigenvectors of the global mode in the form of* $(f_{1,k'_y}, f_{1,k''_y})$ *for the collisionless case (upper plots) and collisional case (lower plots) with* $\beta_c = 2 \times 10^{-3}$ *and no coupling, i.e.* $\epsilon = 0$*. A large resolution of* $N_v = 512$ *has been chosen to show the singular structure of the CvK eigenmodes.*

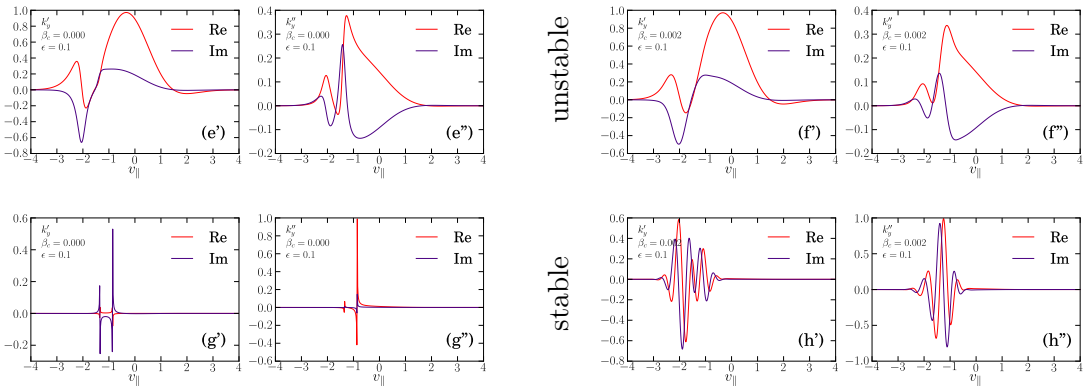

Figure 4.21.: *Eigenvectors of the global Landau eigenmodes in the form of* $(f_{1,k'_y}, f_{1,k''_y})$ *for* $\beta_c = 0$ *and* $\beta_c = 2 \times 10^{-3}$ *with a coupling parameter* $\epsilon = 0.1$*.*

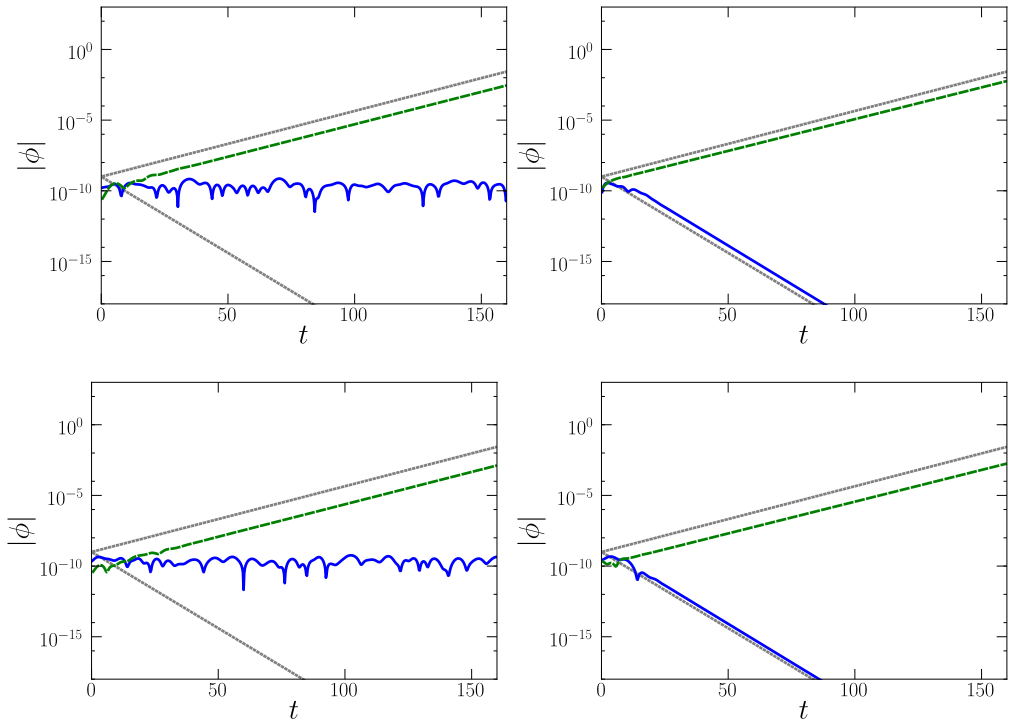

Figure 4.22.: *Solution of the IVP with* $\epsilon = 0.15$ *and* $k_y' = 1.3$ *(solid) and* $k_y'' = 1.8$ *(dashed), with the corresponding Landau solutions (dotted). Without coupling* ($\epsilon = 0$)*, the stable mode can only be resolved with large enough collision, see* $\beta_c = 0$ *(a) and* $\beta_c = 5 \times 10^{-3}$ *(b). With coupling, i.e.* $\epsilon = 0.15$*, the growth rate of the coupled global mode is independent on the collisionality, see (c) with* $\beta_c = 0$ *and (d) with* $\beta_c = 5 \times 10^{-3}$*.*

4.11 | Summary

We investigated the characteristics of marginally stable and damped modes, based on a gyrokinetic Vlasov simulation and also an eigenvalue analysis. In the absence of collisions, we found that the time evolution of the electrostatic potential of the stable ITG modes strongly depends on the initial perturbation in velocity space. Namely, in the case with random noise perturbation, the stable ITG modes ascribed to high poloidal mode numbers do not show damping, but do exhibit a marginal behavior with small-amplitude fluctuations. In the case with Maxwellian perturbation, damping of the electrostatic potential is observed with a damping rate as predicted by the Landau theory. However, the electrostatic potential is subject to recurrence beyond which the simulation becomes ambiguous. Based on the eigenvalue analysis, we have confirmed that such a behavior results from the appearance of the CvK eigenmodes that show marginal stability with different real frequencies, and resultant phase mixing. We found that such CvK eigenmodes are very sensitive to collisional dissipation. Namely, finite collisional dissipation leads to damping of the CvK eigenmodes. Once the CvK eigenmodes are damped down to the rate predicted by the Landau theory, a normal mode corresponding to the eigenstate appears. Consequently, the recurrence phenomenon is suppressed so that the simulation beyond the recurrence time becomes valid. The required critical collisionality $\beta_c^\star$ to reproduce the Landau eigenmode crucially depends on the number of grid points used. Namely, higher (lower) resolution in velocity space generally requires lower (higher) collisionality in order to reproduce the true eigenmode. Once the collisionality β_c exceeds $\beta_c^\star$, i.e., $\beta_c > \beta_c^\star$, the damping rate becomes constant, as is predicted by the Landau theory, and not influenced by the collisionality. As β_c increases, dissipation becomes so large that collisional damping arises physically. Thus, only a limited range of collisionality can be chosen to reproduce the Landau damping a Landau eigenmode. To investigate the validity of the energy transfer from unstable ITG modes to stable modes through mode coupling, we studied a system with two poloidal modes, i.e., one unstable and the other stable, coupled by a vortex flow which corresponds to a tertiary mode. Using the above model, we showed that the growth rate of the unstable global mode is reduced independent on the collisionality. We concluded that the energy transfer from unstable modes to stable modes through linear mode coupling can be properly reproduced without depending on whether damping results from the phase mixing subject to recurrence or the Landau damping. Namely, the effect of Landau damping in the simulation including such coupling characteristics and associated energy transfer can be justified even in the collisionless limit.

5 | Investigation of ITG and ETG turbulences

In the Tokamak, we find many types of *drift wave* instabilities, which are collective plasma oscillations driven by the electrostatic force to ensure a quasi-neutrality of the plasma. Note that a plasma is charge neutral, however, charge imbalances on a small scale are nevertheless possible. In the beginning, it was thought that *density gradient drift waves* are always unstable in slab geometry, as shown by Pearlstein and Berk (1969), and were thus termed *universal instabilities*. However, subsequent analysis by Ross and Mahajan (1978) and Chen et al. (1978) found that the linear instability arises through an erroneous treatment of the plasma dispersion function and showed that the universal modes are either damped or marginally stable. However, it is still speculated by Hirshman and Molvig (1979) and Beasley et al. (1983), that turbulence destabilization through diffusive electrons would drive the universal mode unstable close to the rational surface. Recently, Chowdhury et al. (2010) showed that the universal drift mode can become unstable and may contribute to the particle transport.

Finally, *trapped electrons* may excited another drift wave instability, namely the *trapped electron modes* as discussed by Dannert and Jenko (2005), however, as in our slab geometry $\nabla_\parallel B_0 = 0$, it does not arise here.

Nowadays, the destabilization of drift waves through the temperature gradient, is thought to be responsible for the large, "anomalous" heat transport from the hotter inner core plasma to the cooler outer edge plasma observed in the Tokamak. In this chapter we will thus study the characteristics the of ion/electron temperature gradient drift waves using the gyrokinetic equation system derived in Ch. 2 and numerically solve it using either the gkc++ solver as described in Ch. 3 for the nonlinear case or by solving the dispersion relation in the linear case.

5.1 | The ion temperature gradient mode

The mechanism of the destabilization of the temperature gradient mode can be best understood in the fluid model as given by Cowley et al. (1991) and sketched in Fig. 5.1. In a Tokamak device, a large temperature gradient in the radial direction from the inner, high-density and hot core to the low-density and cooler, outer edge plasma. A small density perturbation, which originates from random fluctuations at the location of

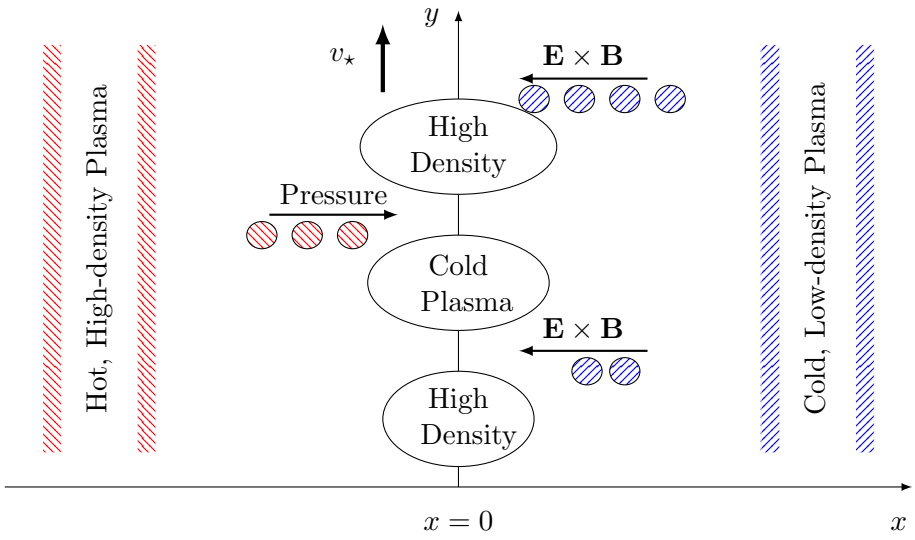

Figure 5.1.: *A simplistic picture of the excitation of an temperature gradient drift mode in slab geometry through the interplay of temperature gradient and* $\mathbf{E}\times\mathbf{B}$ *drift and pressure force.*

$x = 0$ produces an electric field at the origin of the coordinate system. The equilibrium field together with the $\mathbf{E}\times\mathbf{B}$ drift parallel to the temperature gradient, induces an inflow of cold plasma. This inflow cools the perturbation such that its pressure decreases and allows the inflow of hot, high-density plasma with a larger pressure, and leads to an increase of the density of the perturbation. We reach, the original state, where the initial perturbation is amplified and shifted (or drifted) upwards. This self-amplification leads to an exponential growth of the drift wave until nonlinear effects become important.

5.1.1 | Adiabatic electron approximation

A neutral plasma consist of positively charged ions, such as the hydrogen nuclei, and the negatively charged electron species. For a numerical calculation however, the computational requirements are very demanding; thus by using the so-called *adiabatic approximation* for the electrons, a scale-separation is exploited and the electrons are only modelled to save computational resources. The gyrokinetic Poisson's equation (2.56) for a plasma consisting of an ion and an electron species, i.e. $\sigma = \{e; i\}$ with $n_e = n_i = 1$ (and $T_e = T_i = 1$, and $q_i = -q_e = 1$), is given by

$$\lambda_D^2 k_\perp^2 \phi + \sum_\sigma \left(1 - \Gamma_0(b_\sigma)\right) \phi = \sum_\sigma q_\sigma \pi B_0 \int_{\mu=0}^{\infty} \int_{v_\parallel=-\infty}^{\infty} J_0(\lambda_\sigma)\, f_{1\sigma}\, \mathrm{d}v_\parallel\, \mathrm{d}\mu \quad . \tag{5.1}$$

For the study of the ITG, our reference length scale ρ_{ref} is given by the ion gyro-radius ρ_i. As $m_e/m_i \ll 1$, we can assume the electrons to be massless ($m_e \to 0$), so that $b_e \sim 0$

and $\lambda_e \sim 0$ and thus $\Gamma_0(b_e) \sim 1$ and $J_0(\lambda_e) \sim 1$. Additionally, we can safely assume $\lambda_D = 0$; to get the quasi-neutrality equation given by

$$(1 - \Gamma_0(b_i))\,\phi = \pi B_0 \int_{\mu=0}^{\infty} \int_{v_\parallel=-\infty}^{\infty} J_0(\lambda_i)\, g_i \,\mathrm{d}v_\parallel \,\mathrm{d}\mu - n_{1e} \quad , \tag{5.2}$$

where we directly integrated over μ and $v_\parallel$ for the electron species. Finally, we assume a *force-balance* between the pressure (mainly generated by the electrons) and the Lorentz force, given by

$$\nabla p = q_e \left(-\nabla\phi + \frac{\mathbf{v}}{c} \times \mathbf{B}\right) \qquad \rightarrow \qquad \nabla_\parallel p = -q_e \nabla_\parallel \phi \quad , \tag{5.3}$$

where the motion due to drift was neglected and only parallel components are taken into account. Finally, the pressure can be estimated by $p = n_e T_e$ and using $n_e = n_{0e} + n_{1e}$ gives $n_{1e} \propto (q_e/T_e)\phi$. The new relation for n_{1e} is then used to replace n_{1e} on the right-hand side of Eq.(5.2), such that the quasi-neutrality condition becomes independent on n_{1e}. Now, we do not need to solve the Vlasov equation for the electron species anymore, therefore the time step of the simulation *is not restricted* by the thermal velocity of the electrons.

However, the limit of massless electrons $m_e \rightarrow 0$ also implies an infinite thermal velocity $v_{th,e} = \infty$, thus any electrostatic perturbation along the magnetic field line is immediately balanced out by the electrons (short-circuited). To account for this effect, the adiabatic response is modified by $\phi - \langle\phi\rangle_{\mathrm{FS}}$. Here, FS denotes the flux surface average, which is the average of the electrostatic potential along the magnetic field line. The quasi-neutrality condition for the ITG with an *adiabatic electron response* is then given by (assuming $T_i = T_e = 1$)

$$(1 - \Gamma_0(b_i))\,\phi + \underbrace{(\phi - \langle\phi\rangle_{\mathrm{FS}})}_{\text{electron contributions}} = \pi n_0 B_0 \int_{\mu=0}^{\infty} \int_{v_\parallel=-\infty}^{\infty} J_0(\lambda_i)\, g_i \,\mathrm{d}v_\parallel \,\mathrm{d}\mu \quad . \tag{5.4}$$

5.1.2 | Linear study

Instead of directly performing simulations as an initial value problem; for linear investigation we solve the dispersion relation in the two-dimensional sheared slab geometry by integrating the Vlasov's and the Poisson's equation over the velocity space $v_\parallel$ and μ (however, special care has to be taken to keep the gyro-averaging terms and radial dependence). A so-called *integral equation code* therefore been developed, where the complex frequency of an ITG mode can then be found by solving a *nonlinear eigenvalue problem* given by $\mathcal{L}(\omega) = 0$, the structure of the matrix $\mathcal{L}$ is described in more detail in the appendix (A.4). The (numerical) solution of the dispersion relation has the advantage that all branches of the ITG (stable and unstable) can be extracted. This is in contrast to solving the linear equations as an initial value problem, where only the mode

with the largest growth rate dominates the solution in the long-time limit. Note that for the integral over the velocity space, we use the *plasma dispersion function*, which has an infinite number of roots, such that we can expect the solution of the dispersion relation to have infinite many stable branches as well. For an initial investigation, we choose $\hat{s} = 0.2$ and $\eta_i = 5$ as the physical parameters and $N_x = 512$ for the numerical parameter. The dispersion relation is solved with the procedure outlined in Fig. 5.2. We extract the six most unstable branches, shown in Fig. 5.3, where (a) shows the frequencies and (b) shows the growth rates over the poloidal wavenumber k_y. We find various branches of the drift wave, which can be separated into the standard ITG region $k_y \lesssim 1$ and the short-wavelength (shw) ITG region $k_y \gtrsim 1$. Two unstable branches (green and blue) are found for $k_y < 1$ — the standard ITG instabilities. However, a further destabilization of the drift wave (black line) is observed for larger wavenumbers with $k_y > 1$, which is the so-called short-wavelength ITG instability and is found to be unstable over a wide region, i.e. $k_y \sim 2 - 10$. Interestingly, the short-wavelength destabilized mode, is also found to exist in the standard region, where it is just a stable mode. However, around $k_y = 0.8$ the mode becomes destabilized and increases its growth rate until $k_y \sim 1.2$ where it becomes unstable. The short-wavelength ITG instability represents one of the sub-ion gyroradius instability and is for example not found in gyrofluid simulations, as finite Larmor radius effects are only approximately included as described by Dorland and Hammett (1993). Further branches are found (yellow, red, cyan) which are stable over the wavenumbers investigated.

The mode structures (eigenfunction) at $k_y = 0.5$ of the four most unstable eigenmodes in the standard region are shown in Fig. 5.4. The two unstable branches are shown in (a) and (b). The most unstable mode B_1 has a Gaussian shape, while the first subdominant mode B_2 is more extended and tilted. The stable modes B_3 and B_4 are shown in (c) and (d), respectively. Both stable modes have a broader structure compared to the structures of the unstable modes and their oscillatory character increases. This behaviour is quite consistent with Weber type equations quantization in the fluid limit with Hermite function type structures l which is valid for $k_y \ll 1$, see e.g. Idomura et al. (2000). The mode structures of the two most unstable modes in the short-wavelength region at $k_y = 2.5$, B_3 and B_4 are shown in Fig. 5.5. In contrast to the structure of the modes B_3 and B_4 at $k_y = 0.5$ shown previously, their mode structures at $k_y = 2.5$ becomes very narrow and approximately Gaussian, and only extends to less than half the size compared to eigenstructure at $k_y = 0.5$.

5.1.3 | The short-wavelength ITG instability

The short-wavelength ITG (shw-ITG) instability was put into focus by Smolyakov et al. (2002), who investigated the linear destabilization of the drift waves in shearless slab geometry and find that for certain parameter regions, the ITG mode (with adiabatic electrons) is unstable for $k_y \rho_i > 1$. While the main ITG branch is the most unstable

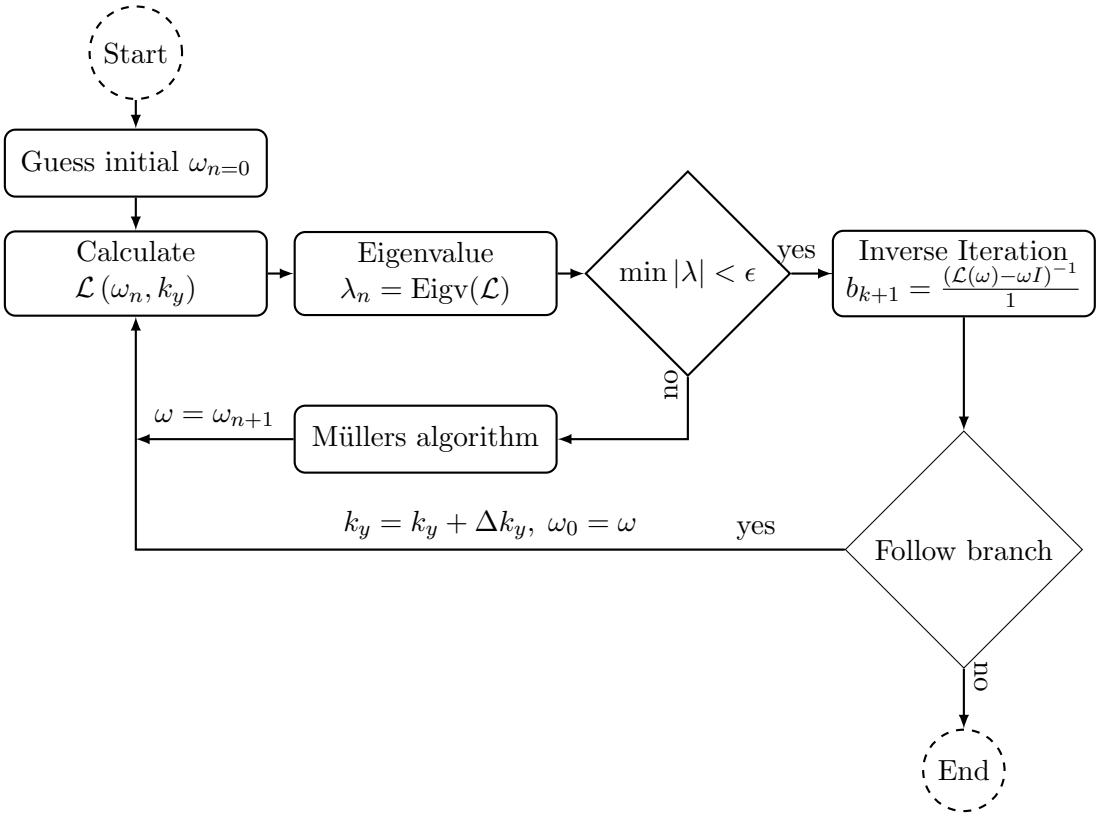

Figure 5.2.: *Flow diagram for solving the dispersion relation in the non-local, two-dimensional sheared-slab geometry. The dispersion relation requires the solution of a nonlinear eigenvalue problem ($det|\mathcal{L}(\omega_n)| = 0$) that is solved iteratively. We start from a fixed poloidal wavenumber k_y, e.g. $k_y = 1$, and choose an initial $\omega_{n=0}$ for the complex frequency. Note that $\omega_{n=0}$ needs to be close to the solution in order to converge. A root finding algorithm – here we used Müllers method – is used to converge the minimum absolute eigenvalue to zero, as in this case and the eigenvalue problem is solved. Once the root is found, we set the search for the root at the position $k_y' = k_y + \Delta k_y$ with $\Delta k_y \ll 1$ and use the previous ω as the new initial guess. As the dispersion relation is an analytic function and thus $\mathcal{L}$ is analytic, the new solution is usually found within a few iterations.*

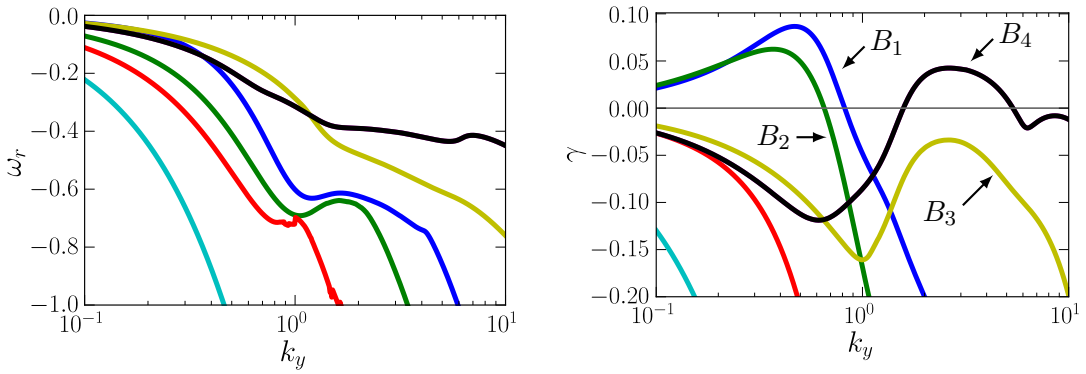

(a) *Frequency* **(b)** *Growth rates*

Figure 5.3.: *Analytic solution of the dispersion relation for* $\eta_i = 5$ *and* $\hat{s} = 0.2$. *Various branches are shown of which three of them are unstable. The unstable branches for* $k_y < 1$ *are refereed to as standard-ITG mode, the unstable branch with* $k_y > 1$ *is the short-wavelength ITG branch.*

branch with its peak growth rate around $k_y\rho_i \sim 0.5$, after becoming stable around $k_y\rho_i \sim 1$, the short-wavelength ITG mode with $k_y\rho_i > 1$ becomes unstable.

Smolyakov et al. (2002) insights triggered follow up investigations confirming the existence the shw-ITG also in the non-local, two-dimensional sheared slab geometry by Gao et al. (2003). Gao et al. (2005) pointed out that *the short-wavelength ITG mode is not a distinguished mode by itself, but a continuation of the standard ITG mode.* This claim is verified in Fig. 5.3b, where the unstable shw-ITG branch (black line) is found to exist in the std-ITG region $k_y \sim 0.5$ as well although being stable there. Here, we note that there is a fundamental difference between the slab geometry and the toroidal geometry, where the drift modes are not destabilized by the parallel ion compressibility but by the magnetic curvature. Due to this reason, the shw-ITG mode was considered to be only a slab mode. Gao et al. (2005) and Gao et al. (2005) found that short-wavelength ETG and ITG, respectively, also exists in the toroidal geometry. However, Hirose et al. (2002) showing toroidicity has a stabilizing effect, which however was relaxed by Chowdhury et al. (2009) who showed that the shw-ITG mode does couple with trapped electrons and becomes unstable over a wider parameter region of the toroidal configurations.

We note that due to the homomorphism between the ETG and ITG in the linear case, the same behavior holds true for the ETG and ITG for investigations of the std-ITG mode with $k_y\rho_i \sim 0.5$. However practically, this is only valid for $k_y\rho_i < 1$, for larger poloidal mode numbers, e.g. for an ITG mode the adiabatic assumption breaks down so that kinetic effects of the electron become important. On the other hand, for an ETG wave, adiabatic ion response is valid even for $k_y\rho_e > 1$, however, as will be discussed

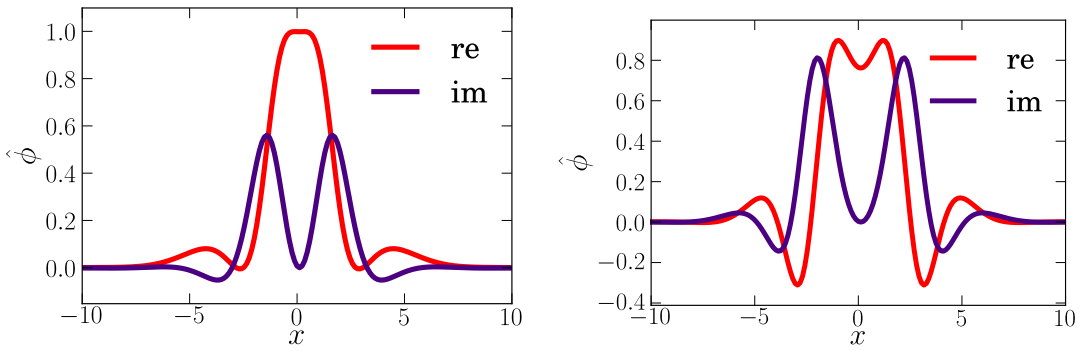

(a) B_1 *at* $k_y = 0.5$

(b) B_2 *at* $k_y = 0.5$

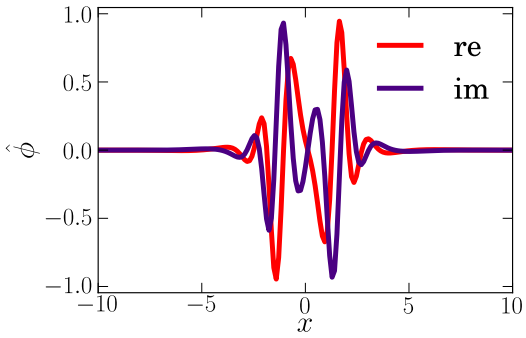

(c) B_3 *at* $k_y = 0.5$

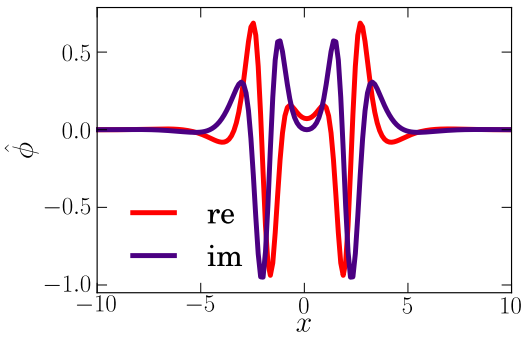

(d) B_4 *at* $k_y = 0.5$

Figure 5.4.: *The eigenmode structures of the first four most unstable branches* $B_1 - B_4$ *at* $k_y = 0.5$ *are shown for* $\hat{s} = 0.2$ *and* $\eta_i = 5$ *(with the phase of the modes are chosen to zero).* A_1*,* A_2 *and* A_4 *have a mirror symmetric eigenstructure, while* A_3 *has an anti-symmetric mode structure.*

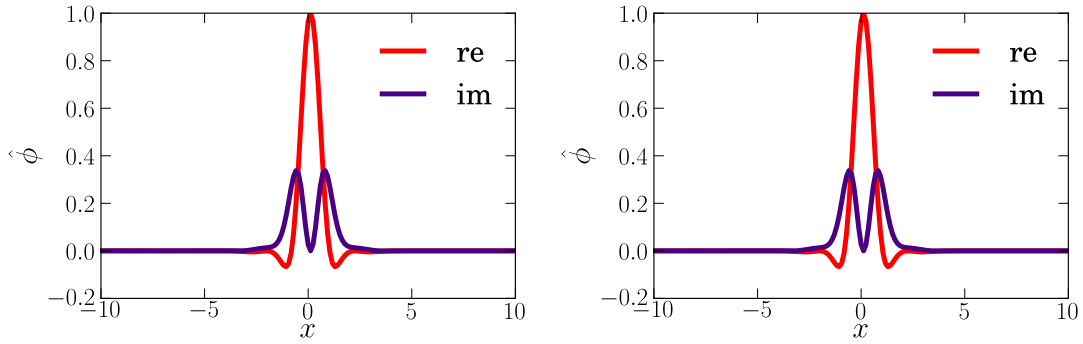

(a) B_3 *at* $k_y = 2.5$ **(b)** B_4 *at* $k_y = 2.5$

Figure 5.5.: *Eigenmodes of the first two most unstable branches at the short-wavelength region are shown for the parameters* $\hat{s} = 0.2$ *and* $\eta_i = 5$ *at* $k_y = 2.5$*. Compared to the two most unstable modes at the standard region Fig. 5.4a and Fig. 5.4b, the eigenmode structures of* B_4 *and* B_3 *are very narrow. Interestingly, although the difference between (a) and (b) are small, their eigenfrequency differs largely.*

later, a finite Debye length has to be taken into account which leads to a damping of the short-wavelength mode.

5.1.4 | Parameter scan over η_i

To improve our understanding of the ITG destabilization, we perform a parameter scan with a fixed magnetic shear $\hat{s} = 0.2$, and a varying ion temperature gradient η_i, to study the destabilization rate γ over the poloidal wavenumbers $k_y \in [10^{-1}, 10]$. Only the growth rate of the most unstable branch (at the specific k_y) is shown in Fig. 5.6. We find that the ITG mode is not excited for a temperature gradient below $\eta_i < 2$. For an increasingly large η_i, first the standard ITG region gets destabilized. Once η_i exceeds a value of $\eta_i \gtrsim 3$, the short-wavelength region also gets destabilized. For an $\eta_i \sim 5$ the dispersion relation exhibits the classical *double-hump* behavior, see Fig. 5.3b, where one peak is attributed to the std-ITG region, the other peak is attributed to the shw-ITG mode. For large $\eta_i > 7$, the ITG is also unstable for wavenumbers exceeding $k_y > 8$. This destabilization arises from the same branch that destabilizes the region $k_y \in [1.2, 8]$. Finally, it is interesting to note that the stable gap between, i.e. $1 < k_y < 1.4$, is found to be persisted throughout the temperature gradients investigated.

5.1.5 | Parameter scan over $\hat{s}$

Here, we fix the temperature gradient to $\eta_i = 5$ and investigate the growth rate dependence on the magnetic shear $\hat{s}$ over $k_y \in [10^{-1}, 10]$. The resulting growth rates of the

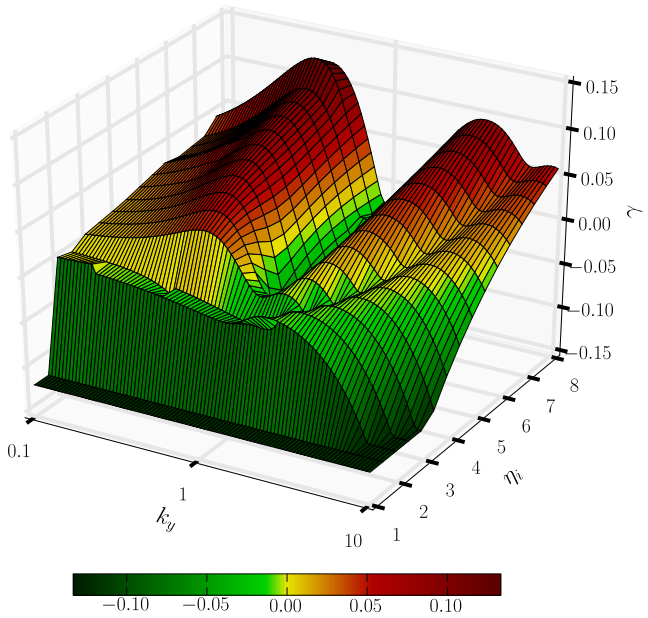

Figure 5.6: *The ITG growth rate of the most unstable branch over η_i and $k_y \in [10^{-1}, 10]$ for a fixed magnetic shear of $\hat{s} = 0.2$. The ITG mode is stable for a temperature gradient $\eta_i < 2$. For $\eta_i > 2$, the standard ITG region ($k_y < 1$) gets destabilized, once the temperature gradient exceeds $\eta_i \gtrsim 3$, the sub-ion gyroradius short-wavelength ITG region gets destabilized, too. The region between $1 < k_y < 1.4$ is stable independently of the temperature gradient and clearly separates the standard- and short-wavelength.*

most unstable branch for the parameter scan $(\hat{s}, k_y)$ are shown in Fig. 5.7. We find that a strong magnetic shear has a stabilizing effect on the ITG mode. Although, the influence of the magnetic shear on the standard region and short-wavelength region differs greatly: a large magnetic shear only weakly stabilizes the standard ITG mode, but the shw-region is much more sensitive on the magnetic shear, and is completely suppressed for $\hat{s} \gtrsim 0.4$. From this threshold, the linear growth rates at $k_y = 2.5$ strongly increases as the magnetic shear decreases. For $\hat{s} \lesssim 0.1$, we find that the growth rates of the short-wavelength region of the ITG exceeds the growth rates of the standard region. In the short-wavelength region, we again find two humps, with a first peak at $k_y \sim 2$ and the second at $k_y \sim 8$, originating from the same branch. For small magnetic shears, $\hat{s} \lesssim 0.1$ both peaks merge. Again, all branches between $1 < k_y < 1.5$ are stable and thus clearly separate the standard-ITG region and the shw-ITG region. The reason of this stabilization gab that is also observed in shearless slab simulations is yet to be understood.

5.1.6 | Quasi-linear heat flux estimates

To estimate the contributions of each unstable branch to the electrostatic heat flux transport in the nonlinear region, we calculate the quasi-linear heat flux contributions of the ITG mode over its poloidal wavenumber. The quasi-linear heat flux estimates are

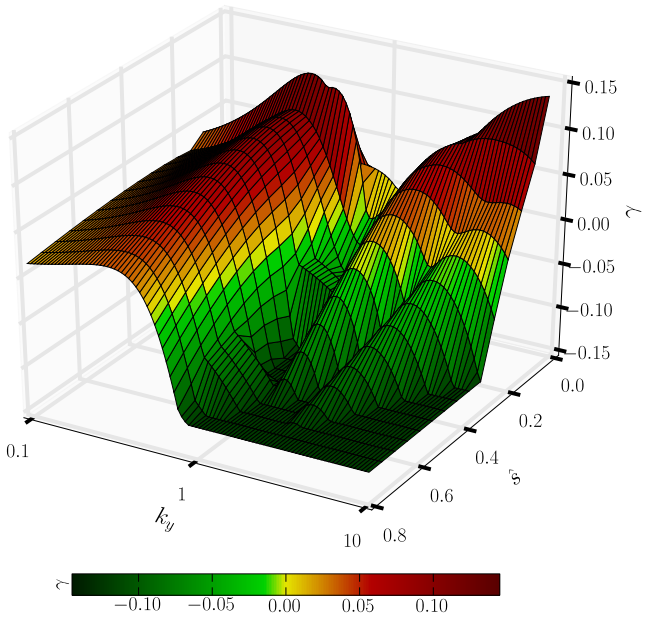

Figure 5.7: *ITG growth rate of the most unstable branch over $\hat{s}$ and k_y with a fixed temperature gradient of $\eta_i = 5$. A large magnetic shear has a stabilizing effect on the ITG mode. We find also that the short-wavelength region is more sensitive on $\hat{s}$ than the standard region. Namely, for a magnetic shear $\hat{s} \gtrsim 0.3$ the short-wavelength instability is suppressed, while for lower magnetic shears, the short-wavelength region is strongly destabilized such that for $\hat{s} \lesssim 0.1$, the linear growth rates of the shw-ITG mode exceeds the growth rates of the standard ITG mode.*

calculated from

$$Q_{\mathrm{ql},k_y} = \sum_{k_x} \left| \frac{\gamma_{k_y}}{k_x^2 + k_y^2} \phi(k_x, k_y) \right| \quad , \tag{5.5}$$

where γ_{k_y} is the growth rate of the ITG branch with the poloidal wavenumber k_y and its mode structure is given by $\phi(k_x, k_y)$, where k_x is the corresponding radial Fourier mode. Both, the growth rates and the mode structures are obtained from the integral code described in Fig. 5.2.

Using $\eta_i = 5$ and $\hat{s} = 0.2$, with the dispersion relation shown in Fig. 5.3, we calculate the contributions to the heat flux using Eq. 5.5 for the unstable branches as shown in Fig. 5.8b. Note the choice of the axes, which are chosen in such a way that the area below each contribution is proportional to the contribution to the total heat flux. As discussed before, the standard region of the ITG includes two unstable branches at $k_y = 0.5$, namely B_1 and B_2. Both are expected to contribute to the heat transport. Although both have a similar growth rate at around $k_y \sim 0.3$, the quasi-linear heat transport predicts that the B_1 branch has a substantially larger contribution to heat transport. We can understand this point by investigating the mode structure of both branches: the eigenstructure of the dominant B_1 branch (blue line) is a smooth Gaussian as shown in Fig. 5.4a, while the sub-dominant mode (green line) in Fig. 5.4b, is stronger oscillatory and tilted which results in a reduced contribution.

For the first sub-dominant mode B_1 of the ITG in the standard region, we find a

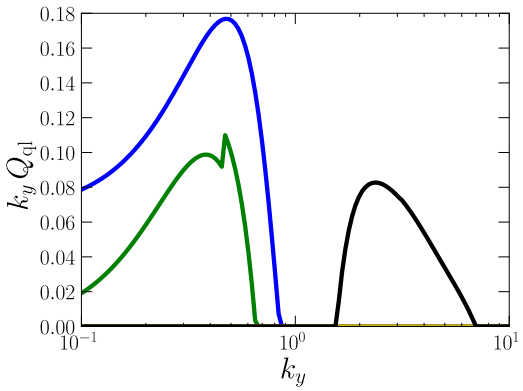

(a) *Quasi-linear heat flux contribution for the unstable part of each branch.*

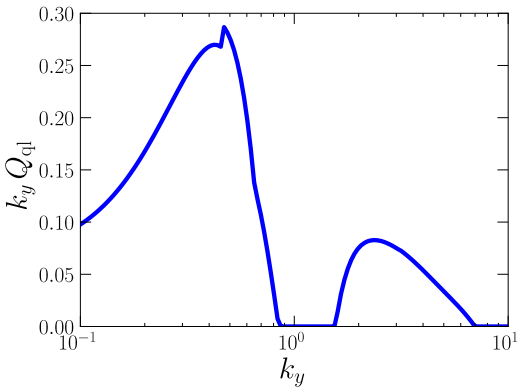

(b) *Total quasi-linear heat flux*

Figure 5.8.: *Quasi-linear heat flux contributions of the ITG mode with $\eta_i = 5$ and $\hat{s} = 0.2$. Left figure shows the separated contributions of each unstable part of the branches. The dominating contributions is from the dominant ITG mode. With the first sub-dominant and the short-wavelength region having are equally contributing. The sub-dominant mode shows a discontinuity due to symmetry change. Right figure shows the summed contributions per k_y, the standard region contributes majority to quasi-linear heat flux.*

discontinuity in the quasi-linear heat transport estimates at around $k_y \sim 0.45$. As the growth rates are smooth, the discontinuity can only be explained in a sudden change of the corresponding mode structure. Indeed, we confirm that the mode structure of B_2 changes at the discontinuity from an anti-symmetric mode structure at $k_y = 0.45$, see Fig. 5.9a, into a symmetric mode structure, see Fig. 5.9b. at $k_y = 0.47$. We ruled out that this rather surprising results originates from a failed converges of the inverse iteration algorithm to extract the mode structure, as the eigenvalue was obtained to a very good accuracy and while both growth rates of B_1 and B_2 are same, their real frequency part is clearly different. However, this result needs to be verified by running gkc++ as an eigenproblem solver as described in Sec. 3.1.7.

The contribution from the short-wavelength region to the heat flux is found to be similar to the contribution from the first sub-dominant mode in the standard region. Although the mode structure at the short-wavelength region is narrow and k_y large suggesting small contributions, it is destabilized over a wide region. Because of that its integrated contribution is comparable to the contribution of the first sub-dominant mode B_1. The total heat flux over all unstable branches is shown in Fig. 5.8a. We find that the majority of the heat flux ($\sim 85\%$) is transported by the standard-ITG mode due to the combined contributions of both unstable branches at the std-ITG region. Compared to that, the short-wavelength contributions are rather small but still substantial.

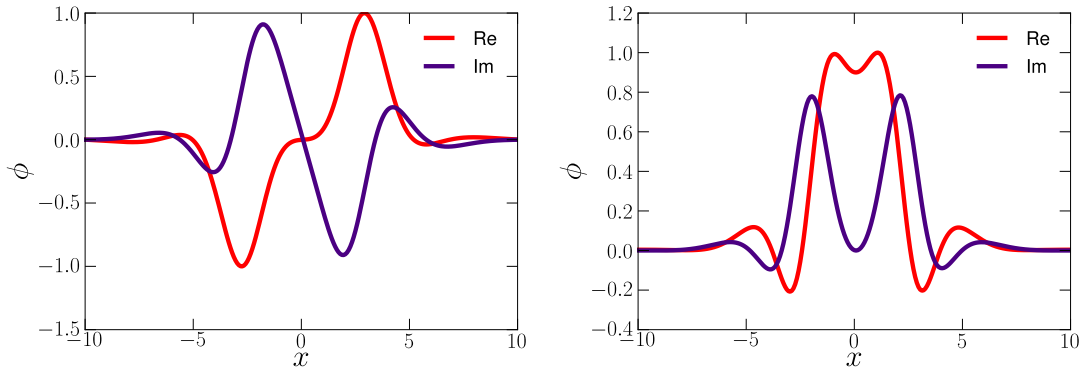

(a) *Mode structure of* B_2 *at* $k_y = 0.45$ **(b)** *Mode structure of* B_2 *at* $k_y = 0.47$

Figure 5.9.: *Eigenmode structure of the first sub-dominant branch* B_2 *in the standard ITG region. At* $k_y \sim 0.5$*, the eigenmode structure of the electrostatic potential changes its symmetry from an anti-symmetric mode structure (left figure) to a mirror-symmetric mode structure (right figure). This results in the discontinuity observed in the quasi-linear heat flux estimates.*

5.2 | The electron temperature gradient mode

The electron temperature gradient is a microscale instability at the order of the electron gyro-radius ρ_e. It contribution to the anomalous heat flux obtained by quasi-linear estimates, see Sec. 5.1.6, is by $\sqrt{m_{ie}} = \sqrt{m_i/m_e} \sim 40$ smaller than the contribution from the ITG. However, Jenko et al. (2000) found by nonlinear gyrokinetic simulations that the ETG may also substantially contribute to the heat flux by developing *streamer like* structures (elongated vortexes), and increasing the heat flux to comparable values as those from the ITG. However, as experimentalists are not able to resolve the electron scale, this finding can not be verified yet.

5.2.1 | Adiabatic ion response

As in Sec. 5.1.1, we seek a scale separation between the ions and electrons through an adiabatic approximation to simplify analysis and simulations. Poisson's equation (2.56) for a plasma consisting of ions and electrons, $\sigma = \{i, e\}$ is given by

$$\lambda_D^2 k_\perp^2 \phi + \sum_\sigma \left(1 - \Gamma_0(b_\sigma)\right) \phi = \sum_\sigma \pi B_0 \int_{\mu=0}^{\infty} \int_{v_\parallel=-\infty}^{\infty} J_0(\lambda_\sigma)\, g_\sigma \, \mathrm{d}v_\parallel \, \mathrm{d}\mu \quad . \tag{5.6}$$

Here, we focus on the evolution of ETG, so that the spatial scale length of interest is of the order of the electron gyro-radius $(x_{\mathrm{ref}}, y_{\mathrm{ref}}) \sim (\rho_e, \rho_e)$. As the mass of the ions is over an order of magnitude larger than the mass of the electrons ($m_{ie} \gg 1$), the ion contribution at the left-hand side of Eq.(5.6) gives $1 - \Gamma_0(b_i) \sim 1$. As $\lambda_i \gg 1$ results in

$J(\lambda_i) \ll 1$, the ion contribution at the right-hand side can be neglected. The simplified Poisson's equation for a investigation of the ETG with adiabatic electrons (ETG-ai) is given by

$$\lambda_D^2 k_\perp^2 \phi + (1 - \Gamma_0(b_e))\,\phi \underbrace{+\phi}_{\text{adiabatic ions}} = \pi B_0 \int_{\mu=0}^{\infty} \int_{v_\parallel=-\infty}^{\infty} J_0(\lambda_e)\, g_e \,\mathrm{d}v_\parallel \,\mathrm{d}\mu \quad , \tag{5.7}$$

where we assumed $T_i = T_e = 1$. In the Poisson's equation, the ion distribution function does not appear anymore reducing the computation time. As the evolution of the ions can be considered slow on time-scales relevant for the electron dynamics, the flux surface averaging term, which is included for the ITG-ae, is not required for the ETG-ai.

We note however that in the linear case, there is no zonal flow generation and thus the flux surface averaging term $\langle\phi\rangle_{FS}$ gives no contributions, such that in the linear case, the equation-system for the ITG-ae and the ETG-ai are identical up to normalization. This changes however once the flux surface averaging term becomes effective, e.g. in the nonlinear region, as the three-wave coupling of the nonlinearity condition produces a zonal-flow from coupling of a Fourier mode with its complex conjugate $k_y = k'_y - \bar{k}'_y = 0$.

5.2.2 | Debye length effects λ_{De}

Effects from a finite Debye length are usually neglected when investigating the ion species as it is orders of magnitude smaller than the ion Larmor radius ($\lambda_{De} \ll \rho_i$). This not necessary holds true when investigating the electrons temperature gradient instabilities, as for a realistic Tokamak plasma, the Debye length λ_{De} is of the order of the electron Larmor radius $\lambda_{De} \sim \rho_e$, as discussed in Wesson and Campbell (2004). The parameter scan over the Debye length parameter λ_{De} is shown in Fig. 5.10. Increasing the Debye length is found to have a strong damping effect on the short-wavelength region of the ETG, while the standard region is practically not influenced. This confirms the findings of Zhe (2004).

5.3 | Nonlinear study of the ETG instability

We extend our analysis by including the $\mathbf{E} \times \mathbf{B}$ nonlinearity in the right-hand side of the Vlasov equation and solving the gyrokinetic equation system as an initial value problem using gkc++ . For an initial study, we use the following parameters: a magnetic shear of $\hat{s} = 0.4$ and an electron temperature gradient of $\eta_e = 5$ with adiabatic ions. Random noise is used as an initial perturbation $f_1 \propto 10^{-7} r f_0$ with r uniformly distributed in $[-1, 1]$, to perturb all finite modes excluding the zonal flow component. The time evolution of the mode power of the electrostatic potential ϕ over time is shown in Fig. 5.11a. The corresponding instantaneous growth rates are also shown in Fig. 5.11b, where a

Figure 5.10: *ETG growth rate of the most unstable branch over λ_{De} and k_y using $\eta_e = 6$ and $\hat{s} = 0.2$. A small Debye length of $\lambda_{De} \sim 0.1$ has effectively no effect on the growth rate of the standard-ETG and short-wavelength region. Increasing the λ_{De} has practically no influence on the standard ETG region, however, the short-wavelength region is strongly damped and suppressed for $\lambda_{De} \gtrsim 0.2$.*

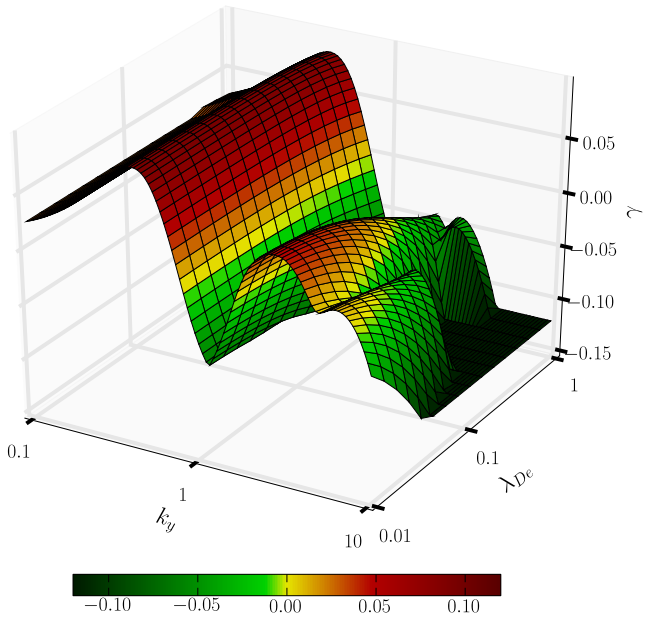

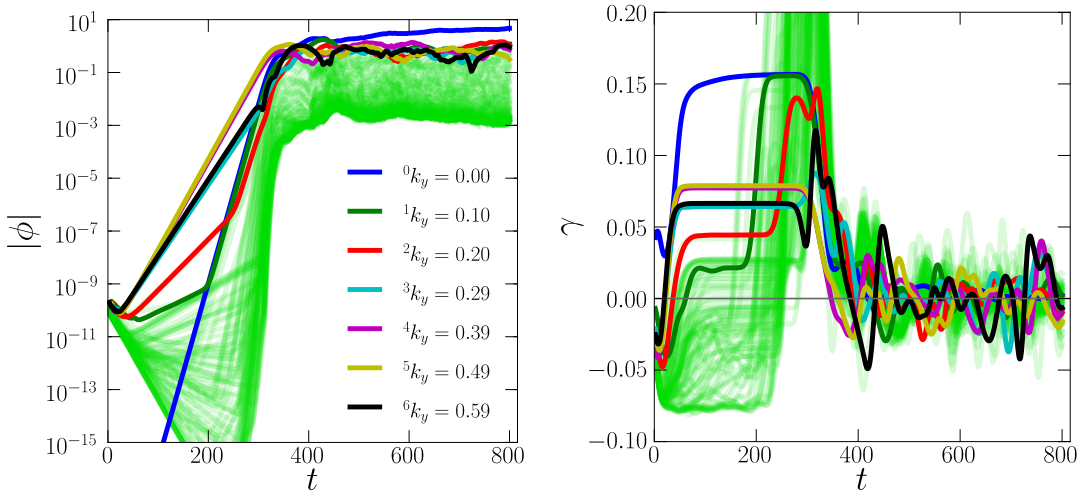

(a) *Time Evolution of Modes* **(b)** *Instant growth rates*

Figure 5.11.: *The time evolution of the electrostatic potential ϕ is shown in the left figure and the right figure shows the corresponding instantaneous growth rates. The first seven poloidal modes are shown using thick lines while larger modes are shown as thin green for better readability. We can distinguish four phases: initial, linear, saturation, and turbulent.*

convolution with a Gaussian kernel was applied to smooth out the high frequency oscillations in order to give a better picture of the time evolution. We can distinguish four phases: *initial*, *linear*, *saturation*, and *turbulence*. The random initial perturbation perturbs unstable eigenmodes as well as sub-dominant eigenmodes. A small collisionality of $\beta_c = 2 \times 10^{-3}$ was included, such that some of the stable eigenmodes can also be resolved. The initial phase is mainly determined from the initial perturbation and the evolution of individual eigenmodes (in velocity space). The electrostatic potential at time $t = 10$ is shown in Fig. 5.12a, which is dominated by the initial random noise perturbation. After the initial phase, $t \gtrsim 20$, the most unstable eigenmodes are dominating and show exponential growth. The time between $20 \leq t \leq 300$ is the so-called linear phase, which is dominated by the most unstable modes. Here, we found that the $m = 4$ and $m = 3$ modes have very similar growth rates, thus the electrostatic potential shows an interference pattern as shown in Fig. 5.12b. Even during the linear phase, the nonlinear Poisson bracket transfers energy to more stable modes, however, first it has negligible effect on the energy transferring mode. Once the energy transfer rates become large enough saturation state sets it. In the saturation phase, around $t > 280$, with an electrostatic potential shown in Fig. 5.12c the nonlinear term becomes important, redistributing the energy to stable modes which get nonlinearly excited exhibiting an exponential growth rate that exceeds the one of the linearly most unstable modes. Also the *zonal flow* mode raises quickly. In the turbulent phase ($t \gtrsim 500$), shown in Fig. 5.12d, the turbulence is fully developed with an energy cascade and a quasi-steady state is reached[1].

In Fig. 5.12d we see elongated electrostatic fields in the poloidal direction. These are the zonal flows (defined by $\phi(k_y = 0)$) and can only be generated through triad mode coupling, either nonlinearly through the Poisson bracket or linearly through e.g. a magnetic island as discussed in Ch. 6. These *zonal flows*, described in more detail by Diamond et al. (2005), are crucial for the turbulence study as they may reduce heat transport by "regulating the turbulence".

5.3.1 | Convergence test on the heat flux

In order to study the ETG, we perform a convergence scan over the discretized dimensions $(x, y, v_\parallel, \mu)$. Our base case is $N_x = 256, N_y = 64, N_v = 64, N_\mu = 8$. Convergence is estimated by analyzing the electron heat flux χ_e, which is calculated from Eq.(2.73). In the nonlinear case, the heat flux is stochastically fluctuating around a quasi-steady state such that only the mean value can be given with errors bars showing the standard deviation. The result of the convergence scan is shown in Fig. 5.13. For the velocity space variables, we find that a surprisingly low resolution is sufficient to resolve the dynamics,

[1] Strictly speaking, in the two-dimensional shear slab geometry, which has neither heat inflow or outflow, no quasi-steady state is reached and thus all nonlinear results presented here should be taken with care

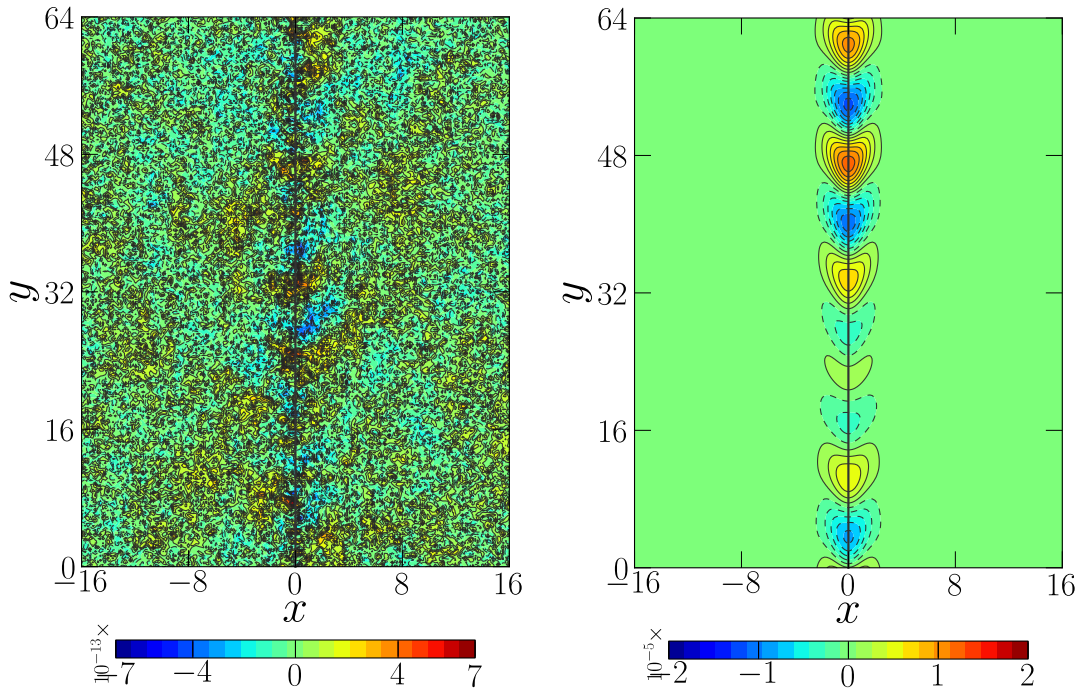

(a) $t = 10$

(b) $t = 250$

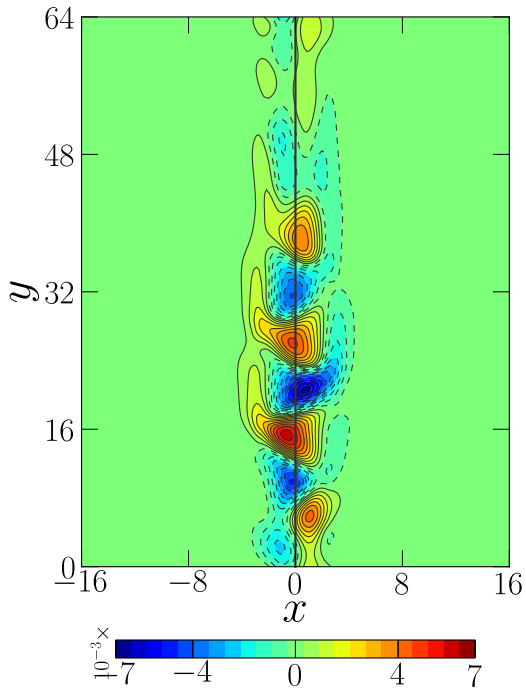

(c) $t = 375$

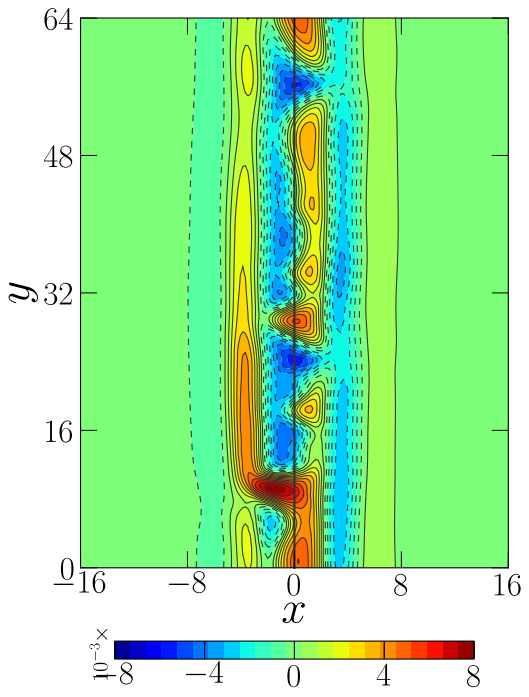

(d) $t = 800$

Figure 5.12.: *Contour plots of the electrostatic potential at* $t = 10,\ 250,\ 375\ 800$. *Physical parameters are given by* $\hat{s} = 0.4$ *and* $\eta_i = 5$. *For the linear phase shown in (b), the modes with* $m = 4$ *and* $m = 5$ *have very similar growth rates and perturbation strength, and thus we see an interference structure in the electrostatic potential.*

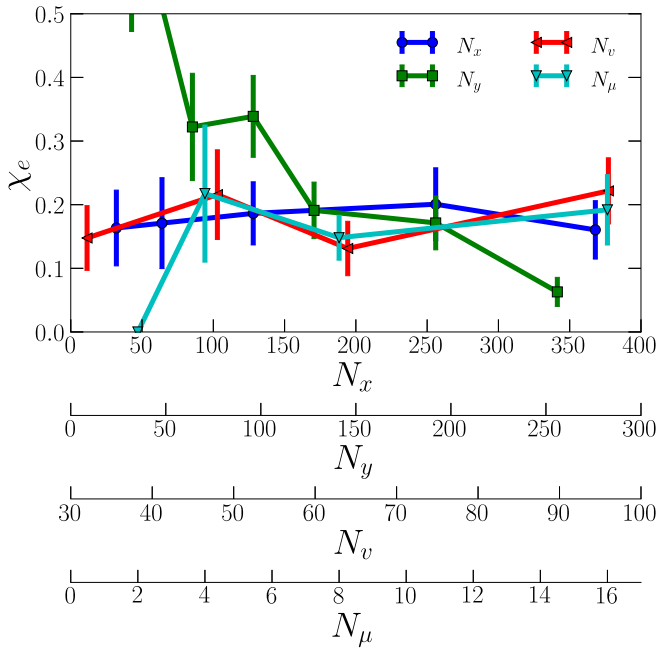

Figure 5.13: *Convergence study for the electrostatic heat flux for various resolution. Physical parameters are chosen to* $\hat{s} = 0.4$ *and* $\eta_e = 5$ *and a box size of* $(L_x, L_y, L_v, L_\mu) = (48, 64, 4, 9)$ *with a base numerical resolution of* $(N_x, N_y, N_v, N_\mu) = (256, 128, 64, 8)$*. Increases the resolution of each dimensions has only slight increase or reduction of the total heat flux thus this represents already a convergent case. The resolution in y dimensions shows to be of spatial importance as it works as a dissipation through energy cascading.* N_x *seems to be already well resolved. The value of* N_μ *can be chosen relatively low, e.g.* $N_\mu \sim 8$*, and give a well converged case.*

namely only about $N_v = 32$ discretization points in the parallel velocity dimension and only four discretization points in N_μ are necessary to give comparable results. We find that the base case chosen represents a well resolved case, as doubling the dimensions gives similar results.

5.4 | Nonlinear study of the ITG

Although the electron heat transport may reach levels corresponding to the ion transport, in the usual case, the ions provide the dominating heat flux contributions. In the linear case, the ITG-ae and the ETG-ai are equivalent up to normalization. In the nonlinear phase however, the flux surface averaging term becomes important which generates zonal flow, which is known to reduce heat flux through flow shearing. The electrostatic potential in the nonlinear phase for $\eta_i = 5$ and $\hat{s} = 0.2$ is shown in Fig. 5.14a, and for $\hat{s} = 0.4$ in Fig. 5.14a. Compared to the ETG-ai, we indeed find very strong zonal flow levels.

5.4.1 | Comparing heat fluxes from ETG with ITG

In Fig. 5.15 the time evolution of the heat flux is shown for $\eta_{i,e} = 5$ and $\hat{s} = 0.3$. The setup is identical except that for the ITG, we included the flux surface averaging term. The linear evolution of both cases is equivalent. After the overshooting (due to

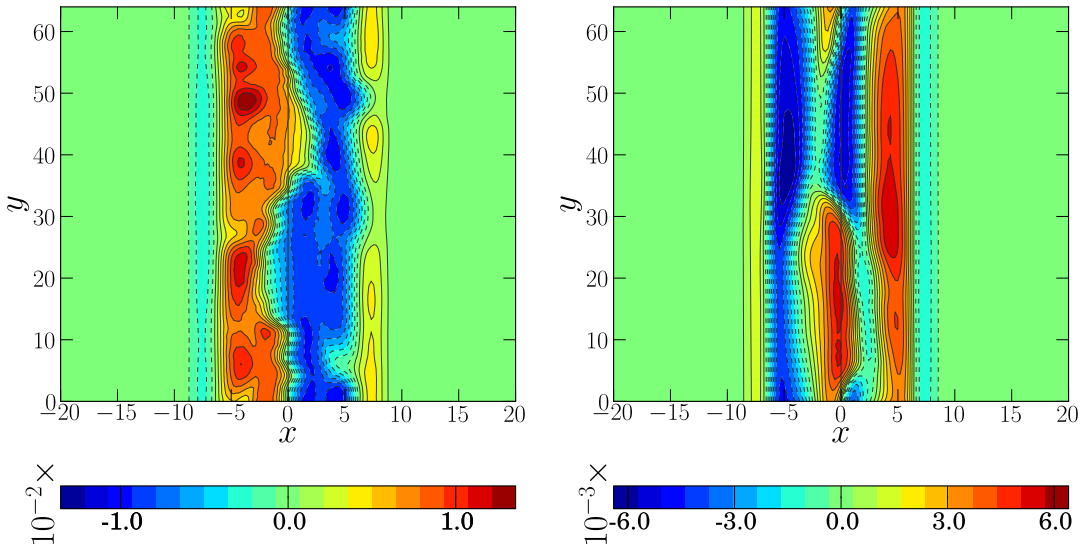

(a) $\hat{s} = 0.2$, $\eta_i = 5$ **(b)** $\hat{s} = 0.4$, $\eta_i = 5$

Figure 5.14.: *Contour plots of the electrostatic potential in quasi-steady state at* $t = 2000$ *for the ITG. Physical parameters are* $\eta_i = 5$ *and* $\hat{s} = 0.2$ *(left figure) and* $\hat{s} = 0.4$ *(right figure). We find a strong zonal flow excitation in contrast to the ETG case shown in Fig. 5.12d.*

Figure 5.15: *Heat flux* χ *for* $\eta_{e,i} = 5$ *and* $\hat{s} = 0.3$. *The heat flux shows a strong overshooting until it stabilizes around* $t = 1500$ *to a quasi-steady-state level. The heat flux of the ETG-ai is usually larger than from ITG-ae, as the zonal flow generation is larger for the ITG, which reduced turbulent transport through flow shearing.*

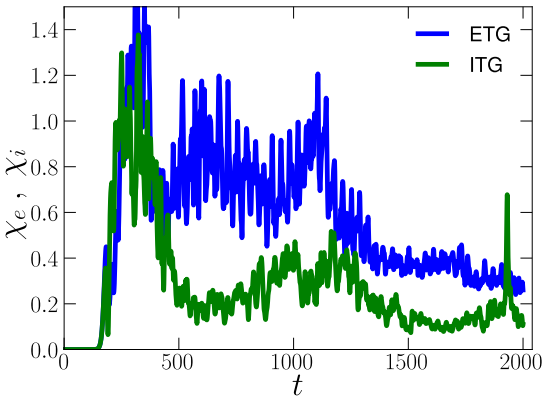

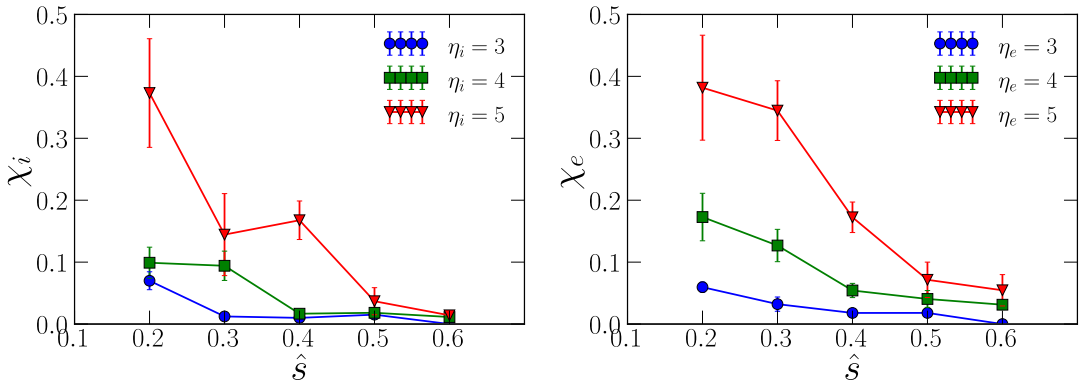

(a) *Heat flux vs. η_i and $\hat{s}$ (ITG)* **(b)** *Heat flux vs. η_e and $\hat{s}$ (ETG)*

Figure 5.16.: *Time evolution of the heat flux χ vs magnetic shear $\hat{s}$ for ITG-ae (left figure) and ETG-ai (right figure). In the nonlinear region, the heat flux reaches a quasi steady-state. Using a least-square fit, the averaged heat fluxes are estimated, where the error bars show the corresponding standard deviations.*

parametric decay) at $t \sim 400$, saturation sets in where the ITG develops an increased zonal flow, which reduces the heat flux due to shear flow to about half of the value of the ETG case. In Fig. 5.16a, we show the heat fluxes obtained for the ITG, whereas in Fig. 5.16b, the heat flux obtained for the ETG, vs the magnetic shear and temperature gradient. We find that increasing the magnetic shear reduces the heat flux independently on the temperature gradient. Also in these cases, we confirm that the flux-averaging term reduces the heat flux levels due to an increased zonal flow.

5.4.2 | Short-wavelength contributions to heat flux

In our linear investigations of the ITG/ETG mode in Sec. 5.1.3, we found that the short-wavelength region has linear growth rates comparable to the standard ITG region. Although the quasi-linear heat flux estimates in Sec. 5.1.6 predicted heat flux contribution from the short-wavelength region smaller than from the standard region — it was still substantial, with contribution up to 20% of the total heat flux. Thus we perform nonlinear simulations to confirm or disproof the quasi-linear estimates. We choose $\eta_i = 5$ and $\hat{s} = 0.2, 0.4, 0.7$, where the case with $\hat{s} = 0.2$ is known to be linearly unstable in the short-wavelength region. The turbulence spectra is shown in Fig. 5.17. The fluctuations of the electrostatic potential are mainly in the standard ITG region. For wavenumbers $k_y > 1$, we have a strong damping of the fluctuations so we may assume that the heat flux contributions for $k_y > 1$ are small. To further confirm this assumption we show the time averaged heat flux spectra in Fig. 5.18 and found that the contributions from the short-wavelength ITG region are indeed negligible. These results suggests that the

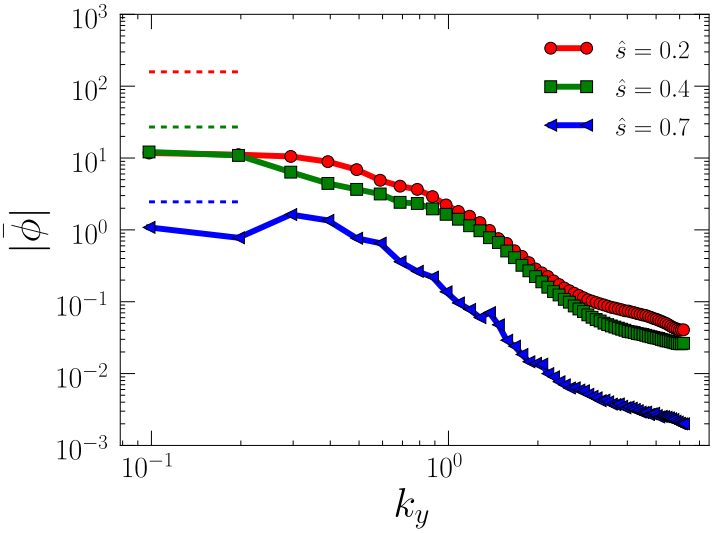

Figure 5.17: *Averaged turbulence spectra (of ϕ) for the ITG between $t = 1000-2000$. Physical parameters are $\eta_i = 5$ and $\hat{s} = 0.2, 0.4, 0.7$. The dashed line corresponds to the zonal flow level. A high zonal flow level is found that exceeds the level of other modes. No significant peak is found where the short-wavelength modes are linearly unstable. For $k_y > 3$ a flattening is found which can be attributed to the remaining aliasing originating from the nonlinear term.*

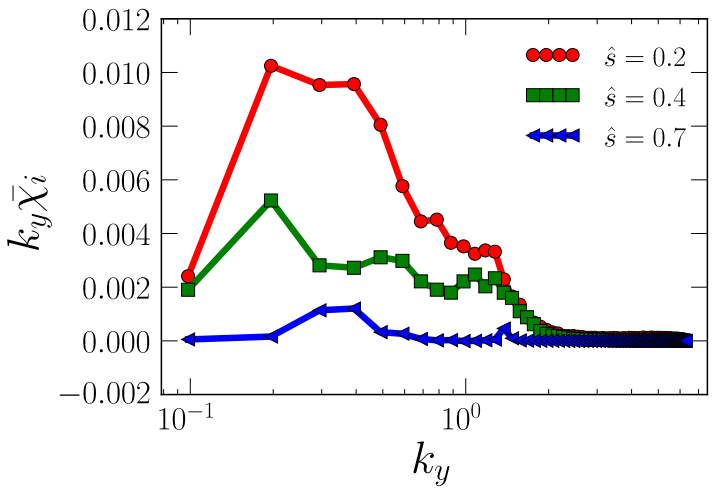

Figure 5.18: *Averaged heat transport vs poloidal mode k_y between $t = 1000 - 2000$. The area between the curves corresponds to the corresponding heat flux contributions. The main heat transport occurs mainly from $k_y < 1$, which can be attributed to the standard ITG mode. The transport through the short-wavelength region for $\hat{s} = 0.2$, for which quasi-linear estimated predicts contributions between $1.5 \leq k_y \leq 8$, is negligible.*

ITG modes at the short-wavelength region are stabilized — where the most likely mechanism would be through shear flows generated from the zonal flows as discussed by Gao et al. (2004). Recently, Chowdhury et al. (2012) also found no substantial heat flux contributions from the ITG in the short-wavelength region in the toroidal configuration.

5.5 | The ITG with kinetic Electrons (linear case)

Including a kinetic electron species does increase the computational cost substantially, when solved as an initial value problem, as not only an additional species has to be advanced, but also the computational time step is significantly reduced by a factor of $\sqrt{m_{ie}}$ in order to guarantee numerical stability. For the linear study, we first use the integral code developed to solve the dispersion relation, as it allows us to extract the linear properties without depending on the choice of a time step.

5.5.1 | Parameter scan over m_{ie}

In numerical simulations, it is advantageous to reduce the ion-electron mass ratio m_{ie} in order to increase the maximum numerically stable time step (due to the CFL condition), as the maximum parallel velocity $v_{\parallel}$ is proportional to $\sqrt{m_{ie}}$. However, we need to verify that the dynamic itself is unaffected by this procedure. In Fig. 5.19, we show the growth rates of the most unstable branch (at fixed k_y) versus the ion-electron mass ratio m_{ie}, and the poloidal wavenumber k_y for a fixed $\eta_e = 0$ and $\eta_e = 2$. For the case with $\eta_e = 0$ in Fig. 5.19a, we find that the growth rates for $m_{ie} < 800$ are sensitive to the mass ratio. For values above $m_{ie} \geq 800$ the standard region of the ITG mode is almost independent, while the stable short-wavelength region still shows a rather strong dependence on m_{ie}; even for an hydrogen-electron mass ratio of $m_{ie} = 1836$. For the case of a non-zero electron temperature gradient $\eta_e = 2$ as shown in Fig. 5.19b, we find that the std-ITG mode as well as the shw-ITG mode only exhibits a weak sensitivity once the ion-electron mass ratio exceeds $m_{ie} \gtrsim 800$. A similar behaviour is found for an electron temperature gradient of $\eta_e = 5$.

For a fixed poloidal mode $k_y = 0.3$, and a fixed ion temperature gradient of $\eta_i = 5$, we investigate the growth rates of the most unstable branch (at fixed k_y) over various m_{ie} and $\eta_e = 0, 2, 5, 7$. From Fig. 5.20a, we can confirm that with increasing mass ratios, the growth rates with kinetic electrons converge to the case with adiabatic electrons. However, convergence is reached only for unrealistically large mass ratios, i.e. $m_{ie} > 10^5$. The reason is probably the resonance effect from the kinetic electrons at the rational surface shown in Fig. 5.20b, where a strong peaking of the eigenfunction is found even for mass ratios of $m_{ie} = 2000$ and $\eta_e = 0$.

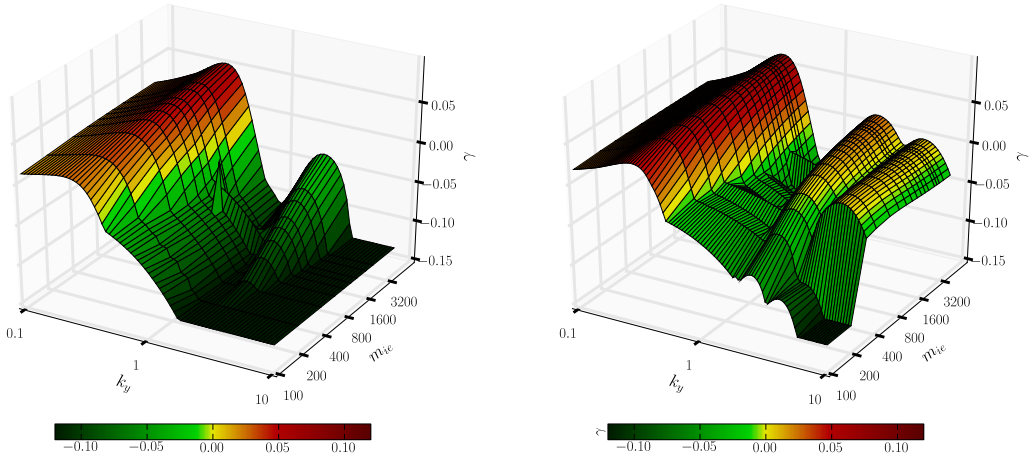

(a) $\eta_e = 0$ **(b)** $\eta_e = 2$

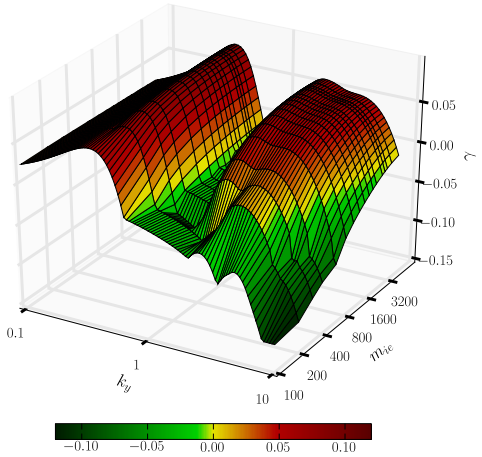

(c) $\eta_e = 5$

Figure 5.19.: *Linear growth rates of the most unstable branch of the ITG mode over k_y and m_{ie} for $\eta_e = 0$, $\eta_e = 2$, and $\eta_e = 5$ for $\eta_i = 5$ and $\hat{s} = 0.4$. The growth rate of the standard region converges for an ion-electron mass ratio of $m_{ie} = 500$ to acceptable values. The electron temperature has a strong influence on the ITG mode itself, namely a larger η_e destabilizes the ITG, moderately for the standard ITG region, strongly for the short-wavelength ITG region. For example, while the short-wavelength region is completely suppressed for $\eta_e = 0$, it becomes unstable once $\eta_e \leq 2$ and reaches for $\eta_e \sim 5$ linear growth rates comparable to the adiabatic case.*

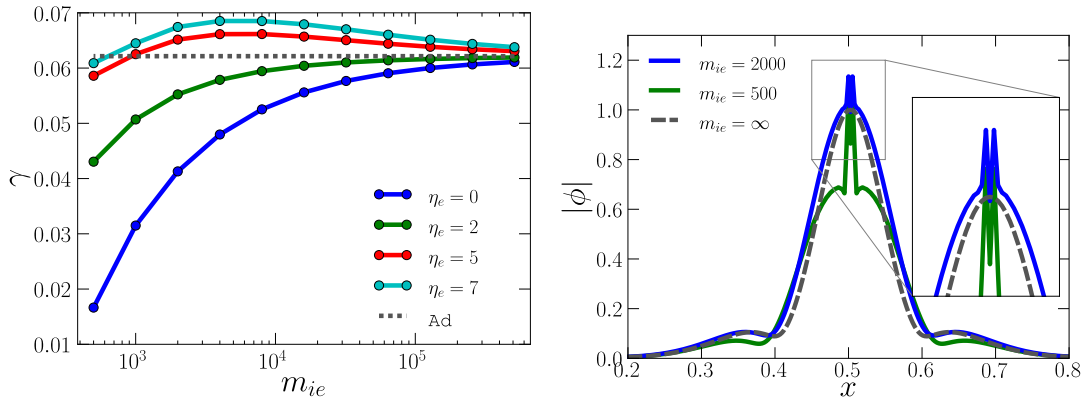

(a) *Growth rates vs ion-electron mass ratio* **(b)** *Eigenfunctions for* $\eta_e = 0$

Figure 5.20.: *(Left figure) Linear growth rates of the most unstable branch at* $k_y = 0.3$ *and* $\eta_i = 5$ *for different ion-electron mass ratios. A convergent case to the adiabatic solution is only found for very large mass ratios. The resonance at the rational surface for the electrons seems to be responsible for this reduction of the growth rate as can bee seen by the peaking of the eigenfunctions.*

5.5.2 | Parameter scan over η_e

Here, we investigate the linear growth rates for a varying electron temperature gradient η_e and a fixed ion temperature gradient of $\eta_i = 5$. The result of this parameter scan is shown in Fig. 5.21. The peak growth rate in the standard ITG region at $k_y\rho_i \sim 0.5$ is only weakly sensitive to the electron temperature gradient. Namely, a larger η_e does destabilize the ITG mode for both: the standard ITG region and the short-wavelength region. We speculate that this difference originates from the resonance discussed in the previous section, which weakens for increasing η_e. For example, in Fig. 5.21 we see that for $\eta_e = 2$, the ITG growth rate at $k_y\rho_i = 0.5$ is already similar to the adiabatic electron case, while for small η_e the short-wavelength region is stable. Destabilization arises once the electron temperature gradient exceeds $\eta_e \gtrsim 2$. However, it remains to be checked if this statement holds when the mass of the kinetic electrons approaches zero, i.e., $m_{ie} \to \infty$. We can assume that for $m_{ie} \to \infty$, the growth rates of the ITG in the shw-region will also converge to the adiabatic case; as the std-region did in Fig. 5.20a — but that remains to be checked.

5.6 | The ITG with kinetic Electrons (nonlinear case)

Here, we briefly study the nonlinear properties of the ITG turbulence including kinetic electrons. The advantage of including kinetic electrons is that the flux surface averaging effect is self-consistently included. Also, in contrast to the adiabatic electron case —

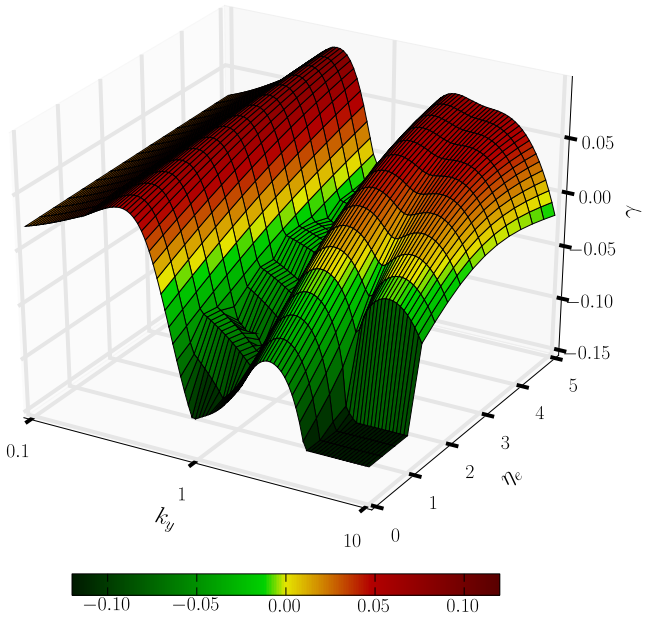

Figure 5.21: *Maximum linear growth rates over k_y and η_e for an ITG drift-wave with $m_{ie} = 1836$ using $\eta_i = 5$. For $\eta_e = 0$ the growth rate of the std-region of the ITG is slightly reduced, while the shw-region is completely stabilized. For $\eta_e = 2$ also the shw-region is destabilized, however, growth rates comparable to the adiabatic case are not reached until η_e increases to $\eta \gtrsim 5$. We note that around $k_y \sim 10$ the shw-part of the ITG and the std-ETG mode will coexist. The possibility of an interaction still needs to be verified.*

where no ion particle flux can be observed as the density perturbation is always out-of-phase by $\pi/2$ with the electrostatic potential — in the kinetic electron case, particle fluxes can be observed for both, the ions and electrons.

5.6.1 | Parameter scan over m_{ie}

The scaling over the ion-electron mass ratio is shown in Fig. 5.22. Note that compared to the adiabatic case, higher heat fluxes are observed. An increased ion-electron mass ratio will effect the zonal flow production as a higher electron mass lowers its thermal velocity and thus the flux surface averaging effect, which increases the zonal flow production, is reduced. Here, we find that for $m_{ie} > 400$, heat fluxes seem to converge. The difference between $m_{ie} = 500$ and a realistic ion mass ratio $m_{ie} = 1837$ is of the order of. $\chi_{i,m_{ie}=1837}/\chi_{i,m_{ie}=500} = 1.1$.

In Fig. 5.23, the ratio of the zonal flow energy ϕ_{ZF} over turbulence energy ϕ_T is shown for different values of m_{ie}. The dashed lines represents the value obtained from the adiabatic case. We can confirm that the zonal flow energy in the case of kinetic electrons is reduced, however, we do not find convergence to the adiabatic case when increasing m_{ie}, as is found by Ishizawa et al. (2011) in local slab geometry, which we conclude to be an effect of the deficiency of the two-dimensional sheared slab geometry.

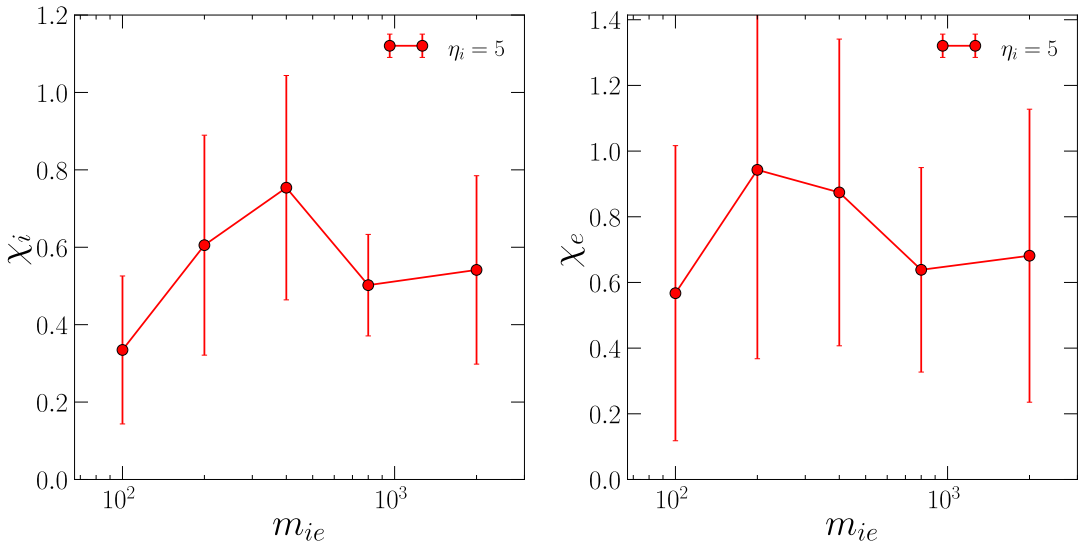

(a) χ_i *over* m_{ie} **(b)** χ_e *over* m_{ie}

Figure 5.22.: *Ion heat flux* χ_i *and electron heat flux* χ_e *over the ion-electron mass ratio* m_{ie} *for* $\eta_i = 5$, $\eta_e = 2$ *and* $\hat{s} = 0.4$. *Convergence is reached for* $m_{ie} \geq 400$, *where the heat flux differences are within the statistical error. Collisionality is chosen to* $\beta_{c,i} = \beta_{c,e} = 5 \times 10^{-4}$.

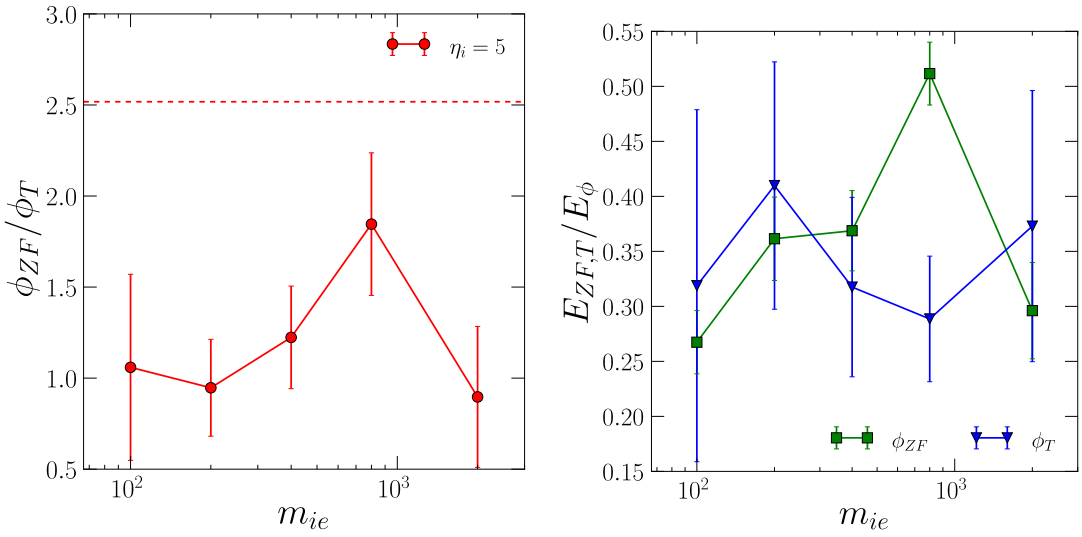

(a) *Turbulence energy over zonal flow energy* **(b)** *Energy in zonal flow and turbulence*

Figure 5.23.: *Ratio of zonal flow energy* ϕ_{ZF} *over turbulence energy* ϕ_t *for different ion-electron mass ratio* m_{ie}. *Higher mass ratio increases zonal flow production from the flux surface averaging. The dashed line in the left figure corresponds to the ratio obtained with adiabatic electrons.*

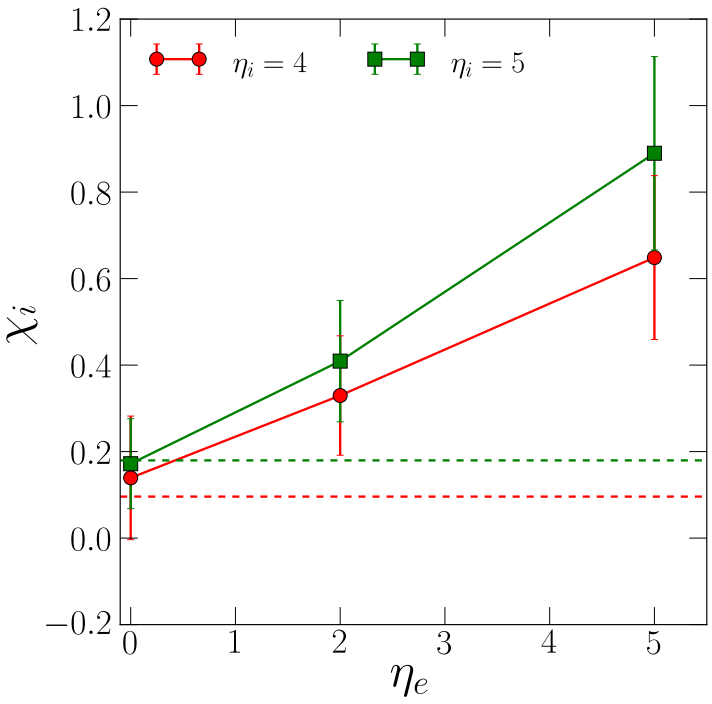

Figure 5.24: *Comparison of the nonlinear heat fluxes with kinetic electrons for* $m_{ie} = 500$ *over* η_e *for the cases with* $\eta_i = 4$ *and* $\eta_i = 5$. *The dashes lines corresponds to the adiabatic case. We find that for* $\eta_e = 0$, *ion heat fluxes are comparable to the adiabatic case. For* $\eta_e > 0$ *heat flux increases.*

5.6.2 | Parameter scan over η_e

We study dependence of the heat flux on the electron temperature gradient. An initial random noise perturbation is set $f_{1\sigma} \propto 10^{-7}$ and the simulation is evolved up to $t_{max} = 800$. For the set of ion temperature gradients $\eta_i = 5$ and $\eta_i = 4$ and various η_e, the ion heat flux χ_i is shown in Fig. 5.24. Heat fluxes obtained with adiabatic electrons are shown using dashed lines. For $\eta_e = 0$, we find ion heat fluxes comparable to the adiabatic case. For $\eta_e = 2$, however, the ion heat flux is already about twice as large as that of the adiabatic case. Increasing to $\eta_e = 5$, we find that the heat fluxes obtained using kinetic electrons once again strongly increase. This increase in heat flux for kinetic electrons may be attributed to the increased linear growth rates as shown in Fig. 5.20a, as well to the reduced zonal flow production.

5.6.3 | Large scale run

To investigate the kinetics of the electrons, we perform a high-resolution simulation, where both, the ion (length) scale and part of the electron (length) scale is resolved. Both, the ITG and the ETG are unstable for temperature gradients of $\eta_i = 5$ and $\eta_e = 5$, respectively. The simulation time extends up to $t_{\max} = 500$, where numerical parameters are chosen to $N_{x,y,v_\parallel,\mu} = (387, 256, 64, 8)$, $L_{x,y,v_\parallel,\mu} = (42, 64, 4, 9)$, and a magnetic shear

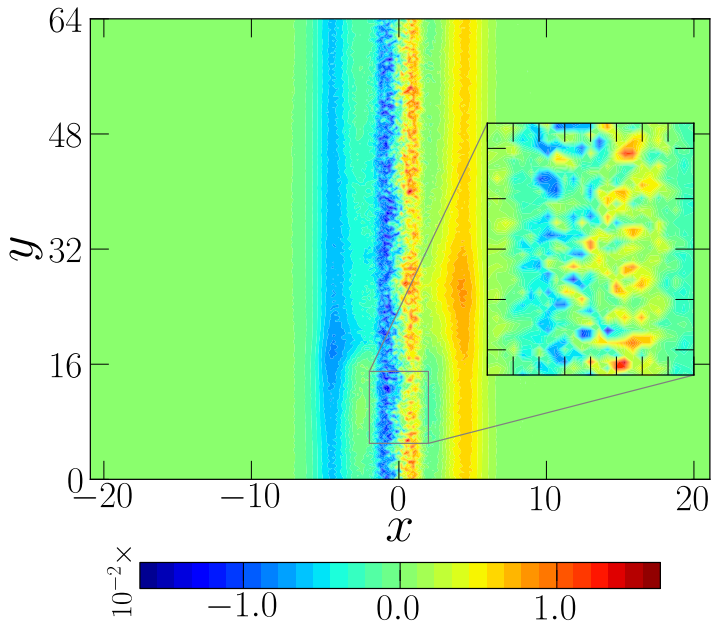

Figure 5.25: *Contour plot of the electrostatic potential at $T = 800$. Resolution is chosen high enough to resolve the electron scale. The ITG dynamics dominants the large scale fluctuations, however, close to the rational surface we find profound small-scale turbulences arising from the electron-dynamics which is shown in the zoom inset plot (a high-pass filter was applied to remove the large-scale fluctuations).*

of $\hat{s} = 0.4$. The ion-electron mass ratio is set to $m_{ie} = 500$. The contour plot at $t = 800$ is shown in Fig. 5.25. Additional to the large-scale fluctuations, we find substantial small-scale fluctuations, which are shown using the zoom inset window. The small-scale contributions are also visible in the turbulence spectra shown in Fig. 5.26 for the kinetic simulation in (a), and in (b) for the corresponding adiabatic simulation for comparison. The kinetic simulation shows a shallow slope $k_{\text{kin}} \propto -0.7$ for the turbulence spectra, compared to the adiabatic case, which in contrast has a very steep slope $k_{\text{ad}} \propto -3.3$. The difference in the slopes between adiabatic simulation and kinetic simulation indicated that saturation through zonal flows and cascading is changed one kinetic electrons are included and η_e is large enough so that the ETG is excited.

5.7 | Summary

Linear properties of the ion and electron drift waves were studied by solving the dispersion relation given as a nonlinear eigenvalue problem. Assuming adiabatic electrons, we found that the ion temperature gradient in sheared slab geometry includes many unstable branches, some of which are even unstable for large wavenumbers, the so-called short-wavelength ITG modes. We found that the short-wavelength ITG modes are linear unstable over a wide parameter region. A vast amount of parameter scans were performed to investigate the destabilization properties. Further, we extended our analysis to investigate the case with kinetic electrons, which included two additional parameters:

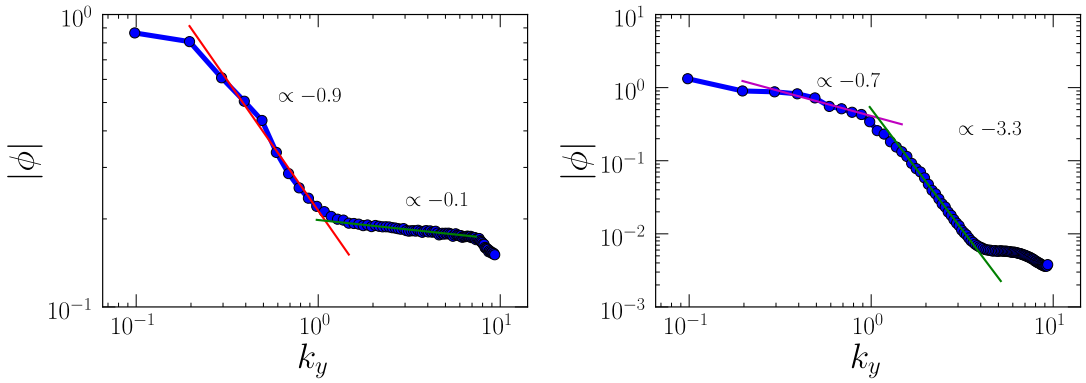

(a) *ITG-ke ($\eta_e = 5$)* **(b)** *ITG-ae*

Figure 5.26.: *Turbulence spectra, kinetic electrons leads to flattening of the turbulence profile for $\eta_i = 5$ and $\eta_e = 5$, showing clear electron kinematics.*

the electron temperature gradient and the ion-electron mass ratio. We could confirm the short-wavelength destabilization of the ITG also in the kinetic case and defined its parameter dependence. We investigated the nonlinear properties of the adiabatic ETG and ITG turbulence using the gkc++ code. Although the ETG and ITG mode are equivalent in the linear region, the electron dynamics in the ITG leads to a short-circuit of the flux surface and thus to an increase zonal flow production rate resulting in a reduced heat flux. Further, we extended our nonlinear analysis to include also kinetic electrons. We found that the ion heat flux strongly depends on the electron temperature gradient. Namely a higher electron temperature gradient resulted in an increased ion heat flux.

6 | The ITG mode in presence of a static magnetic island

Apart from microinstabilities, there are several instabilities on the machine size scale, such as the magneto-hydrodynamic (MHD) instabilities. These instabilities can be roughly categorized into *ideal MHD instabilities*, such as sausage and kink instabilities, and *resistive MHD instabilities*, such as tearing modes. In ideal MHD, the topology of the magnetic field is preserved due to *frozen-in condition* condition, however in resistive MHD, *magnetic reconnection* is capable of modifying the magnetic field topology enabling the access of lower energy states, see e.g. White (1986). The resistive MHD instabilities include the tearing instabilities such as *magnetic islands*, which study and understanding of magnetic islands is crucial for achieving a successful magnetic confinement of the plasma.

During the formation of the magnetic islands, ITG turbulence is usually present — thus this chapter is devoted to study the influence of a magnetic island on the ITG turbulence.

6.1 | Basic properties of magnetic islands

Furth et al. (1963) found that tearing modes are driven by magnetic free energy, determined by the shape of the equilibrium current profile which leads first to a filamentation of the current sheet and finally to the formation of magnetic islands. These magnetic islands preferably develop at a rational surface ($q = n/m$), where a small perturbation of the equilibrium magnetic field connects to itself after n poloidal turns leading to a self-amplification. A simplified sketch of a magnetic island is shown in Fig. 6.1. The *separatrix* (dashed line) separates the inner *closed flux surfaces* from the outer flux surfaces. As Hazeltine and Strauss (1976) argues, magnetic islands form an own set of nested and closed flux surfaces, which extend in radial direction allowing particles to quickly cross them. This leads not only to a *temperature flattening* but also to an increase of particle and heat fluxes. As measured by Isayama et al. (1999) in the JT-60 Tokamak, magnetic islands can grow to substantial sizes, $w \sim 20\rho_i$, strongly reducing the confinement performance.

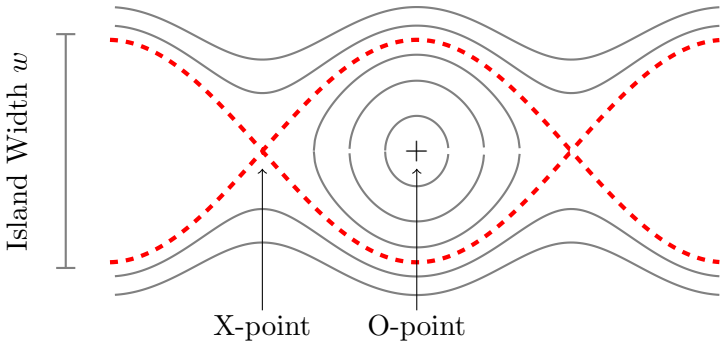

Figure 6.1: *Sketch of the flux surfaces of a magnetic island. The magnetic island changes the topology of the magnetic field, with characteristics points being the O-point, X-point and the separatrix (dashed line).*

6.1.1 | Theoretical investigations

A possible explanation for the physical mechanism of reconnection leading to magnetic island formation was suggested by Sweet (1958) and Parker (1963). The Sweet-Parker mechanism works as follows: in a region with an opposite magnetic field direction, a current sheet is formed by plasma pressure, where the magnetic field lines are diffusing into it and reconnect. This processes is self-amplifying leading to exponential growth. However, this model predicted very small reconnection rates such that Petschek (1964) refined the model by proposing a shock front at the current layer which drives into the diffusive region greatly increasing the reconnection rate.

In the slab geometry, such as investigated here, Furth et al. (1963) showed that the linear growth rates of magnetic island formation are proportional to $\gamma \propto \tau_r^{-3/5}\tau_A^{-2/5}$, where τ_R is the resistive timescale and τ_A the Alfvén timescale. Preferably, only the long-wavelengths are excited, as shorter wavelengths require a stronger bending of the magnetic field lines which is energetically less favorable. Finally, before saturation, the magnetic island first changes from an exponential growth into an algebraic growth in the quasi-linear state as described by Rutherford (1973) and then fully reconnects to a steady state — or in some cases is subject to a secondary current sheet instability may form as found by Loureiro et al. (2005).

6.2 | Numerical study of magnetic island formation

For the numerical study of the formation of magnetic islands in a two-dimensional sheared slab geometry, we will briefly introduce the *reduced MHD* equation system. After an outline of the numerical solution procedure is given, we will present numerical results.

6.2.1 | Introduction to the numerical code

At the rational surface, we can apply the resistive MHD equations in order to investigate the formation of magnetic islands. The equation system to evolve the magnetic flux ψ and the potential vorticity ω is given by

$$\partial_t \psi = -[\phi, \psi] + \eta \nabla_\perp^2 \psi \quad , \tag{6.1a}$$

$$\partial_t \omega = -[\phi, \omega] + \left[\psi, \nabla_\perp^2 \psi\right] + \nu \nabla_\perp^2 (\omega) \quad , \tag{6.1b}$$

where ψ is the magnetic flux, $\omega = \nabla_\perp^2 \phi$ is the potential vorticity, and ϕ is the kinetic flow (or potential). For the derivation of the equation system, the reader is referred to Strauss (1997) and Janvier (2011). For a finite resistivity η, reconnection may occur at the rational surface which triggers the formation of a magnetic islands. Here, a viscosity term ν is included in order to enhance the numerical stability of the simulations. The viscosity ν is usually chosen small compared to the resistivity ($\nu \ll \eta$), so that its physical impact is negligible. To solve the reduced MHD equation system (6.1), the flux ψ is split into the equilibrium part ψ_0 and a perturbed part ψ_1, so that $\psi = \psi_0 + \psi_1$. No background kinetic flow is assumed, so that only the perturbed part ϕ_0 is evolved, i.e., $\phi = \phi_0$. To account for the poloidal periodicity, ϕ_0 and ψ_1 are both expanded in Fourier modes. The linear terms are advanced implicitly using a pseudo-spectral method with a second-order central-difference stencil in radial direction. The Thomas algorithm is applied for inversion in order to handle the stiffness of the equation system arising from the diffusive timescale. The nonlinearity is solved using the *triad mode matching condition* for the poloidal Fourier modes with finite differences in radial direction. Only positive poloidal modes are evolved, as both ϕ and ψ are real fields. Negative modes, which are needed in the triad mode matching condition are obtained from the complex conjugate relation. Aliasing is avoided only in poloidal direction by neglecting modes which exceeds the Nyquist limit.

6.2.2 | Simulation results

For this investigation, the grid size is chosen to $L_x = 6$ and $L_y = 6.4$, with a numerical resolution of $N_x = 4096$ and $N_y = 128$. Resistivity and viscosity are given by $\eta = 2.8 \times 10^{-4}$ and $\nu = 5 \times 10^{-5}$, respectively. A *Harris sheet* profile given by

$$\psi_0 = \frac{1}{\hat{s}} \log\left(\cosh\left(\hat{s}x\right)\right) \quad , \tag{6.2}$$

is chosen as the background magnetic flux, where $\hat{s} = 1$ is the magnetic shear at the rational surface point ($x = 0$). This setup is unstable for a random noise initial perturbation, so that the flow energy (ϕ^2) and flux energy (ψ^2) grow exponentially in time as shown in Fig. 6.2. The evolution of the poloidal Fourier modes for ϕ_0 and ψ_1 are shown in Fig. 6.3. In the linear phase, we find only the $m = 1$ mode to be unstable.

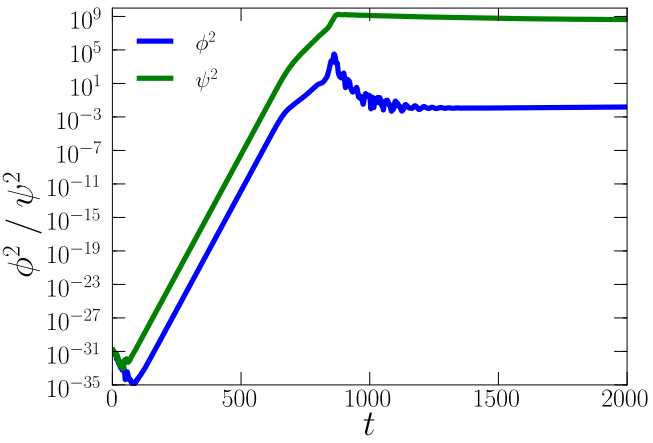

Figure 6.2: *Time evolution of flow energy ($|\phi^2|$) and flux energy ($|\psi^2|$) with an unstable setup resulting in the formation of a magnetic island. Magnetic reconnection at the rational surface is self-amplifying and thus exponential growth is observed until $t \sim 550$. Around $t \gtrsim 550$ the Rutherford regime is entered, where exponential growth is replaced by an algebraic growth. Saturation sets in at $t \sim 600$ and a full reconnection state is reached at $t \sim 1300$. Throughout the whole evolution, we observe that the magnetic flux energy is dominating over the kinetic flow energy.*

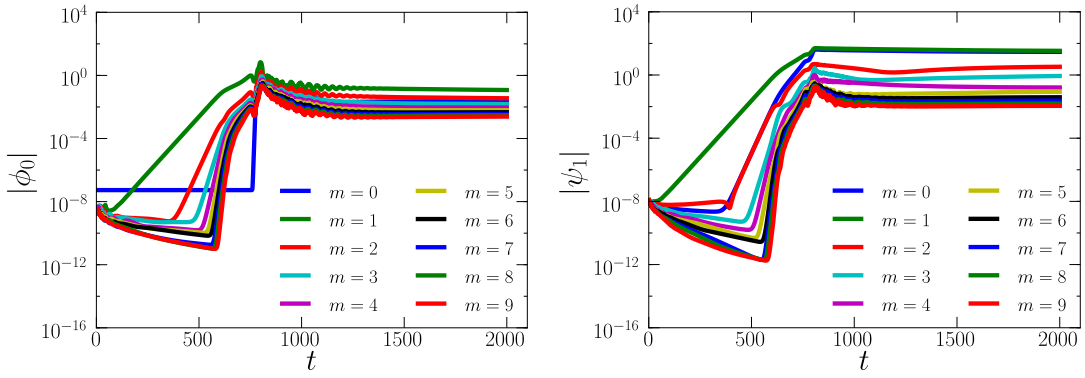

(a) ϕ **(b)** ψ

Figure 6.3.: *Time evolution of the Fourier modes of ϕ_0 and ψ_1. We find that in the linear phase, the $m = 1$ mode is the only unstable mode. The other modes are excited nonlinearly once the evolution enter the saturation phase. At the $t = 2000$, we reached the steady-state full reconnection phase.*

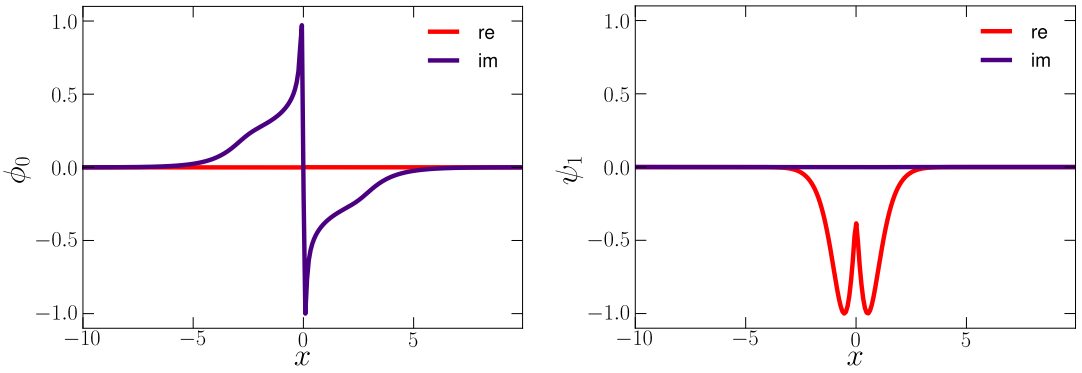

(a) *Kinetic flow eigenfunction* $\hat{\phi}_0$ **(b)** *Magnetic flux eigenfunction* $\hat{\psi}_1$

Figure 6.4.: *Linear (normalized) eigenfunction of magnetic flow* $\hat{\phi}_0$ *and magnetic flux* $\hat{\psi}_1$ *of the unstable* $m = 1$ *mode at* $t = 500$. *The magnetic flow has a strong discontinuity at the rational surface, which is also found in the first derivative of the magnetic flux. Note that without normalization, the* $\hat{\phi}_0$ *eigenfunction would be around one order of magnitude smaller than* $\hat{\psi}_1$.

Once the Rutherford regime is reached, the nonlinear term transfers energy from the unstable mode ($m = 1$) to stable modes and excites them to a finite value. Finally, full reconnection is reached for $t \gtrsim 4000$, where the magnetic island evolution shows a steady-state. The normalized eigenmode for $m = 1$ for the magnetic flow is shown in Fig. 6.4a and flux in Fig. 6.4b. Note that the magnetic flow has only an imaginary part, while the magnetic flux has only a real component. As the real frequency ($\mathrm{Re}(\omega) = 0$) is found to be always zero, this does not change throughout the simulation.

6.3 | Magnetic island influence on the ITG

Here, we study the cross-scale interaction between the ion temperature gradient and a magnetic island. For our model, we assume a static magnetic island in its linear phase, where the temperature collapse did not occur yet. In order to justify the static assumption, we compare the timescales of both instabilities. As discussed in Fig. 2.1, the magnetic island instability is governed by the resistive timescale $\tau_r \propto 1/\omega_r$, which is much slower than the timescale governing the ion temperature gradient given by the drift-frequency $\tau_{\star i} \propto 1/\omega_{\star i}$. As $\tau_r \ll \tau_{\star i}$, the magnetic island is indeed static on a timescale important for the ion temperature gradient evolution.

We note that similar setup were studied by Wang et al. (2009) in the two-dimensional shear slab geometry and by Ishizawa and Diamond (2010) in cylindrical geometry. However, in both references, a gyrofluid simulation model was used which does not include the short-wavelength mode, and as such, the effect of the short-wavelength destabiliza-

tion is yet unclear.

6.3.1 | Inclusion of static magnetic perturbation

In Sec. 2.5.1, we derived the electromagnetic gyrokinetic Vlasov equation, where the magnetic vector potential $A_{1\parallel}$ was self-consistently calculated from Ampère's equation. In order to include the magnetic island as a static perturbation of the equilibrium geometry, we prescribe a fix and time-independent $A_{1\parallel}$. The connection between the magnetic potential in gyrokinetics and magnetic flux used in the resistive MHD equations is simply given by $A_{1\parallel}(x,y) = -\psi_1(x,y)$. The magnetic flow from the island can be neglected as it is an order of magnitude smaller than the magnetic flux. The nonlinear electromagnetic Vlasov equation system in the two-dimensional sheared slab geometry is then given by,

$$\frac{\partial g_{1\sigma}}{\partial t} = -\left[1+\eta_i\left(\frac{v_\parallel^2+2\mu}{2}-\frac{3}{2}\right)\right]\frac{\partial \chi}{\partial y}f_{0\sigma} - [G_{1\sigma},\chi] - \hat{s}xv_\parallel\frac{\partial\left(\phi_1 f_0 + f_{1\sigma}\right)}{\partial y} \quad , \tag{6.3}$$

where the generalized potential $\chi = \phi + \sigma v_\parallel \psi_1$ was used and ϕ is calculated from the gyrokinetic Poisson's equation. For a static (time-independent) ψ_1, the equation simplifies to

$$\begin{aligned}\frac{\partial f_{1\sigma}}{\partial t} = &-\left[1+\eta_i\left(\frac{v_\parallel^2+2\mu}{2}-\frac{3}{2}\right)\right]\frac{\partial\left(\phi+\underline{\sigma v_\parallel\psi_1}\right)f_{0\sigma}}{\partial y} - [\phi, f_{1\sigma}] \\ &- \hat{s}xv_\parallel\frac{\partial\left(\phi_1 f_{0\sigma}+f_{1\sigma}\right)}{\partial y} - \underline{v_\parallel\sigma\left[\psi_1, f_{1\sigma}+\phi f_0\right]} \quad ,\end{aligned} \tag{6.4}$$

where the terms arising from the magnetic island are underlined. Note that we use $f_{1\sigma}$ not $g_{1\sigma}$ on the left-hand side, as loading is not performed due to our static assumption. Interestingly, we find a modification of the source term of the order $\mathcal{O}(1)$, which however, we concluded does not affect the results. We find that the static magnetic island is included through a Poisson bracket term (which in this case is linear). However, as calculating the Poisson bracket involves two Fourier transformations (back and forward); solving Eq.(6.4) is costly even for linear simulations. Thus in the next section we will directly solve the Poisson bracket for the magnetic island using the triad mode coupling condition.

6.3.2 | Expanding the ψ Poisson bracket

We found from the resistive MHD calculations that the magnetic island perturbation ψ_1 is predominately a $m = 1$ instability as shown in Fig. 6.4b. The $m = 1$ mode corresponds to a wavenumber $\bar{k} = 2\pi/L_y$, where the usual definition $k_y = 2\pi/L_y \cdot m$ is used. Thus

the magnetic island has a following poloidal dependence, as given by Euler's formula $e^{ix} = \cos(x) + i\sin(x)$, where $\psi_1(x,y)$ is pure real,

$$\psi_1(x,y) = \tilde{\psi}_1(x)\frac{1}{2}\left\{e^{i\bar{k}y} + e^{-i\bar{k}y}\right\} \quad \left[\equiv \frac{1}{2}\tilde{\psi}_1(x)\left(e^{i\bar{k}y} + \text{c.c.}\right)\right] \quad , \tag{6.5}$$

where $\psi_1(x)$ includes the radial dependence of the magnetic island and the latter part its poloidal dependence. In order to avoid calculating the nonlinear bracket term, we calculate the mode-coupling terms directly. The Poisson bracket for a general ψ_1 is given by

$$\begin{aligned}
&\left[\sum_{k'_y}\tilde{\psi}_1 e^{ik'_y y} \;,\; \sum_{k''_y}\Pi\, e^{ik''_y y}\right] \qquad (6.6)\\
&= \underbrace{\left\{\partial_x \sum_{k'_y}\tilde{\psi}_1 e^{ik'_y y}\right\}\cdot\left\{\partial_y \sum_{k''_y}\Pi\, e^{ik''_y y}\right\}}_{T_1} - \underbrace{\left\{\partial_y \sum_{k'_y}\tilde{\psi}_1 e^{ik'_y y}\right\}\cdot\left\{\partial_x \sum_{k''_y}\Pi\, e^{ik''_y y}\right\}}_{T_2} \quad .
\end{aligned}$$

where we used $\Pi = f_1 + \phi f_0$. We note that $f_{0\sigma}$ has neither x-dependence (local assumption) nor y-dependence, and is only non-zero for the $m = 0$ mode. We now use the fact that ψ_1 has only components in the $m = 1$ (with the wavenumber $\bar{k}$) and is time independent, so that $\sum_{k_y}\tilde{\psi}_1 e^{ik_y y} = \tilde{\psi}_1 e^{i\bar{k}y} + \psi_1 e^{-i\bar{k}y}$.

$$T_1 = \left\{\partial_x\tilde{\psi}_1\left(e^{+i\bar{k}y} + e^{-i\bar{k}y}\right)\right\}\cdot\left\{\partial_y\sum_{k''_y}\Pi\, e^{ik''_y y}\right\} \tag{6.7a}$$

$$= \left\{\tilde{\psi}_{1,x}\left(e^{+i\bar{k}y} + e^{-i\bar{k}y}\right)\right\}\cdot\left\{\sum_{k''_y}(ik''_y)\Pi\, e^{ik''_y y}\right\} \tag{6.7b}$$

$$= \tilde{\psi}_{1,x}\sum_{k_y}(ik''_y)\Pi\left\{e^{i(k''_y+\bar{k})y} + e^{i(k''_y-\bar{k})y}\right\} \quad , \tag{6.7c}$$

and the second term T_2 is given by

$$T_2 = \left\{\partial_y\tilde{\psi}_1\left(e^{+i\bar{k}y} + e^{-i\bar{k}y}\right)\right\}\cdot\left\{\partial_x\sum_{k''_y}\Pi\, e^{ik''_y y}\right\} \tag{6.8a}$$

$$= \left\{\tilde{\psi}_1 i\bar{k}\left(e^{+i\bar{k}y} - e^{-i\bar{k}y}\right)\right\}\left\{\sum_{k''_y}\Pi_x e^{ik''_y y}\right\} \tag{6.8b}$$

$$= \tilde{\psi}_1 i\bar{k}\sum_{k''_y}\Pi_x\left\{e^{i(k''_y+\bar{k})y} - e^{i(k''_y-\bar{k})y}\right\} \quad . \tag{6.8c}$$

To fulfill the mode-matching conditions given by $k_y = \bar{k} + k_y''$ to connecting the appropriate modes, we collect same mode numbers, thus the final equation for a magnetic island with only a $m = 1$ mode is given by

$$\begin{aligned}\frac{\partial f_{1\sigma}^m}{\partial t} = &- \left[1 + \eta_\sigma \left(\frac{v_\parallel^2 - 2\mu}{2} - \frac{3}{2}\right)\right] ik_y \phi^m f_{0\sigma} - ik_y \hat{s} x v_\parallel \left(f_{1\sigma}^m + \phi^m f_{0\sigma}\right) \\ &+ i\tilde{\psi}_{1,x} \left(k_y^{m+1}\Pi^{m+1} + k_y^{m-1}\Pi^{m-1}\right) - i\tilde{\psi}\left(\bar{k}\Pi^{m+1} - \bar{k}\Pi^{m-1}\right)\end{aligned} \tag{6.9}$$

where the abbreviation, e.g. $f_{1\sigma}^{m+1} = f_{1\sigma} e^{-i\frac{2\pi}{L_y}(m+1)y}$ was used.

Notes on the upper boundary

For a numerical simulations, we include only a finite number of poloidal modes, i.e., $m = \{0, 1, 2, \ldots, N\}$, where the highest mode number N is the so-called Nyquist frequency, which has only real components and thus needs to be excluded from the calculations. For the $\partial_t f_{1\sigma}^{N-1}$ mode, the magnetic island contributions are thus given by

$$\frac{\partial f_{1\sigma}^{N-1}}{\partial t} = \ldots + i\tilde{\psi}_x \left(k_y^N \Pi^N + k_y^{N-2}\Pi^{N-2}\right) - i\bar{k}\psi\left(\Pi^N - \Pi^{N-2}\right) \tag{6.10a}$$

$$= \ldots + i\psi_x k_y^{N-2} h^{N-2} + i\bar{k}\psi\Pi^{N-2} \quad , \tag{6.10b}$$

where the Nyquist contributions are neglected and the coupling is cut.

Notes on the zonal flow boundary

A second corner case arises, when calculating the zonal flow defined by the mode number $m = 0$. The coupling term contributions are given by

$$\frac{\partial f_{1\sigma}^{0}}{\partial t} = \ldots + i\tilde{\psi}_x \left(k_y^1 \Pi^1 + k_y^{-1}\Pi^{-1}\right) - \tilde{\psi}\left(k_y^1\Pi^1 - k_y^{-1}\Pi^{-1}\right) \tag{6.11a}$$

$$= \ldots + i\tilde{\psi}_x \left[2k_y^1 \,\mathrm{Re}(\Pi^{-1})\right] - \tilde{\psi}\left[2k_y^1 \,\mathrm{Im}(\Pi^1)\right] \quad , \tag{6.11b}$$

and we see that negative mode number appears. Although we evolve only positive mode numbers, i.e. $m \geq 0$, the negative mode numbers are obtained using the complex conjugate relation. As the real (imaginary) term of $f_{1\sigma}^{m=1}$ oscillates with the global frequency ω_g, the zonal flow amplitude oscillates.

6.3.3 | Calculating the magnetic island width

From numerical simulations in Sec. 6.2.2, we obtained the magnetic flux eigenfunction $\hat{\psi}_1$. We can multiply $\hat{\psi}_1$ by a constant, real scaling factor α to obtain $\psi_1 = \alpha\hat{\psi}_1$ which

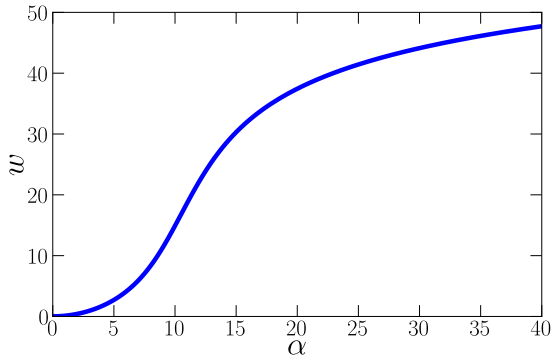

Figure 6.5: *The island width is defined by the maximum separation of the separatrix along the O-point. To obtained the real scaling factor of the eigenfunction α for a specific island width w, a root finding algorithm and the secant algorithm is used to for the integration along the separatrix. For small islands, $w < 5$ we find a strong sensitivity on the perturbation factor. A linear scaling law can be found for intermediate island widths ($10 \geq w \geq 25$). While for very large islands, the island width only weakly depends on the scaling factor.*

is subsequently used in the gyrokinetic simulation. However, there is no direct correspondence between the scaling factor and the magnetic island width w, which is itself given by the maximum separation of the separatrix. What we thus need is a function, which gives us the scaling factor for a desired magnetic island width, i.e. $\Gamma(w) = \alpha$. The magnetic field is given by the equilibrium magnetic field of our two-dimensional sheared slab geometry $\psi_0 = \hat{s}x$ and the scaled magnetic flux eigenfunction $\hat{\psi}_1$ as shown in Fig. 6.4b. First, the island width w for a given α is calculated by integrating along the separatrix of $\psi = \hat{s}x + \alpha\psi_1(x)$. Practically, we start close to the X-point at the radial position $(x, y) = (\epsilon, 0)$ with $\epsilon \ll 1$ and follow the magnetic field line using

$$w = f(\alpha) = 2\int_{y=0}^{L_y/2} \nabla\psi(x, y, \alpha)\, \mathrm{d}y \quad , \tag{6.12}$$

until we reach $y = L_y/2$, where the integration is performed using trapezoidal rule. Finally, to obtain the scaling factor α from a given island width w, the root of $\Gamma(\alpha)$: $0 = f(\alpha) - w$ has to be found. As the function $\Gamma(\alpha)$ is smooth and has a zero crossing, we use the *secant algorithm* with $\alpha_0 = 0$ and $\alpha_1 = 150$ as initial guesses. The function $\Gamma(\alpha)$ to get the island width w for a given scaling factor α is shown in Fig. 6.5 using for $\hat{s} = 0.4$. Note that an approximate linear dependence for α is found only for island widths between $10 < w < 25$.

6.3.4 | Rational surface separation

As was pointed out by Wang et al. (2009), a critical island width exists, where new rational surfaces appear, which may lead to a destabilization of the ITG mode. The *rational surface condition* including a magnetic field perturbation by a magnetic island

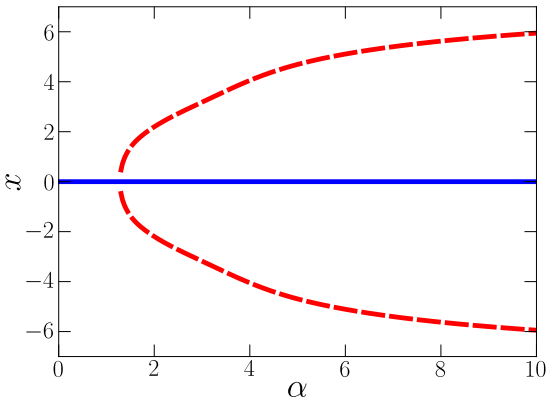

Figure 6.6: *The perturbation of the equilibrium magnetic field with the magnetic flux eigenfunction shown in Fig. 6.4b. For $\alpha = 0$ only the equilibrium rational surface exists at $x_0 = 0$, a finite alpha, $\alpha > 0$, leads to a formation of new rational surfaces at x around the O-point shown by the dashed lines. The magnetic field is given by $\psi = \frac{1}{2}\hat{s}x^2 + \alpha\psi_1$, with $\hat{s} = 0.4$. For an increasing scaling factor α the rational surfaces separation enhances.*

island is given by

$$k_\parallel = \mathbf{k}\cdot\mathbf{B} = \begin{pmatrix} k_x \\ k_y \\ k_z \end{pmatrix} \cdot \begin{pmatrix} \partial_y \left[\tilde{\psi}\cos(\bar{k}y)\right] \\ \hat{s}x + \partial_x \left[\tilde{\psi}\cos(\bar{k}y)\right] \\ 1 \end{pmatrix} \tag{6.13a}$$

$$= \underbrace{k_z + k_y\hat{s}x}_{\text{equilibrium}} + \underbrace{k_y\frac{\partial\tilde{\psi}}{\partial x}\cos(\bar{k}y) - k_x\bar{k}\tilde{\psi}\sin(\bar{k}y)}_{\text{Island perturbation}} = 0 \quad , \tag{6.13b}$$

where $\tilde{\psi} = \alpha\psi$, ψ is the magnetic island eigenfunction and α is the scaling parameter discussed in Sec.(6.3.3). For a further analysis, we neglect $k_z \ll 1$ and investigate the rational surface condition at the O-point, i.e. $y = L_y/2$ of the island, where $\cos(\bar{k}y) = -1$. Also, the ITG mode usually satisfies $k_x \ll 1$ and $k_y \sim 1$. With these approximations, the rational surface condition in Eq.(6.13b) simplifies to

$$k_\parallel = 0 = \hat{s}xk_y - \frac{\partial\tilde{\psi}}{\partial x}k_y \quad . \tag{6.14}$$

Using $\hat{s} = 0.4$ and the numerically obtained magnetic island flux eigenfunction shown in Fig. 6.4b, we apply a root finding algorithm on the above equation for a fixed island width and investigate the convergence points for different initial guesses of x. In Fig. 6.6, the radial position x versus the island scaling parameters α is shown, where the rational condition is satisfied. We find that for small islands, i.e. $\alpha < 2$, only one rational surface exists, however, for larger islands, the rational surface branches and separates such that for large islands, we find that up to three rational surfaces exists.

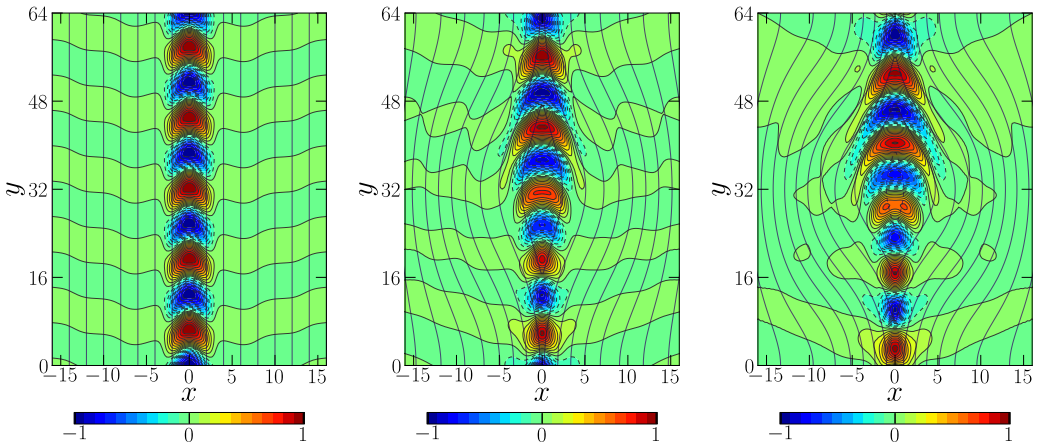

(a) $w = 0$ **(b)** $w = 6$ **(c)** $w = 10$

Figure 6.7.: *(Normalized) contour plots of electrostatic potential of the ITG in its linear phase under the influence of a magnetic island perturbation with a magnetic island width of* $w = 0$, 6 *and* $w = 10$. *The magnetic island has a visible impact on the mode structure of the island.*

6.4 | Linear study of ITG with magnetic island modification

In chapter (5), we studied the linear and nonlinear effects of the ion temperature gradient and electron temperature gradient. In the following sections, we included the magnetic island as a perturbation of the equilibrium and investigate its influence on the drift waves.

6.4.1 | Linear dynamics with adiabatic electrons

First, we concentrate only on the linear dynamics of the drift wave and employ the modified Vlasov equation (6.4) for simulations. As a base setup, we set the physical parameters to $\hat{s} = 0.2$ and $\eta_i = 5$ and assume an adiabatic electron response. The numerical parameters are chosen to $L_{x,y,v_\parallel,\mu;t} = (64, 64, 4, 9; 2400)$ and $N_{x,k_y,v_\parallel,\mu} = (512, 65, 32, 8)$ which is assured to be a converged case.

The magnetic island width is varied by scaling the flux eigenfunction ψ_1 as discussed in Sec.(6.3.3). The long time is required to ensure that the linear eigenstructure is fully established and independent on the initial perturbation. A snapshot of the electrostatic potential taken at $t = 2400$ is shown in Fig. 6.7. Fig. 6.7a corresponds to the original ITG drift wave in the absence of the island (namely $w = 0$). In Fig. 6.7(b-d) the island size is increased from $w = 6$, $w = 12$ to $w = 16$. This fact can be seen by the bending of the poloidal magnetic field lines. We find that for increasing island width, the ITG drift wave is modified, namely the magnetic island has a widening effect on the ITG mode

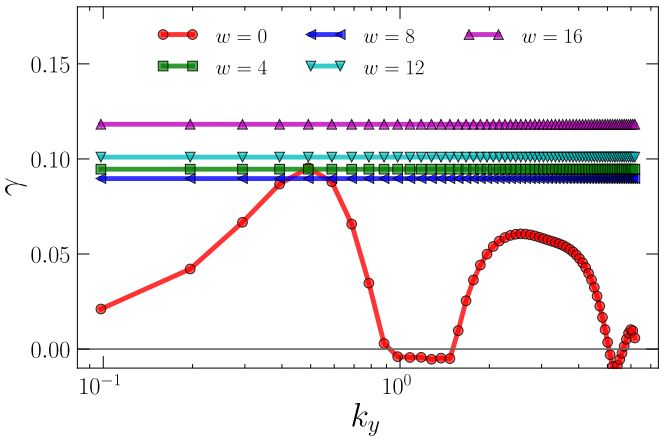

Figure 6.8: *Growth rates of electrostatic potential for $\hat{s} = 0.2$ and $\eta_i = 5$ for island widths of $w = 0, 6, 12$ and $w = 18$. For a non-zero magnetic island width, geometrical coupling leads to a global mode formation with equal growth rates and frequency. For small islands, an initial stabilization effect is observed. However, for large island the destabilization effect dominates.*

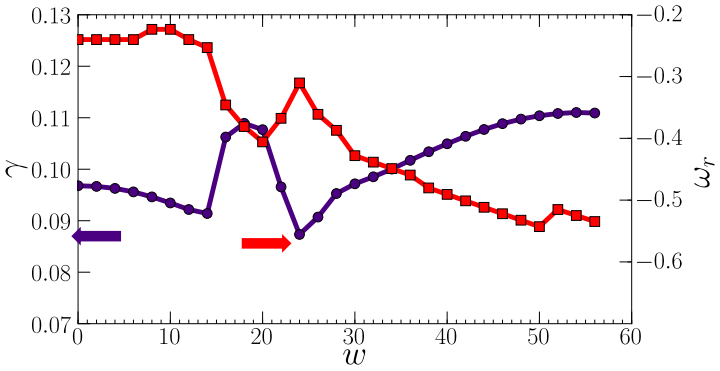

Figure 6.9: *Frequency and growth rates vs magnetic island width for $\eta_i = 5$ and $\hat{s} = 0.2$. An initial stabilization effect is observed for small islands. Medium large islands exist the ITG mode which for very large islands is back to smaller values.*

structure. Qualitatively, the ITG structure is broadened at the O-point to about twice the size compared to the case without the island ($w = 0$ case).

The growth rates of the ITG is shown in Fig. 6.8 for island widths of $0, 4, 8, 12$ and 16. For a magnetic island width of $w = 0$, which corresponds to the classical ITG drift wave without an island, we find that the ITG mode at the standard region has its maximum growth rate at $k_y \sim 0.5$, and at the short-wavelength region $k_y \sim 2.5$. For the case with a finite magnetic island width, i.e. $w > 0$, we find that all poloidal modes have an equal growth rate and frequency - as a direct consequence of the poloidal mode coupling; to which we refer to as *global mode formation*. We find that the global mode formation has a stabilization effect, as the growth rates of the global mode for $w = 6$ and $w = 12$ are smaller than the peak growth rate of the ITG wave in the absence of an island. However, for large island widths, the growth rate increases and becomes larger than the case with $w = 0$. Thus we find a destabilizing effect for large magnetic island widths.

The growth rate of the electrostatic potential over the magnetic island width is shown in Fig. 6.9 as dots. We find an initial stabilizing effect for island widths < 14, with a stabilization of up to $\sim 10\%$ for $w = 14$. This stabilization can be understood by a

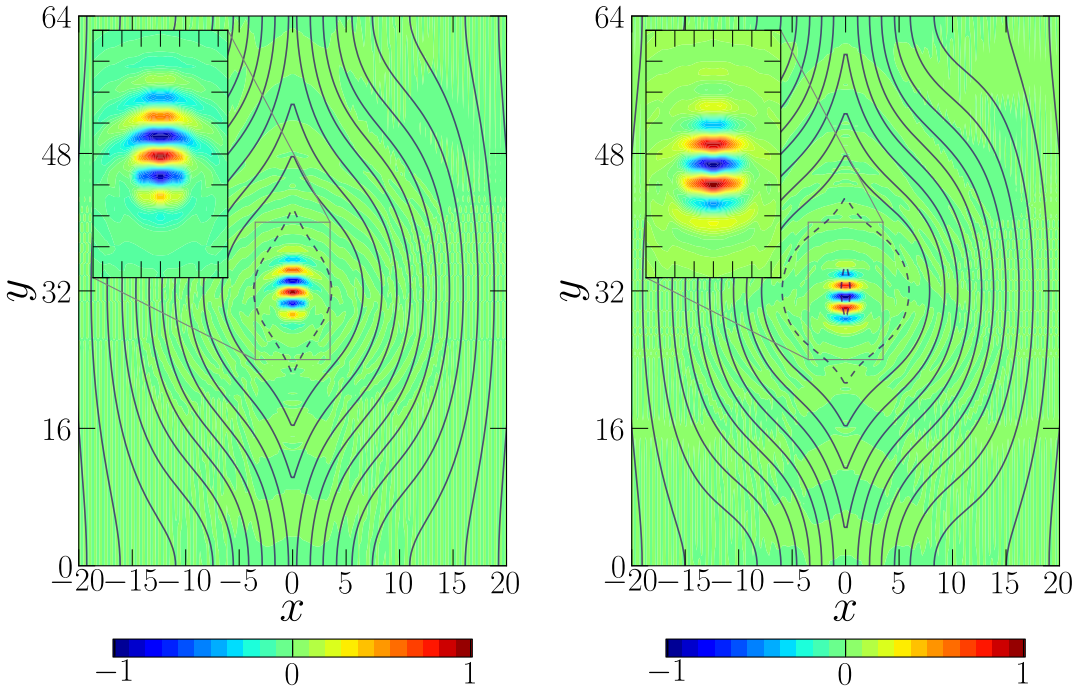

(a) $w = 14$ **(b)** $w = 18$

Figure 6.10.: *(Normalized) contour plots of electrostatic potential for magnetic island widths of* $w = 14$ *(left figure) and* $w = 18$ *(right figure). The rational surface separation leads to an excitation of the short-wavelength part of the ITG at the O-point which dominants the mode structure.*

geometrical coupling of the poloidal modes. The most unstable mode, which determines the growth rate of the electrostatic potential, can dissipate energy through stable modes. As the coupling between the poloidal modes increases with an increasing island widths, the stabilization effect becomes stronger until a critical width of $w = 14$ is reached. For island widths > 14, we find a strong destabilizing effect, with a jump of the real frequency from $\omega_r \sim -0.25$ to $\omega_r \sim -0.4$. The reason of this jump will be investigated in the subsequent section.

In Fig. 6.10, similar to Fig. 6.7, the electrostatic potential for the island widths is shown for the island widths of $w = 14$ in Fig. 6.10a and $w = 18$ in Fig. 6.10b. We find that the mode structure of the electric potential is mainly concentrated at the O-point, showing short-wavelength fluctuations.

The mode spectrum shown in Fig. 6.11 reveals that indeed for large island widths most of the mode power is concentrated at short-wavelength scales, e.g. for $w = 16$ the peak of the mode spectrum is at $k_y \sim 2.5$, which coincides with the peak growth

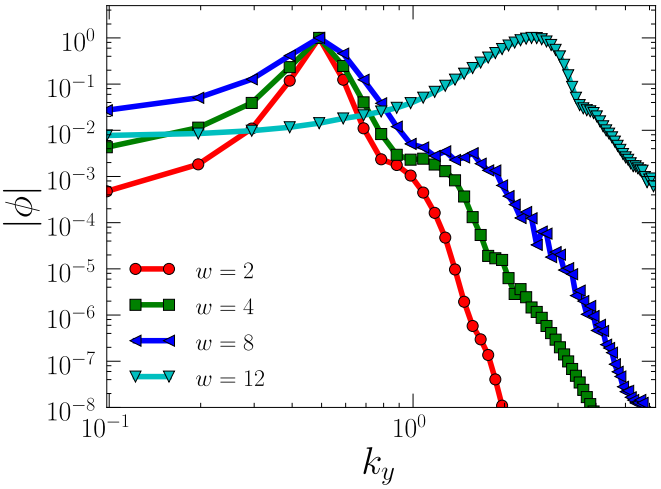

Figure 6.11: *Mode spectrum of the electrostatic potential for k_y for island widths of $w = 2, 4, 8, 12$. For small islands widths the mode spectra coincides with the linear peak growth rate from the standard ITG mode, for large islands, the peak of the mode spectra shifts to the peak growth rate of the short-wavelength ITG mode.*

rate of the short-wavelength ITG mode. For smaller islands, most of the mode power is around $k_y \sim 0.7$, which is also the peak growth rate of the standard-ITG mode. Thus we may conclude, that the global mode is driven by the most unstable linear mode. For increasing island width, and thus with an increasing coupling strength ($\propto w^2$), the spectra becomes broader, which is explained by a more efficient energy transfer between the poloidal modes. However, we also find that the slope at $k_y \sim 2$ is flat, which shows that energy is less effectively dissipated. This could be understood as a contribution from the short-wavelength ITG mode which is itself a free energy source. In the next section, we will investigate the mechanism of the destabilization of the ITG mode in case of a large magnetic island.

6.4.2 | Magnetic island destabilization mechanism

For a preliminary investigation of the destabilization mechanism of large magnetic islands, we use a filter to separate the standard ITG region and the short-wavelength ITG region. Our filtering function κ is defined by

$$\frac{\partial \tilde{f}_1}{\partial t} = \kappa(k_y)\frac{\partial f_1}{\partial t} \quad , \quad \text{where} \quad \begin{cases} \kappa = 1 & \text{for ITG-org} \\ \kappa = \frac{1}{2} + \frac{1}{2}\tanh(k_y - 1.3) & \text{for ITG-shw} \\ \kappa = \frac{1}{2} - \frac{1}{2}\tanh(k_y - 1.0) & \text{for ITG-std} \end{cases} . \quad (6.15)$$

The effect of the filtering on the growth rates without the magnetic island modification, i.e. $w = 0$, can be seen in Fig. 6.12a and is as follows : for the *ITG-org* (the unfiltered case), filtering has no effect, while for the *ITG-std* the short-wavelength domain is suppressed, allowing only unstable modes in the standard ITG region. For the case of the *ITG-shw*, the standard ITG region is suppressed and thus only unstable modes are found in the short-wavelength region, i.e. $k_y > 1$.

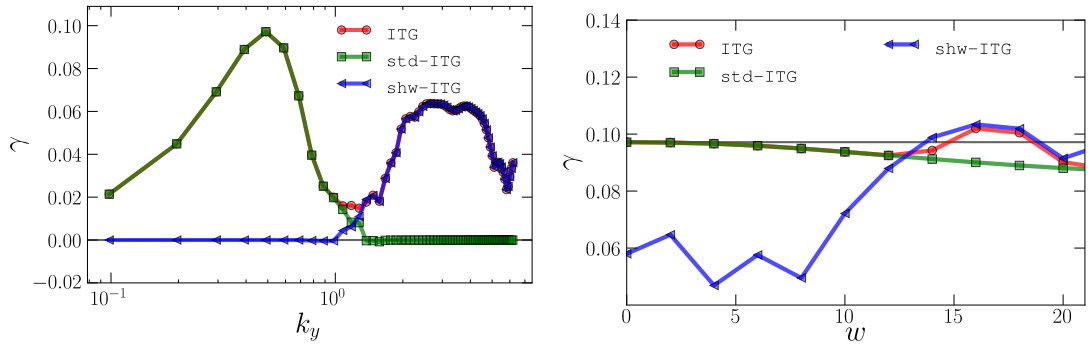

(a) *Filtered growth rates* **(b)** *Growth rates vs island width*

Figure 6.12.: *Linear growth rates for three cases : the original case (ITG), a case with the short-wavelength part suppressed (std-ITG) and a case with the standard part suppressed (shw-ITG). Left figure shows the linear growth rates in the absence of an island. Right figure shows the growth rates with increasing island width - only when the short-wavelength part is present, a destabilization at $w \sim 14$ is observed (right figure).*

In Fig. 6.12b, we perform a parameter scan of the island width vs. the growth rate of the electrostatic potential for all three cases. We find that the destabilization at $w \sim 14$, which is observed in the unfiltered case, is not found in the *std-ITG* case, where the short-wavelength region is filtered out. For islands $w < 30$, we observe a weak stabilization. For even larger island widths, the islands is found to have practically no further influence on the ITG growth rates. For the case of *shw-ITG*, where only the short-wavelength region is unstable, we find a strong destabilization at around $w \sim 8$, which exceeds the growth rates of the *std-ITG* case at $w \sim 12$, which is very close to the value observed in the *ITG* case. From these results, we can conclude that the destabilization found in Fig. 6.9 does indeed arise from the short-wavelength region. In the next section, we will investigate the mechanism of the destabilization.

6.4.3 | Minimal model for destabilization through shw-ITG mode

In order to understand the destabilization of the short-wavelength ITG mode observed in Fig. 6.12b, a reduced model is proposed to analyze the response of the ITG eigenmode structure to the static island. For simplicity, we fix the poloidal direction at $y = 0$ and $y = L_y/2$, which corresponds to the X-point and O-point of the island, respectively. This excludes the poloidal mode coupling from the island which arises from the island poloidal structure in Eq.(6.9). The island's magnetic flux ψ is now only related to the Landau damping and parallel advection term, as $k_\parallel = k_y \hat{s} x \pm k_y \tilde{\psi}_x$. The factor $k_\parallel$, which corresponds to the total B_{y1} including the contribution from the magnetic island at the X- and O-point is shown in Fig. 6.13. At the X-point, the island structure increases

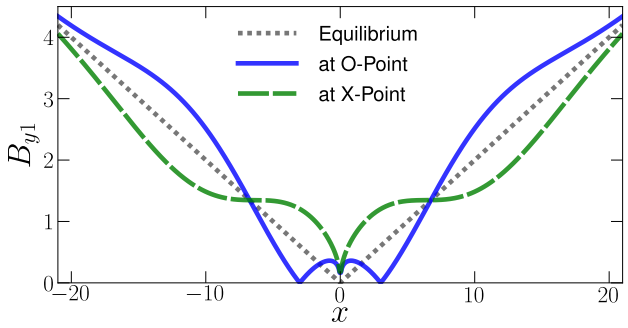

Figure 6.13: *Perturbation of the equilibrium field due to the magnetic island at the X- and O-point, i.e., $y_X = 0$ and $y_O = L_y/2$, respectively. The rational surface formation at the O-point is clearly visible. The field structure at the X-point has a strong increase in magnetic shear.*

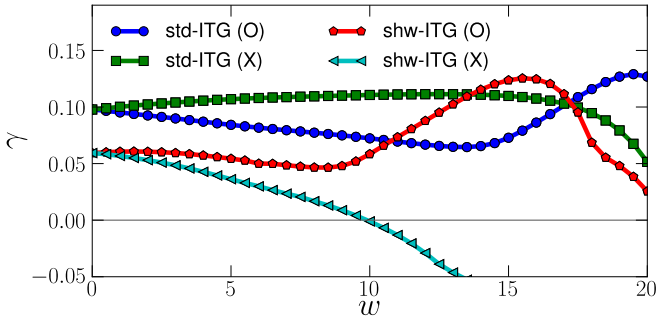

Figure 6.14: *Growth rate of drift turbulence at the island's X- and O- point for $k_y = 0.5$ and $k_y = 2.5$ modes. Rational surface separation at the O-point destabilizes the std-ITG region, as well as the shw-region. The onset of destabilization for the shw-region is earlier compared to the std-region.*

the local shear near the rational surface. However, at the O-point, the island causes two separated rational surfaces, which distance increases with the size of the island. For the perturbed field at the X- and O-point, we evolve only a single poloidal mode, which wavenumber corresponds to the peak growth rate of the std-ITG mode $k_y \sim 0.5$ and of the shw-ITG mode $k_y \sim 2.5$. The growth rate dependence on the island width is shown in Fig. 6.14. For the X-point equilibrium, the std-ITG mode is slightly destabilized, which agrees well with the general behavior of destabilization for weak magnetic shear and stabilization for stronger magnetic shears. The shw-ITG mode, however is very sensitive to the increase of magnetic shear and quickly stabilizes. For the O-point equilibrium, we find that the std-ITG mode is stabilized for small island widths due to the reduction of local shear, however destabilized again for large island widths due to the separation of rational surfaces. As the island width increases and crosses a critical value, the std-ITG mode and also the shw-ITG mode are first destabilized, and then stabilized again, as shown in Fig. 6.14. However, the critical island width for the shw-ITG mode is smaller than the std-ITG. We can understand this underlying mechanism through the response of the ITG eigenmode structures to the island. As shown in Fig. 6.13, for large islands, the rational surface separation occurs, so that a so-called *double ITG mode*, similar to the case found in the negative shear slab geometry by Li et al. (1998), with an increased growth rate is excited. The corresponding eigenfunctions of the std-ITG and shw-ITG modes are shown in Fig. 6.15. As the island width increases further, the double ITG

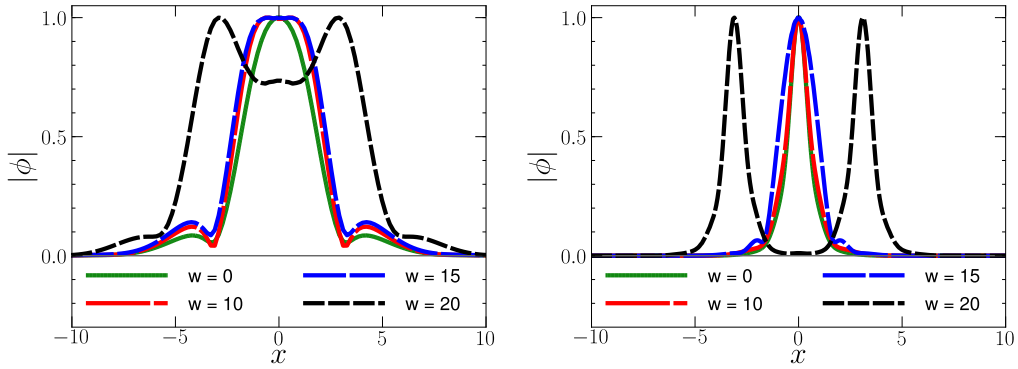

(a) *std-ITG* **(b)** *shw-ITG*

Figure 6.15.: *Eigenfunctions (absolute value) of the std-ITG mode for* $k_y = 0.5$ *and shw-ITG mode for* $k_y = 2.5$ *for different island widths.*

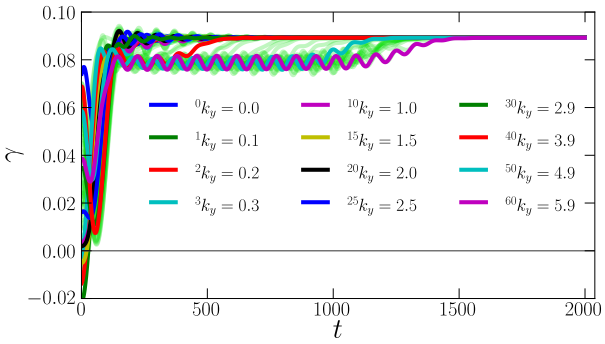

Figure 6.16: *Instant growth rates of various poloidal modes. For* $\hat{s} = 0.2$, $\eta_i = 5$ *and* $w = 8$. *The formation of a global modes is formed. As mode-coupling only coupled the neighboring modes, two coupling groups are found* ($t \sim 800$)*, one for the standard ITG region the other for the short-wavelength region - until the most unstable of them is forming the global mode at* $t \sim 1500$.

modes are first destabilized as the rational surface separation increases. Finally, when the separation is large enough, the double ITG mode structure also separates, so that the mode structures are reduced back to the unstructured with a single rational surface, as shown in Fig. 6.15, which is the reason why the growth rate decreases. As for the difference of the critical island widths for the destabilization of the std-ITG and shw-ITG mode, it may result from the narrow mode width of the shw-ITG mode, which matches the small separation of the rational surface.

6.4.4 | Formation of global mode and zonal flow oscillations

Shown in Fig. 6.16 is the time evolution of the electric field energy for various modes for an magnetic island of size $w = 8$. After an initial phase, the mode coupling induced by the magnetic island forces all modes to grow with the same growth rate, including the stable modes, leading to a so-called global mode formation. The relatively long initial phase occurs because mode coupling is only working between two directly neighboring

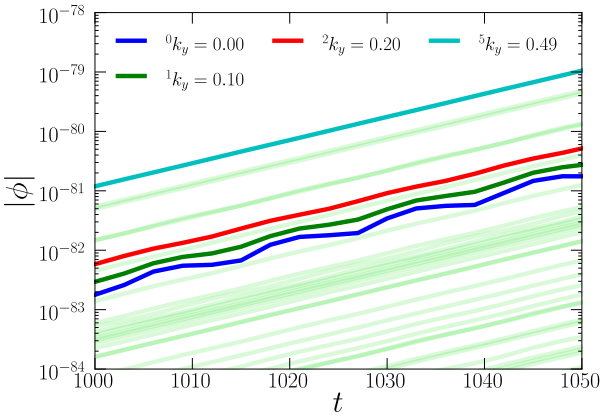

Figure 6.17: *Time evolution of the electrostatic potential for a selected number of modes for an island width of $w = 8$. Mode coupling of the $m = 1$ and $m = -1$ mode induces by the island leads to an oscillating zonal flow proportional to the global drift frequency. The oscillating zonal flow couples again with the $m = 1$ inducing (weak) oscillations. The oscillations strongly decreases with amplitude for higher mode numbers.*

mode.

6.4.5 | Investigation the zonal flow oscillations

In Fig. 6.17, the time evolution of the electrostatic potential is shown for four poloidal modes, i.e. $m = (0, 1, 2, 5)$ between the time $t = 1000 - 1100$. A striking feature is the oscillation of the zonal flow (the $m = 0$ poloidal mode). The oscillation frequency is found to directly correspond to the frequency of the global mode. The origin of the oscillations can be explained by investigating the coupling terms for the evolution of the zonal flow as discussed in Sec.(6.3.2). The contour plots of the zonal flow for close-by times are shown in Fig. 6.18. The zonal flow oscillation also affects other poloidal modes through back-coupling such that, in principle, all poloidal modes are oscillating. However, practically, the amplitude of the oscillations will quickly decrease for higher mode numbers and for $m > 5$ it is hardly noticeable. A consequence of the zonal flow oscillations is that strictly speaking a global eigenmode with a unique frequency ω_g does not exist. However, this is understandable, as the magnetic equilibrium is not invariant in the translation in the y direction (as the magnetic island has a y dependence). There might be the case, where multiple global eigenmodes exist and the inference between them results in the observed oscillations. This question can be answered by running gkc++ as an eigensolver. However, as the size of the eigenvalue spectra is of the order of $N \sim 10^6$ for a reasonable resolution, this is yet out of reach for present day computers.

6.4.6 | Parameter scan over η_i

We perform a parameter scan over η_i in order to gain a better understanding on the impact of a static magnetic island under various conditions. Namely, using previous setup, we investigate the growth rate of the electrostatic potential for different $\eta_i = 3, 4, 5$ vs the magnetic island width; shown in Fig. 6.19. We observe an initial stabilization

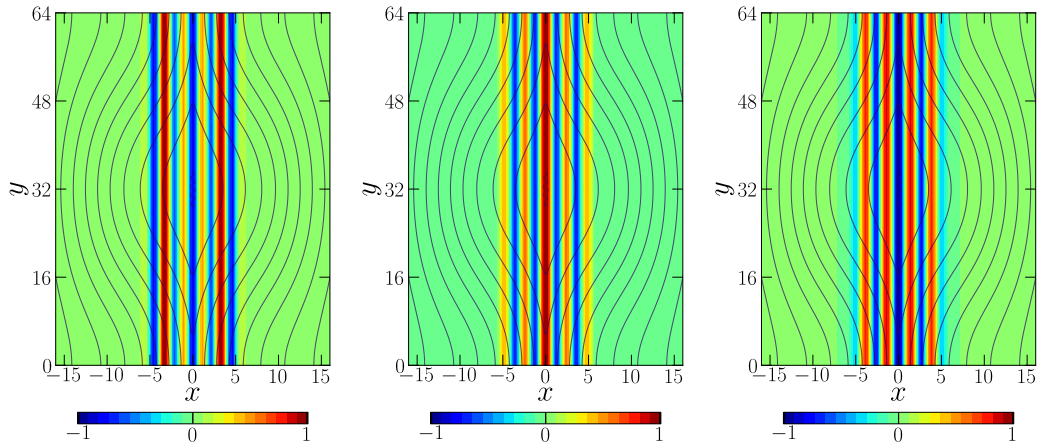

(a) $t = 1000$ **(b)** $t = 1010$ **(c)** $t = 1020$

Figure 6.18.: *(Normalized) contour plots of the zonal flow of the electrostatic potential for* $t = 1000$*,* $t = 1010$ *and* $t = 1020$*. The zonal flow component is oscillating with the global drift frequency (*$\hat{s} = 0.2$*,* $\eta_i = 5$ *and* $w = 8$*).*

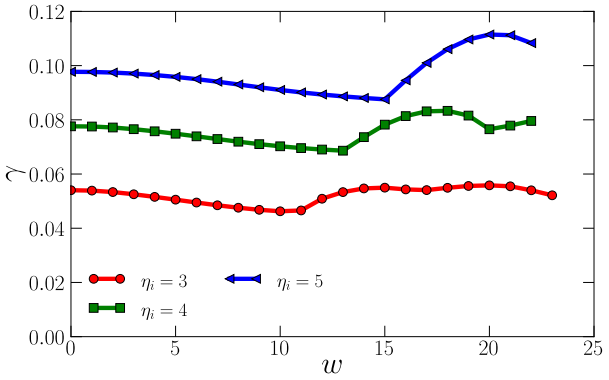

Figure 6.19: *Growth rates* γ *of the electrostatic potential over magnetic island width* w *for* $\hat{s} = 0.2$ *and* $\eta_i = 5, 3, 2$*. A initial stabilization effect is observed for islands* $w \leq 10$*. Destabilization is found for larger islands, where destabilization is stronger for larger temperature gradients* η_i*.*

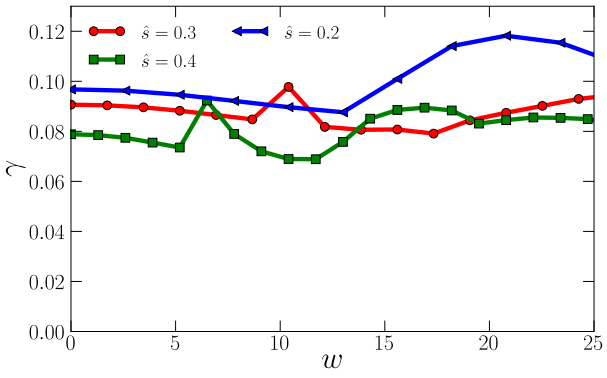

Figure 6.20: *Growth rates of electrostatic potential vs island width for* $\eta_i = 5$ *and* $\hat{s} = 0.2, 0.4, 0.6$. *Stabilization is stronger for larger shear while the short-wavelength is suppressed for larger shear. Interestingly, we observe some resonances, e.g., at* $w \sim 5$ *for* $\hat{s} = 0.4$, *which are found to originate from the short-wavelength ITG.*

effect, which is explained by the dissipation of energy enabled by poloidal coupling. In this picture the most unstable mode can transfer energy to its neighboring modes, which themselves transfer them to more stable neighbors until the stable modes can dissipate the energy. This mechanism provides the stabilization observed for small islands $w \leq 10$ in all three cases of η_i. Consistently, we find a destabilization for large islands, which is strong for $\eta_i = 5$, however, the destabilization strength decreases for smaller temperature gradient.

6.4.7 | Parameter scan over $\hat{s}$

Shown in Fig. 6.20 is the growth rate of the electrostatic potential, with a fixed temperature gradient of $\eta_i = 5$ and various magnetic shears vs the magnetic island width size w. Especially interesting is the strong resonance destabilization for large magnetic shears around an island width of $w = 5$ for the case of $\hat{s} = 0.4$. In this case, we found by investigating the mode spectra that this destabilization is driven by the short-wavelength ITG mode. The exact mechanism of this resonance is yet to be understood.

6.4.8 | Importance of the flux-surface averaging term

In the previous chapter, we noted that in the linear case, the adiabatic ETG and the ITG are equivalent within normalization, except in the nonlinear case where the Poisson equation needs to be modified to account for the flux-surface averaging effect. However, as discussed in Sec.(6.3.2), the zonal flow can also be generated by the magnetic island through poloidal coupling and may have an influence on the linear mode structure through back-coupling. We compared thus two cases using adiabatic electrons: one with and one case without the flux-surface averaging term modification included in Poisson's equation. We found not difference in the growth rates for magnetic island widths $w \leq 20$, so that we may conclude that the influence of the flux-averaging term on the zonal flow is negligible.

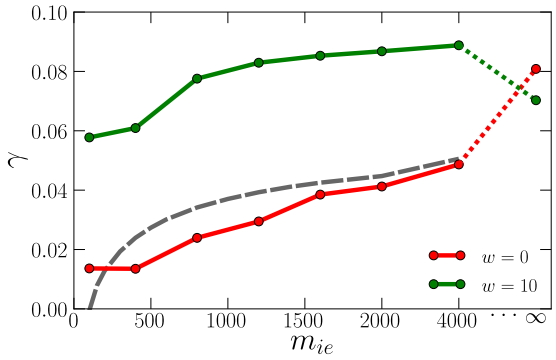

Figure 6.21: *Linear (global mode) growth rates γ vs ion-electron mass ratio m_{ie} for $\eta_i = 5$, $\eta_e = 0$ and $\hat{s} = 0.4$ with a magnetic island width of $w = 0$ and $w = 10$. $m_{ie} = \infty$ denotes the results obtained using adiabatic electrons. In the absence of the island, isothermal kinetic electrons reduces the growth rate of the ITG, thus we do not find convergence to the adiabatic case. This is confirmed by the solution of the dispersion relation as obtained in Sec.5.5 (dashed line). For the case with the magnetic island, a convergent case is reached for $m_{ie} \sim 800$.*

6.5 | Analysis of ITG on magnetic island including kinetic electrons

For the ITG with adiabatic electrons and in the absence of an island, the flux-surface averaging effect of the electrons is taken into account through a modification of the Poisson's equation (5.4). In the case with a non-zero magnetic island width however, this modification term cannot be applied as the magnetic field lines are essentially curved. We thus need to include a kinetic electron species in order to self-consistently account for the flux-surface averaging effect. However, this comes with the expense that the computational cost increases by two order of magnitudes even when the electron scale is not resolved, as the large thermal velocity of the electrons restricts the maximum numerical stable time step. Now, with kinetic electrons, our parameter space increases by additional by two degrees of freedom, namely by the electron temperature gradient η_e and by the ion-electron mass ratio $m_{ie} = m_i/m_e$.

6.5.1 | Parameter scan over the ion-electron mass ratio (m_{ie})

We set a fixed ion and electron temperature gradient, namely $\eta_i = 5$ and $\eta_e = 0$, and investigate the growth rate of the ion temperature gradient for a fixed magnetic island width of $w = 0$ and $w = 10$ vs the ion-electron mass ratio. The results are shown in Fig. 6.21. First, we address the case in the absence of the magnetic island (red circles). We find that increasing m_{ie}, increases the growth rate of the ITG mode. We reach convergence for an mass ratio of around $m_{ie} \sim 1500$. However, even for kinetic electrons with a large $m_{ie} = 4000$, we do not find a convergence to simulations using adiabatic electrons shown here at $m_{ie} = \infty$. To confirm that this discrepancy is not an artifact of the velocity and/or spatial resolution, we additionally show the solution of the dispersion relation (dashed line) obtained using the integral code as discussed in Sec. 5.5 and in Fig. 5.19a. The dispersion relation shows growth rates comparable to the kinetic gkc++ IVP solution from around $m_{ie} \sim 1500$, thus validating our results. We

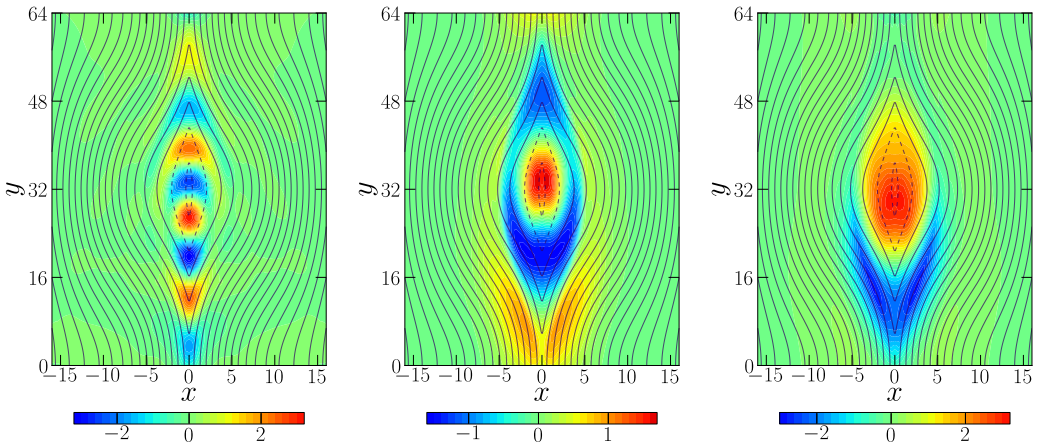

(a) $m_{ie} = \infty$ **(b)** $m_{ie} = 400$ **(c)** $m_{ie} = 2000$

Figure 6.22.: *Electrostatic potential for* $m_{ie} = 400, 800$ *and* $m_{ie} = 2000$ *using* $\eta_i = 5$, $\eta_e = 0$, *and* $\hat{s} = 0.4$. *The global mode structure shows a strong change from the adiabatic case* ($m_{ie} = \infty$) *shown in the left figure, to a mode structure exhibiting a vortex at the O-point once kinetic electrons are included as shown in middle and right figure. We conclude that flux-surface averaging, neglected in the adiabatic case, seems to be important to define the dynamics at the O-point.*

assume that the difference between the adiabatic and kinetic cases follows from a phase-delay response of the kinetic electrons to an electrostatic perturbation at the rational surface. This resonance effect at the rational surface is most probably a failure of our two-dimensional geometry model, where we assumed $k_z = 0$; and needs to be checked using a finite L_z.

For the case with a magnetic island width of 10: the growth rate of the magnetic island is much larger than in the absence of the island. Most probably due to the fact that the magnetic island breaks the resonance of the kinetic electrons at the rational surface. Convergence is reached at $m_{ie} \sim 800$. The corresponding contours of the electrostatic potential are shown in Fig. 6.22. Figure (a) shows the adiabatic simulations, while (b) and (c) are the kinetic simulation with $m_{ie} = 400$ and $m_{ie} = 2000$, respectively. For small mass ratios (b), i.e., $m_{ie} \sim 400$, the mode structure is found to extend along the field lines. At the O-point, a large vortex structure is found, which we interpret as a clear sign of a relatively strong influence of flux-surface averaging effect. The strong influence of the flux-surface averaging effect at the O-point is not surprising, as the field lines are closed around the O-point and any electrostatic fluctuation is short-circuited. The case with $m_{ie} = 2000$ shows an even stronger averaging effect, which is understandable, as the flux-surface averaging effect increases with increasing ion-electron mass ratios (as the thermal velocity of the electrons increases). The change in the poloidal mode spectrum for the kinetic electron case compared to the adiabatic electron case (shown in Fig. 6.11)

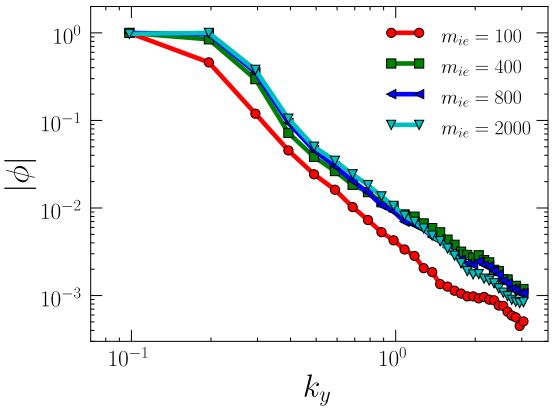

Figure 6.23: *Normalized poloidal mode spectrum for $m_{ie} = 100, 400, 800$ and $m_{ie} = 2000$. Convergence is reached for $m_{ie} \sim 400$. The strong influence of the magnetic island structure in the kinetic electron case is clearly visible in the poloidal mode structure. Large scale structures are dominating in the case with kinetic electrons, in contrast to the case with adiabatic electrons shown in Fig. 6.11, where usually the linear most unstable mode was dominating the global mode for $w < 14$.*

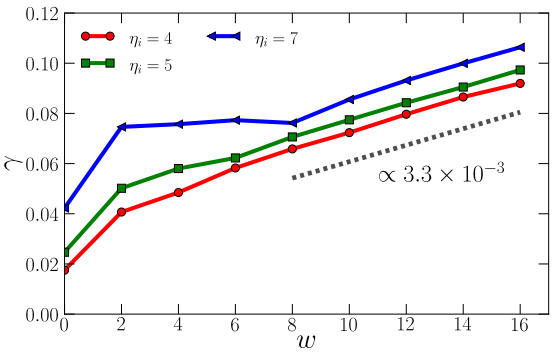

Figure 6.24: *Growth rates of the electrostatic potential vs magnetic island width for varying η_i, with $\eta_e = 0$ and $m_{ie} = 800$. Inclusion of the magnetic island breaks the resonance at the rational surface thus the growth rate increases. For the case $\eta_i = 7$ shows an independence on the growth rate for $2 \geq w \geq 10$ suggesting that small island have a negligible influence on the growth rate. For $w = 8$ a destabilization is observed, independent on the temperature gradient investigated here.*

is clearly visible compared to the kinetic case shown in Fig. 6.23.

6.5.2 | Parameter scan over η_i

We perform parameter scans over the ion temperature gradient η_i for a fixed electron temperature gradient $\eta_e = 0$. The growth rates of the electrostatic potential for $\eta_i = 4, 5$ and $\eta_i = 7$ are shown in Fig. 6.24. In contrast to the case with adiabatic ions, a stabilization effect cannot be found. We can attribute the destabilization for small island widths $\eta_i < 5$ to a change of the electron dynamics, as the stabilizing effect of the electron resonance at the rational surface weakens. For $\eta_i = 7$, we find an almost constant region between $2 \geq w \geq 10$, where the growth rate is approximately constant. Assuming that this is the case, where no electron resonance takes place, we can conclude that the magnetic island has only a very weak stabilizing effect as compared to the adiabatic case, where stabilizing effect was much stronger, e.g., in Fig. 6.9. For an island width larger then $w > 10$, we find a weak destabilization.

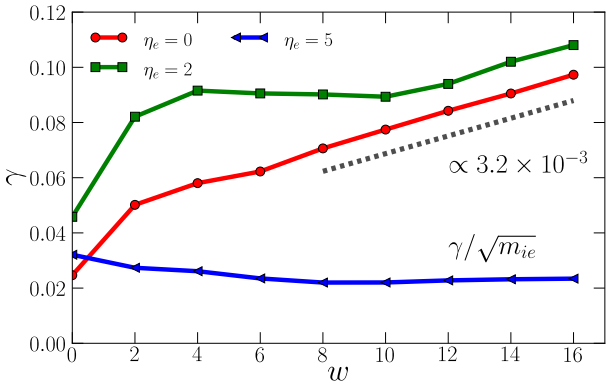

Figure 6.25: *Linear growth rates of electrostatic potential vs magnetic island width for varying η_e using $\eta_i = 5$ and $m_{ie} = 800$. For the case without the island, a resonance of the electrons at the rational surface reduces growth rate. For small island widths the resonance effect is reduced, such that the growth rates quickly rises. For intermediate island widths, a stabilization effect is observed for $\eta_e = 2$ which for a critical island width of $w = 2$ gets destabilized. Note that for the case of $\eta_e = 5$, the ETG is excited and dominated the global mode.*

6.5.3 | Parameter scan over η_e

In Sec. 5.5, we discussed the dispersion relation of the ITG for the two-dimensional sheared slab geometry in case of kinetic electrons. Namely, we found that a finite electron temperature gradient η_e has a destabilizing effect on the ITG. Growth rates comparable to the adiabatic case are found once $\eta_e \sim 2$, which however, is also the threshold where the ETG itself becomes unstable. For larger η_e, the ITG mode is only weakly further destabilized, however, the ETG itself is very sensitive and strongly grows, e.g., for $\eta_e = \eta_i > 2$, we expect growth rates to be $\gamma_{ETG} \sim \sqrt{m_{ie}}\gamma_{ITG}$. In Fig. 6.25, we show the electrostatic potential growth rates vs the island width for three cases of electron temperature gradients : $\eta_e = 0, 2$ and $\eta_e = 5$. For $\eta_e = 2$ a destabilization of the global mode through the ETG mode is not found, as the maximum wave number included in the simulations is much smaller than the peak growth rate of the ETG mode. For intermediate island widths, a stabilization effect on the ITG is observed for $\eta_e = 2$, which for a critical island width of $w = 12$ gets destabilized. For the case of $\eta_e = 5$, the ETG is excited with a much larger growth rates such that linear estimated on the ITG contributions are not possible when using an initial value code.

The contours of the electrostatic potential for $\eta_i = 5$ and $\eta_e = 2$ are shown in Fig. 6.26 for island widths of $w = 8, 10, 12$. In contrast to the isothermal electron case, a strong vortex mode is not found for moderate island widths up to $w \leq 10$. Showing that a finite electron temperature gradient also has a large influence on the dynamics. Interestingly, the destabilization of the ITG for island width $w \geq 10$ coincides with the formation of the vortex at the O-point — which gives a hint that the vortex mode itself may be the responsible mechanism for destabilization. However, further analysis is necessary for a final conclusion.

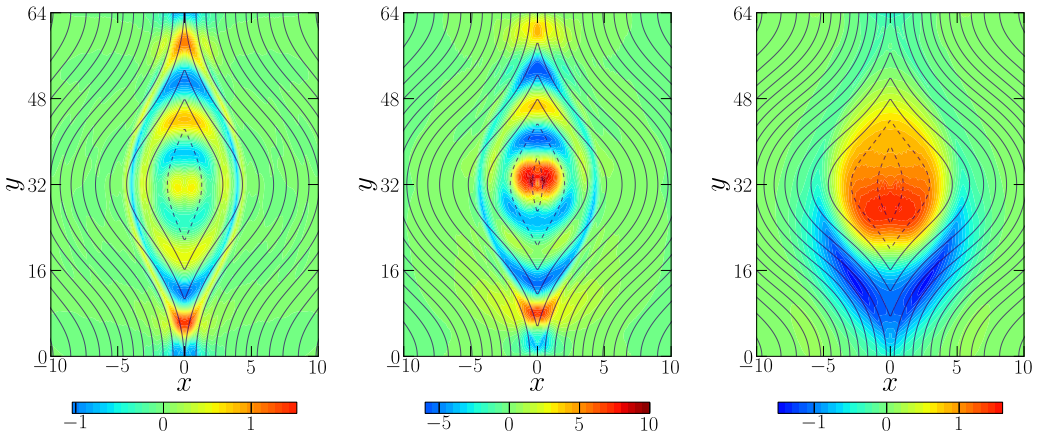

(a) $w = 8$ **(b)** $w = 10$ **(c)** $w = 12$

Figure 6.26.: *Contour of the electrostatic potential at* $t = 800$ *for the kinetic electron case with* $m_{ie} = 800$, $\eta_i = 5$ *and a finite electron temperature gradient of* $\eta_e = 2$. *In contrast to the isothermal electron case, a strong vortex mode is not found for moderate island widths up to* $w \leq 10$. *Showing that a finite electron temperature gradient also has a large influence on the dynamics.*

6.6 | Nonlinear analysis of ITG on magnetic island

Finally, we turn into the analysis of the nonlinear simulations including a magnetic island perturbation. As already stated, kinetic electrons are crucial in nonlinear simulations due to the flux-surface averaging effect. Here, we chose $\eta_i = 5$ and $\eta_e = 5$ in case of the kinetic simulation. Although the linear phase will be dominated by the ETG, we know from previous simulations that the ETG saturates at much smaller amplitudes, such that nevertheless, we expect that the ion dynamics will dominate in the nonlinear phase. The contour plot of the electrostatic potential is shown in Fig. 6.27. For the case without an island shown in (a), we find a relatively strong zonal flow, close to the rational surface, small-scale fluctuations can be seen, which most probably arises from the ETG. For an island width of $w = 4$ and $w = 8$, we found a very strong and extended zonal flows. This zonal flow may arises from the Poisson bracket of the magnetic island contribution, which does increase zonal flow production. For the parameter set presented here, no field perturbations of the electrostatic potential are found at the O-point. However, we note that for some parameters, an extended and static (non-oscillating) vortex is found in the center. Hornsby et al. (2010, 2012) discovered similar vortices in toroidal simulations, which in contrast to ours, were oscillating on a long-timescale. Hornsby et al. (2010, 2012) concluded these oscillations stem from a similar mechanism as the geodesic acoustic modes (GAM) oscillations. However, our as our simulations are restricted to the slab

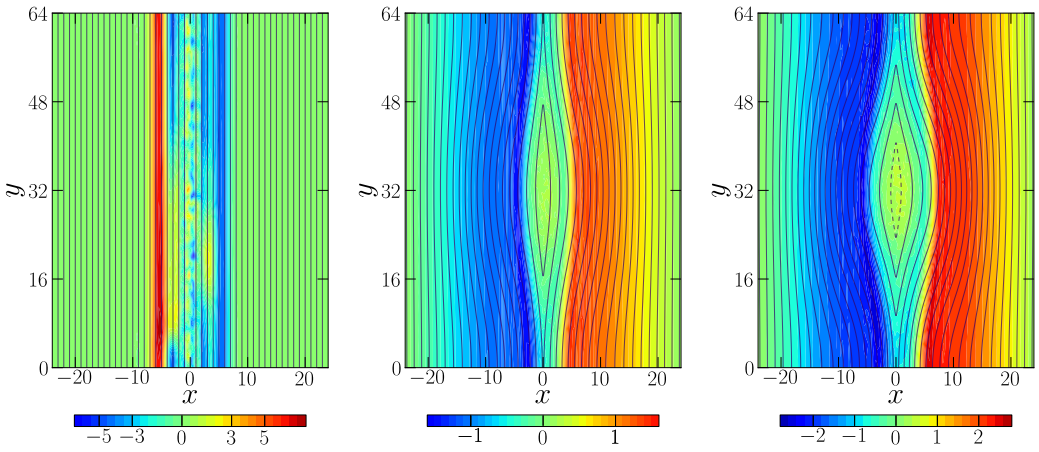

(a) $w = 0$ **(b)** $w = 4$ **(c)** $w = 8$

Figure 6.27.: *Snapshot of the electrostatic potential* ϕ *at* $t = 1800$ *with* $\eta_i = 5$ *and* $\eta_e = 5$. *The magnetic island leads to a strong generation of the zonal flow, which radially extends over wide radial domain. We found that larger islands widths show an increased production of zonal flow.*

geometry, this mechanism is not applicable and thus oscillations of the vortex mode are not observed.

The heat flux over the magnetic island width is shown in Fig. 6.28. Here, we compare the electrostatic heat flux obtained from simulations including adiabatic electrons, with simulations including kinetic electrons. We find that the averaged heat flux strongly increases with increasing island widths. The standard error of the average heat flux estimates is shown using error bars. We speculated two reasons for this very strong increase: First, the magnetic island excites the ITG even apart the rational surface and thus effectively increasing the hear transport (this is relevant as in sheared slab geometry a steady-state turbulence cannot be achieved). Second, the majority of the heat flux is transported by lower mode numbers, suggesting that the island structure has a strong influence on the transport characteristics itself. To confirm last point, we show the in Fig. 6.29 the time-averaged heat flux spectra over the magnetic island width. As the poloidal spectra, the heat flux spectra is qualitatively different between the adiabatic electron case (a) and the kinetic electron case (b). Namely, the kinetic electron case is much more sensitive to the island structure and shows that the majority of the heat flux is transported by low-k_y (large scale) modes and confirms by Hornsby et al. (2010). The heat flux spectra of the ITG-ke is in contrast to the adiabatic case, where the majority of the heat flux is transported at the linear most unstable wavenumber.

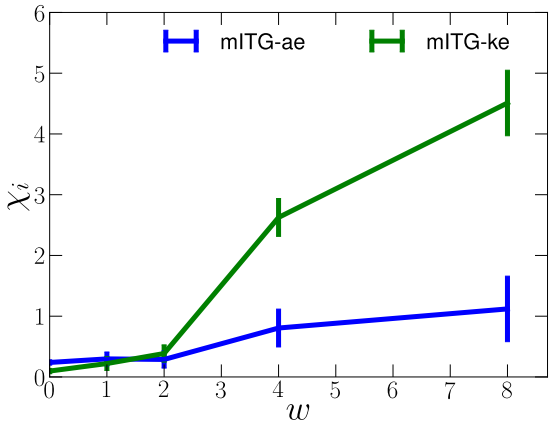

Figure 6.28: *Heat flux dependence (χ_i) vs the magnetic island width (w) for the case with adiabatic electrons (mITG-ae) and the case with kinetic electrons with $\eta_e = 5$ (mITG-ke). A magnetic island strongly increases the ion heat flux, mainly due to the extended turbulence width. The heat flux in the case with kinetic electrons is found to be substantially larger than from the case with adiabatic electrons. The increase can be understood from investigating the heat flux spectra.*

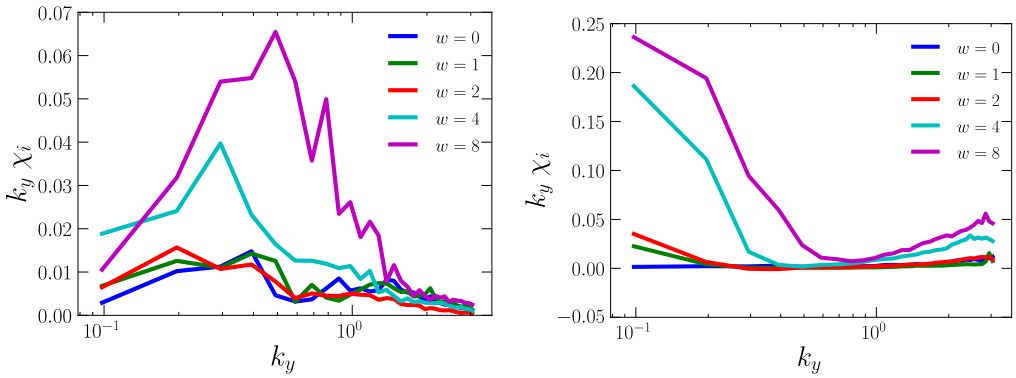

(a) *adiabatic electrons* **(b)** *kinetic electrons*

Figure 6.29.: *Averaged ion heat flux (χ_i) contributions for various magnetic island widths (w), for the case with adiabatic electrons (left figure) and the case with kinetic electrons (right figure). For the case with adiabatic electrons, the main heat flux contributions peak around the mode with maximum linear growth rates. For the case with kinetic electrons, heat flux contributions peak at a scale comparable to the magnetic island structure, showing the island's strong influence on the dynamics.*

6.7 | Summary

We started our discussion with the formations of magnetic island through magnetic reconnection and its numerical simulation. We obtained numerically the magnetic flux eigenfunction which was used in our gyrokinetic simulations as a static perturbation of our two-dimensional sheared slab geometry. The magnetic island introduced a geometrical coupling between the ITG modes; and for large enough islands to the formation of new rational surfaces. For the case of the linear ITG with adiabatic electrons: we found that a small magnetic island has a stabilization effect on the ITG mode by allowing unstable modes to dissipate energy through stable modes. For large islands, we found that the destabilization through rational surface separation dominates. This destabilization mainly originated from the short-wavelength region of the ITG. Using a minimized gyrokinetic model, we found that the so-called double-ITG mechanism is the responsible mechanism for the destabilization which preferably destabilizes the short-wavelength ITG modes due to their smaller radial eigenmode width. We continued our investigation by including kinetic electrons. A resonance of the kinetic electrons at the rational surface which strongly reduced the growth rates of the ITG modes made comparison with the adiabatic electron case difficult. Nevertheless, we could confirm qualitative similarities concerning destabilization for large magnetic islands. The contour plots of the electrostatic potential revealed however that the effect of the kinetic electrons and the flux-averaging effect at the closed flux-surfaces at the O-point had a strong influence on the linear mode structure of the ITG. For the nonlinear case, to account for the flux-surface averaging in presence of curved field lines, kinetic electrons are crucial. We found that the magnetic island strongly increases the nonlinear heat fluxes and in contrast to adiabatic simulations, the main heat flux was transported at spatial scales comparable to the island.

7 | Outroduction

During the previous six chapters, the reader was introduced to many aspects of gyrokinetic theory and its application. In the following two sections, the author would like to to summarize the achievements made during this PhD study, and give an outlook about possible extension of this research.

7.1 | Conclusion

Development of massive parallel gyrokinetic Vlasov code

As a powerful tool to study the multi-scale turbulence, an Euler-type gyrokinetic code, named gkc++ , has been developed by employing C++/Cilk+ . This is the first gyrokinetic code using such an approach as known to the author. The computational requirements are very demanding in the CPU time required for a multi-scale simulation and the datasets which are produced during one simulation run. To tackle the former issue, the author parallelized the code using MPI to domain decompose the numerical grid and solve them on multiple computer nodes. Additionally, OpenMP is used for an efficient in-node parallelization, and Cilk+ to guarantee an optimal vectorization. Such efforts were crucial for the subsequent work in order to evolve the turbulent fluctuations in the five-dimensional phase-space including an arbitrary number of species. To tackle the data analysis, an interface to HDF-5 has been developed in order to efficiently output the large multi-dimensional datasets. Furthermore, a frame-work using python (pytables/scipy) has been developed to analyse the obtained data sets. Finally, to guarantee the correctness of the numerical code on one hand, and to distinguish between numerical properties on the other hand, the dispersion relation of the linear gyrokinetic equation system in the two-dimensional sheared-slab is solved as a non-linear eigenvalue problem for benchmarking.

Clarification of the role of stable modes in a linearly mode coupled discretized gyrokinetic system

Kinetic effects, such as Landau damping and/or the FLR effects play a crucial role in determining the characteristic of the drift waves such as the ion temperature gradient

mode. However, Landau damping in collisionless gyrokinetic Vlasov simulations originates from the phase mixing of marginally stable Case–van Kampen (CvK) eigenmodes, which restricts damping to a finite recurrence time. It is thus questionable, whether the stabilization effect through Landau damped, stable modes is correctly reproduced in the nonlinear saturation state or a linearly coupled system. More specifically, it is an interesting question whether the stabilization effect of stable modes is properly evaluated in case where coupling between the modes arises through an external vortex flow. To resolve this problem, the author investigated the characteristics of marginally stable and damped modes, based on the gkc++ code and eigenvalue analysis. It was found that in the absence of collision, the time evolution of the electrostatic potential of stable ITG modes strongly depends on the initial perturbation in velocity space. Namely, in the case with random noise perturbation, stable ITG modes were not damped, but exhibited a marginal behavior with small amplitude fluctuations. On the other hand, in the case of a Maxwellian perturbation, damping of the electrostatic potential was observed with a damping rate as predicted by Landau's theory. However, the electrostatic potential is subject to recurrence beyond which the simulation becomes ambiguous. Based on the eigenvalue analysis, it is confirmed that such a behavior results from the appearance of the CvK eigenmodes which show marginal stability with different real frequencies, and the resultant phase mixing between them. Note that the damping due to phase mixing is not ascribed to a normal mode as an eigenstate. Furthermore, it is found that such CvK eigenmodes are very sensitive to collisional dissipation. Namely, a finite collisional dissipation leads to the damping of the CvK eigenmodes. Once these CvK eigenmodes are damped down to the rate predicted by the Landau's theory, we found that a normal-mode corresponding to the Landau eigenmode appears. Consequently, the recurrence phenomena is suppressed so that the simulations beyond the recurrence time became valid. The required critical collisionality to reproduce the Landau eigenmode crucially depended on the number of grid points used. Namely, a higher (lower) resolution in velocity space generally required a lower (higher) collisionality in order to reproduce Landau damping through an eigenmode. However, once collisionality was too large, collisional damping arises physically. Thus only a limited range of collisionality can be chosen in order to reproduce the Landau damping through an eigenmode. In addition, in order to investigate the validity of the energy transfer from unstable ITG modes to stable modes through mode coupling, a minimal model was introduced, where two poloidal modes, one unstable mode and one stable mode, are coupled by a tertiary vortex mode. We found two different mechanisms for damping, i.e. damping due to the phase-mixing of marginal CvK eigenmodes without collisional dissipation and Landau damping with weak collision. Those two provide same growth rate up to the recurrence time. Using the above model, we showed that the growth rate of the unstable global mode is reduced independent on the collisionality. We concluded that the energy transfer from unstable modes to stable modes through mode coupling can be properly reproduced without depending on whether damping results from the phase mixing subject to recurrence or

Landau damping through an eigenmode in velocity space.

Discovery of the short-wavelength destabilization of the ITG in the presence of a static magnetic island

The ITG mode is further destabilized at the short-wavelength region, which is found in the gyrokinetic model — but not in the gyrofluid model. First, the existence of the short-wavelength ITG mode was confirmed by applying an analytical approach as well as by employing gyrokinetic simulations. A parameter scan revealed the dominance of the short-wavelength ITG existing over a wide range of parameters and its sensitivity to the destabilization through shearing effects and kinetic electron dynamics. Second, the author considered the ITG instability with a static magnetic island. By using the more accurate gyrokinetic equation system, which includes self-consistently the Landau damping and finite Larmor radius effects, the results obtained from the gyrofluid simulations were be confirmed. Namely, a small magnetic island stabilizes the ITG mode by inducing poloidal coupling between unstable and stable modes. However, it was found that the stabilization effect is weaker in the gyrokinetic model, as gyrofluid simulations overestimated the damping. Also, gyrokinetic simulations confirmed the destabilization of the ITG mode due to the formation of new rational surfaces for large magnetic islands. However, in contrast to gyrofluid simulations, the destabilization effect was mainly caused by the short-wavelength ITG mode due to a resonance effect (double-ITG mode). From a reduced model, we deducted that the destabilization of the short-wavelength mode originated from its smaller mode structure width and thus it is more sensitive to rational surface separation.

Study of multi-scale turbulences interaction including a static magnetic island

In multi-scale turbulence simulation with a static magnetic island, kinetic electrons are required, as the flux-surface averaging can not be modeled with an adiabatic electron response. However, including a kinetic electron species increases the computational requirement by more than one order of magnitude, as not only a further species needs to be evolved, but also because the thermal velocity of the electrons strongly reduces the maximum stable time step in the simulations. To properly calculate the effect of kinetic electrons and also benchmark the simulation code, first, a careful parameter scan has been performed to better understand the effect of kinetic electrons on the ITG instability in the case without magnetic island. Second, for the case with a magnetic island, an electrostatic vortex mode at the O-point of the island is found. It is identified that this structure results from a flux-averaging effect accounted to the electrons, which is not observed in simulations with adiabatic electrons. Furthermore, we observed a strong increase of the heat flux for increasing island widths.

7.2 | Extensions of this PhD study

"Every answer raises more questions" — and this study is no different. During a PhD many interesting ideas or results are found but have to be abandoned due to time restrictions. In the following some ideas are summarized for a continuation of the research presented here:

7.2.1 | Chapter 3: Improving the gkc++ solver

The following research is proposed on this topic:

- Improvement of the hybrid parallelization scheme to hide *MPI latencies* by overlaying communications with computations.
- Usage of accelerators such as GPUs. Cilk+ is specifically designed to exploit the additional computing and parallelization capabilities provided by such co-processors.
- Replace the finite-difference stencils by more advanced stencils such as the IDO-CF scheme suggested by Imadera et al. (2009).

7.2.2 | Chapter 4: Landau damping in the discretized system

The following research is proposed on this topic:

- Numerical study of the collapse of the Case-van Kampen eigenmodes for a finite hyper-diffusivity or even more advanced gyrokinetic collisional operators such as suggested by Abel et al. (2008) and Barnes et al. (2009).
- In collisionless damping, algebraic decay is found for non-entire functions as discussed by Xie (2013). However, it is questionable if algebraic decay is found for a discrete Landau spectra. Some investigations were done on this Ng et al. (2004).
- Investigation of gyrokinetic turbulence and the influence of linear Landau damping characteristics: phase-mixing (with recurrence) or Landau damping through discrete eigenmodes. This research would probably require rewriting gkc++ to use Fourier-Hermite basis for parallel velocity space resolution.
- Investigate of the ITG saturation through stable eigenmodes by projecting the time dependent solution of the nonlinear initial value problem onto the eigenmodes of the linear system.

7.2.3 | Chapter 5: Short-wavelength destabilization of the ITG

The following research is proposed on this topic:

- Investigate the short-wavelength effects in toroidal geometry where trapped electrons can excite it.

- Investigate electromagnetic effects on the short-wavelength ITG mode, see e.g. Gao et al. (2002).
- Role of short-wavelength effects in presence of impurities.

7.2.4 | Chapter 6: Interactions of ITG, ETG and magnetic island

The following research is proposed on this topic:

- Relaxation of the static island assumption by self-consistent investigating the cross-scale interaction between a magnetic island and the ITG mode. A similar study was done by Li et al. (2009) in the gyrofluid limit which remain to be extended into the gyrokinetic framework.
- In cylindrical geometry, magnetic islands are known to rotate. Investigation of the influence of a static magnetic island on the ITG in cylindrical geometry by also taking the rotation of the island into account may provide interesting insights.

7.3 | Final remark

The author would like to thank the reader again for his interest in this topic. If this thesis left some points unclear — or more information is requested, the author encourages the reader to contact him.

A | Benchmarking the numerical code

In order to verify the numerical implementation of the gyrokinetic equation system, we first introduce the plasma dispersion function and Bessel functions, which are later used when deriving the analytic dispersion relation. Finally, we compare the analytic solution from the dispersion relation with the numerical solution obtained from solving an initial value problem using gkc++ .

A.1 | The plasma dispersion function

An integral which often arises in plasma physics, is the *Fried-Conte plasma dispersion function* (PDF) Z given by

$$\mathrm{Z}(\zeta) = \begin{cases} \frac{1}{\sqrt{\pi}} \int_{-\infty}^{\infty} \frac{\exp[-u^2]}{u-\zeta} \,\mathrm{d}u & \mathrm{Im}(\zeta) > 0 \\ \frac{1}{\sqrt{\pi}} \int_{-\infty}^{\infty} \frac{\exp[-u^2]}{u-\zeta} \,\mathrm{d}u + \ \pi i e^{-\zeta^2} & \mathrm{Im}(\zeta) = 0 \\ \frac{1}{\sqrt{\pi}} \int_{-\infty}^{\infty} \frac{\exp[-u^2]}{u-\zeta} \,\mathrm{d}u + 2\pi i e^{-\zeta^2} & \mathrm{Im}(\zeta) < 0 \end{cases} \quad . \tag{A.1}$$

For a numerical computation of the plasma dispersion function, it is convenient to use the similarity to the *complex error function* given by

$$\mathrm{erf}\,(x) = \frac{2}{\sqrt{\pi}} \int_0^x \exp[-t^2] \,\mathrm{d}t \quad , \tag{A.2}$$

as shown by Huba (2009) and which is often available from numerical libraries. The plasma dispersion function is then given through the identity:

$$\mathrm{Z}(\zeta) = i\sqrt{\pi} e^{-\zeta^2} \Big[1 + \mathrm{erf}(\zeta i) \Big] \quad . \tag{A.3}$$

The libraries themselves make use of e.g the two-pole approximation of the plasma dispersion function for it's calculation as discussed by Poppe and Wijers (1990). The real and imaginary part of the plasma dispersion function in the complex plane is shown in Fig. A.1. When using the identity (A.3) for a numerical computation of Z, we found

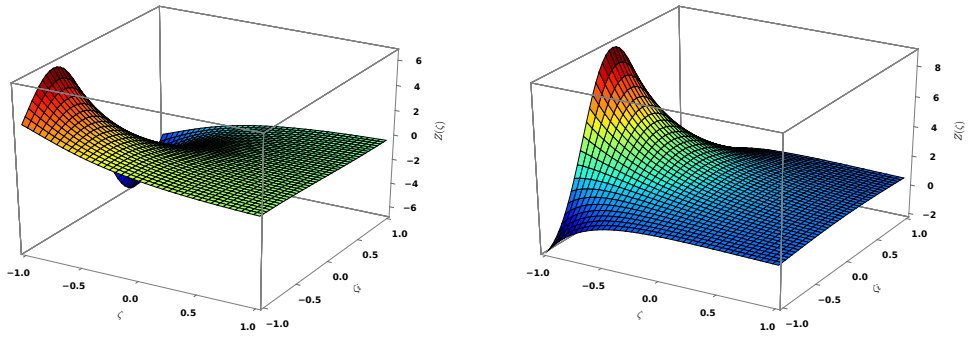

(a) $\mathrm{Re}\,(Z)$ **(b)** $\mathrm{Im}\,(Z)$

Figure A.1.: *The plasma dispersion function Z on the complex plane.*

that for large values of $\mathrm{Im}(\zeta)$, rounding error occur which result in a loss of precisions. This can be avoided if the asymptotic expansion for $|\zeta| \gg 1$ is used given by

$$\overline{\mathrm{Z}(\zeta)} = i\sqrt{\pi}\sigma e^{-\zeta^2} - \zeta^{-1}\left(1 + \frac{1}{2\zeta^2} + \frac{3}{4\zeta^4} + \frac{15}{8\zeta^6} + \dots\right)$$
$$\text{with} \qquad \sigma = \begin{cases} 0 & \zeta_i > 0 \\ 1 & \zeta_i = 0 \\ 2 & \zeta_i < 0 \end{cases} \quad , \tag{A.4}$$

For small values of $|\zeta| \ll 1$, we can the Taylor expansion around $\zeta = 0$,

$$\underline{\mathrm{Z}(\zeta)} = i\sqrt{\pi}e^{-\zeta^2} - 2\zeta\left(1 - \frac{2\zeta^2}{3} + \frac{4\zeta^4}{15} - \frac{8\zeta^6}{105} + \dots\right) \quad . \tag{A.5}$$

A very useful identity of the plasma dispersion functions when calculating terms of the form

$$Z_n(\zeta) = \frac{1}{\sqrt{\pi}}\int_{-\infty}^{\infty} d\zeta \frac{u^n e^{-\zeta^2}}{u - \zeta} \quad , \tag{A.6}$$

can be obtained from recursion relations of the plasma dispersion function, which for

$n = 0, \ldots, 3$ gives

$$\mathrm{Z}_0(\zeta) = \frac{1}{\sqrt{\pi}} \int_{-\infty}^{\infty} \frac{u \ \exp[-u^2]}{u - \zeta} \, \mathrm{d}u = \mathrm{Z} \quad , \tag{A.7}$$

$$\mathrm{Z}_1(\zeta) = \frac{1}{\sqrt{\pi}} \int_{-\infty}^{\infty} \frac{u \ \exp[-u^2]}{u - \zeta} \, \mathrm{d}u = 1 + \zeta \, \mathrm{Z} \quad , \tag{A.8}$$

$$\mathrm{Z}_2(\zeta) = \frac{1}{\sqrt{\pi}} \int_{-\infty}^{\infty} \frac{u^2 \exp[-u^2]}{u - \zeta} \, \mathrm{d}u = \zeta + \zeta^2 \, \mathrm{Z}(\zeta) \quad , \tag{A.9}$$

$$\mathrm{Z}_3(\zeta) = \frac{1}{\sqrt{\pi}} \int_{-\infty}^{\infty} \frac{u^3 \exp[-u^2]}{u - \zeta} \, \mathrm{d}u = \frac{1}{2}\Big[1 + 2\zeta^2\big(1 + \zeta \, \mathrm{Z}(\zeta)\big)\Big] \quad . \tag{A.10}$$

Finally, a generalization of the PDF known as the *incomplete plasma dispersion function* for semi-finite domain was discussed by Baalrud (2013).

A.2 | Notes on the Bessel functions used in gyrokinetics

The Bessel functions of the first kind arise when calculating the gyro-average in Fourier space, and for an integer number n are defined by

$$J_n(x) = \frac{i^{-n}}{\pi} \int_0^{\pi} \mathrm{d}\theta \ e^{ix\cos\theta} \cos(n\theta) \quad . \tag{A.11}$$

Most important are the zeroth-order J_0 and first-order J_1 Bessel functions shown in Fig. A.2a. The Taylor expansion for both functions is given by

$$\mathrm{J}_0(z) = 1 - \frac{\zeta^2}{4} + \frac{\zeta^4}{64} - \ldots \quad , \quad \mathrm{J}_1(z) = \frac{\zeta}{2} - \frac{\zeta^3}{16} + \ldots \quad , \tag{A.12}$$

where we see the identity that $\mathrm{J}_0{}'(z) = -\,\mathrm{J}_1(z)$. The asymptotic expansion of J_α, for a real number α is given by

$$\overline{J_\alpha}(x) = \sqrt{\frac{2}{\pi x}} \cos\left(x - \frac{\alpha\pi}{2} - \frac{\pi}{4}\right) \tag{A.13}$$

gives so that

$$\overline{J_0} = \sqrt{\frac{2}{\pi x}} \cos\left(x - \frac{\pi}{4}\right) \quad , \quad \overline{J_1} = \sqrt{\frac{2}{\pi x}} \cos\left(x - \frac{3\pi}{4}\right) \quad . \tag{A.14}$$

The decaying in leading order for large values is $J_{0,1} \propto x^{1/2}$. A fundamental integration identity of the Bessel function is given by Abramowitz and Stegun (1964) is

$$\int_{x=0}^{\infty} x \, e^{-x^2} \, J_n^2(\alpha x) \, \mathrm{d}x = \tfrac{1}{2} e^{-\alpha^2/2} I_n\left(\frac{\alpha^2}{2}\right) \quad . \tag{A.15}$$

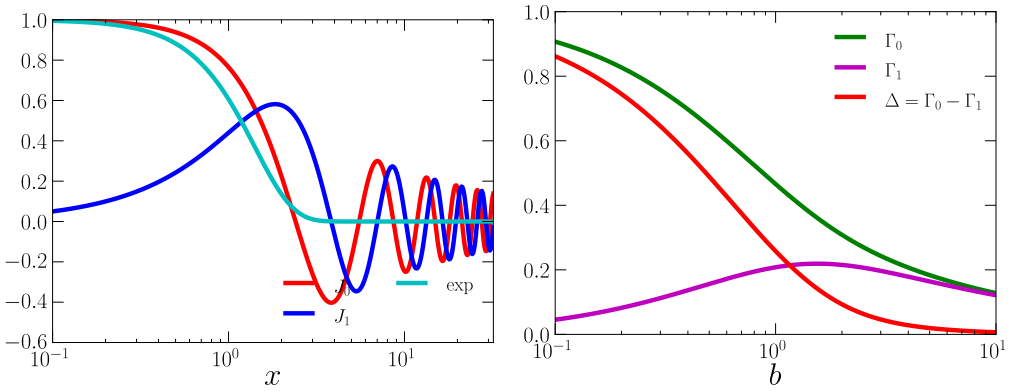

(a) J_0, J_1 *and* exp *functions* **(b)** Γ_0 *and* Γ_1 *functions*

Figure A.2.: *Plot of Bessel functions and* Γ *functions common in gyrokinetics.*

If we substitute above identity with $x = \sqrt{\mu}$, so that $\mathrm{d}x = \frac{1}{2}\frac{1}{\sqrt{\mu}}d\mu$ gives

$$\int_{\mu=0}^{\infty} e^{-\mu} J_n^2(\lambda\sqrt{\mu})\,\mathrm{d}\mu = e^{-b} I_n(b) \quad , \tag{A.16}$$

which for $n = 0$ is used to simplify Eq.(A.23a). A similar integration identity can be obtained, to simplify Eq.(A.23b), namely

$$\int_{x=0}^{\infty} x^3 e^{-x^2} J_n^2(\alpha x)\,\mathrm{d}x = \tfrac{1}{2} e^{-\frac{\alpha^2}{2}} \left[\left(1 - \frac{\alpha^2}{2}\right) I_n\left(\frac{\alpha^2}{2}\right) + \left(\frac{\alpha^2}{2}\right) I_n'\left(\frac{\alpha^2}{2}\right)\right] \quad , \tag{A.17}$$

defining $b = \frac{\lambda^2}{2}$ which results in noting that $I_0' = I_1$, we get

$$\int_{\mu=0}^{\infty} \mu e^{-\mu} J_n^2(\lambda\mu)\,\mathrm{d}x = e^{-b}\left[(1-b)\,I_n(b) + (b)\,I_n'(b)\right] \quad . \tag{A.18}$$

A.3 | Dispersion relation in shearless slab geometry

The electrostatic gyrokinetic Vlasov equation for species σ in a three dimensional slab geometry within the local approximation is given by

$$\frac{\partial f_{1\sigma}}{\partial t} = -\left(1 + \eta_\sigma\left[\frac{m_\sigma v_\parallel^2 + 2\mu B_0}{2T_\sigma} - \frac{3}{2}\right]\right)\frac{\partial \langle\phi\rangle}{\partial y} f_{0\sigma} - v_\parallel\left(\frac{\partial f_{1\sigma}}{\partial z} - q_\sigma \frac{\partial \langle\phi\rangle}{\partial z} f_{0\sigma}\right) \quad ,$$

where $f_{0\sigma}$ is the Maxwellian discussed in Eq.(2.42) and $f_{1\sigma}$ is the perturbed distribution function. Transforming to Fourier space, the gyro-average over $\langle\phi\rangle$ can be calculated

by multiplying the Bessel function $\langle\phi\rangle = J_0(\sqrt{\lambda\mu})\phi$, with the usual definition of μ and λ. We assume a harmonic dependence on $f_{1\sigma}$ such that we can write as $f_{1\sigma} = \hat{f}_{1\sigma}\exp[-i\omega t + i\mathbf{k}\cdot\mathbf{x}]$ and $\phi = \hat{\phi}\exp[-i\omega t + i\mathbf{k}\cdot\mathbf{x}]$, so that (skipping the hat symbol for readability), we get

$$(\omega - v_\parallel k_\parallel) f_{1\sigma} = -\left(1 + \eta_\sigma\left[\frac{m_\sigma v_\parallel^2 + 2\mu B_0}{2T_\sigma} - \frac{3}{2}\right]\right) k_y J_0(\sqrt{\lambda\mu}) - q_\sigma v_\parallel k_\parallel J_0(\sqrt{\lambda\mu})\phi f_{0\sigma} \quad .$$

After reordering we get

$$f_{1\sigma} = \frac{\left(1 + \eta_\sigma\left[\frac{m_\sigma v_\parallel^2 + 2\mu B_0}{2T} - \frac{3}{2}\right]\right) k_y J_0 - v_\parallel k_\parallel J_0}{\omega - v_\parallel k_\parallel}\phi f_{0\sigma} \quad . \tag{A.19}$$

The perturbation of the species σ is connected through the gyrokinetic quasi-neutrality condition (assuming $\lambda_D = 0$) given by

$$\left\{\sum_\sigma \frac{q_\sigma^2 n_\sigma}{T_\sigma}\Big[1 - \Gamma_0(b_\sigma)\Big]\right\}\phi = \sum_\sigma q_\sigma \int_{\mu=0}^{\infty}\int_{v_\parallel=-\infty}^{\infty} J_0(\lambda) f_{1\sigma}\,\mathrm{d}v_\parallel\,\mathrm{d}\mu \quad . \tag{A.20}$$

Note again the back-transformation on the right-hand side of above equation required an additional J_0 factor. First, we assume now a two species plasma with an kinetic ion species and adiabatic electrons and assuming $T_i = T_e = 1$, $n_i = n_e = 1$ and $q_i = 1$ for simplicity, the quasi-neutrality condition becomes

$$\Big[1 - \Gamma_0(b_i) + 1\Big]\phi = \int_{\mu=0}^{\infty}\int_{v_\parallel=-\infty}^{\infty} J_0(\lambda_i) f_{1i}\,\mathrm{d}v_\parallel\,\mathrm{d}\mu \quad . \tag{A.21}$$

Using Eq.(A.19) on the right-hand side of the above equation gives

$$2 - \Gamma_0 = -\int_{v_\parallel=-\infty}^{\infty}\int_{\mu=0}^{\infty} \frac{\left(1 + \eta_i\left[m_i v_\parallel^2 - \frac{3}{2}\right]\right) k_y J_0^2 + \eta_i k_y \mu J_0^2 - v_\parallel k_\parallel J_0^2}{\omega - v_\parallel k_\parallel} f_{0\sigma}\,\mathrm{d}\mu\,\mathrm{d}v_\parallel \quad , \tag{A.22}$$

First step we perform the integration over the first adiabatic constant μ. In the integration, two types of integrands arises which can be analytically calculated through integral identities discussed in Sec. A.2, where

$$\int_{\mu=0}^{\infty} J_0^2(\sqrt{\lambda\mu}) e^{-\hat{\mu}}\,\mathrm{d}\mu = e^{-b} I_0(b) = \Gamma_0 \quad , \tag{A.23a}$$

$$\int_{\mu=0}^{\infty} J_0^2(\sqrt{\lambda\mu}) e^{-\hat{\mu}}\mu\,\mathrm{d}\mu = \Gamma_0 - b\,(\Gamma_0 - \Gamma_1) \quad , \tag{A.23b}$$

where Γ_0 and Γ_1 are defined as $\Gamma_0 = I_0(b)e^{-b}$ and $\Gamma_1 = I_1(b)e^{-b}$, where I_0 (I_1) is the zeroth (first) order modified Bessel function of the zeroth kind. With the above identities and defining $\Gamma_{\overline{01}} = \Gamma_0(b) - \Gamma_1(b)$ and $\Lambda_{k_\perp} = 2 - \Gamma_0(b)$, we arrive at

$$\Lambda_{k_\perp} = -\int_{v_\parallel=-\infty}^{\infty} \frac{\left(1+\eta\left[{v_\parallel}^2 - \frac{3}{2}\right]\right) k_y \Gamma_0 + \eta k_y \left[\Gamma_0 - b\Gamma_{\overline{01}}\right] - v_\parallel \hat{k}_\parallel \Gamma_0}{\omega - v_\parallel \hat{k}_\parallel} f_{0\sigma}\, \mathrm{d}v_\parallel \quad . \tag{A.24}$$

The next step is the integration over the parallel velocity $v_\parallel$, where we make use of the *plasma dispersion function* discussed in Sec.(A.1). Defining $\zeta = \omega/\hat{k}_\parallel$ we obtain

$$\Lambda_{k_\perp} = \left\{ -\left(1-\tfrac{\eta}{2}\right)\tfrac{k_y}{\hat{k}_\parallel}\Gamma_0 Z + \eta\tfrac{k_y}{\hat{k}_\parallel} b\Gamma_{\overline{01}} Z - \eta\tfrac{k_y}{\hat{k}_\parallel}\left(\zeta + \zeta^2 Z\right)\Gamma_0 + \Gamma_0 + \zeta Z \Gamma_0 \right\} \phi \quad , \tag{A.25}$$

$$-\left(1-\tfrac{\eta}{2}\right)\tfrac{k_y}{\hat{k}_\parallel}\Gamma_0 Z + \eta\tfrac{k_y}{\hat{k}_\parallel} b\Gamma_{\overline{01}} Z - \tfrac{k_y}{k_\parallel}\eta\left(\zeta + \zeta^2 Z\right)\Gamma_0 + \zeta Z \Gamma_0 + \Gamma_0 + \Lambda_{k_\perp} = 0 \quad , \tag{A.26}$$

The dispersion relation is solved numerically using a numerically root finding algorithm such as Muller (1956) method, Riddley, Newton iteration or Davies (1986) method. Note that the convergence and the accuracy of the solution highly depends on the method used, however, we found that Müllers method was the best choice in convergence radius, stability and convergence speed.

A.3.1 | Comparison to the numerical solution

Figure A.3 shows the growth rate and frequency obtained from solving the dispersion relation in Eq.(A.26). Physical parameters are chosen to $\eta = 6$, $k_x = 0$ and $k_\parallel = \theta k_y$. The numerical solution of the corresponding initial value problem obtained by using gkc++ is shown by the dots. The numerical parameters, where chosen such that a converged solution was obtained. We find that we can well reproduce the growth rates and frequency of the unstable modes. The stable modes however, are not correctly reproduced in the IVP, as a result of the discretization of the parallel velocity space as discussed in Ch. 4.

A.4 | Dispersion relation in non-local geometry

The local approximation can only be applied for very simple magnetic field geometries, with only limited application to a plasma in the Tokamak. A more realistic geometry is the two-dimensional sheared slab geometry discussed in Sec. 2.10.2, where the parallel wavenumber is given by $k_\parallel = \hat{s}xk_y$. However, in this case the derivative in the parallel direction has an x-dependence, while the gyro-averaged fields are calculated in Fourier space. A Rayleigh-Ritz procedure is used to connect real space quantities with variables

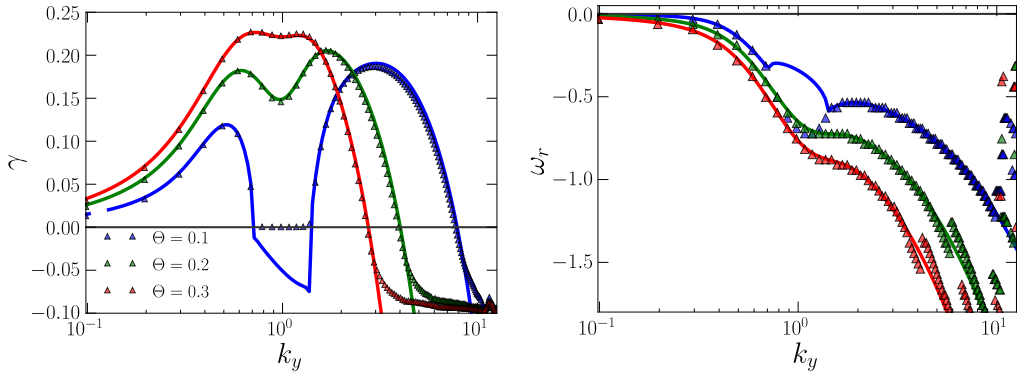

(a) *Growth rates* γ **(b)** *Frequency* ω_r

Figure A.3.: *Benchmark of gkc++ using full gyrokinetic dispersion relation with* $\eta = 6$ *and* $k_x = 0$. *We found very good agreement.*

defined Fourier space. The theoretical outline of this procedure is given by Dong et al. (1987) and Lee et al. (1987), with some further discussions in Gao et al. (2003) and Idomura et al. (2000). From Zhe (2004): in the electrostatic case we get an integral equation of the form,

$$\lambda_D^2 \phi + \sum_\sigma \frac{q_\sigma T_e}{T_\sigma} \left\{ 1 + \int \frac{\mathrm{d}k'}{2\pi} \int \mathrm{d}x \exp\left(i(k'-k)x\right) L_\sigma \right\} = 0 \quad , \tag{A.27}$$

where $\mathcal{L}(\omega)$ is a complex, non-hermitian matrix given by Gao et al. (2003). Equation (A.27) represents a nonlinear eigenvalue problem of the form $\mathcal{L}(\omega)\phi = 0$, which is solved using the procedure as outline in Fig. 5.2.

A.4.1 | Numerical benchmark for sheared slab geometry

Here we use following settings for the kinetic ion species $\eta_i = 5$ and $\hat{s} = 0.2$, while the electrons are assumed to be adiabatic. For the theoretical dispersion relation the integral code is used with $N_x = 128$, and the most unstable modes in the regime between $k_y = 0.1$ and $k_y = 10$ are extracted. The resulting linear growth rates and frequencies over the poloidal mode number are shown in Fig.(A.4), where the results obtained from gkc++ are shown as dots. Note that by using the analytical solution, we find multiple branches of the ITG mode, whereas the solution as an IVP does only resolve the most unstable mode in the long time limit. We can observe this through the frequency jump, which occurs for the low-k_y ITG modes around $k_y = 0.1$ and for the high-k_y modes around $k_y = 1.2$. We find that the growth rates and frequencies are well reproduced with the numerical solution procedure. The eigenfunctions from both approaches are shown in Fig. A.5. Again, we find a good agreement.

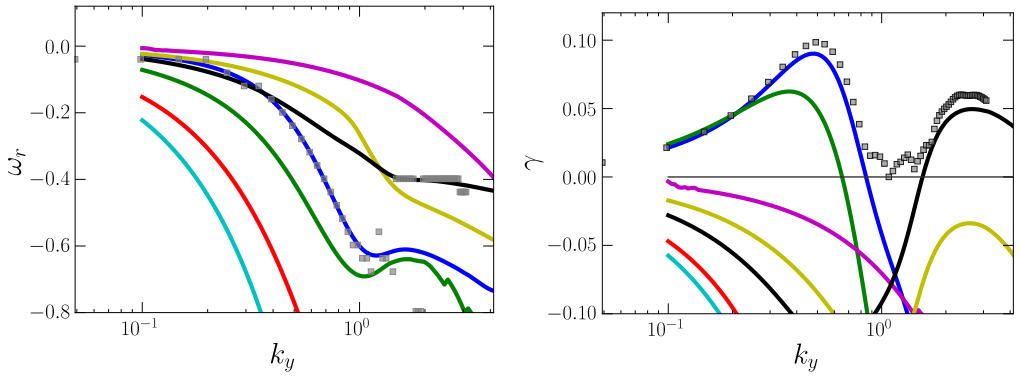

(a) *Frequency* ω_r **(b)** *Growth rates* γ

Figure A.4.: *Benchmark of gkc++ with an adiabatic electron species dispersion relation with* $\eta = 6$ *and* $k_x = 0$*. A good agreement is found.*

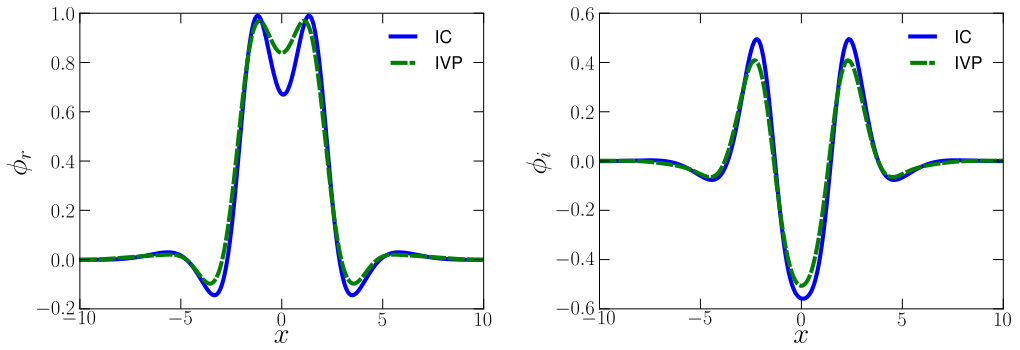

(a) $\mathrm{Re}\,\phi$ **(b)** $\mathrm{Im}\,\phi$

Figure A.5.: *Comparing the eigenfunctions from the initial value code and integral code method. We find a good agreement.*

Bibliography

I. G. Abel, M. Barnes, S. C. Cowley, W. Dorland, and A. A. Schekochihin. Linearized model Fokker-Planck collision operators for gyrokinetic simulations. I. Theory. *Physics of Plasmas*, 15(12):122509, December 2008. doi: 10.1063/1.3046067.

Milton Abramowitz and Irene A. Stegun. *Handbook of Mathematical Functions with Formulas, Graphs, and Mathematical Tables*. Dover Publications, New York, 1964. ISBN 0-486-61272-4.

Gene M. Amdahl. Validity of the single processor approach to achieving large scale computing capabilities. In *Proceedings of the April 18-20, 1967, spring joint computer conference*, AFIPS '67 (Spring), pages 483–485, New York, NY, USA, 1967. ACM. doi: 10.1145/1465482.1465560.

E. Anderson, Z. Bai, J. Dongarra, A. Greenbaum, A. McKenney, J. Du Croz, S. Hammerling, J. Demmel, C. Bischof, and D. Sorensen. Lapack: a portable linear algebra library for high-performance computers. In *Proceedings of the 1990 ACM/IEEE conference on Supercomputing*, Supercomputing '90, pages 2–11, Los Alamitos, CA, USA, 1990. IEEE Computer Society Press. ISBN 0-89791-412-0.

Akio Arakawa. Computational design for long-term numerical integration of the equations of fluid motion: Two-dimensional incompressible flow. part i. *Journal of Computational Physics*, 1(1):119 – 143, 1966. ISSN 0021-9991. doi: 10.1016/0021-9991(66)90015-5.

S. D. Baalrud. The incomplete plasma dispersion function: Properties and application to waves in bounded plasmas. *Physics of Plasmas*, 20(1):012118, 2013. doi: 10.1063/1.4789387.

Satish Balay, Jed Brown, , Kris Buschelman, Victor Eijkhout, William D. Gropp, Dinesh Kaushik, Matthew G. Knepley, Lois Curfman McInnes, Barry F. Smith, and Hong Zhang. PETSc users manual. Technical Report ANL-95/11 - Revision 3.3, Argonne National Laboratory, 2012.

M. Barnes, I. G. Abel, W. Dorland, D. R. Ernst, G. W. Hammett, P. Ricci, B. N. Rogers, A. A. Schekochihin, and T. Tatsuno. Linearized model Fokker-Planck collision operators for gyrokinetic simulations. II. Numerical implementation and tests. *Physics of Plasmas*, 16(7):072107, July 2009. doi: 10.1063/1.3155085.

C. O. Beasley, Jr., K. Molvig, and W. I. van Rij. Universal mode with diffusive electrons: Linear instability and nonlinear saturation. *Physics of Fluids*, 26:678–683, March 1983. doi: 10.1063/1.864183.

OpenMP Architecture Review Board. OpenMP application program interface version 3.0, May 2008.

Vasil Bratanov. Landau and van kampen spectra in discrete kinetic plasma system. 2011.

Vasil Bratanov, Frank Jenko, David Hatch, and Stephan Brunner. Aspects of linear landau damping in discretized systems. *Physics of Plasmas*, 20(2):022108, 2013. doi: 10.1063/1.4792163.

A. Brizard. Gyrokinetic energy conservation and poisson-bracket formulation. *Physics of Fluids B: Plasma Physics*, 1(7):1381–1384, 1989. doi: 10.1063/1.858968.

A. J. Brizard and T. S. Hahm. Foundations of nonlinear gyrokinetic theory. *Reviews of Modern Physics*, 79(2):421, 2007. doi: 10.1103/RevModPhys.79.421.

S. Browne, J Dongarra, N. Garner, K. London, and P. Mucci. A portable programming interface for performance evaluation on modern processors. *The International Journal of High Performance Computing Applications*, 14:189–204, 2000.

A Burckel, O Sauter, C Angioni, J Candy, E Fable, and X Lapillonne. On the effects of the equilibrium model in gyrokinetic simulations: from s-α to diverted mhd equilibrium. *Journal of Physics: Conference Series*, 260(1):012006, 2010.

J. Canosa, J. Gazdag, and J.E. Fromm. The recurrence of the initial state in the numerical solution of the vlasov equation. *Journal of Computational Physics*, 15(1):34 – 45, 1974. ISSN 0021-9991. doi: http://dx.doi.org/10.1016/0021-9991(74)90067-9.

J. R. Cary and R. G. Littlejohn. Noncanonical Hamiltonian mechanics and its application to magnetic field line flow. *Annals of Physics*, 151:1–34, November 1983. doi: 10.1016/0003-4916(83)90313-5.

K.M Case. Plasma oscillations. *Annals of Physics*, 7(3):349 – 364, 1959. ISSN 0003-4916. doi: 10.1016/0003-4916(59)90029-6.

L. Chen, P. N. Guzdar, R. B. White, P. K. Kaw, and C. Oberman. Theory of Universal Eigenmodes in a Sheared Magnetic Field. *Physical Review Letters*, 41:649–653, August 1978. doi: 10.1103/PhysRevLett.41.649.

C.Z. Cheng and G. Knorr. The integration of the vlasov equation in configuration space. *Journal of Computational Physics*, 22(3):330–351, 1976. cited By (since 1996) 293.

J. Chowdhury, R. Ganesh, J. Vaclavik, S. Brunner, L. Villard, and P. Angelino. Short wavelength ion temperature gradient mode and coupling with trapped electrons. *Physics of Plasmas*, 16(8):082511, 2009. doi: 10.1063/1.3212890.

J. Chowdhury, R. Ganesh, S. Brunner, J. Vaclavik, and L. Villard. Toroidal universal drift instability: A global gyrokinetic study. *Physics of Plasmas*, 17(10):102105, 2010. doi: 10.1063/1.3490238.

J. Chowdhury, S. Brunner, R. Ganesh, X. Lapillonne, L. Villard, and F. Jenko. Short wavelength ion temperature gradient turbulence. *Physics of Plasmas*, 19(10):102508, 2012. doi: 10.1063/1.4759458.

P.C. Clemmow and J.P. Dougherty. *Electrodynamics of particles and plasmas*. Addison-Wesley series in advanced physics. Addison-Wesley Pub. Co., 1969.

W. J. Cody. Algorithm 715: Specfun;a portable fortran package of special function routines and test drivers. *ACM Trans. Math. Softw.*, 19(1):22–30, March 1993. ISSN 0098-3500. doi: 10.1145/151271.151273.

James W. Cooley and John W. Tukey. An algorithm for the machine calculation of complex Fourier series. *Math. Comp.*, 19:297–301, 1965. ISSN 0025-5718.

S. C. Cowley, R. M. Kulsrud, and R. Sudan. Considerations of ion?temperature?gradient?driven turbulence. 3(10):2767–2782, 1991. ISSN 08998221. doi: DOI:10.1063/1.859913.

Tilman Dannert. Gyrokinetische simulation von plasmaturbulenz mit gefangenen teilchen und elektromagnetischen effekten. 2006.

Tilman Dannert and Frank Jenko. Gyrokinetic simulation of collisionless trapped-electron mode turbulence. *Physics of Plasmas*, 12(7):072309, 2005. doi: 10.1063/1.1947447.

B Davies. Locating the zeros of an analytic function. *Journal of Computational Physics*, 66(1):36 – 49, 1986. ISSN 0021-9991. doi: http://dx.doi.org/10.1016/0021-9991(86)90052-5.

S. de Souza-Machado, M. Sarfaty, and F. Skiff. Kinetic modes in a hot magnetized and weakly collisional plasma. *Physics of Plasmas*, 6:2323–2331, June 1999. doi: 10.1063/1.873504.

J. Denavit. Simulations of the single-mode, bump-on-tail instability. *Physics of Fluids*, 28(9):2773–2777, 1985. doi: 10.1063/1.865236.

P H Diamond, S-I Itoh, K Itoh, and T S Hahm. Zonal flows in plasma - a review. *Plasma Physics and Controlled Fusion*, 47(5):R35, 2005.

J. Q. Dong, P. N. Guzdar, and Y. C. Lee. Finite beta effects on ion temperature gradient driven modes. *Physics of Fluids*, 30(9):2694–2702, 1987. doi: 10.1063/1.866034.

W. Dorland and G. W. Hammett. Gyrofluid turbulence models with kinetic effects. *Physics of Fluids B*, 5:812–835, March 1993. doi: 10.1063/1.860934.

The MPI Forum. Mpi: A message passing interface, 1993.

Matteo Frigo and Steven G. Johnson. The design and implementation of FFTW3. *Proceedings of the IEEE*, 93(2):216–231, 2005. Special issue on "Program Generation, Optimization, and Platform Adaptation".

Aaron Froese. Comparision of landau damping in two computer modes. 2005.

H. P. Furth, J. Killeen, and M. N. Rosenbluth. Finite-Resistivity Instabilities of a Sheet Pinch. *Physics of Fluids*, 6:459–484, 1963. doi: 10.1063/1.1706761.

Z. Gao, J. Q. Dong, G. J. Liu, and C. T. Ying. Analysis of ion temperature gradient modes in high β plasmas with sheared slab configuration model. *Physics of Plasmas*, 9:569–575, February 2002. doi: 10.1063/1.1436125.

Z. Gao, H. Sanuki, K. Itoh, and J. Q. Dong. Temperature gradient driven short wavelength modes in sheared slab plasmas. *Physics of Plasmas*, 10:2831–2839, July 2003. doi: 10.1063/1.1583712.

Z. Gao, H. Sanuki, K. Itoh, and J. Q. Dong. Short wavelength ion temperature gradient instability in toroidal plasmas. *Physics of Plasmas*, 12(2):022502, February 2005.

Zhe Gao, H. Sanuki, K. Itoh, and J. Q. Dong. Temperature gradient driven short wavelength modes in sheared slab plasmas. 10(7):2831–2839, 2003. ISSN 1070664X. doi: DOI:10.1063/1.1583712.

Zhe Gao, J. Q. Dong, and H. Sanuki. Effects of flow shear on temperature gradient driven short wavelength modes. *Physics of Plasmas*, 11(6):3053–3059, 2004. doi: 10.1063/1.1723422.

Zhe Gao, H. Sanuki, K. Itoh, and J. Q. Dong. Short wavelength electron temperature gradient instability in toroidal plasmas. 12(2):022503, 2005. ISSN 1070664X. doi: DOI:10.1063/1.1840709.

Tobias Görler. Multiscale effects in plasma microturbulence. 2009.

T. S. Hahm. Nonlinear gyrokinetic equations for tokamak microturbulence. *Physics of Fluids*, 31(9): 2670–2673, 1988. doi: 10.1063/1.866544.

D. R. Hatch, M. J. Pueschel, F. Jenko, W. M. Nevins, P. W. Terry, and H. Doerk. Origin of magnetic stochasticity and transport in plasma microturbulence. *Phys. Rev. Lett.*, 108:235002, Jun 2012. doi: 10.1103/PhysRevLett.108.235002.

R. D. Hazeltine and H. R. Strauss. Tokamak heat transport due to tearing modes. *Phys. Rev. Lett.*, 37: 102–104, Jul 1976. doi: 10.1103/PhysRevLett.37.102.

V. Hernandez, J. E. Roman, and V. Vidal. SLEPc: Scalable Library for Eigenvalue Problem Computations. *Lecture Notes in Computer Science*, 2565:377–391, 2003.

Vicente Hernandez, Jose E. Roman, and Vicente Vidal. SLEPc: A scalable and flexible toolkit for the solution of eigenvalue problems. *ACM Trans. Math. Software*, 31(3):351–362, 2005.

A. Hirose, M. Elia, A. I. Smolyakov, and M. Yagi. Short wavelength temperature gradient driven modes in tokamaks. *Physics of Plasmas*, 9:1659–1666, May 2002. doi: 10.1063/1.1469025.

S. P. Hirshman and Kim Molvig. Turbulent destabilization and saturation of the universal drift mode in a sheared magnetic field. *Phys. Rev. Lett.*, 42:648–651, Mar 1979. doi: 10.1103/PhysRevLett.42.648.

W. A. Hornsby, A. G. Peeters, A. P. Snodin, F. J. Casson, Y. Camenen, G. Szepesi, M. Siccinio, and E. Poli. The nonlinear coupling between gyroradius scale turbulence and mesoscale magnetic islands in fusion plasmas. *Physics of Plasmas*, 17(9):092301, 2010. doi: 10.1063/1.3467502.

W. A. Hornsby, A. G. Peeters, M. Siccinio, and E. Poli. On the dynamics of vortex modes within magnetic islands. *Physics of Plasmas*, 19(3):032308, 2012. doi: 10.1063/1.3692094.

J. D. Huba. NRL Plasma Formulary. Naval Research Laboratory, Washington, D.C., 2009.

Y. Idomura, M. Wakatani, and S. Tokuda. Gyrokinetic theory of slab electron temperature gradient mode in negative shear tokamaks. *Physics of Plasmas*, 7(6):2456–2468, 2000. doi: 10.1063/1.874085.

Yasuhiro Idomura, Tomo-Hiko Watanabe, and Hideo Sugama. Kinetic simulations of turbulent fusion plasmas. *Comptes Rendus Physique*, 7(6):650 – 669, 2006. ISSN 1631-0705. doi: 10.1016/j.crhy.2006.06.007.

Yasuhiro Idomura, Masato Ida, Shinji Tokuda, and Laurent Villard. New conservative gyrokinetic full-f vlasov code and its comparison to gyrokinetic particle-in-cell code. *Journal of Computational Physics*, 226(1):244 – 262, 2007. ISSN 0021-9991. doi: 10.1016/j.jcp.2007.04.013.

Kenji Imadera. Kinetic analysis based on lie perturbation theory for relativistic electron beam and global turbulent plasma transport. 2011.

Kenji Imadera, Yasuaki Kishimoto, Daisuke Saito, Jiquan Li, and Takayuki Utsumi. A numerical method for solving the vlasov, poisson equation based on the conservative ido scheme. *Journal of Computational Physics*, 228(23):8919 – 8943, 2009. ISSN 0021-9991. doi: 10.1016/j.jcp.2009.09.008.

A Isayama, Y Kamada, T Ozeki, and N Isei. Measurement of magnetic island width in long-pulse, high-β_n discharges in jt-60u. *Plasma Physics and Controlled Fusion*, 41(1):35, 1999.

A. Ishizawa and P. H. Diamond. Ion-temperature gradient modes affected by helical magnetic field of magnetic islands. *Physics of Plasmas*, 17(7):074503, 2010. doi: 10.1063/1.3460346.

Akihiro Ishizawa, Tomo-Hiko Watanabe, and Noriyoshi Nakajima. Gyrokinetic simulations of slab ion temperature gradient turbulence with kinetic electrons. *Plasma and Fusion Research*, 6:2403087–2403087, 2011.

Miho Janvier. Study of the nonlinear dynamics of double tearing modes to understand explosive magnetic reconnection in fusion and astrophysical plasmas. 2011.

F. Jenko, W. Dorland, M. Kotschenreuther, and B. N. Rogers. Electron temperature gradient driven turbulence. *Physics of Plasmas*, 7(5):1904–1910, 2000. doi: 10.1063/1.874014.

Kirby II Karniadakis. *Parallel Scientific Computing in C++ and MPI*. 2007.

Takafumi Kawano, Kenji Imadera, Jiquan Li, and Yasuaki Kishimoto. Numerical method for eulerian vlasov simulation based on multi-moment scheme. *Plasma and Fusion Research*, March 2011.

Georg Knorr. Plasma simulation with few particles. *Journal of Computational Physics*, 13(2):165 – 180, 1973. ISSN 0021-9991. doi: http://dx.doi.org/10.1016/0021-9991(73)90021-1.

Georg Knorr and Magdi Shoucri. Plasma simulation as eigenvalue problem. *Journal of Computational Physics*, 14(1):1 – 7, 1974. ISSN 0021-9991. doi: http://dx.doi.org/10.1016/0021-9991(74)90001-1.

R. A. Kolesnikov, W. W. Lee, H. Qin, and E. Startsev. High frequency gyrokinetic particle simulation. *Physics of Plasmas*, 14(7):072506, 2007. doi: 10.1063/1.2751600.

L.D. Landau. On the vibration of the electronic plasma. *J. Phys. USSR*, 10:25, 1946.

Xavier Lapillonne. Local and global eulerian gyrokinetic simulations of microturbulence in realistic geometry with applications to the tcv tokamak. 2009.

J. D. Lawson. Some Criteria for a Power Producing Thermonuclear Reactor. *Proceedings of the Physical Society B*, 70:6–10, January 1957. doi: 10.1088/0370-1301/70/1/303.

W.W Lee. Gyrokinetic particle simulation model. *Journal of Computational Physics*, 72(1):243 – 269, 1987. ISSN 0021-9991. doi: http://dx.doi.org/10.1016/0021-9991(87)90080-5.

Y. C. Lee, J. Q. Dong, P. N. Guzdar, and C. S. Liu. Collisionless electron temperature gradient instability. *Physics of Fluids*, 30(5):1331–1339, 1987. doi: 10.1063/1.866248.

Sanjiva K. Lele. Compact finite difference schemes with spectral-like resolution. *Journal of Computational Physics*, 103(1):16 – 42, 1992. ISSN 0021-9991. doi: DOI:10.1016/0021-9991(92)90324-R.

A. Lenard and Ira B. Bernstein. Plasma oscillations with diffusion in velocity space. *Phys. Rev.*, 112: 1456–1459, Dec 1958. doi: 10.1103/PhysRev.112.1456.

J. Li, L. Huang, and W. Qu. *Physics of Plasmas*, 5(4):959–965, 1998. doi: 10.1063/1.872664.

Jiquan Li, Y. Kishimoto, Y. Kouduki, Z.X. Wang, and M. Janvier. Finite frequency zonal flows in multi-scale plasma turbulence including resistive mhd and drift wave instabilities. *Nuclear Fusion*, 49 (9):095007, 2009.

Z. Lin and W. W. Lee. Method for solving the gyrokinetic Poisson equation in general geometry. Phys. Rev. E, 52:5646–5652, November 1995. doi: 10.1103/PhysRevE.52.5646.

N. F. Loureiro, S. C. Cowley, W. D. Dorland, M. G. Haines, and A. A. Schekochihin. x-point collapse and saturation in the nonlinear tearing mode reconnection. *Phys. Rev. Lett.*, 95:235003, Nov 2005. doi: 10.1103/PhysRevLett.95.235003.

F. Merz, C. Kowitz, E. Romero, J. E. Roman, and F. Jenko. Multi-dimensional gyrokinetic parameter studies based on eigenvalue computations. *Computer Physics Communications*, 183:922–930, April 2012. doi: 10.1016/j.cpc.2011.12.018.

N. Miyato, B. D. Scott, D. Strintzi, and S. Tokuda. A Modification of the Guiding-Centre Fundamental 1-Form with Strong $\mathbf{E} \times \mathbf{B}$ Flow. *Journal of the Physical Society of Japan*, 78(10):104501, October 2009. doi: 10.1143/JPSJ.78.104501.

Y. Morinishi, T.S. Lund, O.V. Vasilyev, and P. Moin. Fully conservative higher order finite difference schemes for incompressible flow. *Journal of Computational Physics*, 143(1):90 – 124, 1998. ISSN 0021-9991. doi: 10.1006/jcph.1998.5962.

David E. Muller. A method for solving algebraic equations using an automatic computer. *Mathematical Tables and Other Aids to Computation*, 10(56):pp. 208–215, 1956. ISSN 08916837.

M. Nakata, T.-H. Watanabe, H. Sugama, and W. Horton. Effects of parallel dynamics on vortex structures in electron temperature gradient driven turbulence. *Physics of Plasmas*, 18(1):012303, 2011. doi: 10.1063/1.3535584.

C. S. Ng, A. Bhattacharjee, and F. Skiff. Complete spectrum of kinetic eigenmodes for plasma oscillations in a weakly collisional plasma. *Phys. Rev. Lett.*, 92:065002, Feb 2004. doi: 10.1103/PhysRevLett.92.065002.

D.R. Nicholson. *Introduction to plasma theory.* Wiley series in plasma physics. Wiley, 1983. ISBN 9780471090458.

Y. Nishimura, Z. Lin, J.L.V. Lewandowski, and S. Ethier. A finite element poisson solver for gyrokinetic particle simulations in a global field aligned mesh. *Journal of Computational Physics*, 214(2):657 – 671, 2006. ISSN 0021-9991. doi: 10.1016/j.jcp.2005.10.011.

E. N. Parker. The Solar-Flare Phenomenon and the Theory of Reconnection and Annihiliation of Magnetic Fields. ApJS, 8:177, July 1963. doi: 10.1086/190087.

L. D. Pearlstein and H. L. Berk. Universal eigenmode in a strongly sheared magnetic field. *Phys. Rev. Lett.*, 23:220–222, Aug 1969. doi: 10.1103/PhysRevLett.23.220.

A. G. Peeters, D. Strintzi, Y. Camenen, C. Angioni, F. J. Casson, W. A. Hornsby, and A. P. Snodin. Influence of the centrifugal force and parallel dynamics on the toroidal momentum transport due to small scale turbulence in a tokamak. *Physics of Plasmas*, 16(4):042310, 2009. doi: 10.1063/1.3097263.

HE Petschek. The physics of solar flares. *NASA SP-50*, 425, 1964.

G. P. M. Poppe and C. M. J. Wijers. More efficient computation of the complex error function. *ACM Trans. Math. Softw.*, 16:38–46, March 1990. ISSN 0098-3500. doi: http://doi.acm.org/10.1145/77626.77629.

Jack Poulson, Bryan Marker, Robert A. van de Geijn, Jeff R. Hammond, and Nichols A. Romero. Elemental: A new framework for distributed memory dense matrix computations. *ACM Transactions on Mathematical Software*, 39(2):13:1–13:24, February 2013.

M.J. Pueschel, T. Dannert, and F. Jenko. On the role of numerical dissipation in gyrokinetic vlasov simulations of plasma microturbulence. *Computer Physics Communications*, 181(8):1428 – 1437, 2010. ISSN 0010-4655. doi: 10.1016/j.cpc.2010.04.010.

Jose E. Roman, Matthias Kammerer, Florian Merz, and Frank Jenko. Fast eigenvalue calculations in a massively parallel plasma turbulence code. *Parallel Computing*, 36(5-6):339–358, 2010. ISSN 0167-8191. doi: 10.1016/j.parco.2009.12.001. Parallel Matrix Algorithms and Applications.

D. W. Ross and S. M. Mahajan. Are drift-wave eigenmodes unstable. *Physical Review Letters*, 40: 324–327, January 1978. doi: 10.1103/PhysRevLett.40.324.

P. H. Rutherford. Nonlinear growth of the tearing mode. *Physics of Fluids*, 16(11):1903–1908, 1973. doi: 10.1063/1.1694232.

D D Ryutov. Landau damping: half a century with the great discovery. *Plasma Physics and Controlled Fusion*, 41(3A):A1, 1999.

Shinsuke Satake, Ryutaro Kanno, and Hideo Sugama. Development of a non-local neoclassical transport code for helical configurations. *Plasma and Fusion Research*, 3:S1062–S1062, 2008.

B. Scott. The gyrokinetic equation, 2006.

Ryutaro Kanno Shinsuke Satake and Hideo Sugama. Development of a non-local neoclassical transport code for helical configurations. *Proceedings of ITG/ISHW 2007*, 2008.

Magdi M. Shoucri. Nonlinear evolution of the bump-on-tail instability. *Physics of Fluids*, 22(10):2038–2039, 1979. doi: 10.1063/1.862470.

Albert Simon and Marshall N. Rosenbluth. Single-mode saturation of the bump-on-tail instability: Immobile ions. *Physics of Fluids*, 19(10):1567–1580, 1976. doi: 10.1063/1.861362.

A. I. Smolyakov, M. Yagi, and Y. Kishimoto. Short wavelength temperature gradient driven modes in tokamak plasmas. *Phys. Rev. Lett.*, 89:125005, Aug 2002. doi: 10.1103/PhysRevLett.89.125005.

H. R. Strauss. *Journal of Plasma Physics*, 57(01):83–87, 1997. doi: 10.1017/S0022377896005296.

P. A. Sweet. The Neutral Point Theory of Solar Flares. In B. Lehnert, editor, *Electromagnetic Phenomena in Cosmical Physics*, volume 6 of *IAU Symposium*, page 123, 1958.

G. Szepsi. Derivation of the fully electro=magnetic, non-linear, gyrokinetics vlasov-maxwell equations in a rotating frame of reference for gkw with lie transform perturbation method. 2012.

X. Lapillonne T. Görler, S. Brunner, T. Dannert, F. Jenko, F. Merz, and D. Told. The global version of the gyrokinetic turbulence code gene. *Journal of Computational Physics*, 230(18):7053 – 7071, 2011. ISSN 0021-9991. doi: 10.1016/j.jcp.2011.05.034.

P. W. Terry, D. A. Baver, and Sangeeta Gupta. Role of stable eigenmodes in saturated local plasma turbulence. *Physics of Plasmas*, 13(2):022307, 2006. doi: 10.1063/1.2168453.

The HDF Group. Hierarchical data format version 5, 2000-2013.

N.G. van Kampen. On the theory of stationary waves in plasmas. *Physica*, 21(6-10):949 – 963, 1955. ISSN 0031-8914. doi: 10.1016/S0031-8914(55)93068-8.

A.A. Vlasov. On the oscillation properties of an electron gas. *Zh.Eksper. Teoret. Fiz*, 1938.

CF von Weizsäcker. Über elementumwandlungen im innern der sterne. i. *Phys. Zs*, 38:176, 1937.

CF von Weizsäcker. Uber elementumwandlungen in innern der sterne. ii. *Physikalische Zeitschrift*, 39: 633, 1938.

Z. X. Wang, J. Q. Li, Y. Kishimoto, and J. Q. Dong. Magnetic-island-induced ion temperature gradient mode. 16(6):060703, 2009. ISSN 1070664X. doi: DOI:10.1063/1.3166600.

Tomo-Hiko Watanabe and Hideo Sugama. Kinetic simulation of a quasisteady state in collisionless ion temperature gradient driven turbulence. *Physics of Plasmas*, 9(9):3659–3662, 2002. doi: 10.1063/1.1501823.

J. Wesson and D.J. Campbell. *Tokamaks*. International series of monographs on physics. Clarendon Press, 2004. ISBN 9780198509226.

R. B. White. Resistive reconnection. *Reviews of Modern Physics*, 58:183–207, January 1986. doi: 10.1103/RevModPhys.58.183.

H.-S. Xie. A $1/t$ damped electrostatic electron plasma wave. *ArXiv e-prints*, April 2013.

Shanjie Zhang and Jianming Jin. *Computation of special functions*. 1996. ISBN 0-471-11963-6.

Gao Zhe. A new kinetic mode driven by electron temperature gradient. *Chinese Physics Letters*, 21(5): 881, 2004.